Wideband Circularly Polarized Elements and Arrays for Wireless Systems

By

Long Zhang

A Thesis Submitted to the University of Kent
For the Degree of Doctor of Philosophy
In Electronic Engineering

June 2017

Abstract

Circularly polarized (CP) antennas have received increasing interest during recent decades due to their unique features such as the mitigation of multi-path fading, reduction of the "Faraday rotation" effect when signals propagate through the ionosphere and immunity of the polarization mismatching between transmitting and receiving antennas. Due to the requirements of high date rate and large system capacity, CP antennas deployed in various wireless systems are always demanded to have wide bandwidth. Furthermore, other system requirements such as polarization diversity, wide-angle beam scanning and low power consumption impose additional requirements to CP antennas. Therefore, it is becoming a more stringent requirement to design wideband CP antennas with diverse features to fulfill the requirements of various wireless systems.

In this thesis, six different types of wideband CP antenna elements and arrays are designed, fabricated and characterized to meet the different demands of wireless systems. Chapters 3-5 investigate three different types of wideband CP antenna elements while Chapters 6-8 investigate three different kinds of wideband CP array antennas. In Chapter 3, an ultra-wideband CP element with a bandwidth of 100% (3:1) is proposed. It overcomes the problem of limited 3 dB axial ratio (AR) bandwidth for single-feed CP antennas and achieves high front-to-back ratio (FBR) by using a novel ground plane with simple configuration, which makes it a good candidate for high-performance Global Navigation Satellite System (GNSS) receivers. Chapter 4 presents a wideband loop antenna with electronically switchable circular polarizations. It solves the issue of narrow overlapped bandwidth under different polarization states for a polarization reconfigurable CP antenna. Because of the available orthogonal polarizations across a wide bandwidth, this antenna can be deployed in wireless communications which implement polarization diversity. The third antenna element investigated in Chapter 5 tackles the difficulty of designing wideband wide AR beamwidth CP antennas. It achieves wide AR beamwidth within a 42% bandwidth, which is suitable for wideband wide-angle CP beam-scanning applications.

The second main part of this thesis focuses on the investigation of wideband CP arrays. In Chapter 6, a dual-CP beam-scanning array is investigated, which can scan its beam independently in right-hand circular polarization (RHCP) and left-hand polarization (LHCP) from 27 GHz to 30 GHz. It tackles the problem of low isolation between the two orthogonally polarized ports across a wide bandwidth at Ka-band. A single-layer high-

efficiency CP reflectarray is proposed in the following Chapter. The proposed design solves the issues of bandwidth limitation and low aperture efficiency for single-layer CP reflectarrays. It achieves the widest bandwidth compared with other CP reflectarrays reported in terms of 3 dB AR bandwidth, 3 dB gain bandwidth, larger than 50% aperture efficiency and undistorted radiation pattern bandwidth. In Chapter 8, we investigate the first application of tightly coupled array (TCA) concept into ultra-wideband arrays with CP radiation. Instead of trying to reduce the mutual coupling among the elements, it exploits the strong mutual coupling to improve the bandwidth of a CP array. By using the strong coupling in a constructive way, it overcomes the bandwidth limitation of CP arrays which are constituted by narrow-band elements.

Acknowledgement

At first, I would like to express my sincere gratitude to my supervisor, Prof. Steven Gao who has offered me important supports both financially and mentally during the tough and long voyage. Without his support and guidance, I would not able to complete my PhD research work. It really benefits me a lot during all the discussions and talks with him in the past three years and I also believe that all these benefits will be helpful to my future career.

I would also like to thank Dr. Paul R. Young as my co-supervisor. He has helped me a lot in preparing manuscripts. His profound knowledge on microwave circuits and SIWs have broadened my research interests and helped bridge some of my research works.

I also thank Dr. Qi Luo for his help on revising manuscripts, carrying out research projects and all other daily routines. His help smooth the majority of my difficulties.

I would like to thank all the current and past team members, Mr. Wenting Li, Mr. Chao Gu, Mr. Hang Xu, Mr. Chunxu Mao, Dr. Yunaming Cai, Dr. Fan Qin, for their kind help and suggestions to my research work.

Special thanks to Mr. Simon Jakes who has helped me fabricate all the antennas. Hopefully, I could meet someone with such excellent fabrication skills in the future. I also thank the academic staff, technicians and colleagues at the School of EDA who has helped me during my PhD study period.

Finally, I would like to thank my parents and my wife who gave me persistent encouragements during all these years. No matter wherever I am, they will be always by my side and help me get through all the difficulties.

Contents

Abbreviation

CP	Circularly Polarized
AR	Axial Ratio
RHCP	Right-Hand Circular Polarization
LHCP	Left-Hand Circular Polarization
LP	Linearly Polarized
GNSS	Global Navigation Satellite System
RFID	Radio Frequency Identification
WLAN	Wireless Local Area Networks
DBS	Direct Broadcasting Services
FBR	Front-to-Back Ratio
GPS	Global Positioning System
IRNSS	Indian Regional Navigation Satellite System
LOS	Line of Sight
MIMO	Multiple Input Multiple Output
OFDM	Orthogonal Frequency Division Multiplexing
RA	Reflectarray
HPBW	Half-Power Beamwidth
AE	Aperture Efficiency
UWB	Ultra-wideband
CPW	Coplanar Waveguide

VHF	Very High Frequency
CPS	Coplanar Stripline
Balun	Balanced-to-Unbalanced
Co-pol	Co-polarization
Cross-pol	Cross Polarization
MEFSSs	Miniaturized-Element Frequency Selective Surfaces
TDU	Time Delay Unit
SMM	Spiral-Mode Microstrip
CPRGP	Compact-Size Cross-Plate Reflector Ground Plane
VSWR	Voltage Standing Wave Ratio
PIN	Positive Intrinsic Negative
PET	Piezoelectric Transducer
DC	Direct Current
RF	Radio Frequency
HFSS	High-Frequency Structure Simulator
ADS	Advanced Design System
SPDT	Single-Pole Double-Throw
BFN	Beam-Forming Network
F/D	Focal Length to Diameter Ratio
BW	Bandwidth
TCA	Tightly Coupled Array

TCDA	Tightly Coupled Dipole Array
CP-TCCDA	Circularly Polarized Tightly Coupled Crossed Dipole Array
QoS	Quality of Service
MM-Wave	Millimeter-Wave
SIW	Substrate Integrated Waveguide

List of Figures

List of Tables

Chapter 1. Introduction

1.1 Motivation

Circularly polarized (CP) antennas are a type of antenna with the tip of the radiated electric-field vector rotated along a circle [1]. They have several distinctive advantages compared with linearly polarized (LP) antennas, such as the mitigation of multi-path interferences or fading [2, 3], the ability to reduce 'Faraday rotation' effect caused by the longitudinal magnetic field originating from the plasma in the ionosphere [4, 5] and the immunity of polarization mismatching between transmitting and receiving antennas [6]. Because of these advantages, CP antennas are widely deployed in various wireless systems including satellite communications, Global Navigation Satellite System (GNSS), wireless power transmission, radio frequency identification (RFID), mobile communications, wireless local area networks (WLAN) and Direct Broadcasting Services (DBS).

On the increasing demand of larger system capacity and higher data rate to wireless systems, antennas are usually required to have wide bandwidth. Different to the bandwidth requirements for LP antennas, the bandwidth requirements for CP antennas are more stringent since both the impedance bandwidth and the axial ratio (AR) bandwidth need to be considered. Normally, the AR bandwidth of a CP antenna is narrower than its impedance bandwidth or they are not completely overlapped, which results in a decreased available bandwidth. In addition to the bandwidth requirements, it is preferable to design a CP antenna with other attractive features such as low profile, compact structure, low cost, simple feeding configuration, high front-to-back ratio (FBR), reconfigurable ability, and wide AR beamwidth, etc. It is very challenge to design a wideband CP antenna which has all aforementioned features. Therefore, different wideband CP antennas with diverse features are needed for various wireless systems.

One main application of CP antennas is their wide deployment in GNSS systems which have found important applications globally in both the military arena as well as commercial and consumer markets [7]. To increase the positioning speed, reliability and availability, the antenna should be able to receive signals from various navigation systems such as global positioning system (GPS), GLONASS, Galileo, Compass and even Indian Regional Navigation Satellite System (IRNSS). Consequently, the operation bandwidth of a high-performance GNSS antenna should extend from 1.1 GHz to 1.62 GHz and even 2.5 GHz (for IRNSS) with good circular polarization properties. Moreover, since non-LOS (line of sight) multi-path signals could be generated by reflection of satellite signals, the

system performance will be degraded once these multi-path signals are received by antennas [8]. Utilization of a choke ring ground plane is an effective way to mitigate multi-path signals through suppression of plane wave propagating along ground planes [9]. However, the limited working bandwidth and bulky structure make the choke ring ground plane not suitable for wideband application and expensive to fabricate. Therefore, there is an urgent demand to design a wideband CP antenna covering the whole GNSS bands (from 1.1 GHz to 2.5 GHz) with good multi-path mitigation ability.

Another fascinating application of CP antennas is their expandability to reconfigurable antennas. One aspect of their unique re-configurability is to design polarization reconfigurable antennas which can radiate in right-hand circular polarization (RHCP) and left-hand circular polarization (LHCP). It is known that CP polarization reconfigurable antennas can be used to implement polarization diversity for wireless communications [10] and realize frequency reuse for system capacity improvement in satellite communication systems [11]. The channel capacity of a 2×2 MIMO orthogonal frequency division multiplexing (OFDM) system is improved by using CP reconfigurable antennas compared with the single polarization system under both LOS and non-LoS indoor environment [12]. In spite of these advantages, the introduction of polarization re-configurability makes it harder to design wideband CP antennas along with this distinct feature.

Besides improving the bandwidth of CP antennas, widening the AR beamwidth has received increasing interest due to their applications in GNSS systems [7] and wide-angle CP beam-scanning arrays [13]. Several researches on this topic were reported including a square-ring slotted patch antenna [14], an asymmetric microstrip antenna with integrated circular-patches [15] and an elliptical vertical patch antenna backed by an elliptical air cavity [16]. Although these CP antennas can achieve more than 120^{o} AR beamwidth, their AR bandwidths are smaller than 5%. For high-data-rate wireless systems with the additional requirement on wide-angle CP beam-scanning, it is necessary and also very challenging to design wideband CP antennas with simultaneous wide AR beamwidth.

On the other hand, array antennas are necessary when high gain performance is desired for wireless systems. Recently, designing wideband CP arrays is becoming increasingly important to multifunctional systems, high-data-rate communication links, high-resolution radar and tracking systems, software radios and electronic warfare applications [17-19]. Traditional arrays usually comprise a great number of elements and rather complicated feeding networks. To simplify the feeding structure of array antennas, reflectarrays (RAs) are promising alternatives. However, one major drawback of RAs is their

narrow bandwidth due to the inherent narrow bandwidth of microstrip elements and the differential spatial phase delay [20]. Considering that it is more difficult to design elements with wideband CP reflection performance and wideband CP feeds, the bandwidth enhancement of CP reflectarrays is thus more challenging than LP reflectarrays.

It is widely considered that the mutual coupling in arrays deteriorates their performance. Nevertheless, Munk used strongly coupled short dipoles to design a wideband array which achieved an impedance bandwidth of 4.5:1 [21]. This reveals a new kind of wideband array, the tightly coupled array. Although various designs based on this concept have achieved several octave bandwidths, they are all linearly polarized and only the impedance bandwidth improvement is considered. On this occasion, designing a CP tightly coupled array for the first time is thus indispensable and valuable.

In summary, there are different requirements for CP antennas when they are deployed in various wireless systems. Among these requirements, large bandwidth is usually desired. In addition, CP antennas need to be designed elaborately for different systems to fulfill diverse objectives.

1.2 Main Contributions

The major novelty and contributions of this research are summarized as follows:

I. The design of an ultra-wideband CP antenna with enhanced front-to-back ratio (FBR) for GNSS application

- The proposed CP antenna has an impedance bandwidth and AR bandwidth of 3:1 (1.0 GHz to 3.0 GHz) which can fully cover the whole GNSS bands.
- A simple but effective impedance matching method to achieve broadband impedance matching
- A novel cavity is proposed to achieve high FBR.
- The antenna has average 30dB FBR across the GNSS bands for multi-path mitigation.

II. The design of a wideband polarization reconfigurable CP loop antenna for application of polarization diversity in wireless communications

- The presented antenna can switch its polarization to RHCP or LHCP electronically within a wide bandwidth.

- Detailed theoretical analysis of the impedance matching method which uses a single-section transmission line with specific characteristic impedance and non-quarter wavelength length to match an antenna with a complex input impedance
- Size reduction of the CP loop antenna

III. The design of a wideband inverted S-shaped CP antenna with wide AR beamwidth for wide-angle CP beam-scanning application

- A novel inverted "S" antenna with a simple configuration and wide AR bandwidth
- The antenna achieves maximum 140^{o} 3 dB AR beamwidth with a rear ground plane.
- The AR beamwidth of the inverted "S" antenna is larger than the half-power beamwidth (HPBW) in nearly all elevation planes within a wide bandwidth

IV. The development of a multi-layer wideband dual-CP patch array for Ka-band satellite communications

- The presented multi-layer patch array is able to implement dual-CP operation at 30 GHz.
- Unequal-length crossed slots are etched on the parasitic patch to improve the AR performance.
- High isolation between the RHCP and LHCP ports
- Independent beam-scanning ability in orthogonal polarizations

V. The development of a single-layer wideband high-efficiency CP reflectarray for satellite communications

- A novel reflectarray phasing element which achieves 2:1 CP bandwidth
- The proposed reflectarray has the widest bandwidth in terms of 3 dB AR bandwidth, larger than 50% aperture efficiency (AE) bandwidth and 3 dB gain bandwidth compared with other reported single-layer CP reflectarrays.
- The proposed reflectarray can maintain pencil-shaped beams, low sidelobe (-15dB) and low cross-pol (-15dB) across a 2:1 bandwidth.

VI. The development of an ultra-wideband tightly coupled array with circular polarization

- It is the first CP tightly coupled array which aims to improve the AR bandwidth of a CP array by taking advantages of strong mutual coupling among the elements.
- Detailed analysis of AR bandwidth improvement principles as well as the limitation of the AR bandwidth enhancement of the proposed array
- A planar and relatively simpler power divider network compared with those used in LP tightly coupled array

1.3 Publication List

Journal Publications

[1] **L. Zhang**, S. Gao, Q. Luo, P. R. Young, et al., "Single-Feed Ultra-Wideband Circularly Polarized Antenna with Enhanced Front-to-Back Ratio," IEEE Transactions on Antennas and Propagation, vol. 64, pp. 355 - 360, Jan. 2016.

[2] **L. Zhang**, S. Gao, Q. Luo, P. R. Young and Q. Li, "Planar Ultra-Thin Small Beam-Switching Antenna," IEEE Transactions on Antennas and Propagation, vol. 64, pp. 5054 - 5063, Dec. 2016.

[3] **L. Zhang**, S. Gao, Q. Luo, P. R. Young, et al., "Inverted-S Antenna with Wideband Circular Polarization and Wide Axial Ratio Beamwidth," IEEE Transactions on Antennas and Propagation, vol. 65, pp. 1740 - 1748, Apr. 2017.

[4] **L. Zhang**, S. Gao, Q. Luo, P. R. Young and Q. Li, "Wideband Loop Antenna with Electronically Switchable Circular Polarization," IEEE Antennas and Wireless Propagation Letters, vol. 16, pp. 242 - 245, 2017.

[5] **L. Zhang**, S. Gao, Q. Luo, W. Li and Q. Li, "Single-Layer Wideband Circularly Polarized High-Efficiency Reflectarray for Satellite Communications," IEEE Transactions on Antennas and Propagation, major revision.

Conference Publications

[1] L. Zhang, S. Gao, Q. Luo and W. Li, "Wideband Circularly Polarized Wide-Beamwidth Antenna Using S-Shaped Dipole," International Workshop on Antenna Technology (iWAT), 2017. (**Shortlisted to the best student paper finalist**)

[2] L. Zhang, S. Gao, Q. Luo and Y. Geng, "Low-profile compact-size electronically beam-switching antenna for wireless communications," European Conference on Antennas and Propagation (EuCAP), 2015.

[3] L. Zhang, S. Gao and Q. Luo, "Polarization reconfigurable loop antenna for satellite communications," Loughborough Antennas and Propagation Conference (LAPC), 2014.

1.4 Outline of Thesis

This thesis is organized into nine chapters.

Chapter 1 provides a brief description of the research background and motivation. Moreover, the main novelty and contribution of this thesis have been summarized.

Chapter 2 describes the state-of-the-art on wideband CP antenna elements and arrays. Different methods to achieve CP radiation and relevant operating principles are introduced. Then, various wideband CP elements and arrays are reviewed and the chapter is ended with some remarks on design objectives and considerations.

Chapter 3 presents the detailed design, fabrication and characterization of an ultra-wideband CP antenna with improved FBR. The antenna configuration is explained along with its working mechanisms. Then a novel cavity is proposed to improve the antenna performance. The operating principle of the proposed cavity is also provided. The performance of this UWB CP antenna is verified by measurement results and the comparison with other wideband CP antennas of the same type to demonstrate its distinct advantages.

Chapter 4 illustrates the design of wideband polarization reconfigurable CP loop antennas. Firstly, a dual-loop antenna which can radiate LHCP, RHCP and LP waves is presented. To reduce its size, a single-loop antenna with switchable LHCP and RHCP radiation is proposed. The impedance matching method for these two CP loop antennas is analyzed in detail and can also be used in other antennas. Both simulation and measurement results indicate that the presented CP loop antennas have wideband polarization reconfigurable ability.

Chapter 5 presents the design of a novel inverted S-shaped CP antenna with wide AR bandwidth and wide AR beamwidth. The CP operating principles and the mechanism of wide AR beamwidth are both explained. To validate the design concept, an inverted S-shaped element and a 4-element linear array are fabricated and measured. The measurement results confirm that both the element and linear array have wide bandwidth and wide AR beamwidth characteristics.

Chapter 6 presents the development of a wideband dual-CP array for Ka band satellite communications. The multi-layer CP patch element with modified parasitic patch is characterized at first. Based on this wideband patch element, a dual-CP array which can radiate in both RHCP and LCHP state is designed, fabricated and measured.

Chapter 7 describes the development of a single-layer wideband high-efficiency CP reflectarray. Firstly, the design of the unit cell and its reflection performance is provided. Then, a wideband CP reflectarray based on this element is designed. Theoretical analysis is given to analyze the effect of the angularly rotated elements to the performance of the reflectarray as well as the influence of differential spatial phase delay. Finally, a 15×15 element reflectarray is fabricated and characterized to verify the analysis and the design concept.

Chapter 8 presents the development of a wideband CP tightly coupled array. To begin with, LP tightly coupled arrays are reviewed briefly. Then the tightly coupled unit cell is proposed and simulated. Following the improved bandwidth compared to the isolated element of the same size, the principles of AR bandwidth improvement is provided and verified by simulation results. Finally, a 4×4 CP tightly coupled array along with the complete feeding network is prototyped and measured.

Chapter 9 concludes the entire thesis by highlighting the research outcomes and provides insight into possible future work.

Chapter 2. Literature Review

2.1 Introduction

Various CP antenna elements and arrays have been designed and proposed. To classify these CP antennas, terminologies such as "single-feed" and "dual-feed" are usually used to sort the CP antennas in terms of the feeding configuration. Instead of using these apparent terminologies which describe the geometrical characteristics of CP antennas, this chapter will start with the design theory and methodologies of CP antennas, which gives an in-depth understanding of the operating principles of different CP antennas. The CP antennas can also be classified by their different operating mechanisms.

Due to the increasing demands for larger capacity and higher data rate in wireless systems, CP antennas are required to achieve wider bandwidth. During recent decades, a variety of wideband CP antennas have been proposed for applications in various wireless systems. To give an overview of these wideband CP antennas, the state-of-art on wideband CP antennas are reviewed in the manner of different operating principles. At the end of the third section, a table summarizing the performances of these antennas is presented.

In the circumstances where signal transmitter and receiver are placed far apart, array antennas with higher gain are always desired to overcome the free-space losses. The design methodologies of CP array antennas are partly overlapped to LP array antennas while there are some particular design approaches for CP arrays such as the sequential rotation method. For a clearly understanding of the wideband CP array antennas, different types of wideband CP arrays are reviewed in detail in the fourth section of this chapter. A table which gives the comparison of these wideband CP arrays is also presented at the end of this section.

Based on the review of wideband CP antenna elements and arrays, a brief summary is given. Some major design objectives for the further development of wideband CP elements and arrays are also listed at the end of this chapter.

2.2 Design Theory and Methodology

As is well known, there are numerous antennas developed with CP radiation. Although they are of different geometries, they can roughly be divided into three types according to their CP operating principles. The first type is associated with patch antennas, which uses the two orthogonal modes of TM_{10} and TM_{01} to obtain CP radiation. The second type is originated from the definition of a CP wave, which aims to produce two

orthogonal electric fields with quadrature phase difference. The last type relates to the widely deployed spiral antennas and helical antennas, which takes advantage of travelling-wave current along curved structures. This section describes these three approaches with the aim of providing a theoretical foundation for the whole thesis.

2.2.1 Using Orthogonal Modes of Patch Antennas

For a rectangular microstrip patch antenna shown in Figure 2.1, it is well known that the dominant mode with the lowest resonant frequency is either TM_{010}^{x} (if $L > W > h$) or TM_{001}^{x} (if $W > L > h$) [22]. According to the cavity model of the patch antenna, we could sketch the distributions of the tangential electric field along the side walls of the cavity for these two modes, which are shown in Figure 2.2.

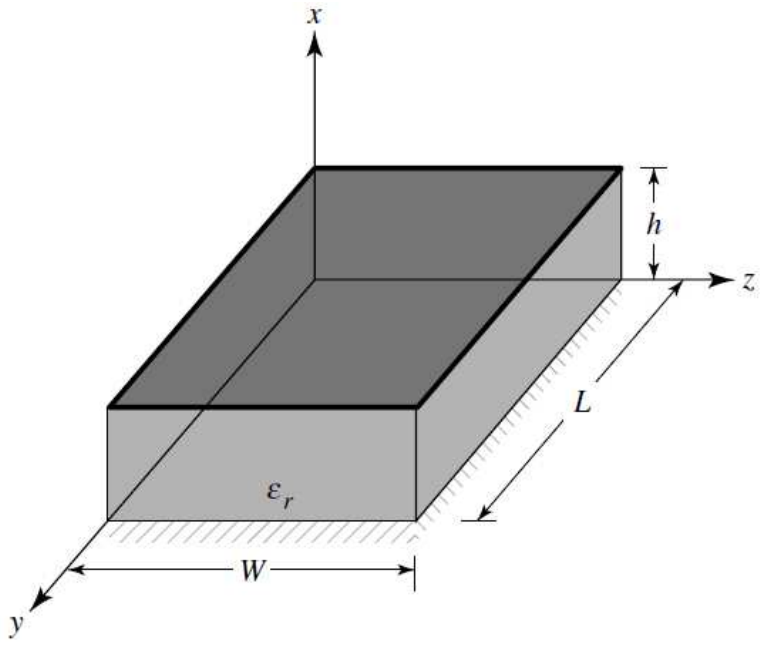

Figure 2.1 Geometry of a rectangular microstrip patch antenna [22].

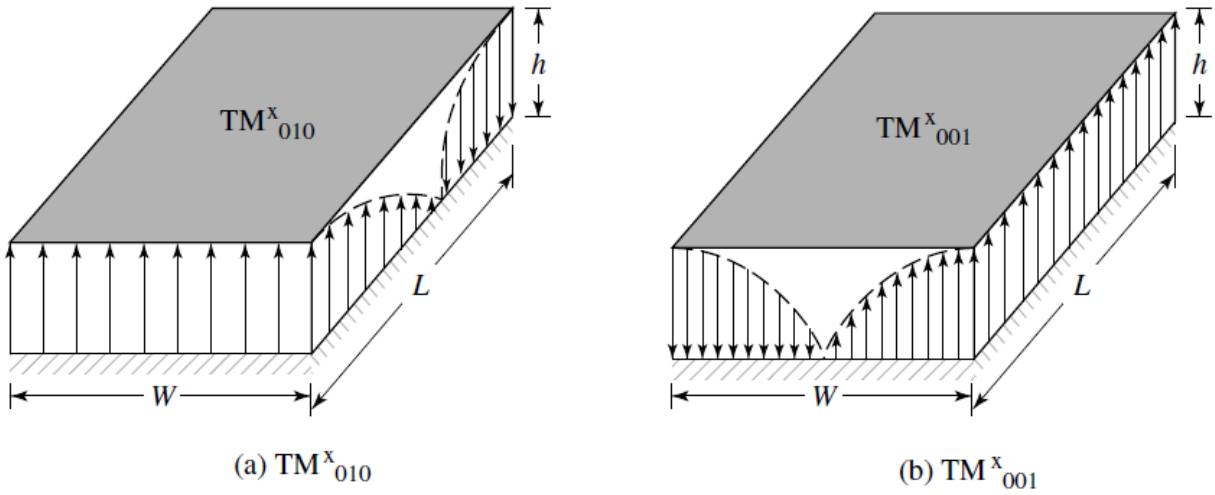

(a) TM x 010 (b) TM x 001

Figure 2.2 Distributions of the tangential electric field for two orthogonal modes [22].

To obtain CP radiation from a patch antenna, the two orthogonal modes need to be excited simultaneously with a 90° phase difference. This can be accomplished by adjusting the physical dimensions of the patch antenna and using either single, or two, or more feed [22]. For a square patch antenna, the easiest way to achieve CP radiation is to feed the element at two adjacent edges with quadrature phase difference, as shown in Figure 2.3. The feeding at one edge excites the TM_{010}^{x} mode while excites TM_{001}^{x} mode at the other edge. The 90° phase difference can be provided by a 90° power divider or a 90° hybrid.

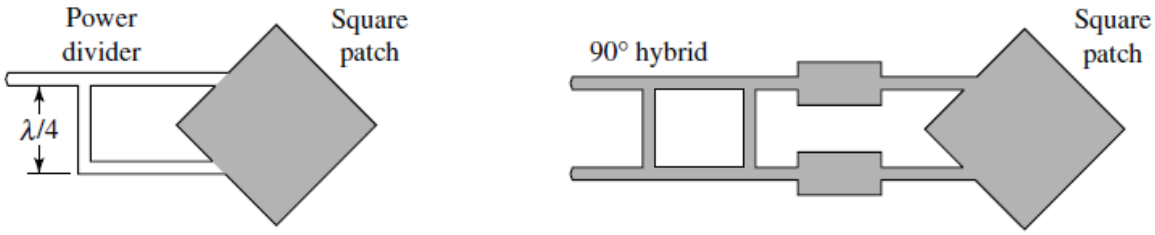

Figure 2.3 Square patch for CP radiation [22].

Although the above method achieves good CP radiation, the external 90° power divider and the 90° hybrid increase the complexity of the antenna. Patch antennas can also obtain CP radiation with a single feed. One way to accomplish this is to feed the patch at specific feeding point to excite two orthogonal degenerate modes. By introducing an appropriate asymmetry to the patch, these two modes will have slightly different resonant frequencies. It is thus possible that the radiated electric field of one mode can lead by 45° while that of the other can lag by 45° and thus a quadrature phase difference can be obtained between these two degenerated modes at some frequencies [23].

To illustrate how the CP radiation is established through using orthogonal degenerated modes, a brief analysis is given as follows. Considering a nearly square patch ($L \approx W$) shown in Figure 2.4, two orthogonal modes TM_{010}^{x} and TM_{001}^{x} can be excited once the feeding point is in the diagonal line of the patch.

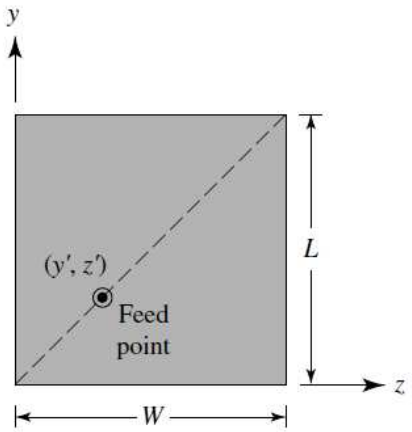

Figure 2.4 Geometry of a nearly square patch [22].

In the broadside direction, the TM_{010}^{x} mode produces a far-field electric field E_y which is linearly polarized along y direction while the TM_{001}^{x} mode produces a far-field electric field E_z which is linearly polarized along z direction [22]. These fields can be expressed as

$$E_y = c\frac{\sin(\pi y'/L)}{k^2(1-j/Q_t)-\left(k_y\right)^2} \tag{2.1}$$

$$E_z = c\frac{\sin(\pi z'/W)}{k^2(1-j/Q_t)-(k_z)^2} \tag{2.2}$$

$$k_y = \frac{\pi}{L} \tag{2.3}$$

$$k_z = \frac{\pi}{W} \tag{2.4}$$

where c is a constant and Q_t represents the total quality factor of the antenna. Since the feed point $(y',\ z')$ is selected along the diagonal so that

$$\frac{y'}{L} = \frac{z'}{W} \tag{2.5}$$

Substituting (2.5) to (2.1) and (2.2), then the ratio of E_y and E_z is

$$\frac{E_y}{E_z} = \frac{k^2(1-j/Q_t)-(k_z)^2}{k^2(1-j/Q_t)-\left(k_y\right)^2} \tag{2.6}$$

To obtain CP radiation in broadside direction, E_y/E_z should be $e^{\pm j\pi/2}$ [24]. From the derivation in [22, 24], $E_y/E_z = e^{\pm j\pi/2}$ yields

$$\frac{L}{W} = 1 + \frac{1}{Q_t} \tag{2.7}$$

Thus, good CP radiation can be achieved at boresight if a nearly square patch with the length and width ratio given by (2.7) is excited with a feed along the diagonal. The CP operating frequency is between the two resonant frequencies of the TM_{010}^{x} and TM_{001}^{x} modes.

Besides feeding the nearly square patch antenna along the diagonal, other methods can also be applied to excite the two orthogonal degenerate modes. These methods include cutting thin slots on the patch [25] and using a corners-truncated patch [26].

2.2.2 Using Orthogonal Electric Fields in Phase Quadrature

The radiated electric field of a CP antenna can be written in the following form

$$\vec{E}(\theta,\varphi) = \vec{\theta}E_\theta(\theta,\varphi)e^{j\emptyset_1} + \vec{\varphi}E_\varphi(\theta,\varphi)e^{j\emptyset_2} \tag{2.8}$$

where $E_\theta(\theta,\varphi)$ and $E_\varphi(\theta,\varphi)$ denote the magnitudes of the radiated electric fields, $\emptyset_1$ and $\emptyset_2$ denote the phase of the radiated electric fields.

CP radiation can be obtained once

$$E_\theta(\theta,\varphi) = E_\varphi(\theta,\varphi) \tag{2.9}$$

$$\emptyset_1 - \emptyset_2 = \pm\pi/2 \tag{2.10}$$

From (2.8) to (2.10), it is evident that a CP antenna can be designed by exciting two orthogonal electric fields in phase quadrature. One straightforward way to realize this condition is to feed two dipoles which are placed perpendicularly to each other with 90^o phase difference, as shown in Figure 2.5.

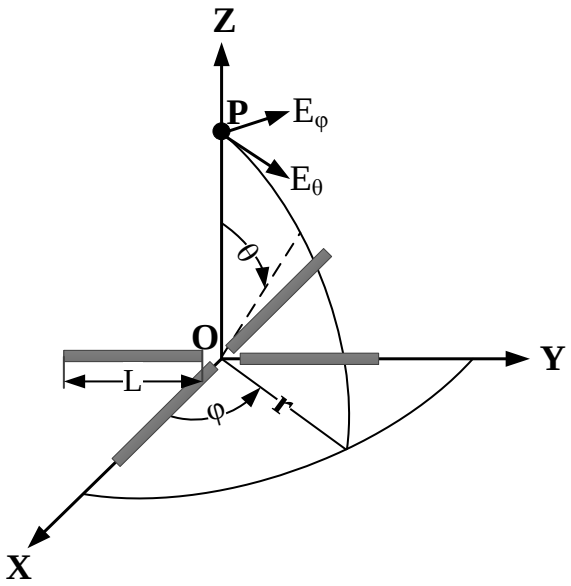

Figure 2.5 Geometrical arrangement of crossed dipoles with quadrature phase difference.

According to the classical antenna theory [22], the electric field radiated by the dipole placed along x-axis in the **xoz** plane can be written as

$$E_{\theta 1}(\theta,\varphi) = j\eta\frac{I_1 e^{-jkr}}{2\pi r}\left[\frac{\cos\left(kL\cos\left(\frac{\pi}{2}-\theta\right)\right)-\cos(kL)}{\sin\left(\frac{\pi}{2}-\theta\right)}\right] \tag{2.11}$$

$$E_{\varphi 1}(\theta,\varphi) = 0 \tag{2.12}$$

where η is the intrinsic impedance of the medium, which equals to 120π for free space; I_1 is the magnitude of electric current flowing along the dipole; k is the free space wave number.

If half-wavelength dipole is used, then (2.11) can be rewritten as

$$E_{\theta 1}(\theta,\varphi) = j\frac{60 I_1 e^{-jkr}}{r}\left[\frac{\cos\left(\frac{\pi}{2}\cos\left(\frac{\pi}{2}-\theta\right)\right)}{\sin\left(\frac{\pi}{2}-\theta\right)}\right] \tag{2.13}$$

Similarly, the electric field radiated by the dipole placed along y-axis in the **yoz** plane can be written as

$$E_{\theta 2}(\theta, \varphi) = j\frac{60I_2 e^{-jkr}}{r}\left[\frac{\cos\left(\frac{\pi}{2}\cos\left(\frac{\pi}{2}-\theta\right)\right)}{\sin\left(\frac{\pi}{2}-\theta\right)}\right] \tag{2.14}$$

Notice that the electric field direction of the dipole along x-axis is actually in x direction at boresight while the electric field direction of the second dipole along y-axis is actually in y direction at the boresight, the radiated electric fields of the two dipoles are thus orthogonal to each other at the observation point P in z-axis. From (2.13) and (2.14), the magnitudes of these two orthogonal electric fields will be identical if the two dipoles are fed equally ($I_1 = I_2$). Introducing 90^o phase difference between the feed of these two dipoles will bring quadrature phase difference between the two radiated orthogonal electric fields, which fulfills the requirement of (2.10). Therefore, good CP radiation can be achieved in broadside direction if the two perpendicularly placed dipoles are fed equally with quadrature phase differences.

2.2.3 Generating Travelling-Wave Electric Current along Curved Structure

The third way to obtain CP radiation is generating travelling-wave electric current along a curved structure, such as a spiral, helical or loop structure. As the nature of these types of antenna is similar, for a brief explanation of the CP radiation, only the case of travelling-wave current along a loop structure is considered here.

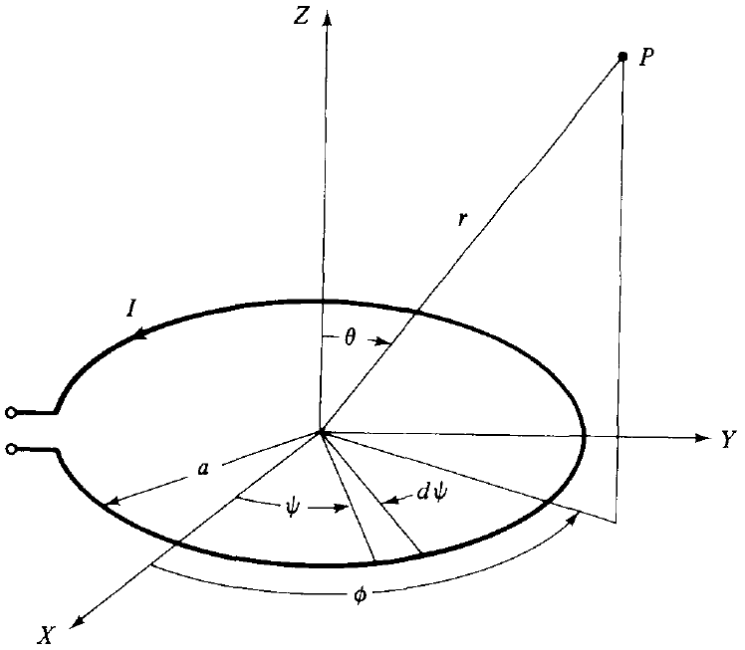

Figure 2.6 One-wavelength loop with travelling-wave electric current [1].

Considering a one-wavelength loop antenna ($ka = 1$), as shown in Figure 2.6, is placed in free space and supports an electric current distribution $Ie^{j(\omega t - ka\psi)}$. Notice that ψ denotes the angle measured form the x-axis and $ka = 1$, thus the current distribution $Ie^{j(\omega t - ka\psi)}$ indicates the amplitude of the electric current along the loop is constant and the phase of the electric current undergoes progressive variation along the loop, which represents a travelling-wave current distribution.

The far-field electric field E_θ and E_φ of this loop antenna can be represented by [1]

$$E_\theta(\theta, \varphi) = (4jIa\cos\theta)e^{-j\varphi}\int_0^{\pi/2} \sin^2\psi \cos(\sin\theta\cos\psi)d\psi \tag{2.15}$$

$$E_\varphi(\theta, \varphi) = (4Ia)e^{-j\varphi}\int_0^{\pi/2} \cos^2\psi \cos(\sin\theta\cos\psi)d\psi \tag{2.16}$$

The normalized plots of $|E_\theta|$ and $|E_\varphi|$ in the elevation plane are shown in Figure 2.6. As shown, the one-wavelength loop antenna with travelling-wave current distribution has a figure of eight pattern for E_θ and an almost omnidirectional pattern for E_φ. More importantly, it is observed that $|E_\theta| = |E_\varphi|$ at $\theta = 0^o$ and $\theta = 180^o$ direction.

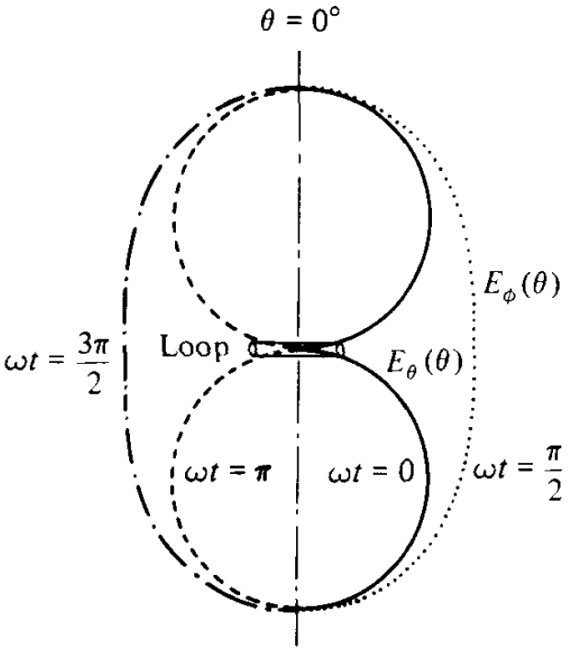

Figure 2.7 Normalized E-field patterns of a travelling-wave loop antenna [1].

Substituting $\theta = 0^o$ to (2.15) and (2.16), we could rewrite them as

$$E_\theta(\theta, \varphi) = j\pi Iae^{-j\varphi} = \pi Iae^{-j\varphi}e^{j\pi/2} \tag{2.17}$$

$$E_\varphi(\theta, \varphi) = \pi Iae^{-j\varphi} \tag{2.18}$$

Dividing (2.17) by (2.18) yields $e^{j\pi/2}$, which indicates that pure CP radiation can be obtained at $\theta = 0^o$. Likewise, pure CP radiation can also be achieved at $\theta = 180^o$.

2.3 Wideband CP Antennas

Different approaches to the design of CP antennas were introduced in the preceding sections. The design examples given are of the simplest form and generally suffer a very limited bandwidth. A wide range of CP antennas based on these basic designs have been developed to improve the bandwidth. It is thus meaningful to give a comprehensive review of these wideband CP antennas.

2.3.1 Wideband CP Microstrip Patch Antennas

As indicated in Section 2.2.1, patch antennas can be used to obtain CP radiation if the two orthogonal modes TM_{10} and TM_{01} are excited with additional 90^o phase difference. The basic form of these CP patch antennas include the corners-truncated square patch [26], rectangular patch [27], elliptical patch [28] and slot loaded square patch [29]. However, these basic CP patch antennas have very narrow bandwidth, typically 1%-2%. To improve the bandwidth especially the AR bandwidth of CP patch antennas, various methods are adopted.

Instead of introducing single rectangular slot or crossed slot on a patch antenna, a modified slot shape can be used to improve the CP bandwidth of patch antennas. In [30], dual square-shaped slots are connected and removed from a square patch to achieve wider bandwidth, which is shown in Figure 2.8. These two slots bring two hybrid operating modes, which operate very close in frequency and hence help achieve wider bandwidth compared with conventional CP patches (AR bandwidth around 8%).

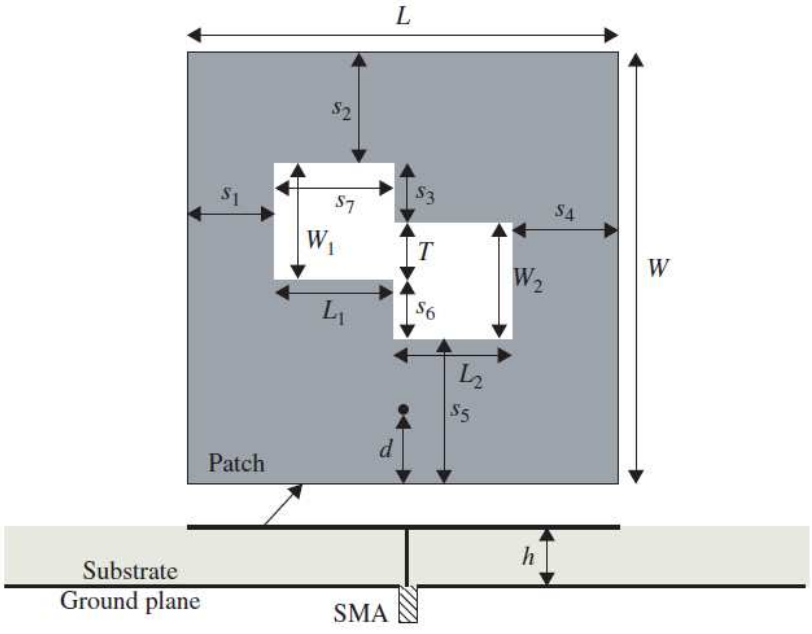

Figure 2.8 Geometry of a modified slot loaded square patch antenna [30].

Another way of increasing the bandwidth of CP patch antennas is to introduce an air gap between the patch and the ground plane, or replace the dielectric substrate by an air substrate or foam. This method can be explained by the reduction of quality factor of patch antennas. It is indicated in [22] that the percent bandwidth of a diagonal-feed nearly square patch antenna is

$$BW(percent) \approx 12\frac{AR}{Q_t} \tag{2.19}$$

where the AR is specified in dB.

As shown in (2.19), the bandwidth of a CP patch antenna is inverse proportional to the total quality of the antenna. It is also well known that smaller dielectric constant of the substrate yields a lower Q_t of patch antennas. Therefore, the bandwidth improvement of a CP patch antenna can be achieved by using a substrate with smaller dielectric constant.

Figure 2.9 shows an inverted-L patch antenna which has a thick air substrate. The inverted-L patch is formed by a horizontal portion of a square patch and a vertical portion of an isosceles triangular shape. By using the corners-truncated square patch, CP radiation is obtained and the AR bandwidth is enhanced to 7% due to the utilization of the air gap.

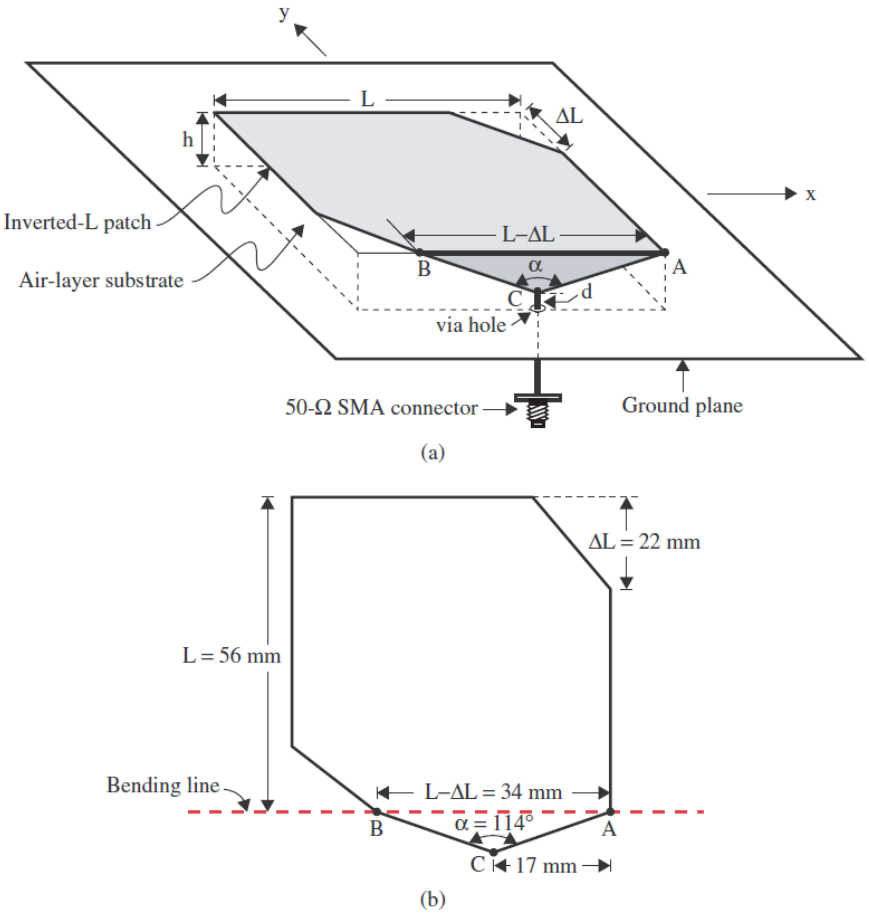

Figure 2.9 Geometry of a broadband CP inverted-L patch antenna [31].

It is worth mentioning that the bandwidth of CP patch antennas with an air gap (substrate) can be improved further when combined with other techniques such as using a L-shaped probe feed [32-34], a meandering strip feed [35] or a ground plane [36].

The stacked patch is another popular way to improve the bandwidth of CP microstrip antennas [37-39]. Figure 2.10 shows the configuration of a design, which demonstrates around 10% 3 dB AR bandwidth [40]. The improvement of the bandwidth is attributed to the two different resonances of the driven patch and parasitic patch which when appropriately designed, can produce CP radiation with two close resonant frequencies. The bandwidth can then be improved if these two resonances are combined effectively.

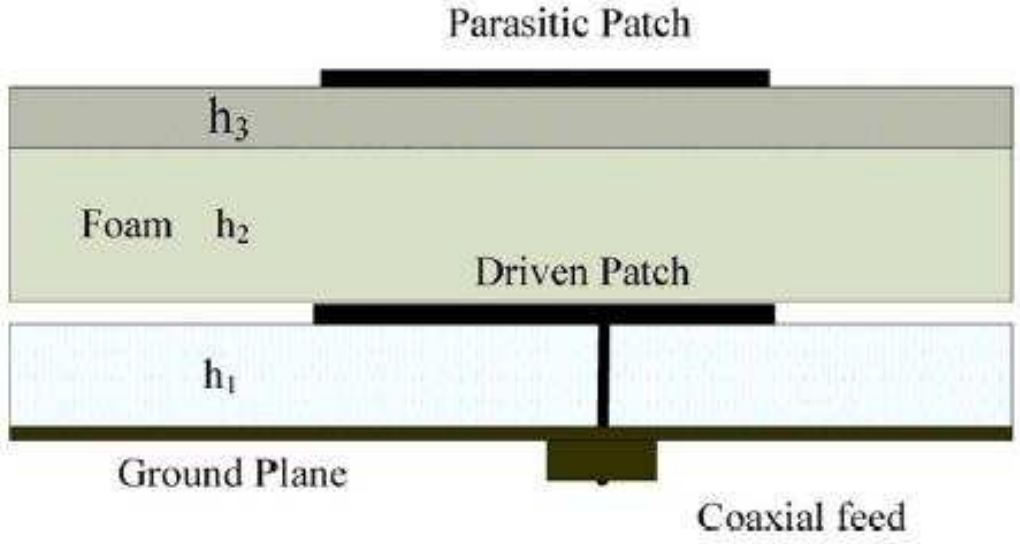

Figure 2.10 Geometry of a stacked CP patch antenna [40].

Numerous CP stacked patch antennas have been designed with the purpose of extending the AR bandwidth further. By choosing different substrates with high and low dielectric constants for the driven patch and parasitic patch, respectively, the 3 dB AR bandwidth of a patch antenna can reach to 18% [41]. A slot loaded, air gap supported, stacked CP patch antenna achieves 20% 3 dB AR bandwidth [42]. The AR bandwidth can even be increased to 30% when four parasitic patches are used and placed in a rotation arrangement [43].

All preceding CP patch antennas are fed by a single coaxial cable and are called single-feed CP antennas. When 90^o power dividers or hybrid couplers are used, two or more feeding points exist and lead to so-called dual-feed or multi-feed CP patch antennas. Since the 90^o power dividers and hybrid couplers can maintain balanced output magnitudes and quadrature phase differences in relatively wider bandwidth, the dual-feed and multi-feed CP patch antennas have wider AR bandwidth than the single-feed CP patch antennas.

A wideband CP patch antenna with dual capacitively coupled feeds, which achieves 35% 3 dB AR bandwidth is shown in Figure 2.11 [44]. A 90° Wilkinson power divider is used to provide the quadrature phase difference between the two feeding ports. Through using air gap and capacitive feeding, both the impedance bandwidth and the AR bandwidth are greatly improved.

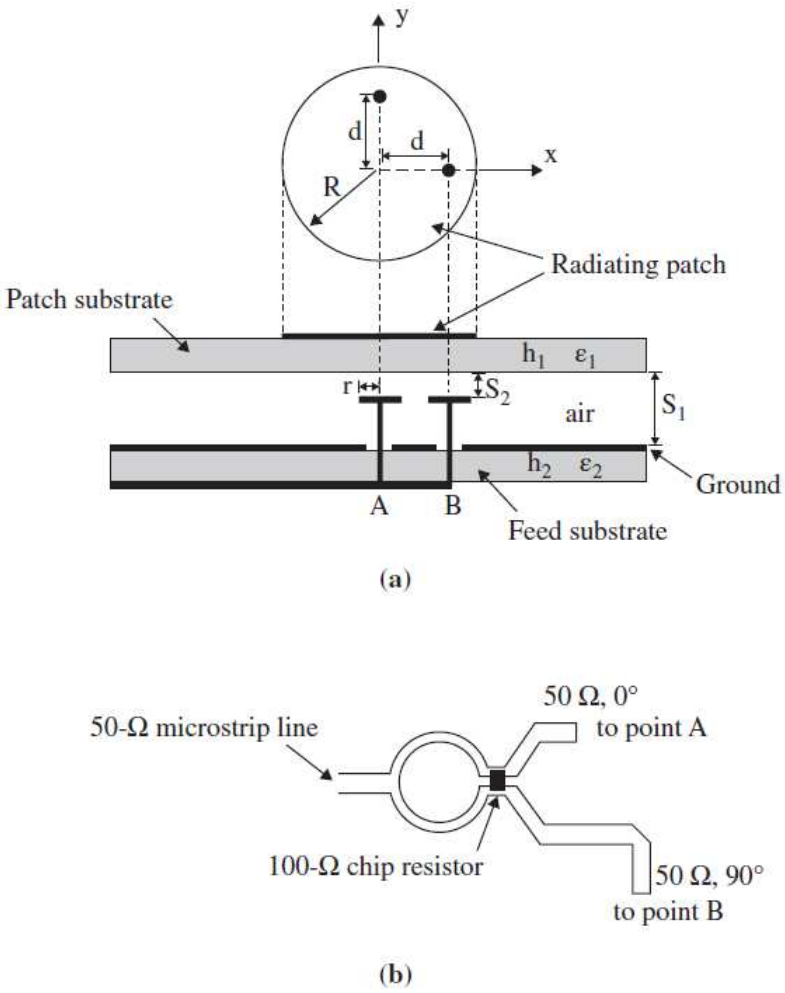

Figure 2.11 Configuration of a CP patch antenna with dual capacitively coupled feeds: (a) side view of the antenna, (b) 90° Wilkinson power divider [44].

Figure 2.12 shows an L-probe fed circular patch antenna with four feeds [45]. As shown, four L-shaped probes formed by its vertical and horizontal portions are orthogonally oriented and positioned at a distance of "S" away from the circumference of the patch. The L-probe feeds are soldered to the output lines of the feed network and excite the radiating patch by proximity coupling. The broadband feed network consists of a cascade of a 3 dB Wilkinson power divider for wideband impedance matching and balanced power splitting, and a novel broadband 90° Schiffman phase shifter for wideband 90° phase shifting. Due to these wideband feeding structures, this CP patch antenna achieves around 80% 3 dB AR bandwidth.

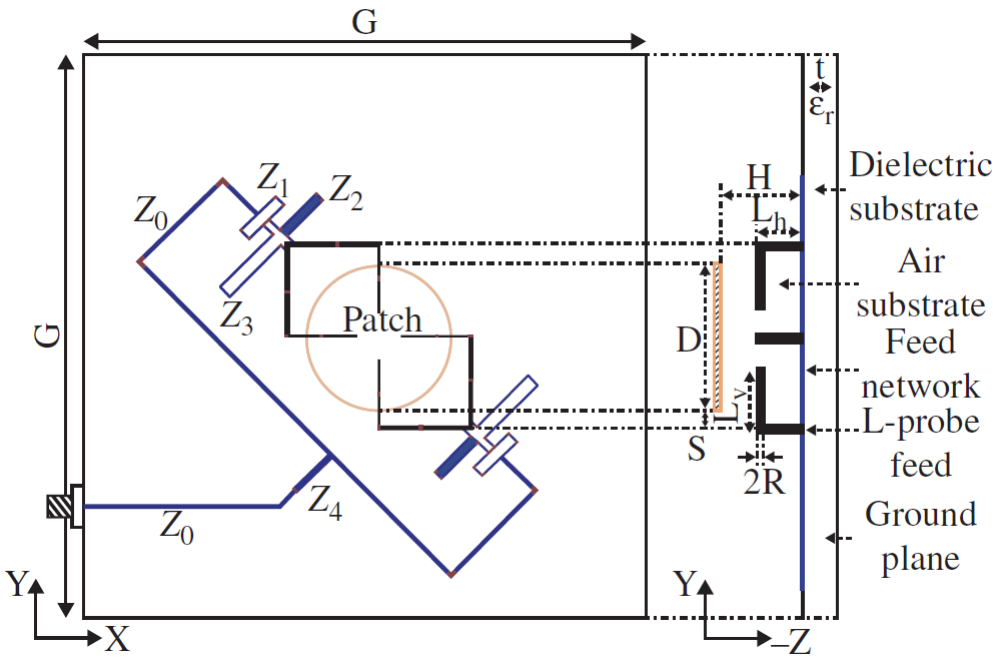

Figure 2.12 Geometry of an L-probe fed circular patch antenna with four feeds [45].

2.3.2 Wideband CP Crossed Dipoles

In additional to the CP patch antennas, crossed dipoles can also be used to produce wideband CP radiation [46-49]. Figure 2.13 shows the configuration of a CP crossed dipole [46]. As shown, two pairs of linear dipoles are printed orthogonally on both sides of a substrate. There is a ring shaped line which connects the two orthogonal dipoles, providing quadrature phase difference between the dipole pairs. A ground plane is placed below to form an air gap and produce unidirectional radiation patterns. The measured 3 dB AR bandwidth of this CP crossed dipole is around 15%.

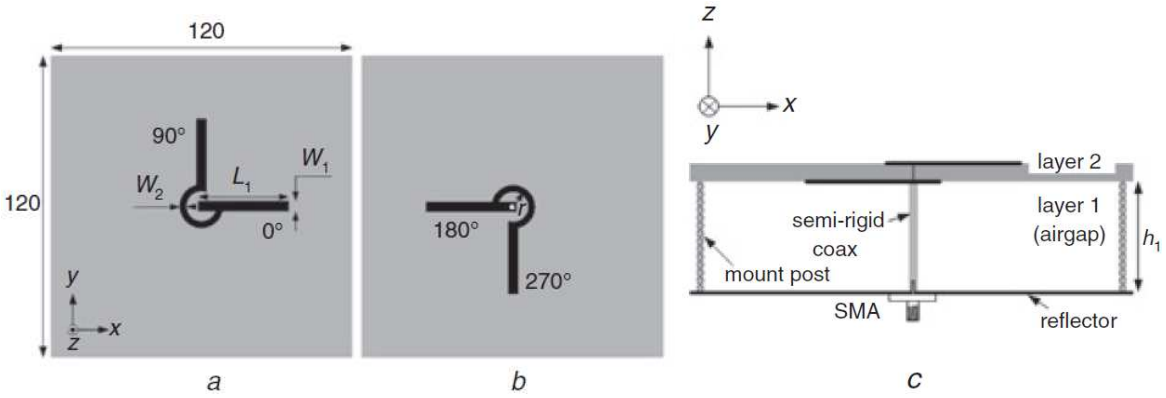

Figure 2.13 Geometry of a CP crossed dipole: (a) top view of layer 2, (b) bottom view of layer 2, (c) side view [46].

To increase the bandwidth of CP crossed dipoles, parasitic loops are introduced [47]. The coupling from the crossed dipole to the four parasitic loops helps excite the loops and

yields another CP resonance. When the additional CP resonance is combined with the original one caused by the crossed dipole, a wider bandwidth can be attained.

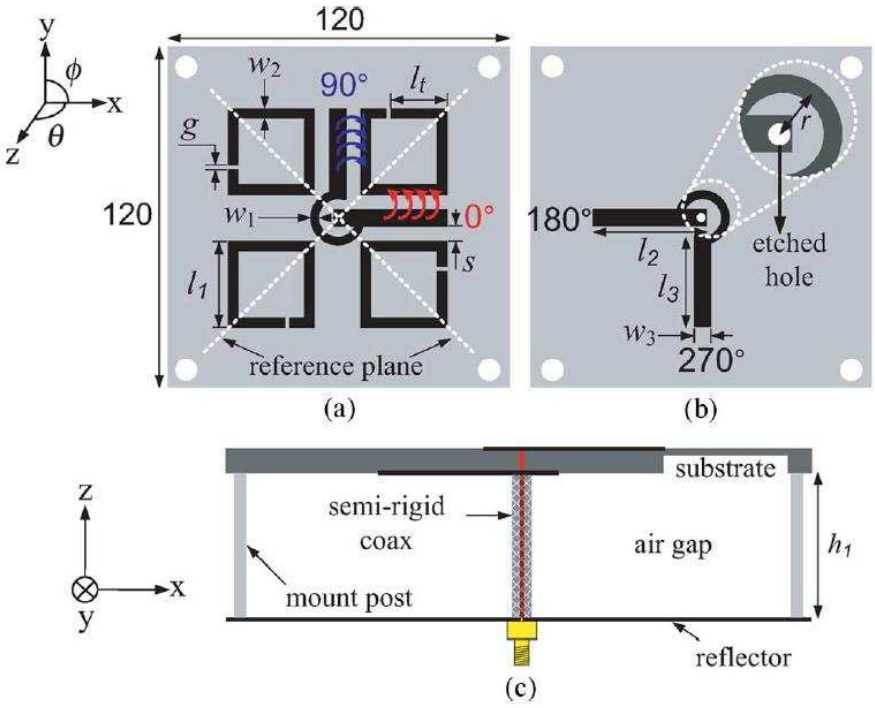

Figure 2.14 Geometry of a CP crossed dipole with parasitic loops [47].

The bandwidth of CP crossed dipoles can also be improved by changing the shape of the dipoles [48]. Figure 2.15 shows a modified CP crossed dipole with flat-patch shaped dipoles. Due to this modification, the quality factor of the printed dipole is reduced and thus a wider bandwidth can be obtained. The measurement results confirm that this CP crossed dipole achieves a 3 dB AR bandwidth of 27%.

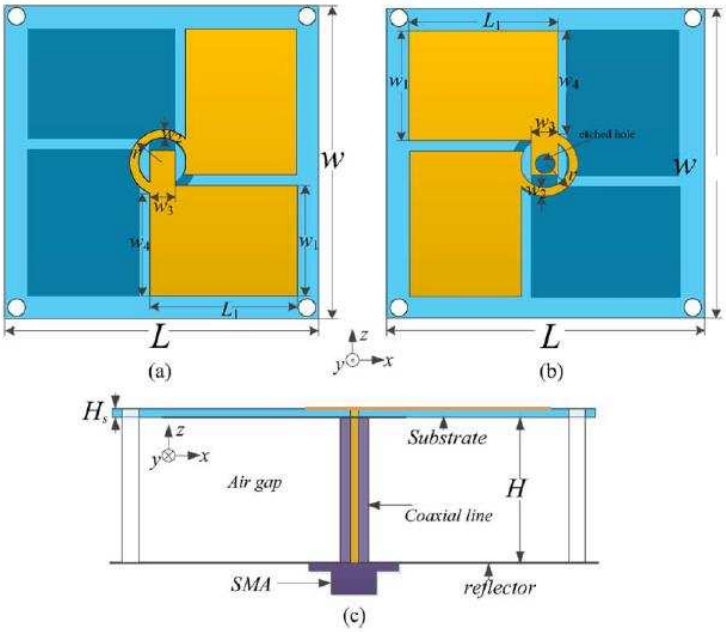

Figure 2.15 Geometry of a modified CP crossed dipole [48].

2.3.3 Wideband CP Slot Antennas

Printed slot antennas usually have broader bandwidth than the microstrip patch antennas [29]. Therefore, it is expected that the CP slot antenna will have wider AR bandwidth when CP radiation is generated by slot antenna. Various CP slot antennas can be found in [50-55].

The simplest way to generate CP radiation for a printed slot antenna is by using 90° hybrid couplers or power dividers to excite two orthogonal magnetic currents with quadrature phase difference. Figure 2.16 shows a CP square slot antenna fed by a three-stage 90° hybrid coupler [50]. The coupler can excite two orthogonal magnetic currents along the two adjacent sides and provide 90° phase difference between these two orthogonal magnetic currents for CP radiation. This antenna realizes 22% 3 dB AR bandwidth.

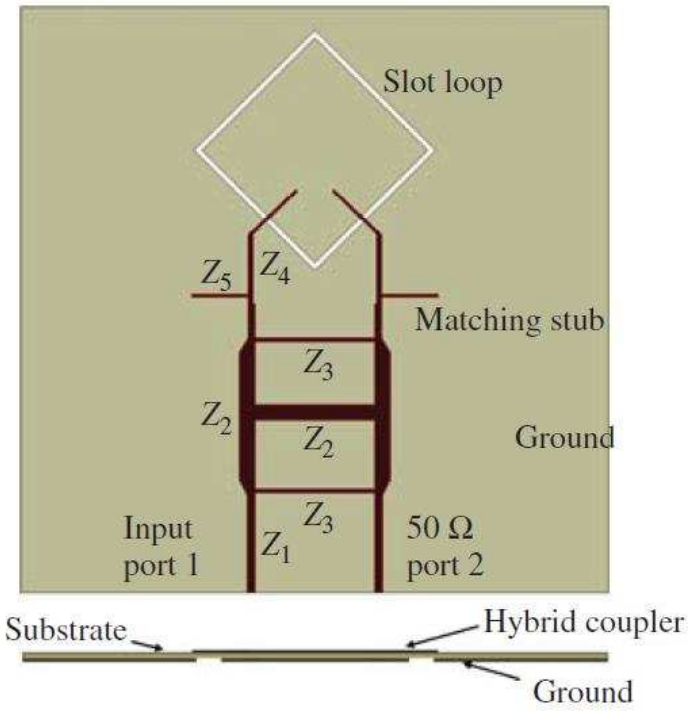

Figure 2.16 Geometry of a square ring slot antenna excited by a 90° hybrid coupler [50].

CP radiation can also be achieved for slot antennas without 90° hybrid couplers or power dividers. A good example is given by Figure 2.17 which shows a circular slot antenna fed by a conventional microstrip line. To achieve CP radiation, the microstrip line is bent to inverted-L shape. With this bending, the L-shaped line can provide two orthogonal electric currents along x- and y- directions, which in turn excites two orthogonal magnetic currents across the circular aperture. The 90° phase difference can be obtained by tuning the parameter l_s. The measured 3 dB AR bandwidth of this antenna is around 44%.

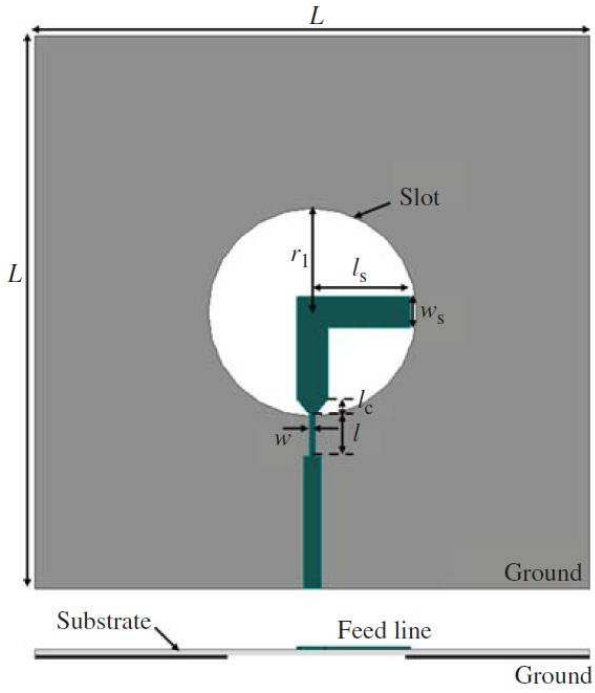

Figure 2.17 Geometry of a circular slot antenna excited by a microstrip line [51].

The above two CP slot antennas both have a dual-layer structure. It is also possible to acquire a CP slot antenna with a single-layer structure where the feed line and the slot are in the same plane [52-54]. Figure 2.18 shows a square slot antenna fed by a coplanar waveguide (CPW). Similarly to the two above mentioned CP slot antennas, the working mechanism of this CP slot antenna can also be explained by the excitation of the dual-orthogonal magnetic currents. The two orthogonally placed feeding strips excite the orthogonal magnetic currents while the required 90° phase difference between these two currents for CP radiation can be obtained by tuning the lengths of these two strips.

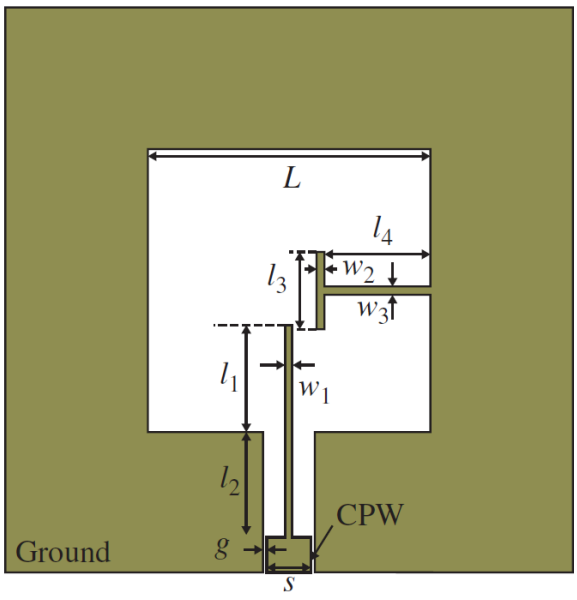

Figure 2.18 Geometry of a CPW-fed slot antenna [53]

It is also possible to combine the CP slot antenna with the patch antenna to improve the bandwidth of the CP slot antenna. Figure 2.19 demonstrates a microstrip line fed circular slot antenna with a parasitic patch antenna [55]. The CP radiation of the circular slot is achieved by the inverted-L shaped feeding line, similar to the CP slot antenna analyzed in Figure 2.17. As the parasitic patch is also excited, an additional CP resonance is generated and the 3 dB AR bandwidth can be enlarged to 45% once the CP resonances from the slot and the patch are combined constructively.

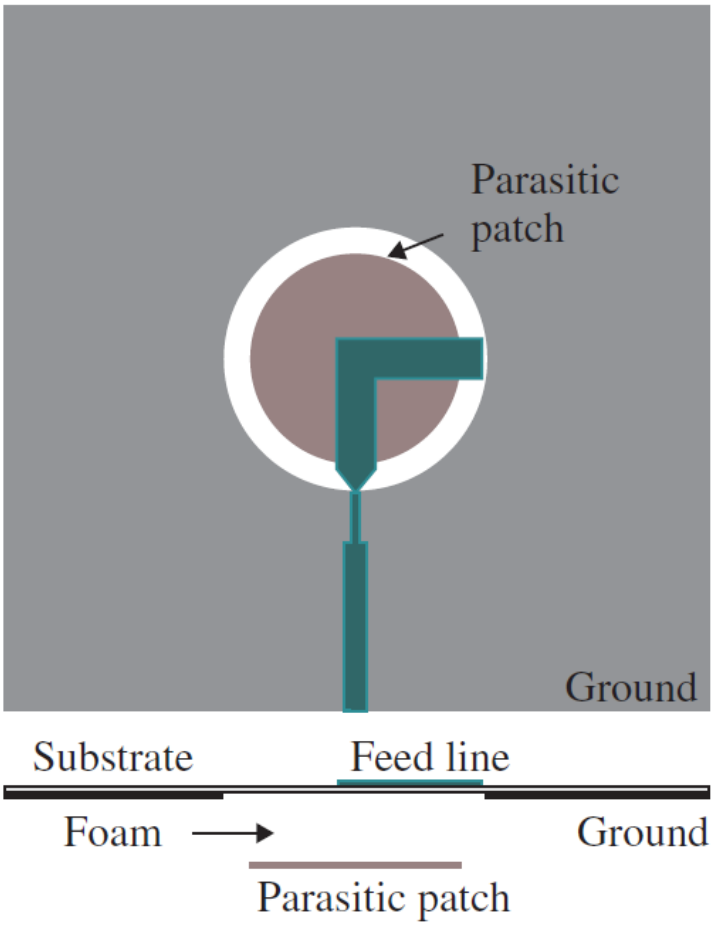

Figure 2.19 Geometry of a microstrip-fed slot antenna with a parasitic patch [55].

2.3.4 Wideband CP Travelling-Wave Antennas

Another important category of wideband CP antennas is the travelling-wave CP antennas, including helical antennas [56-58], spiral antennas [59-61] and CP loop antennas [62-64].

Figure 2.20 shows a helical antenna with the ground plane. The geometrical configuration of a helix usually consists of N turns, diameter D and spacing S between each turn. The total length of the antenna is $L = NS$ while the total length of the wire is $L_n = NL_0 = N\sqrt{S^2 + C^2}$ where $L_0 = \sqrt{S^2 + C^2}$ is the length of the wire between each turn and $C = \pi D$

is the circumference of the helix. Another important parameter is the pitch angle α which is the angle formed by a line tangent to the helix wire and a plane perpendicular to the helix axis. The pitch angle is defined by

$$\alpha = \tan^{-1}\frac{S}{\pi D} = \tan^{-1}\frac{S}{C} \tag{2.20}$$

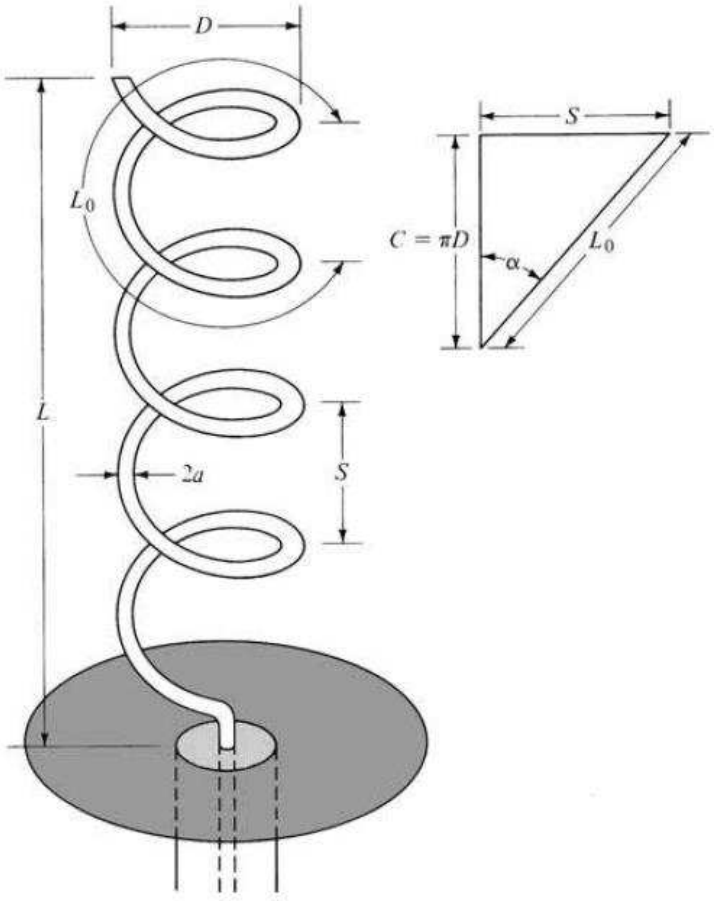

Figure 2.20 Helical antenna with ground plane [22].

When $\alpha = 0^o$, the winding is flattened and the helix reduces to a loop antenna of N turns. On the other hand, when $\alpha = 90^o$ then the helix reduces to a linear wire. When $0^o < \alpha < 90^o$, then a true helix is formed with a circumference greater than zero but less than the circumference when the helix is reduced to a loop ($\alpha = 0^o$).

The helical antenna can operate in many modes; however, the two principals are the normal (broadside) and the axial (end-fire) modes. The three-dimensional amplitude patterns representative of a helix operating, respectively, in the normal (broadside) and axial (end-fire) modes are shown in Figure 2.21. The axial mode is widely used since it can achieve circular polarization over a broad bandwidth (usually 2:1). To excite this mode, the circumference of the helix must be in the $\frac{3}{4}\lambda_0 < C < \frac{4}{3}\lambda_0$ range, with the spacing about $S \approx \lambda_0/4$ and the pitch angle $12^o < \alpha < 14^o$.

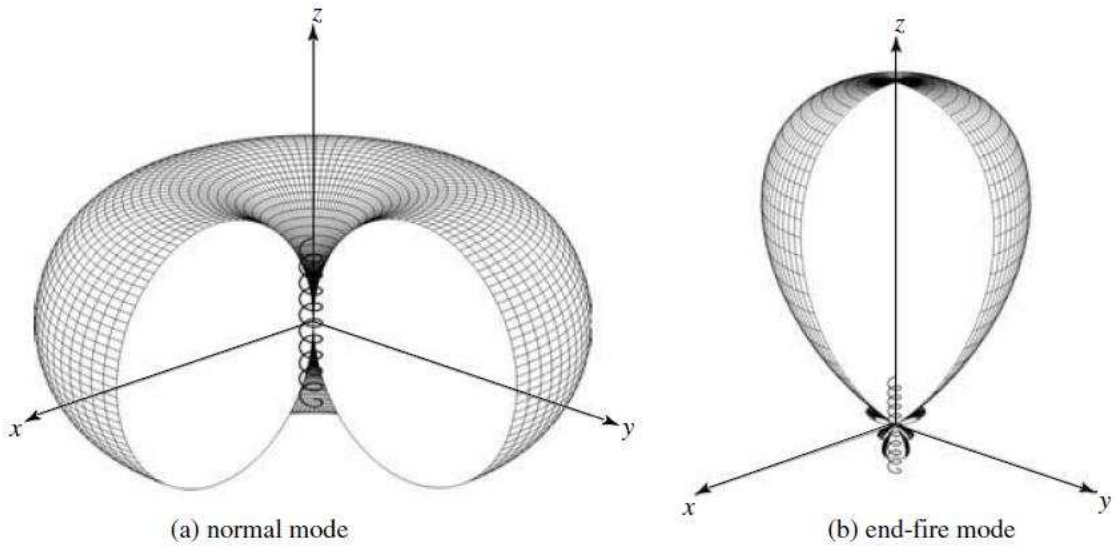

Figure 2.21 Three-dimensional normalized radiation patterns for normal and axial modes helical antennas [22].

Although the helical antenna has a 2:1 CP bandwidth in its axial mode, one major drawback of this kind of CP antenna is its considerable height. When operating at low frequencies such as VHF band, the physical size can become rather large. To achieve low-profile helical antennas, smaller pitch angle and smaller number of turns or stub loaded helical antennas have to be designed [65-67]. However, the 3 dB AR bandwidth in these designs reduces to around 10%.

Another type of widely known and widely deployed CP antenna is the spiral. As the geometry dimensions of spirals are determined by angles, they are frequency independent and can achieve rather broadband CP radiation. Figure 2.22 shows a two-arm Archimedean spiral antenna whose radius is defined by $r = a\varphi$, where a is a constant and φ is the rotating angle.

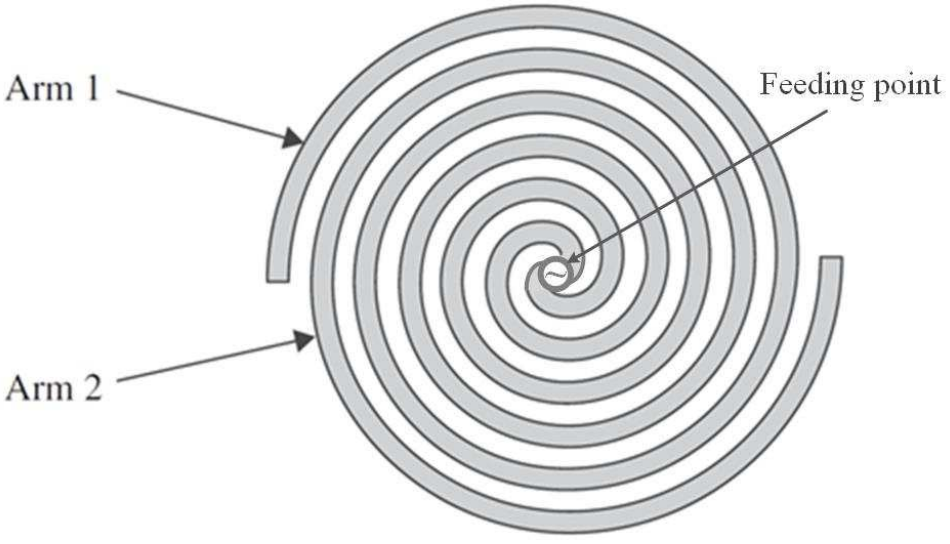

Figure 2.22 Archimedean spiral antenna [6].

Compared with helical antennas, the spirals have much lower height and can be printed on a substrate as a planar antenna. The bandwidth of spirals can be designed to several octaves, which is wider than the bandwidth of helical antennas (usually 2:1). However, the spirals need a balanced feed to maintain symmetrical characteristics, which increases the complexity. One method that achieves geometrical balancing requires that the coax is embedded into one of the arms of the spiral. To maintain symmetry, a dummy cable is usually placed into the other arm [22]. If the feed line is electrically unbalanced, a balun must be used, such as tapered microstrip balun [68] and microstrip line to coplanar stripline (CPS) balun [69].

Due to the considerable height of helical antennas and the need of ultra-wideband baluns for spirals, there is an increasing interest in designing travelling-wave CP antennas with lower height and simpler configuration. A curl-shaped antenna with travelling-wave current excited along the wire achieves a AR bandwidth of 6.7% [62]. Travelling-wave current can also be generated by an open-loop antenna, which is shown in Figure 2.23 [63]. As indicated in section 2.2.3, good CP radiation can be obtained if a travelling-wave current is excited along a circular loop configuration and the CP open-loop in [63] achieves a AR bandwidth of 12%.

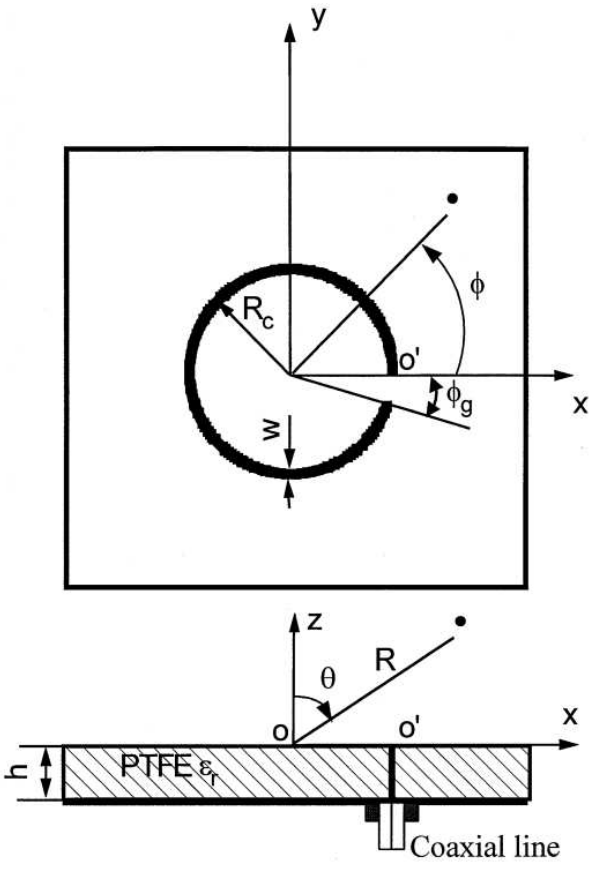

Figure 2.23 Geometry of a probe-feed printed circular open-loop antenna [63].

To improve the AR bandwidth of the CP loop antennas, an additional parasitic open loop can be placed inside the original loop [64, 70]. Figure 2.24 shows an open-loop antenna with a parasitic loop which achieves 16% AR bandwidth. By incurring another CP resonance with higher resonant frequency than the original loop. A sleeve balun is used to feed the antenna, which has much simpler configuration than those baluns used for spirals.

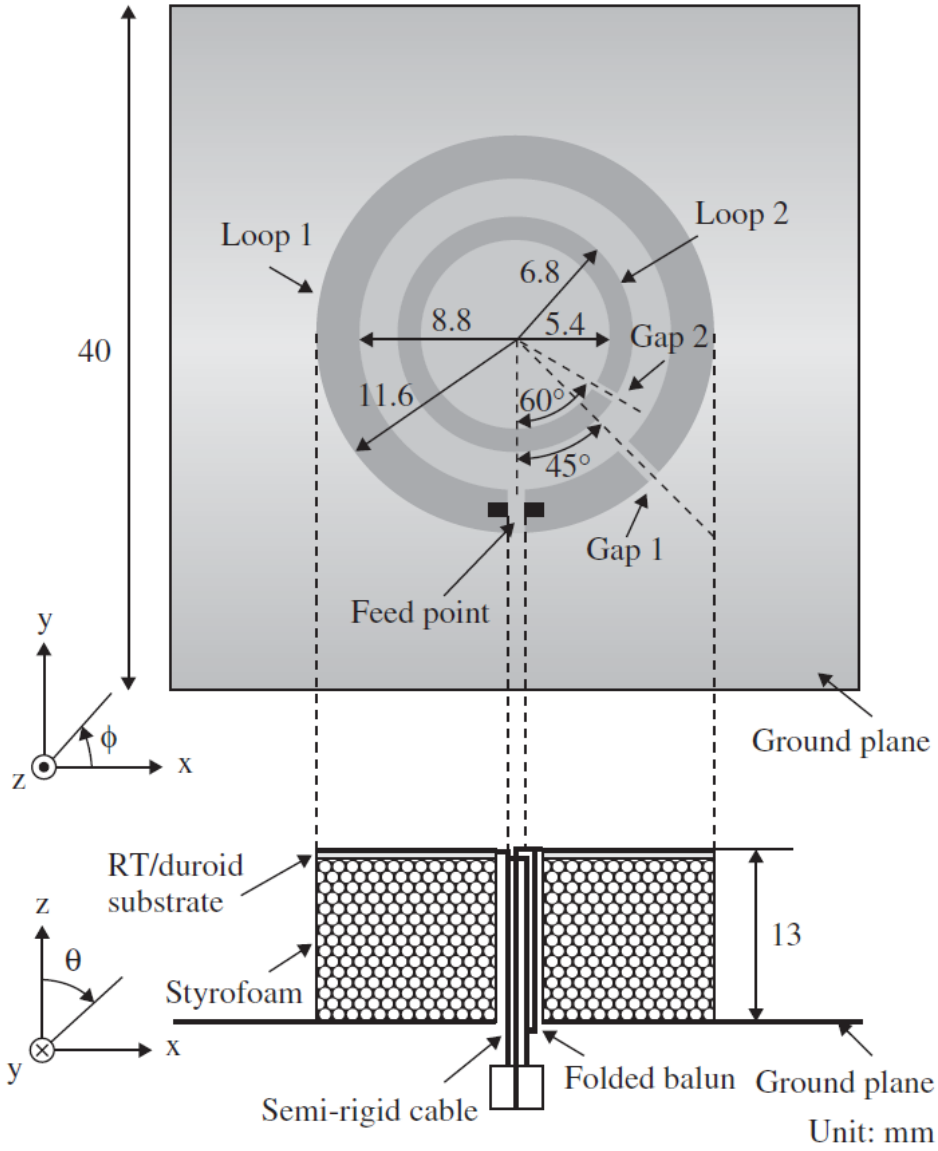

Figure 2.24 Geometry of a probe-feed printed dual open-loop antenna [70].

Using a dual-loop structure in series-fed or parallel-fed can improve the bandwidth of CP loop antennas further, as shown in [64, 71]. As demonstrated in [64], the dual-loop structure in series-fed and parallel-fed can achieve 30% and 50% AR bandwidth, respectively. Compared with helical antennas and spiral antennas, the CP loop antennas have relatively narrower bandwidth. Nevertheless, they feature smaller size, planar structure and simple configuration, which make them easy to fabricate and implement.

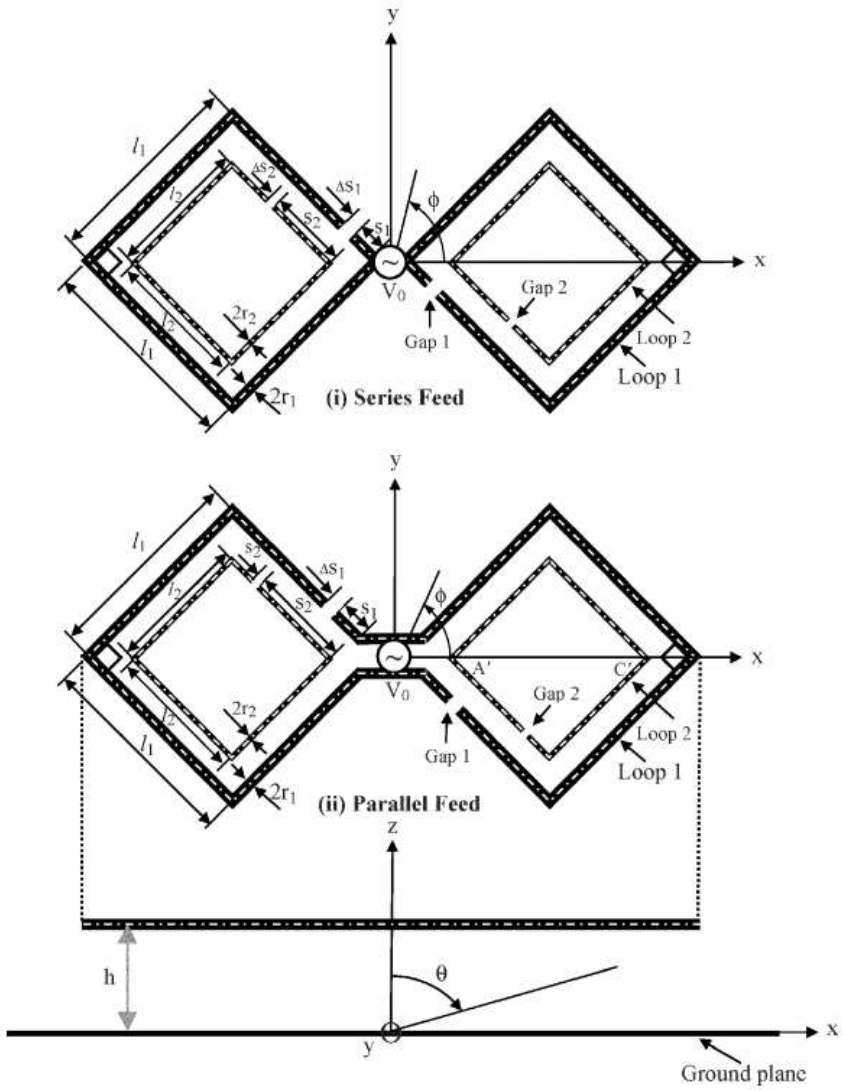

Figure 2.25 Geometry of series and parallel-fed dual rhombic-loop antennas [64].

2.3.5 A Comparison among Different Types of Wideband CP Antennas

Table 2.1 gives the comparison among different kinds of wideband CP antennas. As shown, CP patch antennas are usually small size and can achieve bandwidths from several percentage to 25%. Stacked patches with multi-feed structures are effective techniques to improve the AR bandwidth of patch antennas at the expense of higher profile and more complex configuration. CP crossed dipoles have simple configuration and moderate CP bandwidth. CP slot antennas have the lowest height and can achieve up to a AR bandwidth of 45%. Helical antennas and spiral antennas are two types of travelling-wave antennas which can achieve superior bandwidth performance. However, helical antennas normally have the largest height while the bandwidth will degrade if the height reduces. Spirals have the widest bandwidth among all CP antennas and thus are widely deployed. Nevertheless, spirals are rather large and the balanced feeding always requires a UWB balun which is

difficult to design and implement. The CP loop antennas are another kind of traveling-wave antenna, which has moderate size, height and complexity while achieving 10% ~ 50% AR bandwidth.

Table 2.1 Comparison of Wideband CP Antennas

Antenna Type	Reference NO.	3 dB AR Bandwidth	Size	Height	Fabrication Complexity
Patch	Slot loaded patch [30]	8%	Small	Low	Low
	Patch with air substrate [31-34]	7% ~ 25%	Small	Medium	Medium
	Stacked patch [40-43]	10% ~ 30%	Small	Low	Medium
	Multi-feed patch [44, 45]	30% ~ 70%	Small	Low	Medium
Crossed Dipole	[46-49]	15% ~ 27%	Small	Medium	Low
Slot Antenna	Dual-layer slot [50, 51]	22% ~ 44%	Small	Low	Low
	Coplanar slot [52-54]	10% ~ 40%	Small	Low	Low
	Slot with parasitic patch [55]	45%	Small	Medium	Low
Helical Antenna	Axial model helix [56-58]	~67%	Small	Large	Low
Spiral	[59-61]	>100%	Large	Medium	Large
CP Loop	Single open-loop [63]	12%	Small	Low	Low
	With parasitic loop [64, 70]	16%	Small	Low	Low
	Dual-loop structure [64, 71]	30% ~ 50%	Medium	Low	Medium

2.4 Wideband CP Array Antennas

The preceding section gives an overview of various wideband CP antennas. For applications where high gain is needed, CP array antennas are required. Therefore, it is also necessary to review wideband CP arrays. Different from LP arrays, there are some special ways to design CP arrays with wideband performance, such as the sequential rotation method. Wideband CP reflectarrays are also reviewed due to their greatly simplified feeding structure and promising applications for a wide range of wireless systems.

2.4.1 CP Array with Traditional RF Power Divider

Like LP array antennas, CP arrays can be built by feeding CP elements constructively. Several designs can be found in [62, 72-74]. Without considering the scanning performance of the array, the bandwidth of conventional CP arrays is mainly determined by the bandwidth of elements and the mutual coupling normally degrades the bandwidth performance.

A linear array consisting of four CP stacked patches is shown in Figure 2.26 [72]. The array has a 3 dB AR bandwidth of 5%, which is smaller than the bandwidth of the CP element. To obtain wider array bandwidth, CP elements with wider bandwidth can be employed. Figure 2.27 shows a 1×10 linear array consisting of ten crossed bowtie dipoles [73]. The 3 dB AR bandwidth of the element is 52% while the bandwidth of the array is 37%. As indicated by these two CP linear arrays, the 3 dB AR bandwidth is usually narrower than the bandwidth of the element due to the influence of the mutual coupling among the elements.

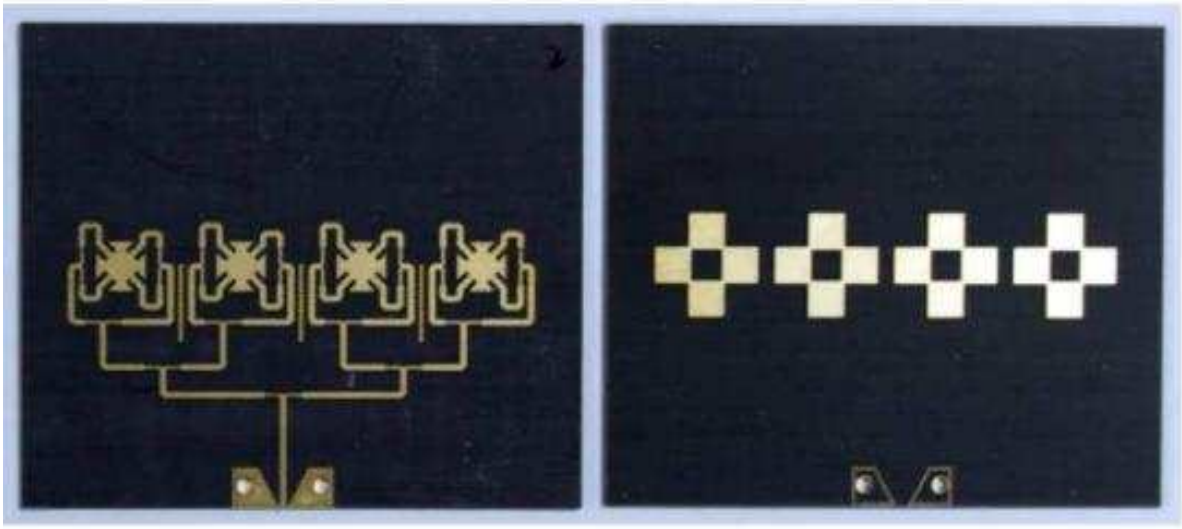

Figure 2.26 Photograph of a linear CP patch array [72].

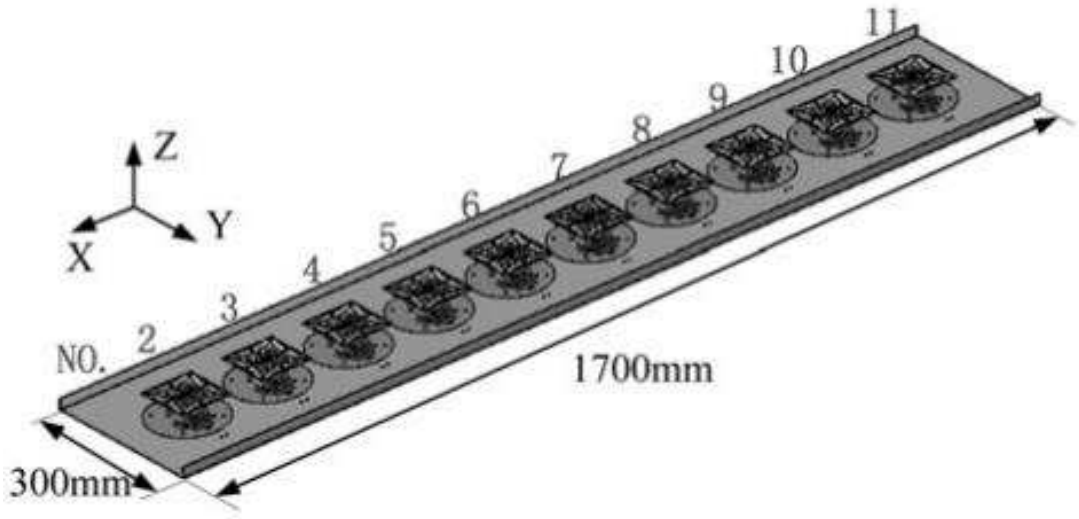

Figure 2.27 Configuration of a linear CP crossed dipole array [73].

CP planar arrays can also be designed by using a corporate feeding network. A 2×2 monofilar Archimedean spiral array antenna is shown in Figure 2.28. Each spiral element is fed by a microstrip line through the proximity feeding method [74]. A 1:4 T-type power divider network is placed behind the array aperture to afford corporate feeding. The measured 3 dB AR bandwidth of the array is around 10%, which is also smaller than the element's bandwidth of 12%.

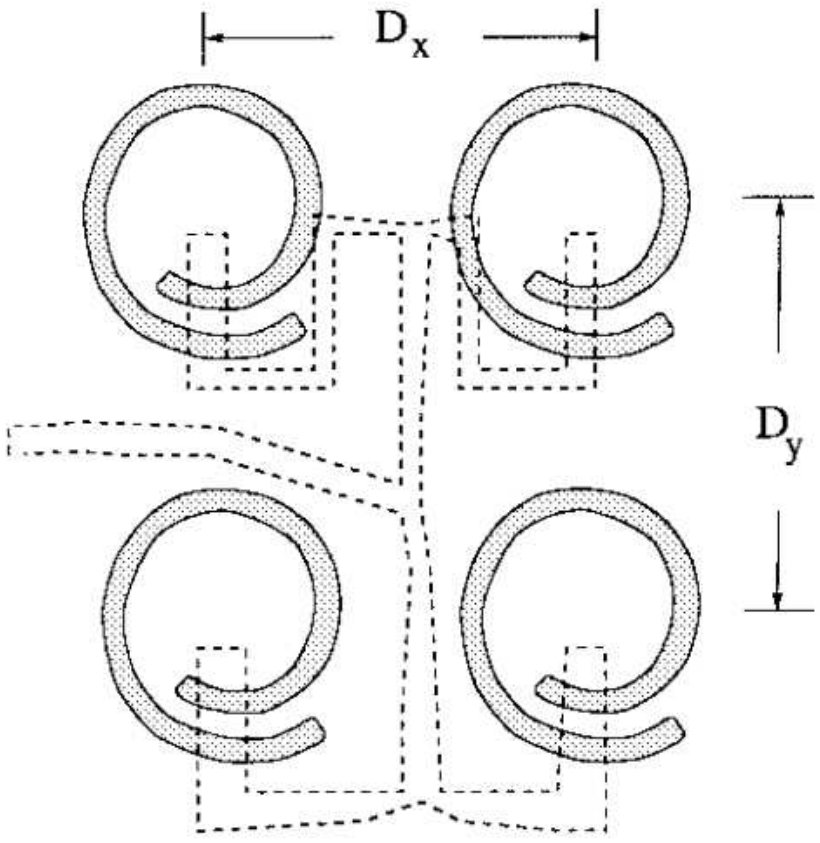

Figure 2.28 Geometry of a 2×2 monofilar Archimedean spiral array [74].

2.4.2 Wideband CP Sequentially Rotated Array

An interesting design is the sequentially rotated array which can be implemented by using both LP elements [75] and CP elements [76]. To illustrate its operating principle, let us examine a basic sequentially rotated array consisting of four LP patches with unique angular and feeding phase arrangements, as shown in Figure 2.29. Four patches are oriented in a sequentially angular rotated arrangement with 0°, 90°, 180° and 270° feeding phase, respectively.

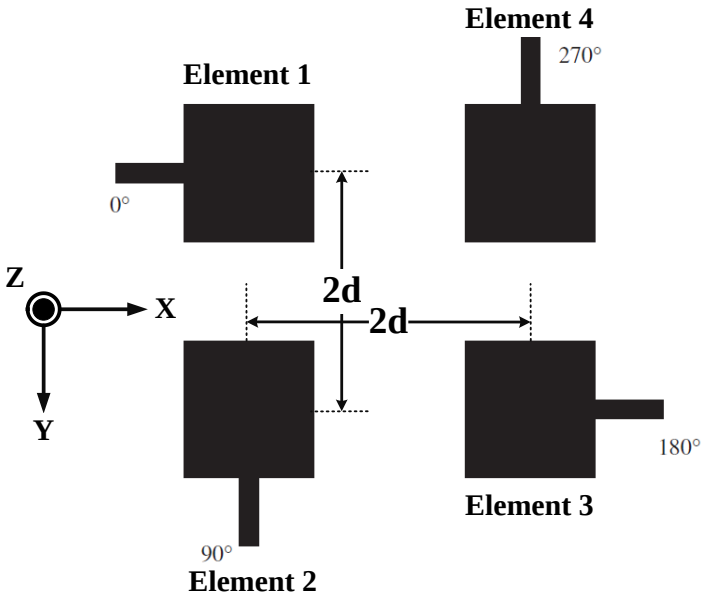

Figure 2.29 Configuration of a CP sequentially rotated array using LP patch elements [75].

The element distance between each element is d, and the far-field radiated electric fields of the four patches are $\overrightarrow{E_1}$, $\overrightarrow{E_2}$, $\overrightarrow{E_3}$ and $\overrightarrow{E_4}$. Referring to the geometry relationship between elements and the feeding phase distribution, the total far-field electric field $\overrightarrow{E_t}$ in the x-z is as follows:

$$\begin{aligned}\overrightarrow{E_t} = \overrightarrow{E_1}e^{-jk_0 d\sin\theta}e^{j0^o} + \overrightarrow{E_2}e^{-jk_0 d\sin\theta}e^{j90^o} \\ +\overrightarrow{E_3}e^{jk_0 d\sin\theta}e^{j180^o} + \overrightarrow{E_4}e^{jk_0 d\sin\theta}e^{j270^o}\end{aligned} \tag{2.21}$$

where θ is the elevation angle. Notice that the four patches are of equal size and fed with the same microstrip line. Thus, it is evident that

$$\begin{aligned}\overrightarrow{E_1} = -\overrightarrow{E_3} \\ \overrightarrow{E_2} = -\overrightarrow{E_4}\end{aligned} \tag{2.22}$$

Substituting (2.22) to (2.21) and (2.21) reduces to

$$\begin{aligned}\overrightarrow{E_t} = \left(\overrightarrow{E_1}e^{j0^o} + \overrightarrow{E_2}e^{j90^o}\right)\left(e^{-jk_0 d\sin\theta} + e^{jk_0 d\sin\theta}\right) \\ =\left(\overrightarrow{E_1}e^{j0^o} + \overrightarrow{E_2}e^{j90^o}\right)(2\cos(k_0 d\sin\theta))\end{aligned} \tag{2.23}$$

Notice that element 1 and 2 are of the same size and perpendicular to each other, thus $\left|\overrightarrow{E_1}\right| = \left|\overrightarrow{E_2}\right|$ and the two electric fields are orthogonal. Therefore, it is indicated from (2.23) that pure CP radiation has been achieved in the x-z plane. The expression $2\cos(k_0 d \sin\theta)$ represents the two-element array factor. It is worth to mention that CP radiation can also be achieved in the y-z plane with the same principles.

The above derivation gives detailed explanation why the CP radiation is achieved through sequentially rotated LP patches. The AR bandwidth of the array can be increased substantially through this method [75]. A simple explanation of this is shown in Figure 2.30. The solid arrows represent the fundamental mode TM_{10} while the dashed arrows denote the higher modes which contribute to the cross-pol. As shown, the co-pol (fundamental mode) component gets enhanced while the cross-pol electric fields are cancelled. Therefore, the AR bandwidth can be improved. Another distinct advantage of the sequentially rotated array is that the mutual coupling of the array is significantly less than that of a convention CP array. This is due to the fact that all the adjacent elements of this array are orthogonally oriented and hence cause very little coupling between neighboring elements [75].

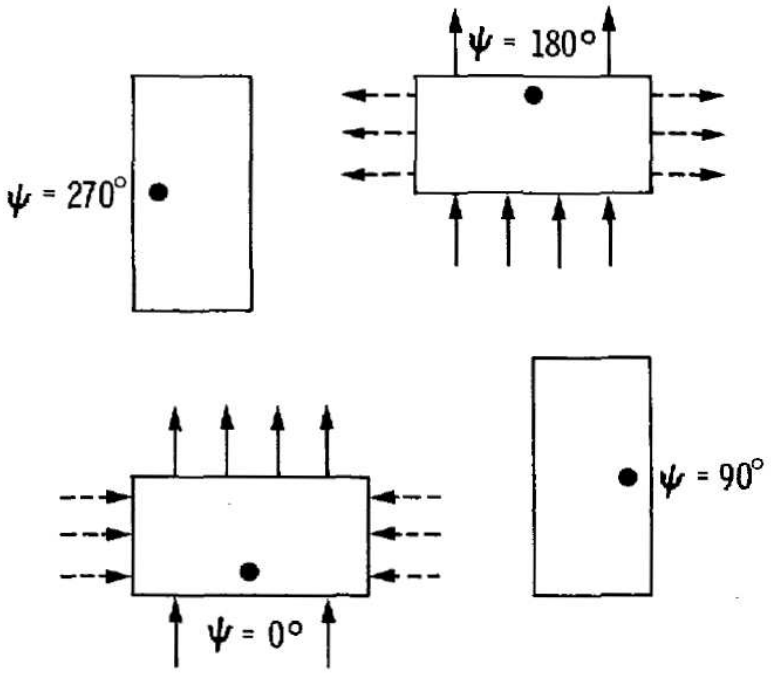

Figure 2.30 Mechanism of cross-pol cancellation of sequentially rotated elements [75].

Numerous wideband CP arrays based on the sequential rotation method have been developed. As it is a general method, it can be used to extend the AR bandwidth of various kinds of arrays, such as the CP patch array [77], CP crossed dipole array [47] and CP slot array [78].

A 64-element CP patch array with sequentially rotated elements is shown in Figure 2.31. The geometry of a truncated corner CP patch element and a 4-element subarray using the sequential rotation method are shown in Figure 2.31 (a) and (b) respectively. The full 64-element array which employs the sequential rotation method for the second time at the 16-element subarray level is shown in Figure 2.31 (c). Due to the double use of the sequential rotation, the undesired radiation from the feed network is cancelled and the 3 dB AR bandwidth is 14% which is much wider than the bandwidth of a CP truncated corner element (smaller than 5%).

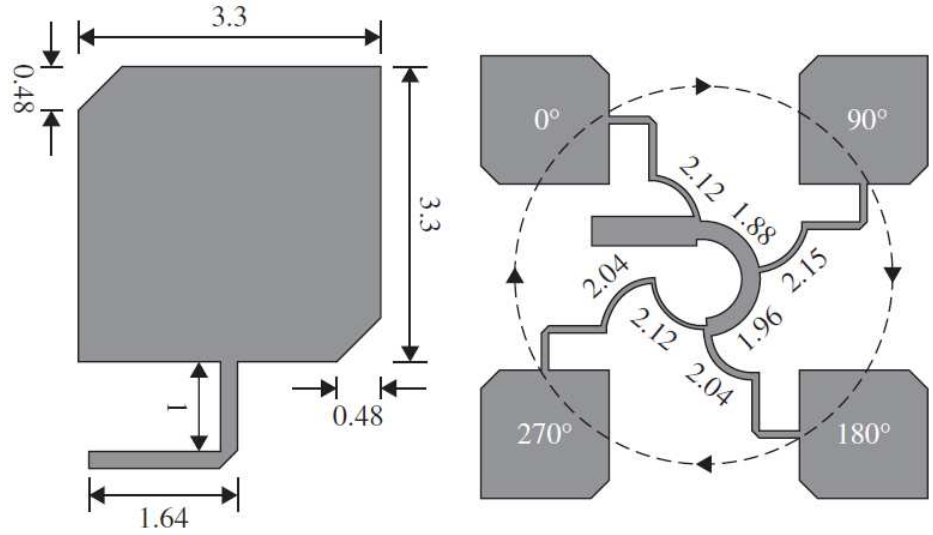

(a) (b)

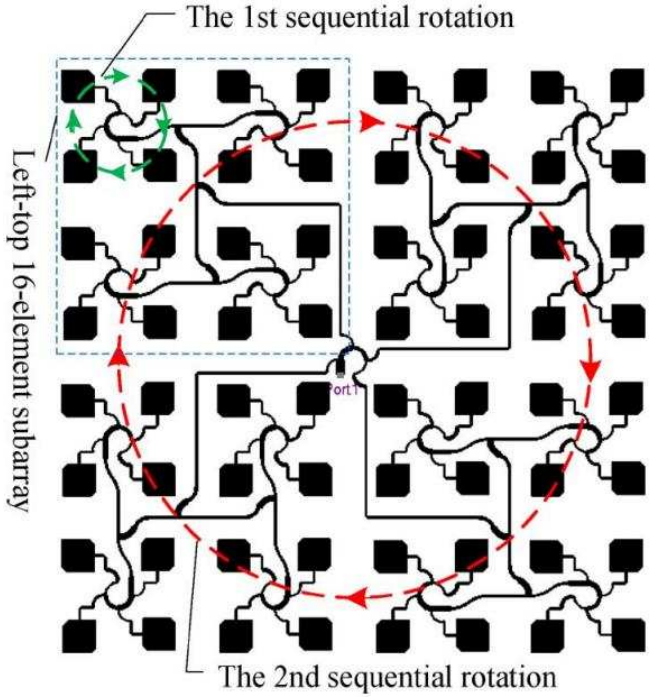

(c)

Figure 2.31 Configuration of a 64-element sequentially rotated array [77].

Figure 2.32 shows the geometry of a sequentially rotated crossed-dipole array. The 3 dB AR bandwidth of this 2×2 array is around 56% which is about twice the bandwidth of a single crossed dipole element (28%).

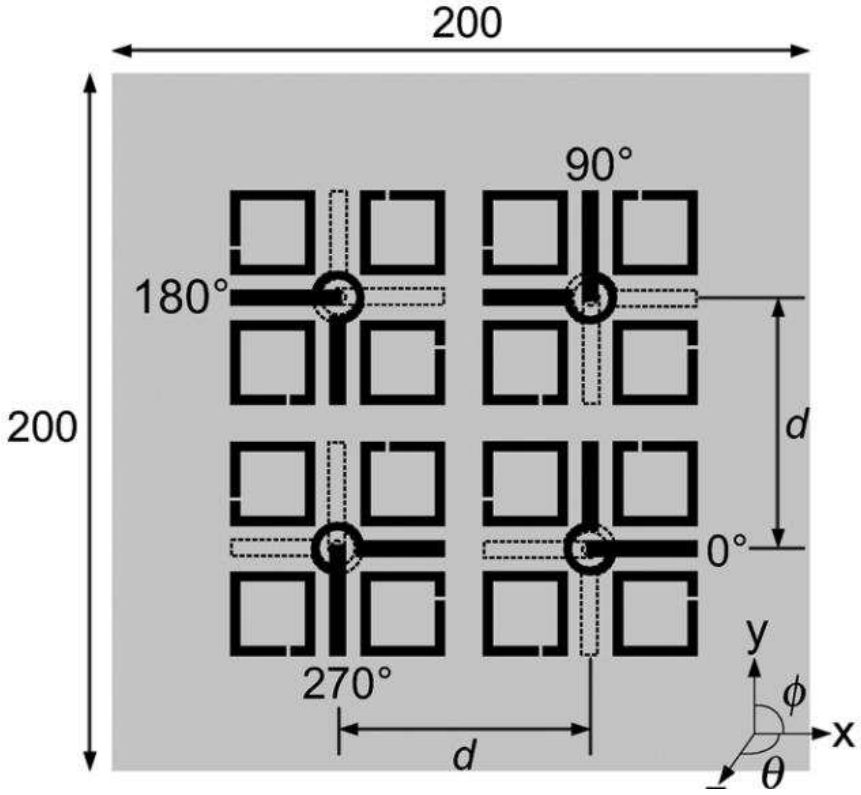

Figure 2.32 Configuration of a sequentially rotated crossed dipole array [47].

The sequential rotation method can also be applied to CP slot arrays, with one example shown in Figure 2.33 [78]. The 4×2 array achieves 29% 3 dB AR bandwidth while the 3 dB AR bandwidth of the elliptical slot element is just 7%.

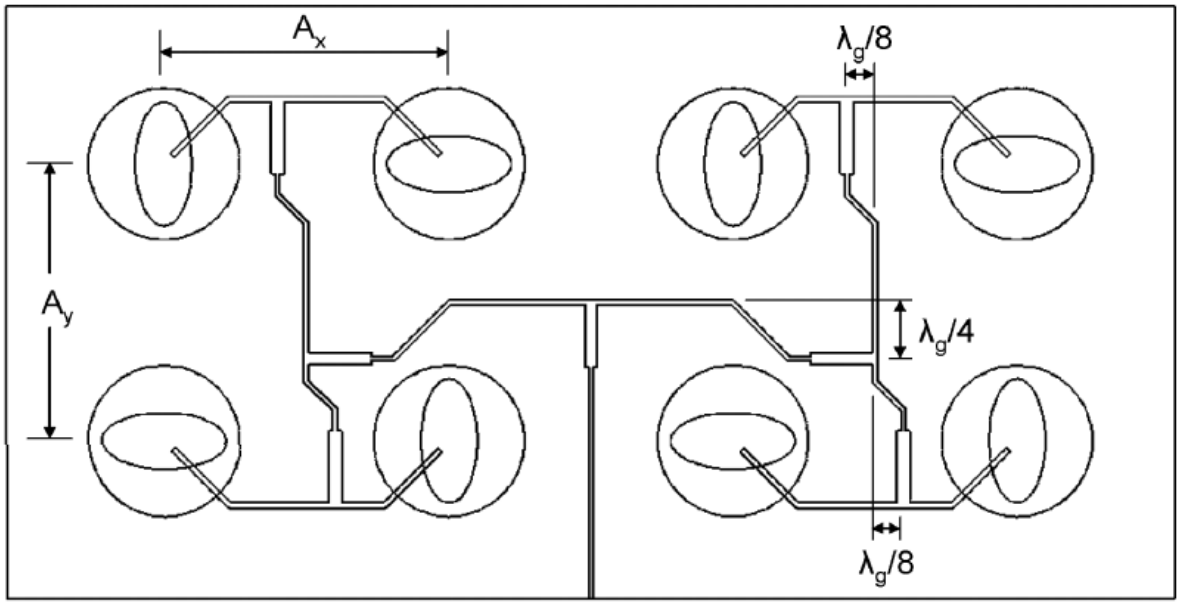

Figure 2.33 Configuration of a sequentially rotated elliptical slot array [78].

2.4.3 Wideband CP Printed Reflectarray

Printed reflectarrays consist of a large number of radiating elements with pre-adjusted phases and an illuminating feed [79]. The printed reflectarrays combine the advantages of phased arrays and parabolic antennas and thus received increasing interest in recent decades.

Although there are numerous advantages for printed reflectarrays, one major drawback of this type of array is their narrow bandwidth, which is mainly caused by the narrow bandwidth of the printed phasing elements and differential spatial phase delay from the feed to each element.

Various approaches have been utilized to improve the bandwidth of CP reflectarrays, such as using stacked patches [80], utilizing multi-resonance phasing elements [81] and using spatial time-delay units [82].

A dual-layer T-shaped phasing element and a prime-focus 81-element CP reflectarray are shown in Figure 2.34. As shown, the phasing element is comprised of two stacked T-shaped patches. With this dual-layer structure, the phasing element has a wider bandwidth and the CP reflectarray can achieve a 3 dB AR bandwidth of 28%.

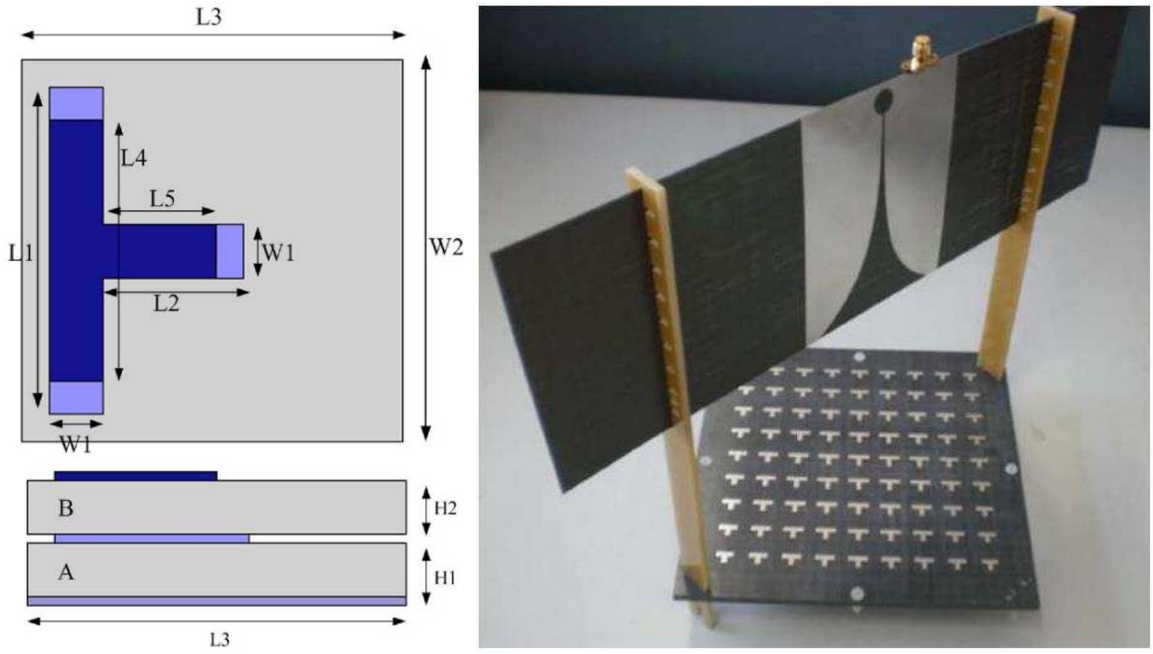

(a) (b)

Figure 2.34 Geometry of a dual-layer stacked patch and the photo of the fabricated CP reflectarray [80] .

Figure 2.35 shows two multi-resonance phasing elements for CP reflectarrays. By using these multi-resonance phasing elements, the resultant reflectarrays can obtain 3 dB AR bandwidths of 41% and 43%, respectively.

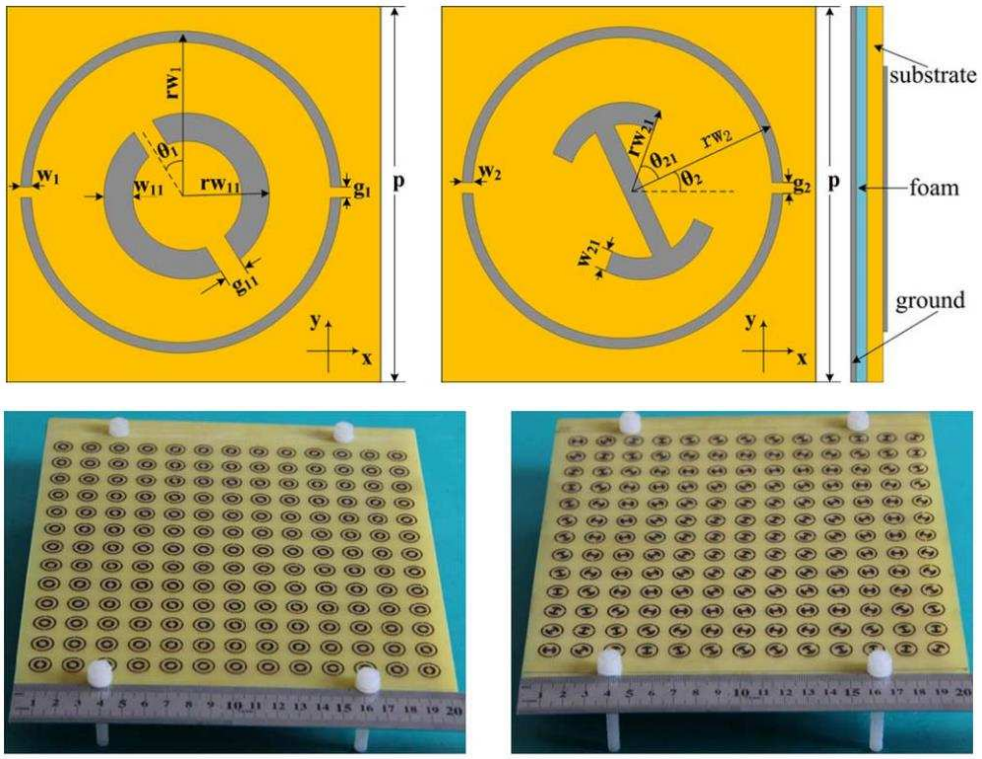

Figure 2.35 Geometry of the multi-resonance phasing elements and the photo of the fabricated CP reflectarrays [81].

The spatial time-delay unit which is the unit cell of anisotropic ground-plane-backed miniaturized-element frequency selective surfaces (MEFSSs), is capable of providing constant time delays over wide bandwidths [82]. When designed appropriately, it can also create 90° phase shift between the two orthogonal electric field components of the reflected wave, as shown in Figure 2.36. Based on this TDU element, a CP reflectarray can be designed with 40% 3 dB AR bandwidth.

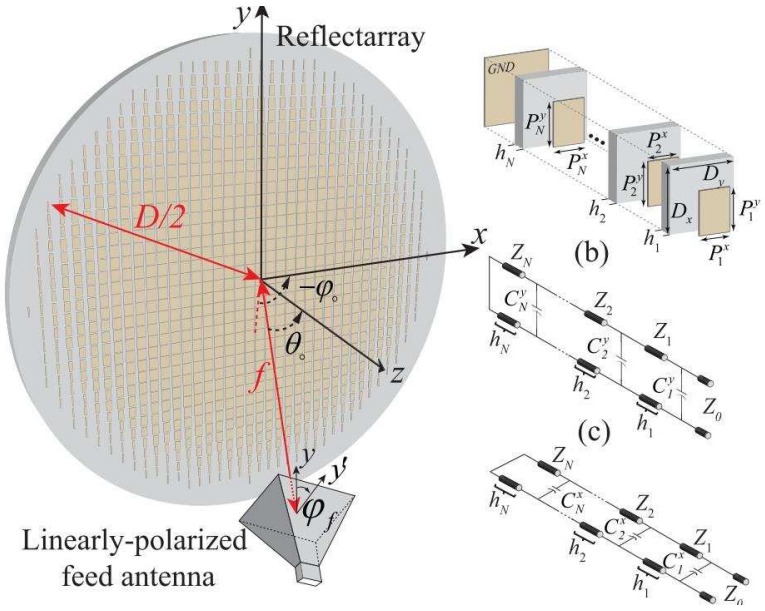

Figure 2.36 Geometry of the spatial TDU and the TDU based CP reflectarray [82].

2.4.4 Wideband CP Sub-wavelength Reflectarray

Another practical way to improve the bandwidth of the CP array is using the sub-wavelength elements whose size is much smaller than the resonant size [83]. Two designs are reviewed here to demonstrate the functionality of this kind of CP array.

The first one is a $\lambda/3$ rectangular patch elements based CP reflectarray which is shown in Figure 2.37. By using this sub-wavelength patch element, the designed CP reflectarray has a 3 dB AR bandwidth of 11%, which is much wider than the bandwidth of half-wavelength patch based CP reflectarray [84].

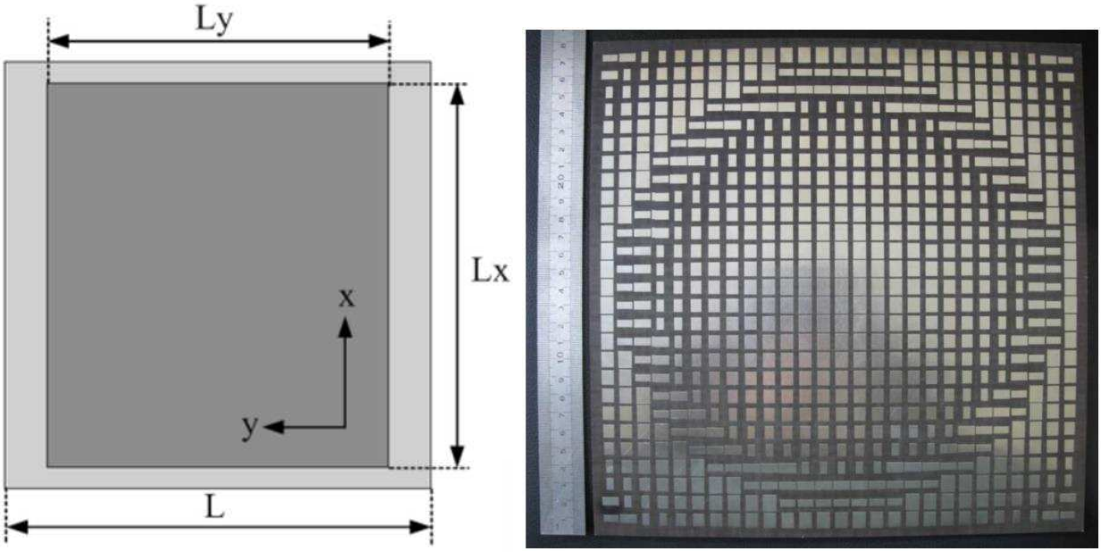

Figure 2.37 Configuration of the $\lambda/3$ rectangular patch elements based CP reflectarray [84].

Another sub-wavelength element based wideband CP reflectarray can be found in [85]. The sub-wavelength element is a multi-resonance element consisting of a Jerusalem cross and an open loop, which occupies around $\lambda/3$ space.

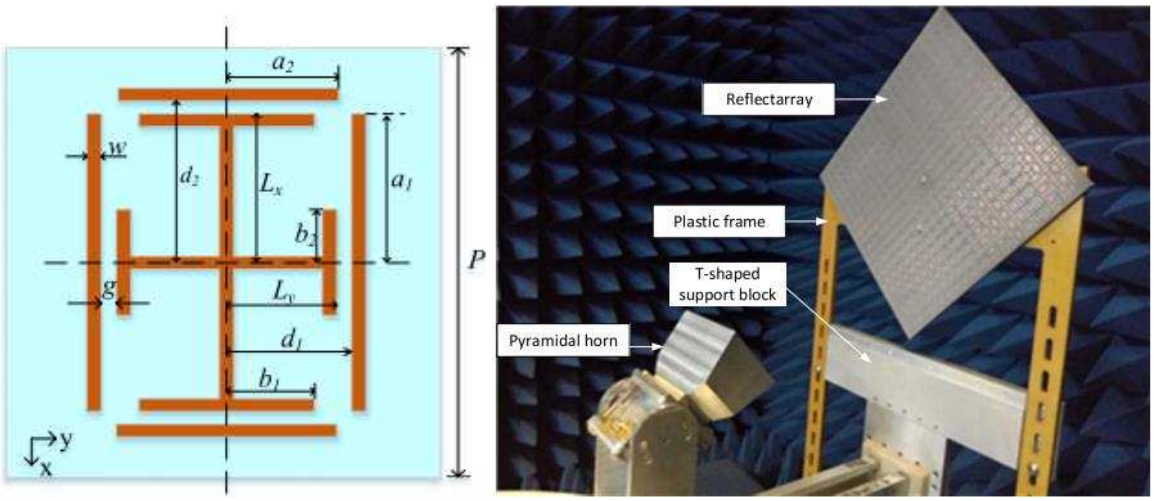

Figure 2.38 Configuration of multi-resonance sub-wavelength element and the wideband reflectarry [85].

The Configuration of the multi-resonance sub-wavelength element and the wideband reflectarray are shown in Figure 2.38. With the superposed effect of the multi-resonance element and sub-wavelength technique, the presented CP reflectarray achieves 50% 3 dB AR bandwidth.

2.4.5 A Comparison among Different Types of Wideband CP Arrays

Table 2.2 gives a comparison among the different types of wideband CP arrays.

Table 2.2 Comparison of Wideband CP Arrays

Array Type	Element Type & Reference NO.	3 dB AR Bandwidth	Element Number	Height	Fabrication Complexity
Conventional CP Array	Stacked patch [72]	5%	1×4	Low	Medium
	Crossed bowtie dipole [73]	37%	1×10	Medium	Medium
	Monofilar Archi-medean spiral [74]	10%	2×2	Low	Low
Sequentially Rotated CP Array	Single-layer corner truncated patch [77]	14%	8×8	Low	Low
	Crossed dipole [47]	56%	2×2	Medium	Medium
	Slot antenna [78]	29%	4×2	Low	Low
CP Printed Reflectarray	Stacked patch [80]	28%	9×9	Large	Medium
	Multi-resonance element [81]	43%	13×13	Large	Medium
	Spatial time-delay unit [82]	40%	~1000	Large	Medium
CP Sub-wavelength Reflectarray	Rectangular patch [84]	11%	27×27	Large	Medium
	Multi-resonance element [85]	50%	20×20	Large	Medium

It is indicated by Table 2.2 that the conventional CP array has the narrowest bandwidth among all types of CP arrays when similar elements are used. Normally, the bandwidth of the conventional CP array is smaller than its element's bandwidth due to the influence of mutual coupling. The sequential rotation method is an effective way to improve the bandwidth of CP arrays. More importantly, it is a general method and thus can be applied to various CP arrays. With this method, the bandwidth of a CP array consisting of narrow-band elements can be improved greatly. Printed CP reflectarrays are a kind of array which simplify the bulky and complicated feeding network of traditional phased arrays by using spatial feeding. Due to this greatly simplified feeding structure, the fabrication complexity and cost of large element number arrays are greatly reduced. Therefore, very large arrays can be designed in a relatively easier way. It is shown in the table that the 3 dB AR bandwidth of CP reflectarray with a great number of elements can still reach 40%. The sub-wavelength technique utilizes the mutual coupling among the elements to improve the bandwidth of CP reflectarrays. As the element space is rather small in this kind of array, more elements can be placed within the same array aperture. It can be seen from the table that the sub-wavelength CP reflectarray can achieve up to 50% 3 dB AR bandwidth.

2.5 Main Challenges and Research Objectives

This chapter introduced the design theory and methodology of CP antennas. Then, various types of wideband CP antenna elements and arrays were reviewed. Comparisons were given in terms of bandwidth, size, height and fabrication complexity. Through the comprehensive review and comparison of various wideband CP elements and arrays, a more clear understanding of the state-of-art development of wideband CP elements and arrays is enabled. It is also indicated by the literature review and the performance comparison that the main challenges in designing CP elements and arrays lie in the following aspects:

1. From Table 2.1, it is shown that low-profile CP elements with single feed generally demonstrate 3 dB AR bandwidth smaller than 50%. Using dual feed or multi feed will improve the bandwidth of CP elements but increases the size and the fabrication complexity. It is challenging to design wideband CP elements with compact size, low cost and low fabrication complexity.
2. To fulfill different system requirements, CP antennas need to possess other features, such as polarization reconfigurable ability for polarization diversity

application, and wide AR beamwidth for wide-angle beam scanning application. However, these additional requirements may degrade the bandwidth performance of CP antennas and also increases the design difficulty and fabrication cost. Therefore, another challenge is how to design CP antennas with diverse features while maintaining wide bandwidth and low design difficulty and fabrication cost.

3. It is observed from Table 2.2 that the 3 dB AR bandwidth of low-profile CP array antennas is typically smaller than 60%. To reduce the feeding network complexity of CP arrays, reflectarrays can be used. However, it is challenging to design wideband CP reflectarrays with single-layer structure and low profile. Vivaldi elements can be used to constitute an ultra-wideband CP array but the considerable antenna height and the bulky and complicated external 90^o hybrid coupler limit its application. It is also challenging to design wideband CP direct radiating arrays with low profile and relatively simple feeding networks.

To tackle these challenges, different CP elements and arrays are proposed and investigated in the following Chapters. The main research objectives of this thesis are summarized below.

1. Design wideband CP antennas with more compact structure, lower profile and lower fabrication complexity. The spiral antenna can achieve a CP bandwidth larger than 100% (3:1). However, the need of a UWB balun to feed spiral antennas makes it difficult to design and fabricate. Thus, it is highly desirable to design a UWB CP antenna with simple configuration and low fabrication complexity.
2. Design wideband CP antennas with other attractive features, such as reconfigurable polarizations for polarization diversity and wide AR beamwidth for wide-angle beam-scanning array. It is also aimed to achieve these additional features in a cost-efficient way, i.e. using low cost switches such as PIN diodes to achieve the reconfigurability and designing the wide AR beamwidth antenna with simple configuration and compact size.
3. Design a low-profile single-layer CP reflectarray with AR bandwidth larger than 60%. Conventional designs use multi-layer or true-time-delay techniques to improve the bandwidth performance of CP reflectarrays. However, these techniques increase the antenna height, fabrication complexity and the cost. Thus, another objective of this research is to design a wideband CP reflectarray with low profile, low fabrication complexity and cost.

4. Design an ultra-wideband CP direct radiating array with lower antenna height and simpler feeding network compared with the CP Vivaldi array. To reduce the antenna height, low-profile elements are needed while single-feed elements are required to reduce the complexity of feeding network. One promising way to fulfill all these requirement is designing a low-profile CP tightly coupled array.

Chapter 3. Ultra-wideband Circularly Polarized Crossed Dipole with Enhanced Front-to-Back Ratio

3.1 Introduction

As indicated in Chapter 1, GNSS systems have found important applications globally in both the military arena and commercial and consumer markets [7]. However, there are several challenges in developing high-performance GNSS antennas. One of the challenges is that the operation bandwidth for a high-performance GNSS antenna should extend from 1.1 GHz to 1.62 GHz and even to 2.5 GHz (for IRNSS) with good circular polarization properties.

Designing such a wideband circularly polarized antenna is always challenging. Spiral antennas exhibit interior broadband circular polarization characteristics and thus are extensively studied [59, 61, 86]. However, the requirement of a UWB balun for the spiral antennas makes them difficult to implement. Moreover, their bi-directional radiation properties make these conventional spiral antennas unsuitable for GNSS applications since a directional radiation pattern is needed to decrease the effects of the reflections from the ground [87].

Multi-path mitigation is another big challenge for high-performance GNSS antenna design. Since non-LOS (line of sight) multi-path signals could be generated by reflection of satellite signals, the system performance will be degraded once these multi-path signals are received by antennas [8]. Choke ring ground plane [88] is an effective way to mitigate multi-path signals through suppression of plane wave propagating along ground planes. Based on choke ring ground plane, a novel wideband non-cutoff ground plane has been presented in [87]. Choke rings are, however, rather bulky and expensive. In order to reduce the complexity as well as the cost of choke ring ground plane, a compact-size cross-plate reflector ground plane (CPRGP) has been proposed [89]. Nevertheless, the bandwidth of these ground planes is limited and none of them are able to cover the whole GNSS bands.

To solve these two issues, in this Chapter, an ultra-wideband CP antenna with high front-to-back ratio is presented. It is able to cover all GNSS frequency bands and a part of S-band. At first, a crossed elliptical dipole CP antenna is proposed and a simple but effective impedance matching method is given. Then, a novel cavity with unequal-length crossed fins is designed to obtain low backward radiation and high FBR. The proposed ultra-wideband CP antenna can work from 1 GHz to 2.87 GHz while maintain very low back-lobe level across the whole GNSS band.

This Chapter is organized as follows: Section 3.2 introduces the antenna structure and explains the simple but effective impedance matching method for bandwidth enhancement; Section 3.3 presents the novel cavity and its operation mechanism; Section 3.4 presents the measurement results and comparisons with simulation results as well as the analysis of electric fields above the cavity aperture; the summary is given in Section 3.5.

3.2 Antenna Configuration and Impedance Matching

3.2.1 Antenna Geometry

A single-feed crossed dipole with integrated phase delay lines, producing circular polarization, was initially presented in [46]. However, the input impedance of this antenna is about 122+j122 Ω and thus cannot be directly connected to a 50Ω feed line. To compensate the impedance mismatching as well as enhance the axial ratio (AR) bandwidth, parasitic open loops have been used [47]. Through changing the shape of dipole, this kind of antenna can be designed for wideband [48, 90] or multi-band [91, 92] operation.

To improve the bandwidth of CP crossed dipoles further, elliptical dipoles are employed in this Chapter. The evolution of the CP crossed dipole is shown in Figure 3.1, where the integrated phase delay line is not shown for simplicity. As the fan-shaped dipole and elliptical dipole have smaller quality factor (Q) and larger bandwidth than linear dipoles, the bandwidth of the CP crossed dipole consisting of elliptical dipoles is expected to be wider than the CP crossed dipole comprised of linear dipoles.

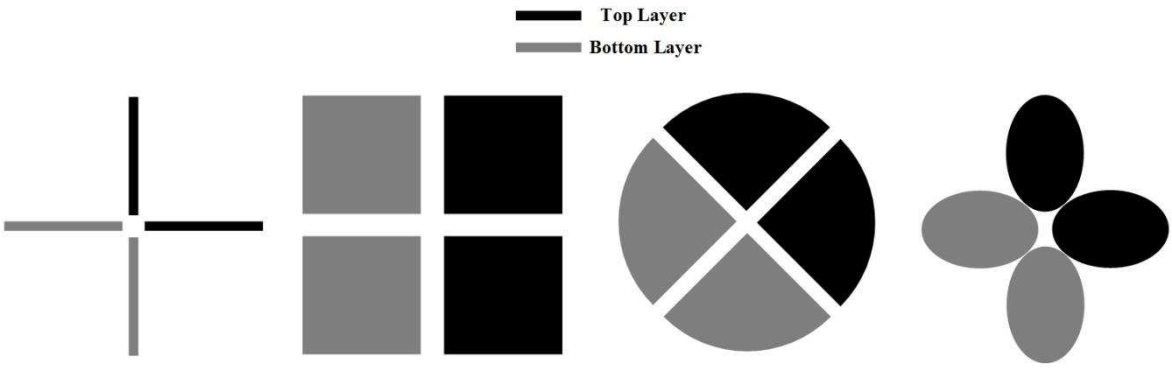

Figure 3.1 Evolution of the CP crossed dipole.

Figure 3.2 shows the geometry of the proposed single-feed ultra-wideband CP antenna. The antenna consists of two pairs of double-sided elliptical dipoles which are placed perpendicularly to each other. The dipole arm 1 & 2 and 3 & 4 are both connected by ring-shaped phase delay lines, which introduce a 90^{o} phase difference between the orthogonally placed dipole pairs to produce circularly polarized radiation.

The antenna is etched on a 0.817 mm thick Rogers RO4003 substrate with a relative permittivity of 3.55 and a loss tangent of 0.0027. The four elliptical dipole arms are all characterized by a major axis length R_1 and minor axis length R_2 while the phase delay line is a 3/4 ring with inner radius R_3 and line width W_2. A pair of partly overlapped rectangular patches with width W_1 are printed on both sides of the substrate and are used for placing the coaxial feed line. Besides, the patches are employed to tune the impedance matching of the proposed antenna, which is discussed in detail in the following section.

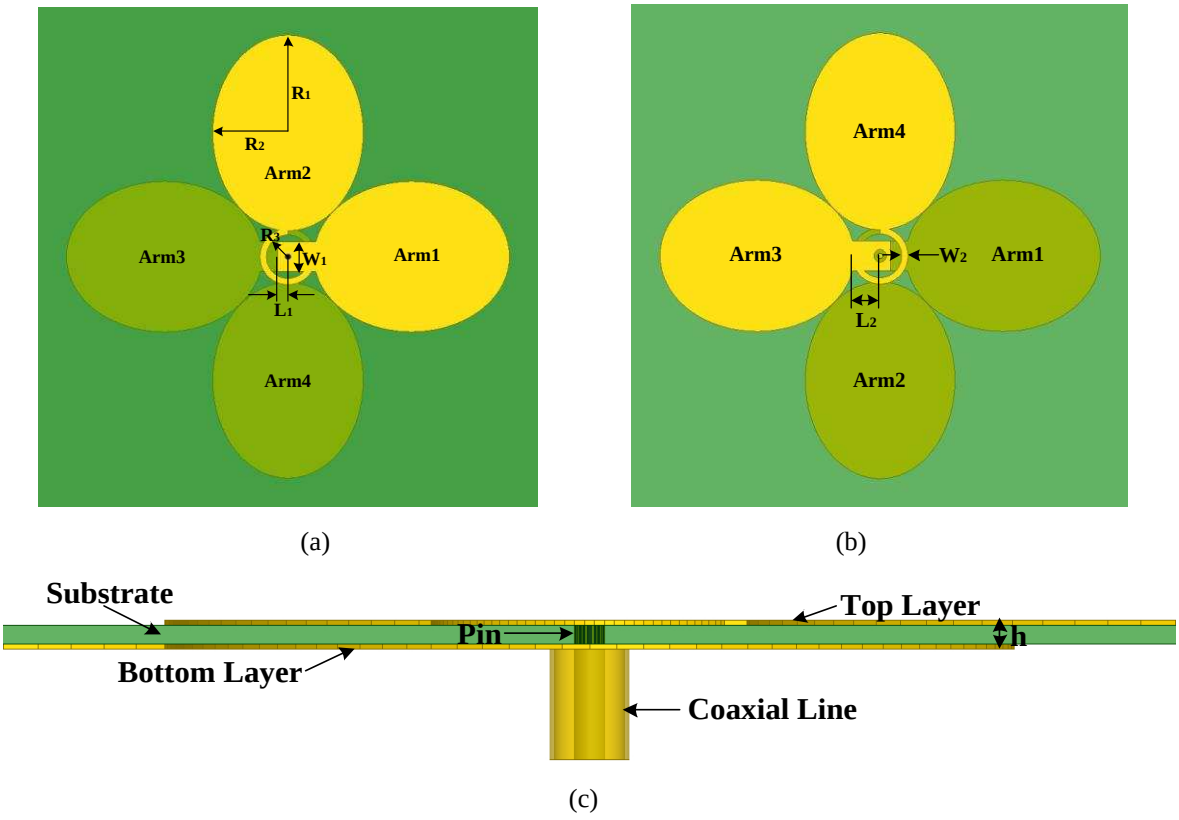

Figure 3.2 Geometry of the proposed antenna: (a) top view, (b) bottom view, (c) side view.

Similar to other crossed dipole CP antennas, the proposed antenna has bidirectional radiation. As shown in Figure 3.2, the inner conductor of the coaxial cable connects to the dipole arm 1 and 2 while the outer conductor is connected to the dipole arm 3 and 4. With this feeding structure, arm 1 & 3 and arm 2 & 4 form the horizontal and vertical dipoles respectively.

3.2.2 Impedance Matching

The impedance matching for a crossed dipole CP antenna is usually challenging. Methods such as using 75 Ω coaxial line [46], employing parasitic elements [47] and changing the shape of dipole [48] have been proposed to achieve good impedance matching. However, these approaches are either complex or space-consuming.

A simple but effective impedance matching method has been utilized in the proposed antenna, which is easier to be implemented than the aforementioned ones. By using this method, a 3:1 impedance bandwidth can be achieved without increasing complexity and space of the presented antenna.

A magnified picture of the partly overlapped rectangular patch is given by Figure 3.3. As shown in the picture, the pair of rectangular patches is printed on both sides of the substrate with an overlapped area of $W_1 \times L_1$. This overlapped structure of two patches results in a pair of parallel-plate capacitors, i.e. capacitor C_1 and C_2 shown in Figure 3.3. It is found that these two capacitors can effectively enhance the impedance characteristics of the proposed antenna and thus broaden the bandwidth.

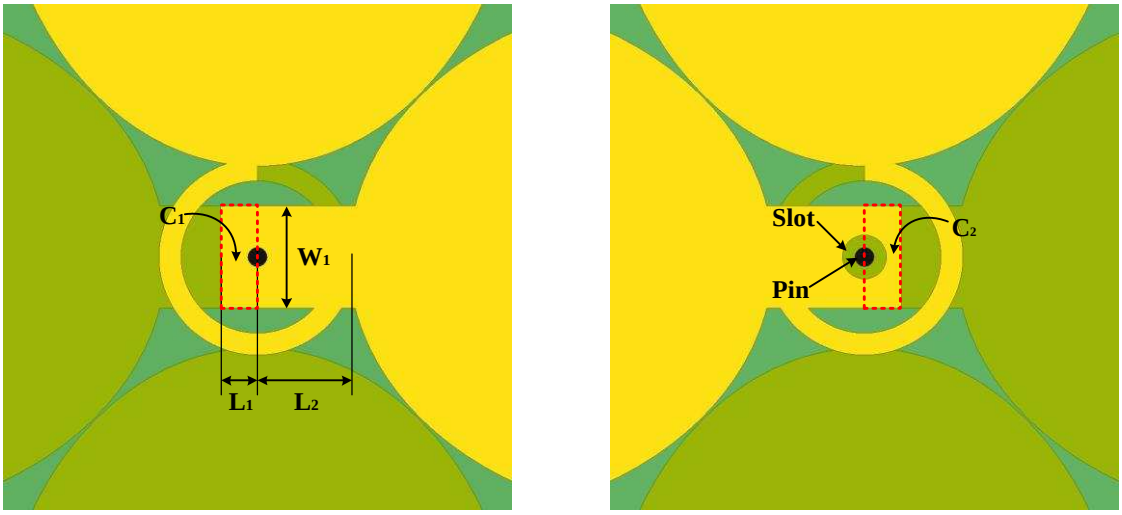

(a) (b)

Figure 3.3 Configuration of overlapped rectangular patch: (a) top view, (b) bottom view.

To analyze the proposed impedance matching method, qualitatively, the equivalent circuit model of the antenna is provided in Figure 3.4. The symbol Y_A denotes the antenna admittance without the overlapped rectangular patches while C_1 and C_2 denote the parallel-plate capacitors and Y_{in} represents the total input admittance of the proposed antenna.

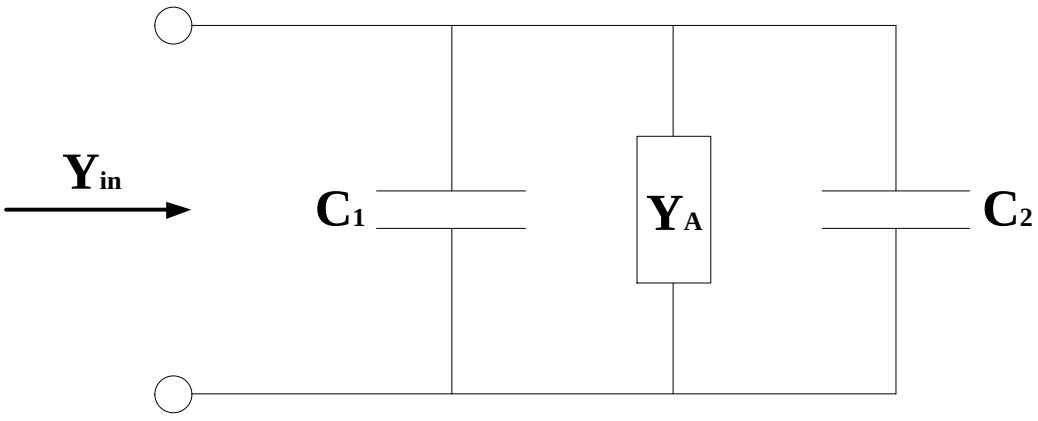

Figure 3.4 Equivalent circuit model of the proposed antenna.

Using the formula provided in [93], the capacitance of parallel-plate capacitors C_1 and C_2 can be calculated by the following equation when the electric charge density on the plates is uniform and the fringing fields at the edges can be neglected.

$$C_1 = C_2 \approx \frac{\varepsilon_r \varepsilon_0 W_1 L_1}{\mathrm{h}} \tag{3.1}$$

The approximation derives from the small slot on bottom rectangular patch and thus the input admittance Y_{in} of antenna can be denoted by:

$$Y_{\mathrm{in}} \approx Y_{\mathrm{A}} + 2j\omega \frac{\varepsilon_r \varepsilon_0 W_1 L_1}{\mathrm{h}} \tag{3.2}$$

It is shown in (3.2) that the antenna input admittance Y_{in} is affected by the rectangular patch width W_1 and length L_1. Therefore, the impedance characteristic of the antenna can be tuned by these two parameters to achieve a good impedance matching.

In order to demonstrate, intuitively, the effect of changing parameters W_1 and L_1, the simulated input impedances are studied while keeping the other antenna geometry parameters fixed, as in Table 3.1.

Table 3.1 Antenna Parameters

L_2	W_2	R_1	R_2	R_3	h
6.2mm	1.5mm	23.4mm	18mm	5.2mm	0.817mm

The simulated input impedance of the proposed antenna for various values of L_1 is shown in Figure 3.5. The rectangular patch width W_1 is kept constant as 7.5mm while the length L_1 is varied. As can be seen from Figure 3.5, the input impedance without the overlapped patch (L_1 = 0 mm) is large inductively and the majority of the impedance loci fall outside the VSWR = 2 circle, indicating that the bandwidth at this state is very narrow. By increasing L_1, the impedance loci begin to move along the admittance circle due to the increasing capacitance of C_1 and C_2. This phenomenon can be well explained by (3.2) as well.

Figure 3.6 depicts the input impedance loci under different patch widths, W_1, when patch length L_1 is 2.5 mm. Similar to the phenomenon observed in Figure 3.5, the impedance loci will move along the admittance circle when W_1 becomes larger. This impedance matching procedure is similar to the method using lumped LC elements to tune the impedance bandwidth. However, the proposed method is more advantageous in terms of antenna efficiency and complexity due to the absence of a lossy π-type or M-type LC circuit. Moreover, there are no adequate spaces to place external impedance matching circuit while the proposed method needs nearly no additional spaces to implement and thus it is very

effective for the impedance matching of the proposed antenna.

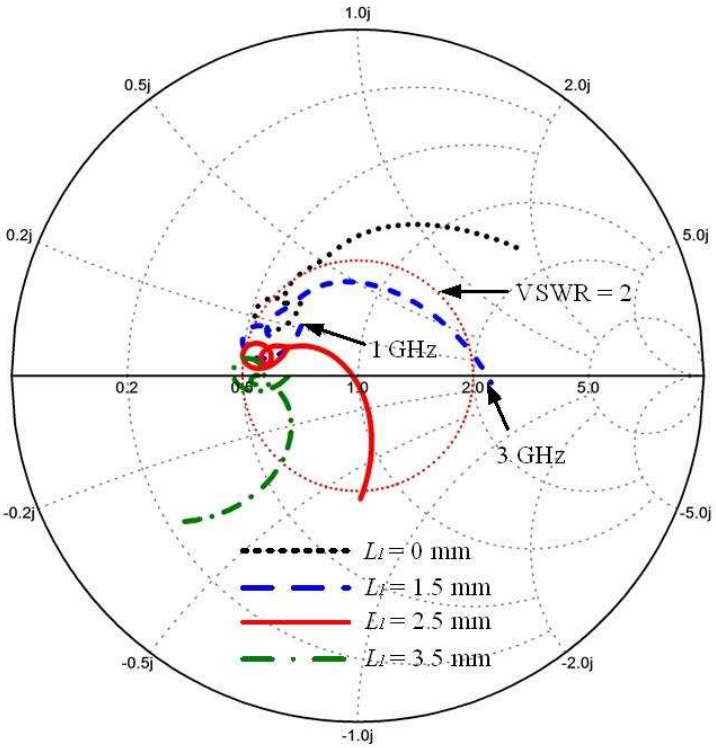

Figure 3.5 Simulated input impedance of the proposed antenna with different patch length L_1.

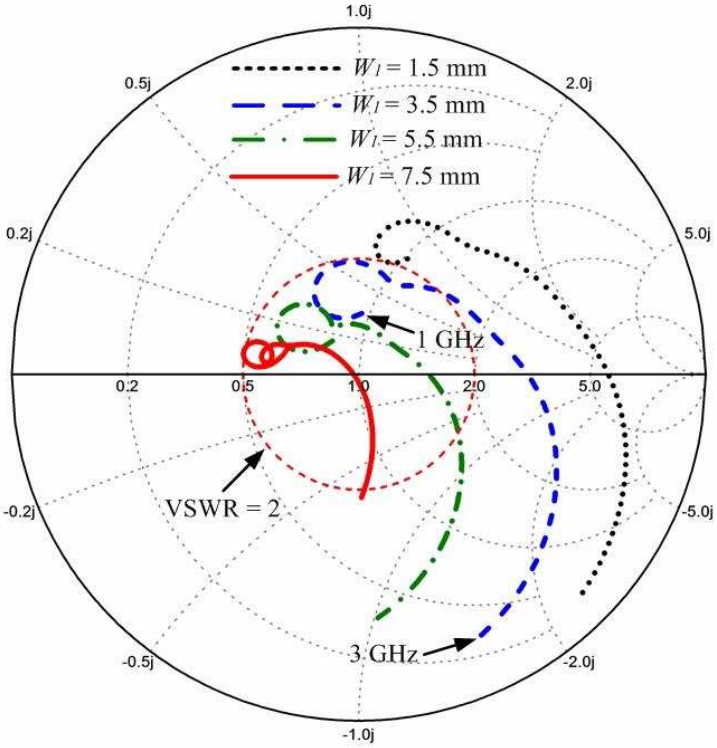

Figure 3.6 Simulated input impedance of the proposed antenna with different patch width W_1.

3.3 Cavity Design for FBR Improvement

Multipath interference, caused by the deleterious superposition of signals received at a user's antenna via multiple paths from a satellite, is one key source of error in relative positioning GNSS systems [3]. For GNSS receiving antennas, multi-path mitigation is critical for achieving high performance. Theoretically, a good multipath mitigating GNSS antenna should be able to have a cross-polarization rejection ratio (or polarization isolation) $\geq$ 15 dB for signals incoming at any positive elevation angle and back radiation less than -10 dB to decrease the effects of the reflections from the ground [87]. In addition, the pattern roll-off from zenith to horizon should be between 8 and 14 dB, while phase center variation should be less than 2 mm [89].

The aforementioned requirements are very difficult to achieve simultaneously and thus certain compromises need to be made in the antenna design procedure. Moreover, considering that the proposed antenna in Section 3.2 is ultra-wideband, further compromise is expected to be made. Also, since the proposed crossed elliptical dipole antenna is bi-directional, making the antenna radiate in one direction, i.e. improving front-to-back ratio (FBR), is regarded as the main goal during the antenna optimization procedure.

3.3.1 Working Mechanism of the Cavity

The proposed cavity is shown in Figure 3.7. It can be seen from Figure 3.7 that the ground plane is composed of a cylindrical cavity with crossed unequal length fins. The cavity is designed in such a way to reduce the back-lobe of the antenna maximally.

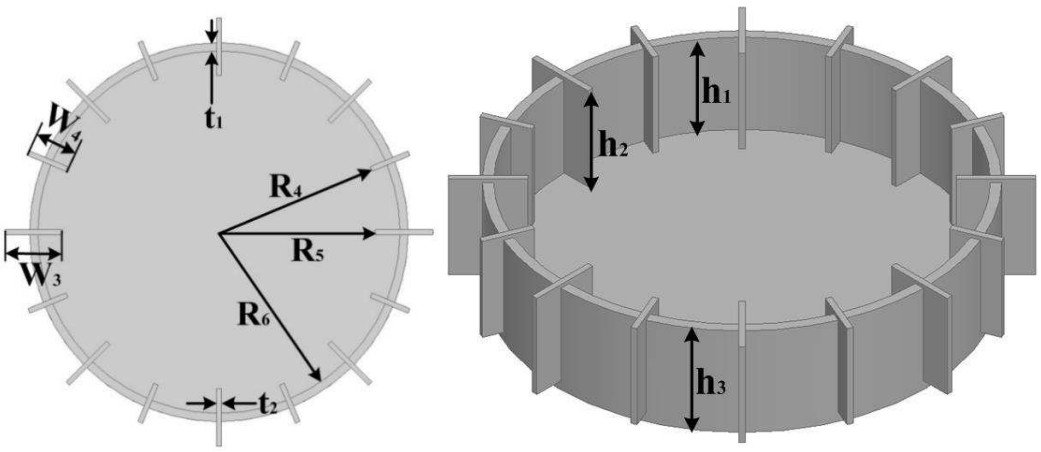

Figure 3.7 Geometry of the proposed cavity.

It is well known that the plane wave propagating along the ground plane will re-radiate at the ground plane edge and thus increase the side-lobes as well as the back-lobe of the antenna. Therefore, suppression of plane waves along the ground plane can reduce

the back-lobe of the antenna. To explain the working mechanism of the proposed cavity in terms of the suppression of plane waves along the ground plane, similar analysis methods to [87] are adopted.

Considering the two TEM plane waves Ⅰ and Ⅱ shown in Figure 3.8, they can be denoted by the following equations respectively.

$$E_x(y,t) = E_{x0}\cos(ky - \omega t + \varphi_1) \tag{3.3}$$

$$E_z(y,t) = E_{z0}\cos(ky - \omega t + \varphi_2) \tag{3.4}$$

The boundary condition of flat conductor ground plane imposes that no tangential electric field can exist, i.e.

$$E_t = 0 \tag{3.5}$$

This equation indicates that plane wave Ⅰ cannot propagate along the circular ground plane while wave Ⅱ can exist. Considering the situation in Figure 3.8 (b), wave Ⅰ cannot propagate along the cavity bottom due to the boundary condition given by (3.5). In contrast to the flat circular ground plane, wave Ⅱ cannot propagate along the proposed cavity either since there is a mandatory boundary condition imposed by the vertical cylindrical wall as well as the crossed fins. Therefore, it can be expected that the proposed cavity can offer better ability in the suppression of plane waves along the ground plane compared to a regular circular flat ground plane.

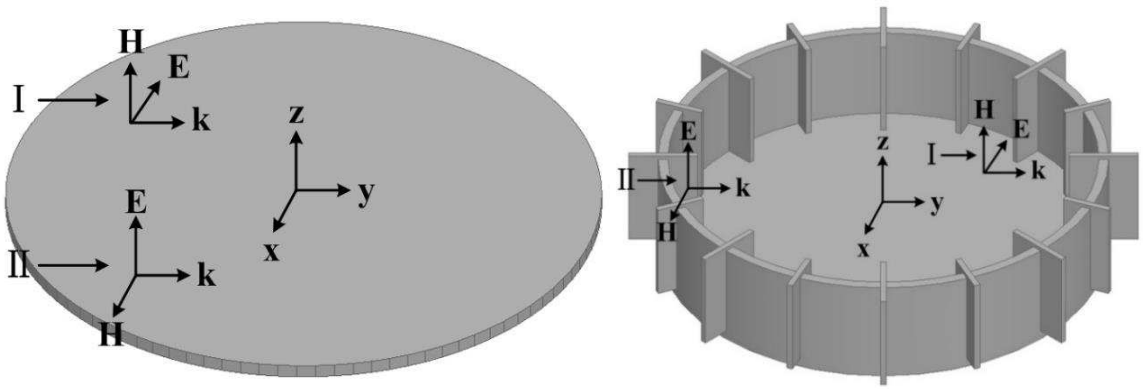

(a) (b)

Figure 3.8 Two plane waves on: (a) flat circular ground plane, (b) proposed cavity.

As indicated in Section 3.2, the proposed antenna radiates in bi-direction, RHCP towards the broadside and LHCP backwards. Conventionally, a large ground plane or a cavity is required to reduce the back-lobe of such kinds of antenna by reflecting the downward waves into the upward direction. The proposed cavity placed underneath the antenna can afford better back-lobe reduction ability by minimizing diffracted waves; the mechanism can be explained as follows.

Figure 3.9 depicts the propagation of downward LHCP wave excited by the antenna under different situations. When the proposed antenna is placed above a large flat ground plane, the majority of the LHCP wave will be reflected by the ground plane. However, considerable downward waves can still propagate across the ground plane due to the diffraction of these waves and result in a large back-lobe. This diffraction effect can be decreased by replacing the flat ground plane with a cylindrical cavity shown in Figure 3.9 (b) as the peripheral vertical wall can stop part of the diffracted waves.

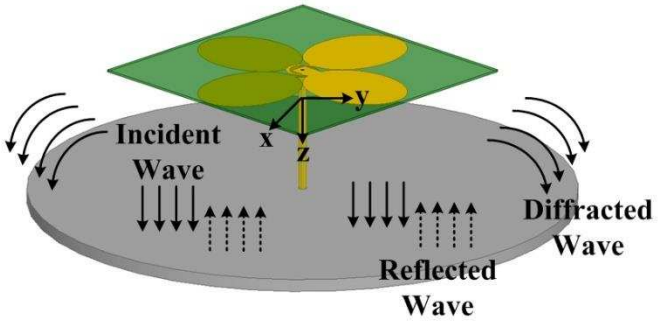

(a)

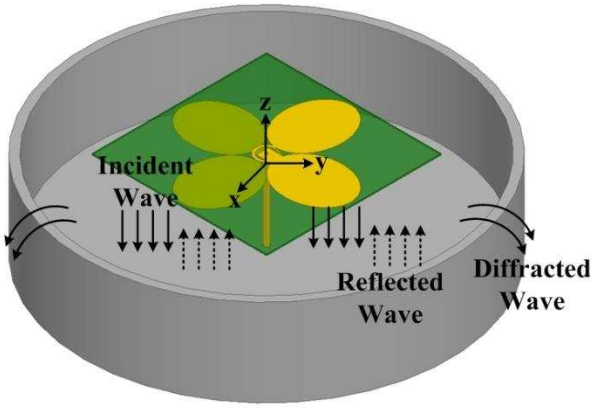

(b)

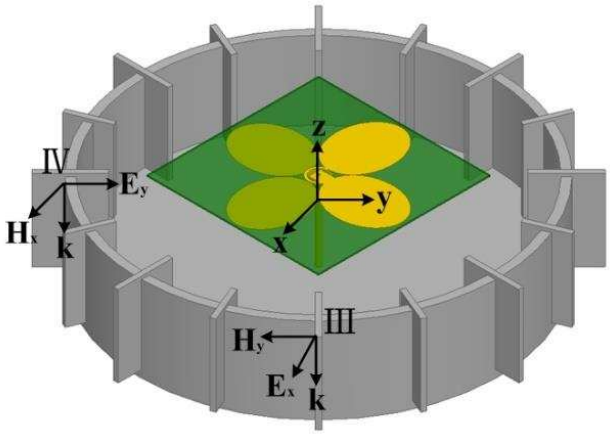

(c)

Figure 3.9 Downward wave above: (a) flat circular ground plane, (b) cylindrical cavity, (c) the proposed cavity.

A LHCP wave depicted in Figure 3.9 can be expressed as:

$$\vec{E}(z,t) = \overrightarrow{E_x}\cos(-kz - \omega t + \pi/2) + \overrightarrow{E_y}\cos(-kz - \omega t) \quad (3.6)$$

where $|\overrightarrow{E_x}| = |\overrightarrow{E_y}|$. As a circularly polarized wave, the electric field vector $\vec{E}$ will rotate on the x-y plane. To analyze the downward wave around the peripheral wall of the proposed cavity, two transient plane waves Ⅲ and Ⅳ whose electric fields are along the +x and +y direction, respectively, have been plotted in Figure 3.9 (c). These two waves cannot propagate along the vertical fins due to the boundary condition given by (3.5). Actually all the 16 vertical fins can be used to block the diffracted waves when the direction of the transient $\vec{E}$ vector is parallel to these fins. Therefore, the proposed cavity is more advantageous for back-lobe reduction than the regular cylindrical cavity.

3.3.2 Comparison with Other Ground Planes

It has been shown in Section 3.3.1 that the proposed cavity can offer better back-lobe reduction ability than a flat ground plane and regular cylindrical cavity. This performance enhancement is mainly from the suppression of plane waves along the ground plane and the blocking of diffracted waves around the edge of the ground plane. To verify this analysis, a comparison between a flat plane ground, regular cylindrical cavity and the proposed cavity, in terms of the back-lobe reduction, is given in this sub-section.

The geometry dimensions of proposed cavity are given in Table 3.2.

Table 3.2 Cavity Dimensions (mm)

W_3	W_4	R_4	R_5	R_6	h_1	h_2	h_3	t_1	t_2
35	25	100	95	110	50	52	55	5	3

For the flat ground plane and regular cylindrical cavity, the most critical dimensions for back-lobe reduction are the ground plane size as well as the height from antenna to ground plane. To make a reasonable comparison, the proposed antenna in Section 3.2 is placed at a height of h_1 = 50 mm above the ground plane for all three cases. Meanwhile, the radius of the ground plane is kept at 110mm.

The simulated back-lobe levels for the three ground plane reflectors are shown in Figure 3.10. As can be seen, the back-lobe is very high when a flat ground plane is placed underneath the ultra-wideband CP antenna. By using the regular cylindrical cavity, back-lobes smaller than -12 dB can be achieved across the whole GNSS band (1.1 - 1.62 GHz). Further back-lobe reduction has been observed through utilizing the proposed cavity. It can

be noted that a minimum 8 dB and 2dB enhancement in back-lobe reduction can be achieved compared to flat ground plane and regular cylindrical cavity respectively when the proposed cavity is used as a reflector of ultra-wideband CP crossed elliptical dipole. It is also worth pointing out that using more fins such as 32 will help little in performance enhancement of the proposed antenna. Therefore, the presented cavity is integrated with 16 fins for the reduction of manufacture complexity.

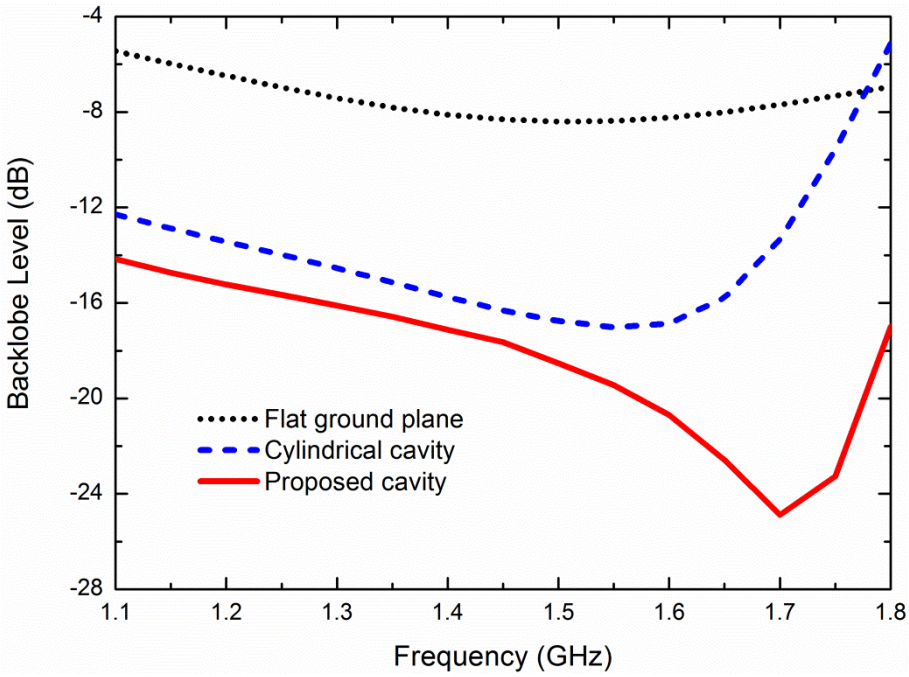

Figure 3.10 Comparison of back-lobe level using different ground plane reflectors.

Table 3.3 gives a comparison between the proposed cavity and other ground planes in terms of the FBR, multipath mitigation ability, size and cost. As shown, the proposed cavity has better performance and higher fabrication cost than the conventional flat ground plane and cylindrical cavity. It is cheaper and simpler than the choke ring ground plane but with degraded performance.

Table 3.3 Comparison with Other Ground Planes

Ground Plane Type	Size (Radius (R), Height (H))	Average FBR	Multipath Mitigation Ability	Cost
Flat Ground Plane	R = 130 mm, H=5 mm	20 dB	weak	low
Cylindrical Cavity	R = 130 mm, H=55 mm	25 dB	weak	low
Choked Ring Cavity	R = 130 mm, H=55 mm	30 dB	strong	high
Proposed Cavity	R = 130 mm, H=55 mm	30 dB	medium	medium

3.3.3 Cavity Optimization

Dimensions such as the length of fins and the radius of cavity play an important role in back-lobe reduction. Figure 3.11 depicts the back-lobe level and antenna gain under different pairs of W_3 and W_4. As indicated, the antenna gain under three states is similar. Under equal-length fins, the back-lobe degrades when the fin length increases. The back-lobe level with unequal-length fins is similar to the equal 25mm fins situation across the GNSS band. However, the latter case features a sharp increase in back-lobe level at higher frequency and thus the unequal-length fins are chosen.

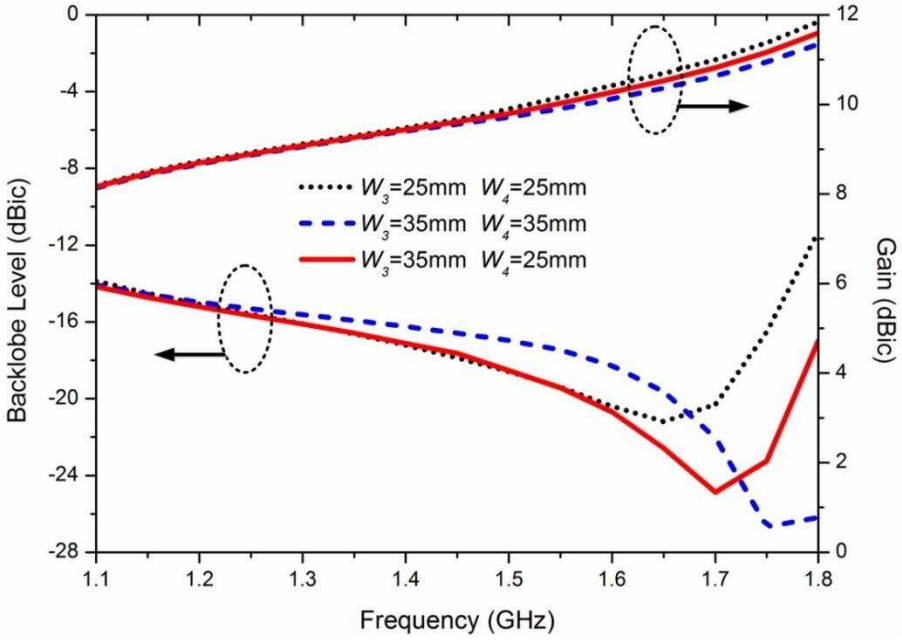

Figure 3.11 Back-lobe level and antenna gain under different W_3 and W_4.

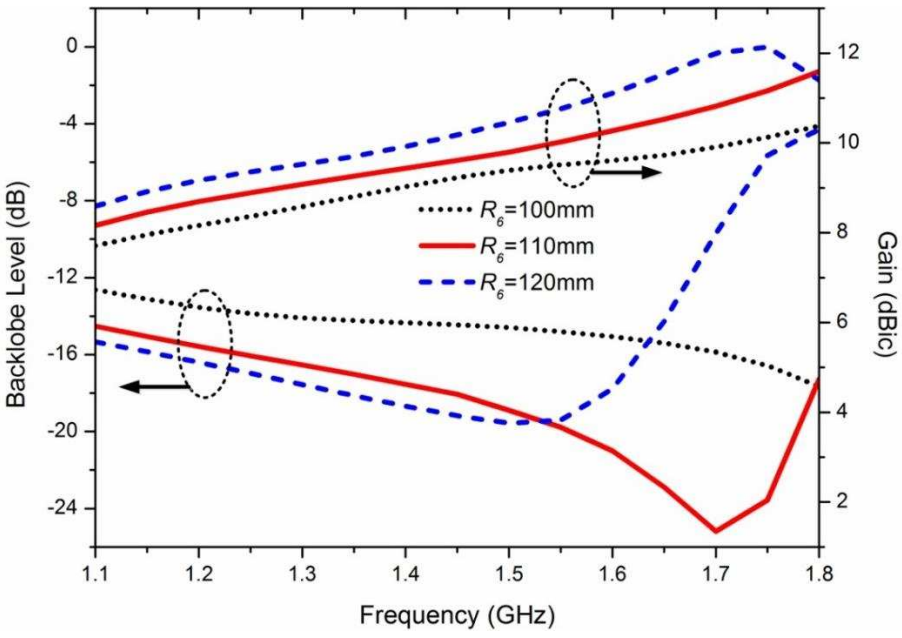

Figure 3.12 Back-lobe level and antenna gain under different R_6.

It is shown in Figure 3.12 that the antenna gain increases with larger cavity radius. However, the back-lobe increases after exceeding 1.5 GHz when R_6 is 120mm. Since the aim is to keep low back-lobe radiation across the GNSS band, the cavity radius R_6 is therefore to be kept at 110mm. With this cavity radius, the proposed antenna can achieve average 9 dBic gain and -17 dB backlobe.

3.4 Results and Discussions

In this section, the simulated and measured results including the VSWR, AR, radiation pattern and antenna gain of the proposed antenna are given to verify its performance.

3.4.1 Prototype Development

The prototype of the proposed ultra-wideband cavity backed CP antenna is shown in Figure 3.13. The rim of this cavity is made by gluing two semi-circle shaped conductors together.

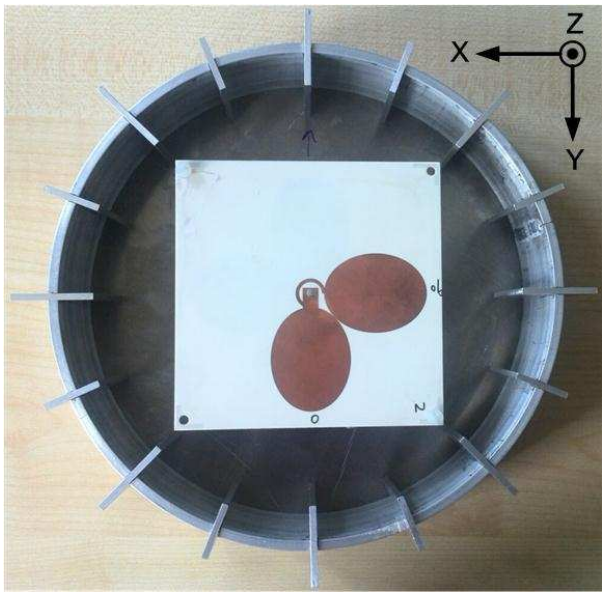

Figure 3.13 The prototype of ultra-wideband cavity backed CP antenna.

3.4.2 VSWR

The simulated and measured VSWRs of the proposed antenna are shown in Figure 3.14. As can be seen, the measured VSWR is in good agreement with simulation. The simulated and measured results both indicate a 0.9 GHz to 2.95 GHz (3.28:1=106%) impedance bandwidth can be achieved by the proposed antenna for VSWR=2.

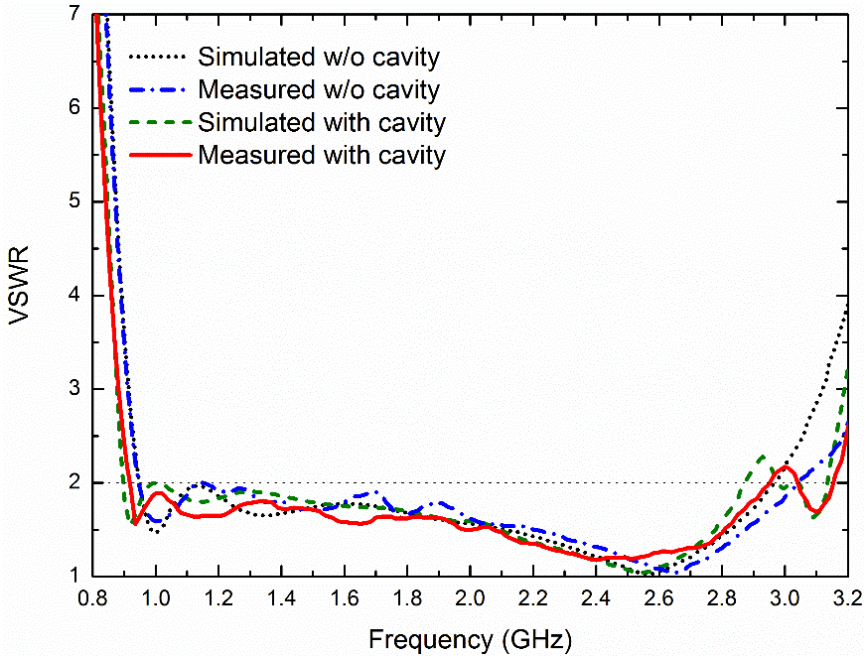

Figure 3.14 Simulated and measured VSWR of the proposed antenna with and without cavity.

3.4.3 Axial Ratio Bandwidth

The "phase-amplitude method" presented in [94] is used to measure the AR and LHCP and RHCP radiation patterns of the proposed antenna. As shown in [94], the following formulas can be used to calculate the RHCP and LHCP electric field components of a CP antenna:

$$E_{LHCP} = \frac{1}{\sqrt{2}}\{[H_A\cos(H_P) + V_A\sin(V_P)] + j[H_A\sin(H_P) - V_A\cos(V_P)]\}$$
$$E_{RHCP} = \frac{1}{\sqrt{2}}\{[H_A\cos(H_P) - V_A\sin(V_P)] + j[H_A\sin(H_P) + V_A\cos(V_P)]\} \quad (3.7)$$

The horizontal and vertical amplitude (H_A, V_A) and phase components (H_P, V_P) are quantities that are measured at each measurement angle in the far field of the antenna, with the source horn orientated at angles 0° and 90°. After obtaining the amplitude (H_A, V_A) and phase components (H_P, V_P) at each measurement angle, the RHCP and LHCP radiation patterns can be plotted.

To produce the AR versus frequency figure at broadside direction, the cross-polar power at broadside direction is calculated first at each frequency point.

Then the AR can be calculated by

$$\mathrm{AR} = 20\log_{10}\left(\frac{1+e}{1-e}\right) \quad (3.8)$$

Where $\mathrm{e} = 10^{-P_{dB}/20}$ and P_{dB} is the cross-polar power.

To evaluate the CP performance of the proposed antenna, the AR characteristics versus frequency relationship is given in Figure 3.15. As shown, the measured 3 dB AR bandwidth with cavity is from 1 GHz to 2.87 GHz (2.87:1=97%), which can cover the whole GNSS bands and a part of S band. It is also shown that the cavity improves the AR performance at low frequencies but degrades the AR performance at high frequencies when compared with the results without cavity used.

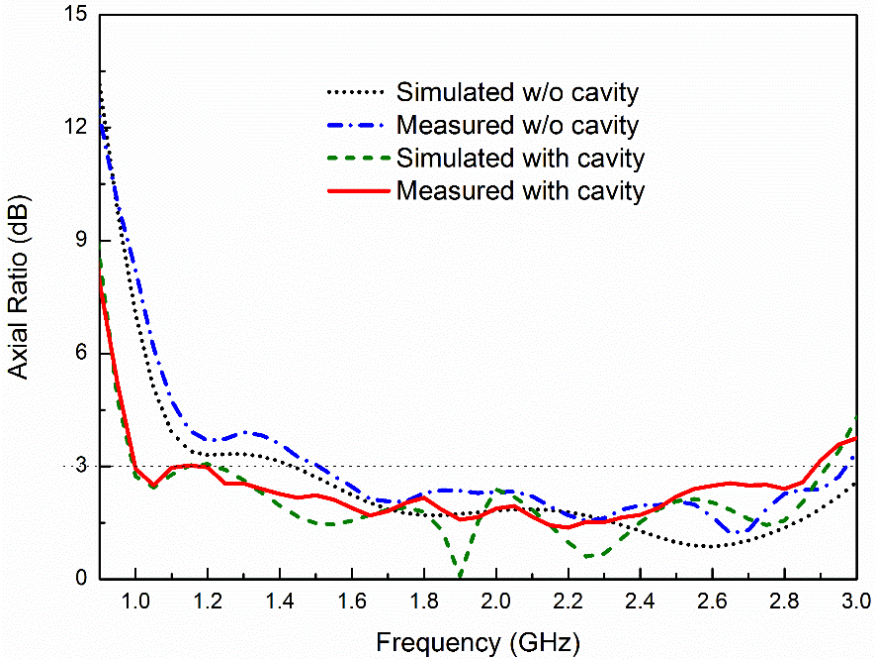

Figure 3.15 Simulated and measured AR of the proposed antenna.

3.4.4 Radiation Patterns and Gain

Figure 3.16 shows the radiation patterns of the proposed ultra-wideband CP antenna in the two main planes (XoZ and YoZ planes) at 1.1 GHz, 1.4 GHz, 1.7 GHz and 2.4 GHz. As shown, good agreements between the simulated and measured results are observed.

As shown in Figure 3.16, the proposed antenna can achieve larger than 30dB FBR across the whole GNSS frequency band. The 3 dB AR beamwidth is about 129^o (x-z plane) and 120^o (y-z plane) at 1.1 GHz, 156^o (x-z plane) and 63^o (y-z plane) at 1.4 GHz, 66^o (x-z plane) and 84^o (y-z plane) at 1.7 GHz.

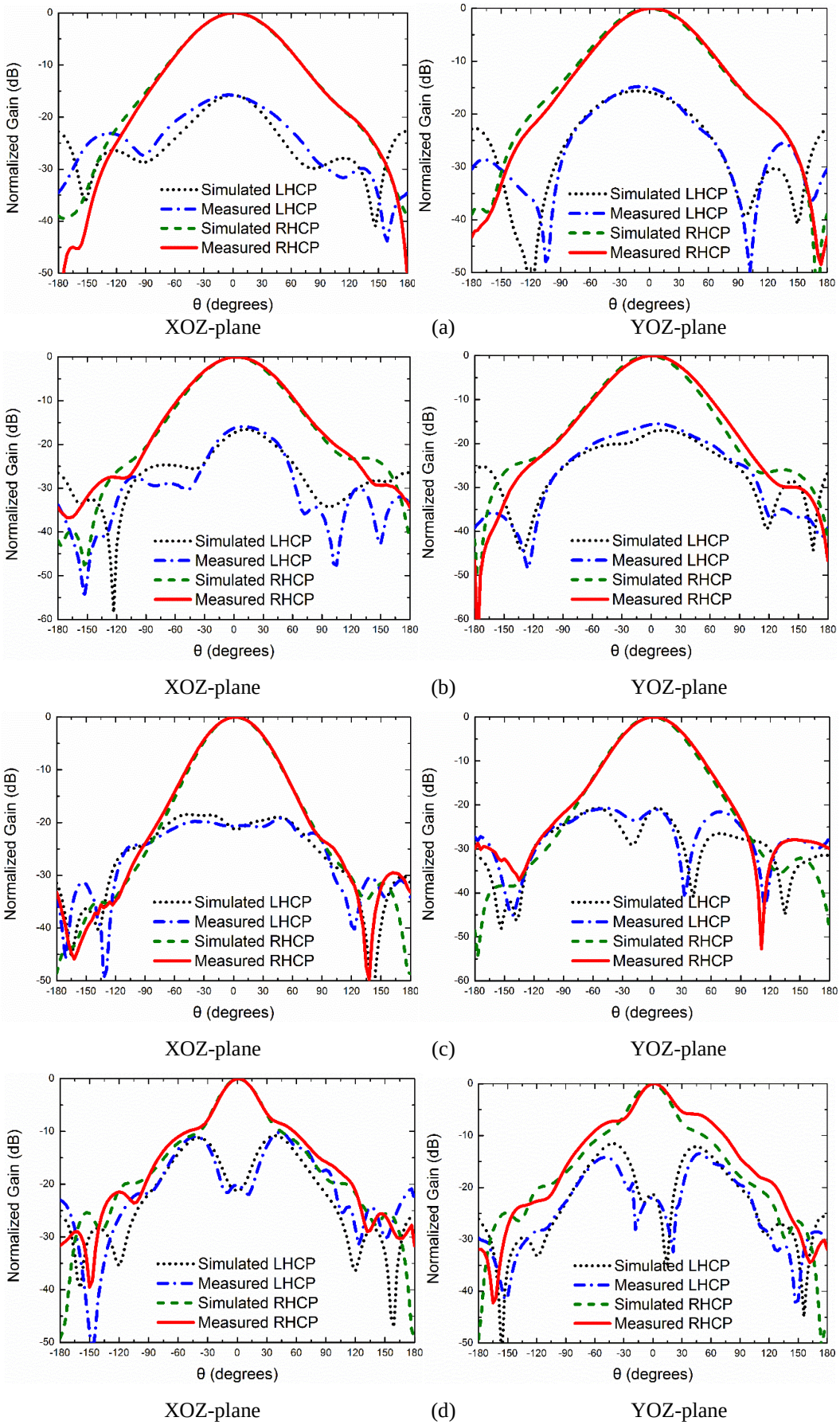

Figure 3.16 Simulated and measured radiation patterns at: (a) 1.1 GHz, (b) 1.4 GHz, (c) 1.7 GHz, (d) 2.4 GHz.

Figure 3.17 shows the simulated and measured gain with and without the integrated cavity. As shown, the antenna gain is around 9 dBic when the cavity is employed, which also indicates an average 6 dB gain enhancement is achieved compared with the results measured from the antenna only. The difference between the measured and simulated results may term from the measurement errors.

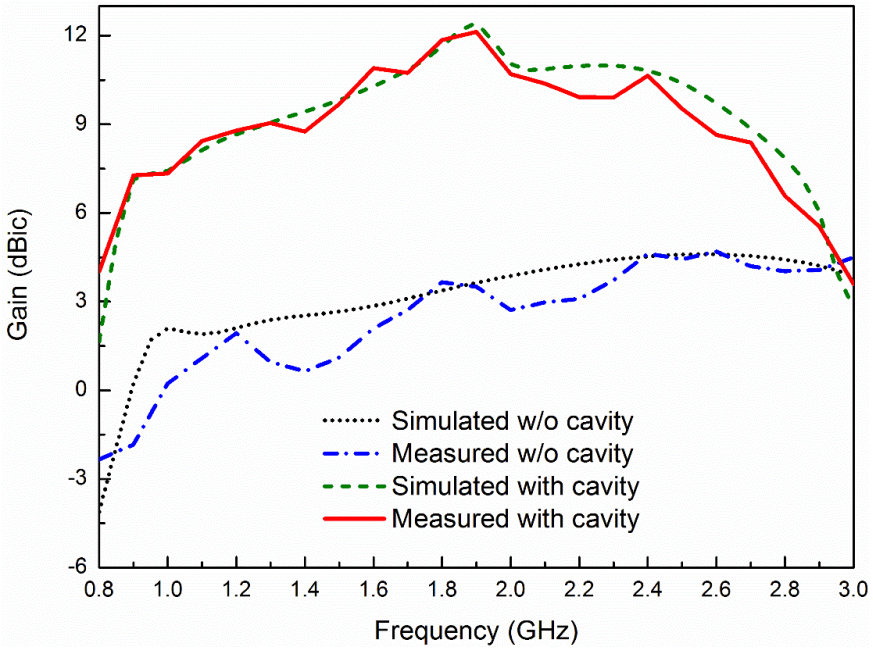

Figure 3.17 Simulated and measured gain with and without cavity.

3.4.5 Analysis of the CP Characteristics

To investigate the ultra-wideband CP characteristic of the proposed antenna, the electric field distributions above the aperture at 1 GHz, 1.8 GHz and 2.6 GHz are given in Figure 3.18.

As can be seen, the distribution of electric field is varied at different frequencies. From Figure 3.18 (a), it can be noticed that the maximum electric field at phase angle 0^o and 90^o appears at the end of the elliptical dipole arms. This indicates that the proposed antenna works in a half-wavelength dipole mode at 1 GHz. When the frequency increases to 1.8 GHz, the strongest electric field occurs at the side edge of the elliptical dipole arm. Therefore, it can be concluded that the resonance length of the proposed antenna is decreased, which makes the antenna work at a higher frequency band. At 2.6 GHz, the strong electric field no longer appears just around the antenna (see phase angle 90^o in Figure 3.18 (c)) and there are evident strong fields between the antenna and the cavity. Comparing this field distribution with those at lower frequencies, it is found that a higher mode is excited, which results in the deterioration of radiation pattern shown in Figure 3.16 (d).

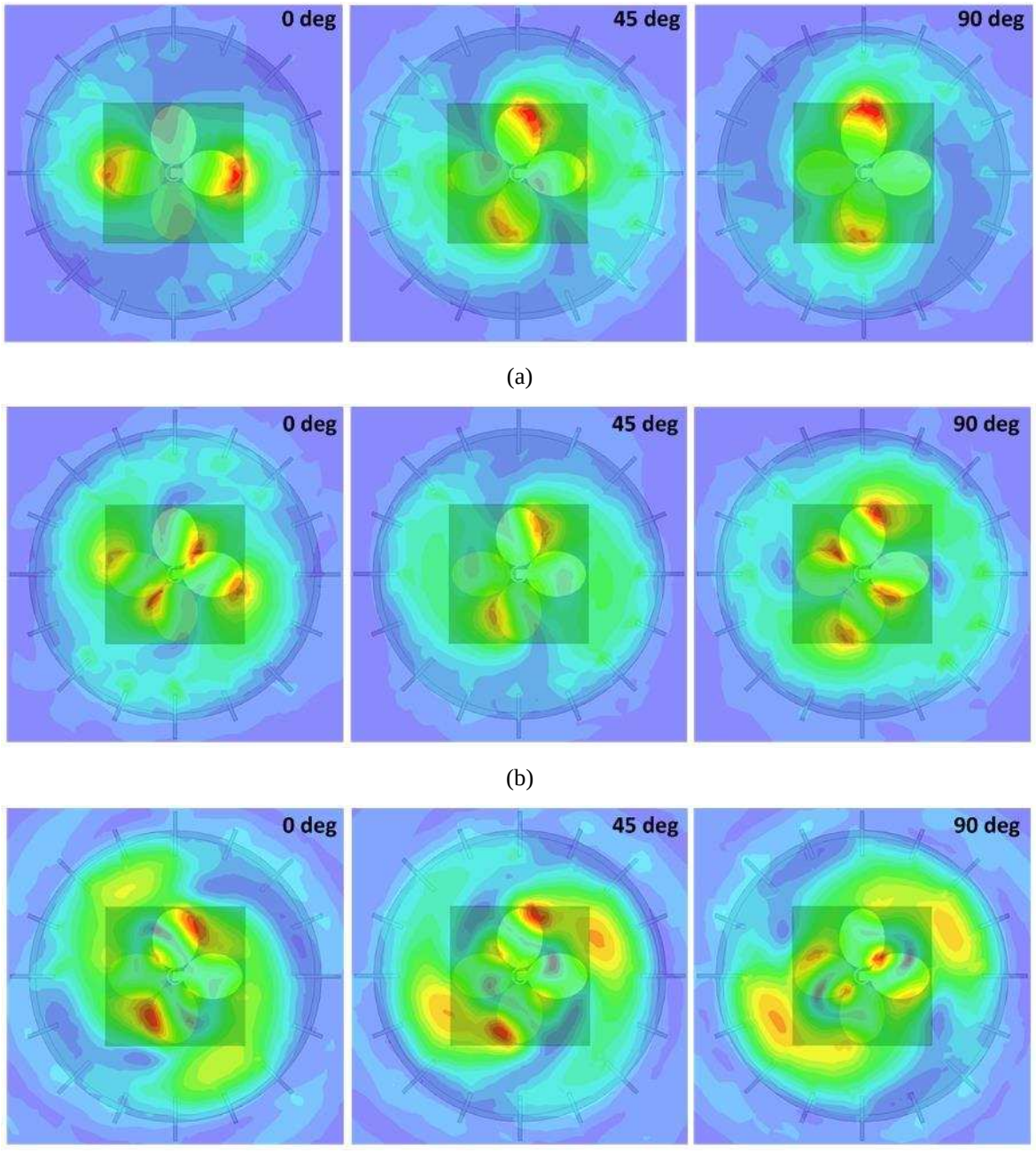

Figure 3.18 Electric field distribution in the cavity aperture at different frequencies: (a) 1 GHz, (b) 1.8 GHz, (c) 2.6 GHz.

From the different electric field distributions at phase angle 0^o, 45^o and 90^o in Figure 3.18, it can be seen that a right-hand rotated electric field has been produced at all given frequencies. This indicates that the antenna is circularly polarized in an ultra-wideband frequency range.

In addition, the electric fields are almost all bounded by the cavity and little field can propagate over the cavity as shown in Figure 3.18 (a) and (b). This phenomenon verifies the back-lobe reduction ability of the proposed antenna, which was analyzed in Section 3.2.

3.4.6 A Comparison among Wideband CP Crossed Dipoles

Table 3.4 gives a comparison between the proposed antenna and other CP crossed dipoles in terms of impedance bandwidth, 3 dB AR bandwidth and average FBR. It can be seen that the proposed antenna has much wider CP bandwidth and larger FBR compared with other reported CP crossed dipole antennas.

Table 3.4 Comparison of CP Crossed Dipole Antennas

Ref. No.	Antenna Size (at center freq.)	Impedance Bandwidth	3 dB AR Bandwidth	Average FBR
[46]	0.92λ×0.92λ	31%	15%	15dB
[47]	1.0λ×1.0λ	38%	28%	15dB
[48]	0.52λ×0.52λ	50%	27%	<10dB
[90]	0.17λ×0.17λ	12%	3%	-
This work	0.7λ×0.7λ (without cavity) 1.5λ×1.5λ (with cavity)	106%	97%	30dB

3.5 Summary

A single-feed ultra-wideband circularly polarized antenna has been proposed and investigated in this Chapter. A simple but effective impedance matching method is employed to enlarge the impedance bandwidth and a cavity is presented to reduce the back-lobe of the antenna. Good agreement between simulation results and measurement proves that this design can work in a nearly 100% bandwidth region as a CP antenna. Analysis of the electric field above the cavity, as given in this Chapter, has explained the ultra-wideband CP operation of the proposed antenna. With a lower than -15dB back-lobe level and a larger than 30dB FBR, this antenna is very promising for high-performance GNSS applications.

Chapter 4. Wideband Polarization Reconfigurable Loop Antenna

4.1 Introduction

An ultra-wideband CP crossed dipole which achieves around 100% 3 dB bandwidth is presented in Chapter 3. Although it has superior bandwidth performance, it works in one polarization status only. For some applications, the polarization diversity is demanded. In these circumstances, wideband antennas with reconfigurable polarizations are required.

Polarization reconfigurable antennas have received considerable interest since polarization diversity can be used to mitigate the detrimental fading caused by multipath effects in wireless local area networks (WLAN) [10], provide effective modulation scheme in active read/write microwave tagging systems [95] and realize frequency reuse for doubling the system capability in satellite communication systems [96].

It is stated in [97] that the channel capacity of a 2×2 MIMO orthogonal frequency division multiplexing (OFDM) system is improved by using circular-polarization reconfigurable antennas compared with the single polarization system under both line-of-sight (LOS) and non-LoS (NLOS) indoor environments. A more comprehensive experiment held in [98] has shown that polarization reconfigurable antennas used in conjunction with adaptive space–time modulation techniques provide additional degrees of freedom to the current adaptive MIMO systems, increasing quality, capacity and reliability. These studies have verified experimentally the benefits of deploying polarization reconfigurable antennas at the system level.

Polarization reconfigurable antennas with switchable circular polarization have been widely investigated. For example, a PIN diode controlled U-slot patch antenna was proposed in [99]. Its polarization states can be switched between the two circular polarization senses. A piezoelectric transducer (PET) based antenna with similar functionality was designed in [100]. There are also some studies focusing on polarization reconfigurable antennas with full polarization configurability (two orthogonal linear polarizations and two circular polarizations) [101, 102]. However, the 3 dB axial ratio (AR) bandwidths of the aforementioned antennas are relatively narrow. The 3 dB AR bandwidths of [99-102] are 2.8%, 1%, 4.5% and 3.8% respectively. In specific application such as satellite communication where the spectrum requirements are relatively rich, these narrow band antennas will be of limited application due to their bandwidth restriction. In this case, developing a wideband polarization reconfigurable antenna with more than 10% 3 dB AR bandwidth is important for dual-CP satellite communications [103].

This Chapter includes two parts. First, a novel polarization reconfigurable dual-loop antenna which could alter its polarization states electronically to RHCP, LHCP or LP is proposed. To reduce the size of the dual-loop structure, a wideband single-loop antenna with switchable circular polarization is presented in the second part. The proposed antenna can achieve more than 12% overlapped operating bandwidth under both LHCP and RHCP states. Moreover, the theoretical analysis of the impedance matching method is conducted with analytical formulas derived and the derived formulas can be used for impedance matching of various kinds of antennas.

This Chapter is organized as follows: the polarization reconfigurable dual-loop antenna and its performance are given. Then, the wideband single-loop antenna with switchable circular polarization is presented in Section 4.3. The impedance matching method and relevant theoretical analysis of this method are also provided. A conclusion is given at the end.

4.2 Polarization Reconfigurable Dual-Loop Antenna

4.2.1 Antenna Configuration and Operation Mechanism

As indicated in Section 2.3.4, travelling-wave current can be excited for a loop antenna if a small gap is inserted to form an open-loop structure. Once the travelling-wave current is excited along the loop, CP radiation can be achieved as explained in Section 2.2.3. It is noted that the open-loop antenna can radiate RHCP or LHCP wave according to different gap position, as shown in Figure 4.1. Therefore, a polarization reconfigurable antenna can be obtained if the two gaps can be inserted into the same loop and one of them is functioned as a gap while the other one is shorted. RF switches such as PIN diodes can realize this functionality when they are biased separately. Based on this conception, a polarization reconfigurable antenna consisting of PIN diodes loaded loops is proposed, as shown in Figure 4.2, where it is concluded that RHCP radiation is achieved when diodes 1 and 3 are turned on while diodes 2 and 4 are turned off because anti-clockwise travelling-wave electric current is excited in this case. Similarly, clockwise travelling-wave electric current can be excited once diodes 2 and 4 are turned on and thus LHCP radiation is realized under this state. When the four diodes are all turned on, standing-wave current distributions are excited along both loops and thus LP radiation is achieved.

As shown in Figure 4.2, each loop has a radius R and width w_1. It is printed on a FR4 substrate with a relative permittivity of 4.4, loss tangent of 0.02 and height of 1.6 mm. A

coplanar stripline (CPS) is used at the feed input for impedance matching and relevant analysis of this impedance matching method will be given in the Section 4.3.3.

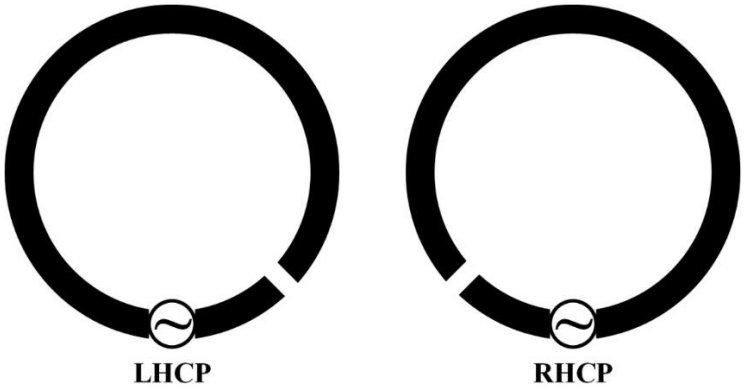

Figure 4.1 LHCP and RHCP open loop antenna based on different gap position.

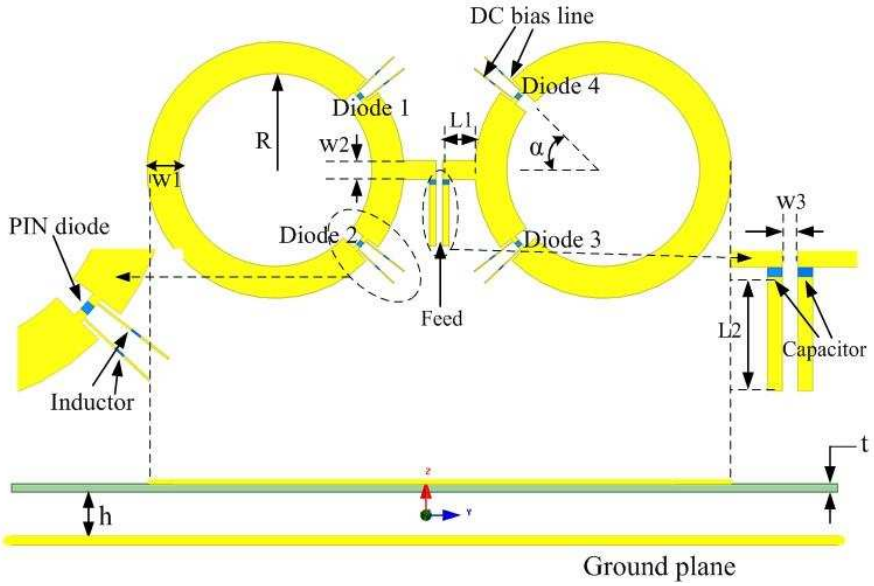

Figure 4.2 Geometry of the polarization reconfigurable dual-loop antenna.

Detailed antenna design parameters are given in Table I.

Table 4.1 Dual-Loop Antenna Parameters

R	α	w1	w2	w3	L1	L2	h
15mm	45^o	5mm	3mm	1mm	5mm	9.5mm	10mm

To obtain accurate simulation results, the DC bias circuit is taken into account in the simulation model. When the selected Infineon BAR50-02V diode is forward biased, a resistor with 10 ohms resistance is used while a 0.15pF lumped capacitor is used when the PIN diode is reversely biased. Furthermore, eight 100nH inductors are embedded in the DC bias line, which are used for RF choking. Additionally, a 10pF capacitor is placed in the CPS for the purpose of DC blocking.

4.2.2 Simulation Results and Discussion

The numerical analysis is conducted with the aid of Ansoft HFSS. By changing the status of the four PIN diodes, the proposed antenna can radiate RHCP, LHCP and LP waves, respectively.

4.2.2.1 Reflection Coefficients

The reflection coefficient (S_{11}) of the proposed antenna under three different polarization states is shown in Figure 4.3. It is indicated that a 12% and 7% impedance bandwidth (S_{11} < -10dB) have been achieved for CP and LP, respectively.

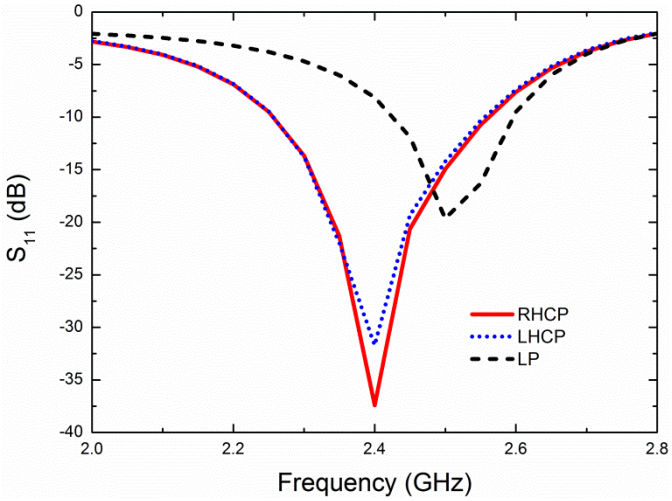

Figure 4.3 Simulated reflection coefficients under three states.

4.2.2.2 Axial Ratio Bandwidth

Figure 4.4 depicts the AR of proposed polarization reconfigurable antenna versus frequency in the broadside direction under RHCP and LHCP situation. A 5% 3 dB AR bandwidth is achieved under both RHCP and LHCP states.

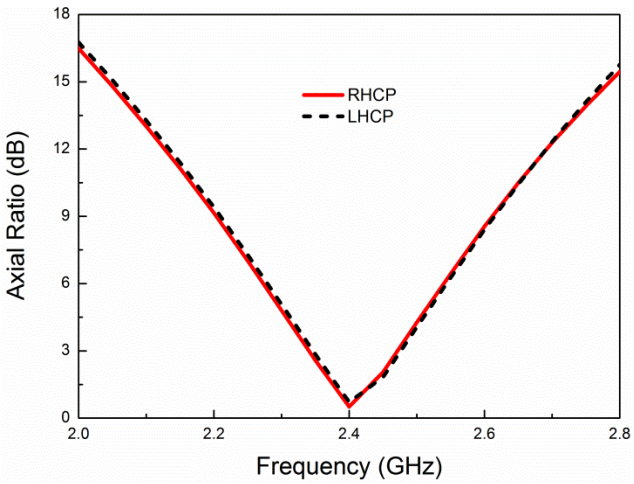

Figure 4.4 Simulated AR under two states.

4.2.2.3 Radiation Patterns

The simulated radiation pattern at 2.4 GHz for different polarization states are plotted in two planes ($\varphi = 0^o, 90^o$), as shown in Figure 4.5. Over 9.8 dBi peak gain is achieved for all polarization due to the presence of the ground plane. It is also noticed that low side lobe level of -26 dB for circular polarization and -23 dB for linear polarization have been obtained, which verifies the proposed antenna as a good unidirectional antenna.

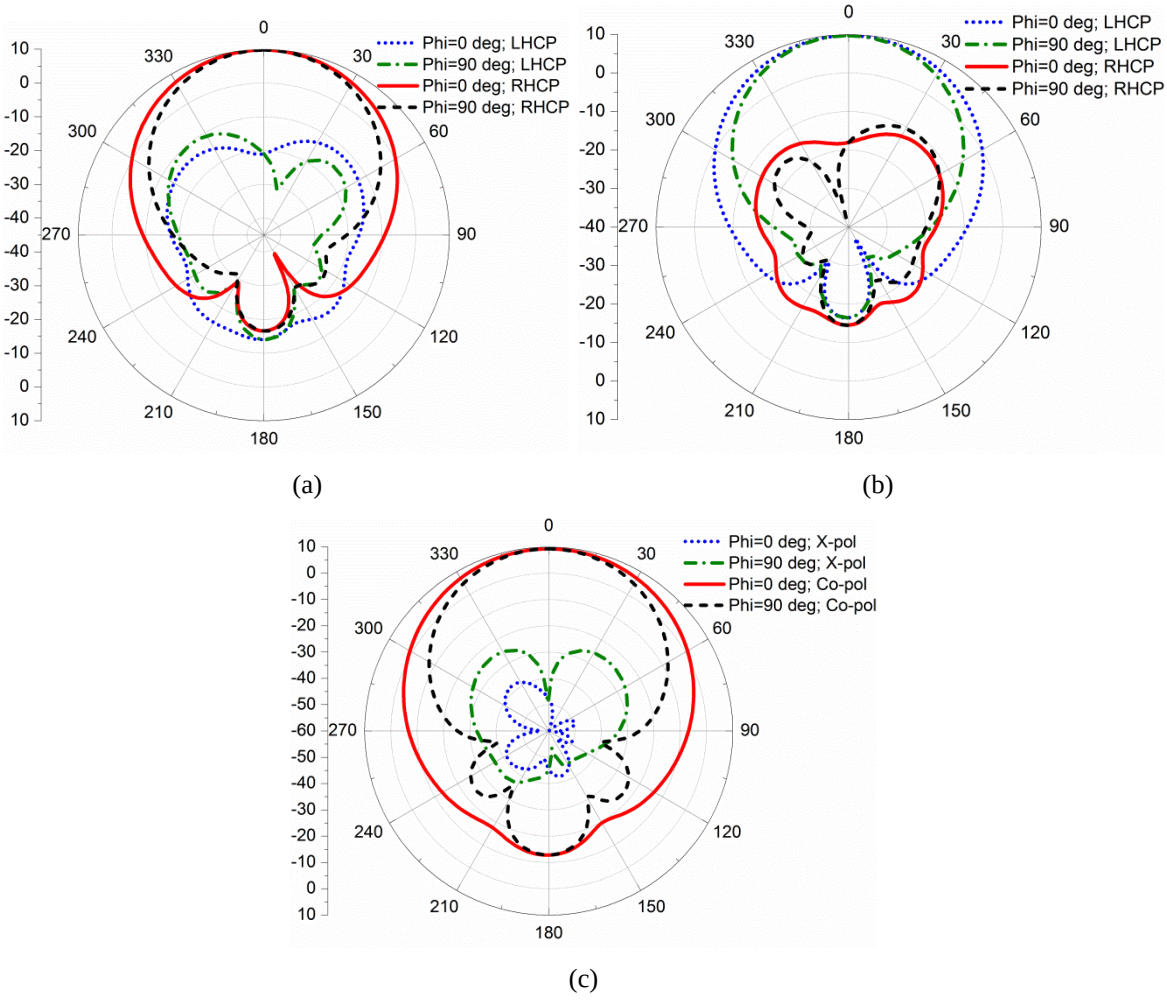

Figure 4.5 Simulated radiation pattern at 2.4 GHz under different polarization states. (a) RHCP, (b) LHCP, (c) LP.

4.2.2.4 Discussion

As shown in Figure 4.3, the impedance bandwidth of the CP state and LP state are not overlapped well. It is thus meaningful to increase the overlapped impedance bandwidth under CP and LP modes, which facilitates the overall bandwidth of the dual-loop antenna. A preliminary method is to change the loop dimensions or the inserted PIN diode's rotation angle. However, this strategy will degrade the AR characteristic. Since the impedance bandwidth is much wider than the AR bandwidth for CP, it is possible to shift the imped-

ance bandwidth to higher frequency by using a CPS with different impedance and length. This impedance tuning process using a specific transmission line will be discussed in detail in the following Section 4.3.3.

4.2.3 Experimental Results

The prototype of the proposed dual-loop antenna is shown in Figure 4.6. The antenna is fed by a semi-rigid coaxial line which is passed through the ground plane via a hole. The DC lines isolated with inductors and are connected to a DC voltage source when the antenna is under test.

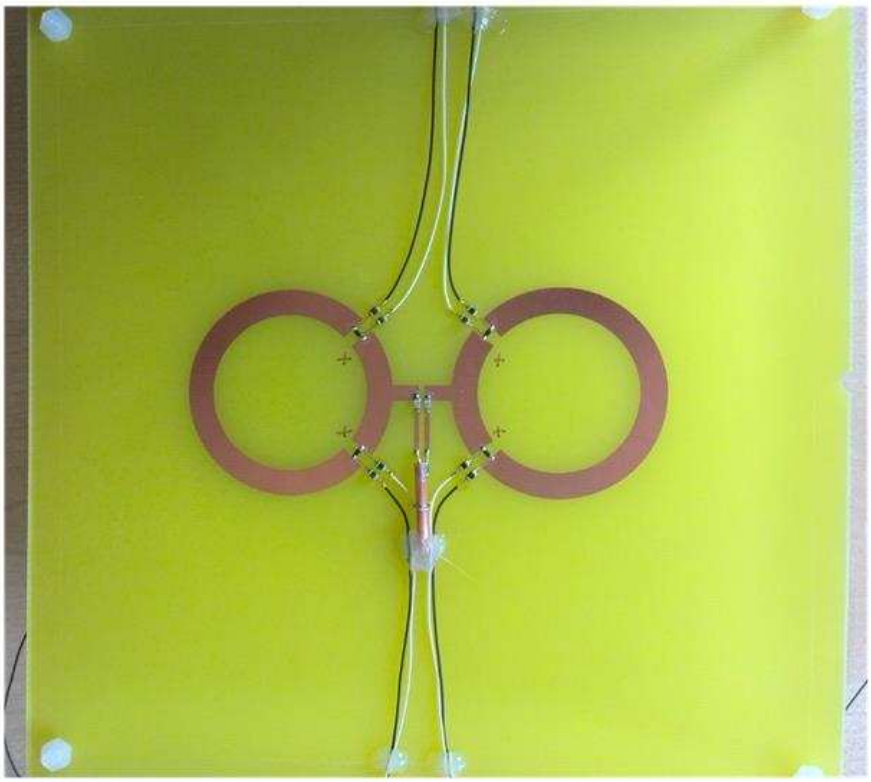

Figure 4.6 Prototype of the polarization reconfigurable dual-loop antenna.

The measured S_{11} of three different polarization states are shown in Figure 4.7. There is a frequency shift compared to simulated results for all polarization states. The measured impedance bandwidths for circular polarization and linear polarization are about 14% and 6% respectively. There is also a slight discrepancy in measured S_{11} between RHCP and LHCP. These differences may be caused by the permittivity variation of FR4 substrate and fabrication accuracy.

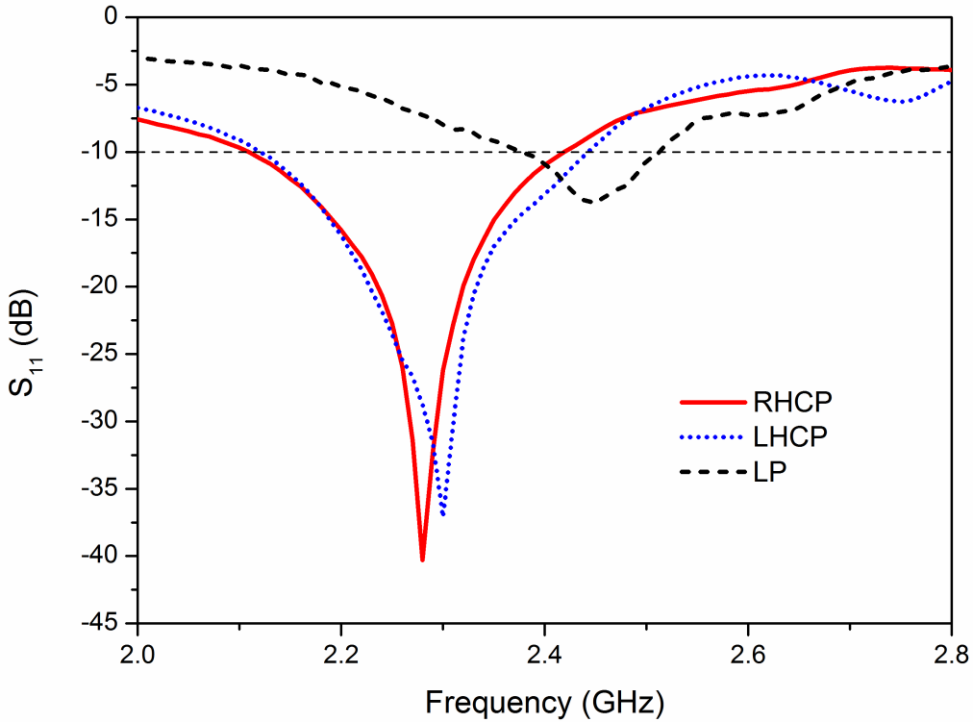

Figure 4.7 Measured reflection coefficients under three states.

4.3 Wideband Polarization Reconfigurable Single-Loop Antenna

In the Section 4.2, a dual-loop antenna which can change its polarization status to three different states is presented. However, the 3 dB AR bandwidth of this dual-loop antenna is only 5%. To reduce the size, a single-loop antenna with switchable circular polarization is proposed in this section. Furthermore, a parasitic open-loop concentric ring is introduced which effectively improves the 3 dB AR bandwidth under both RHCP and LHCP states.

4.3.1 Antenna Configuration and Operating Principles

The configuration of the polarization reconfigurable single-loop antenna is shown in Figure 4.8. Two loops are printed on both sides of a 0.8 mm thick Rogers RO4003 substrate. The outer loop is loaded by two PIN diodes and is printed on the top layer of the substrate. The inner loop with two small gaps is etched on the bottom layer of the substrate. In order to feed this antenna, a coplanar stripline (CPS) is introduced. This CPS feeds the antenna from the inside of the loop and is also used as an impedance transformer. Beneath the antenna board, there is a ground plane reflecting the downward waves which also helps generate CP radiation [104].

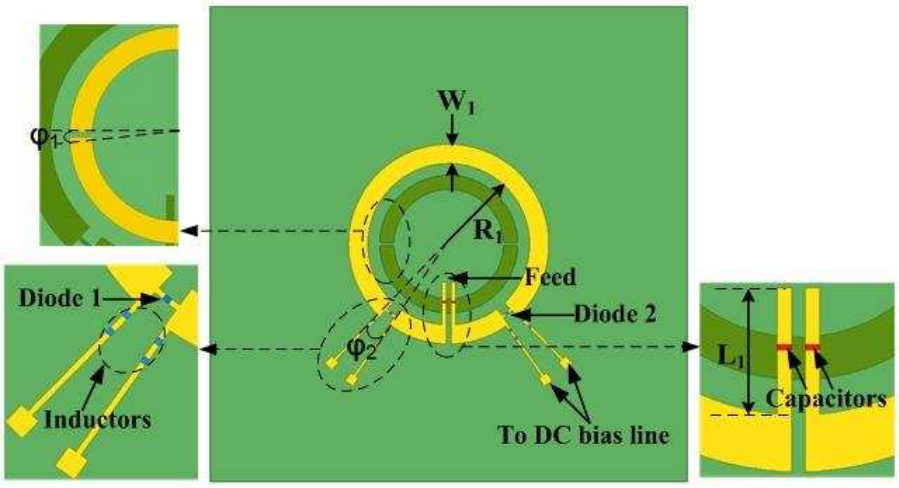

(a)

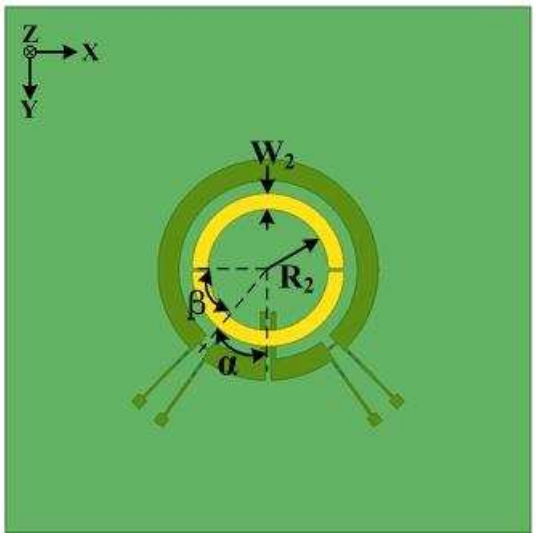

(b)

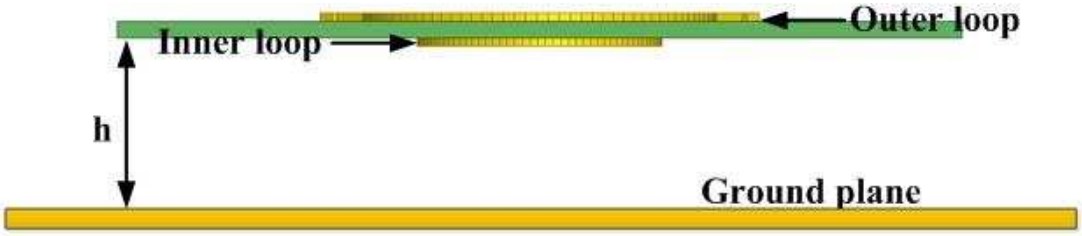

(c)

Figure 4.8 Geometry of the polarization reconfigurable single-loop antenna: (a) top view, (b) bottom view, (c) side view.

There are two magnified pictures in Figure 4.8 (a) showing the PIN diodes bias circuit and DC blocking. Regarding the control of the PIN diodes, two DC bias lines are introduced with small square pads for soldering. Inductors are inserted into the DC bias lines for RF choking and the values of these inductors are also important to the CP performance of the proposed antenna. The DC blocking is implemented by two capacitors to stop the DC current flowing to the antenna feeding.

The antenna dimensions are shown in Table 4.2.

Table 4.2 Single-Loop Antenna Parameters

R_1	R_2	W_1	W_2	L_1	φ_1	φ_2	α	β	h
17mm	11.5mm	4mm	3mm	9mm	3^o	7^o	40^o	50^o	27.2mm

As explained in Section 4.2.1, travelling-wave electric currents with different flow directions result in switchable radiation polarizations for the dual-loop structure. Likewise, for the single-loop antenna, RHCP radiation is achieved when diode 2 is turned on while diode 1 is off due to the anti-clockwise electric current flow. LHCP radiation is realized when diode 1 is turned on and diode 2 is off.

4.3.2 Investigation of AR Bandwidth Enhancement

As indicated in the introduction of this Chapter, the AR bandwidths of state-of-the-art polarization reconfigurable CP antennas are relatively narrow. It is therefore essential to enhance the AR bandwidth of this kind of antenna for some applications such as wideband satellite communication.

It has been found that the AR bandwidth of a CP loop antenna can be enhanced by adding a smaller parasitic open loop inside the original one [64, 71, 105]. The idea is to create another minimum AR point beyond the single minimum AR point produced by a CP loop without any parasitic structures. By appropriately combing these two minimum AR points, the CP bandwidth can be enhanced significantly.

Unlike traditional CP loop antennas with only single-sense circular polarization, the AR bandwidth enhancement for dual-sense CP loop antenna is more complicated. It is no longer feasible to improve the AR bandwidth of a dual-sense CP loop antenna by simply adding a single-gap loaded parasitic loop. If a parasitic loop with a gap near PIN diode 1 is placed inside the original loop shown in Figure 4.8, the AR bandwidth under the RHCP state can be enhanced. However, the 3 dB AR bandwidth of LHCP cannot be improved since the distance between the gap and the PIN diode 2 is too far to compensate the magnitude variation of the current on the primary loop. To improve the bandwidth of both RHCP and LHCP, an idea is to utilize a double-gap loaded parasitic loop, where the two gaps are symmetrically placed and are of equal distances to PIN diodes 1 and 2, respectively.

Ansys HFSS is used to analyze the effect of the dual-gap loaded parasitic loop on the axial ratio of the proposed antenna. Figure 4.9 shows the comparison between the polariza-

tion reconfigurable antennas with and without a double-gap loaded parasitic element in the LHCP state. It is found that the axial ratio is larger than 3 dB when the double-gap loaded parasitic loop is not present. Compared with the result observed in [64], where the AR is still less than 3 dB even when the parasitic loop is removed, it is concluded that the dual-gap loaded parasitic loop is different from single-gap loaded parasitic loop in helping compensate the magnitude variation of the current on the primary element.

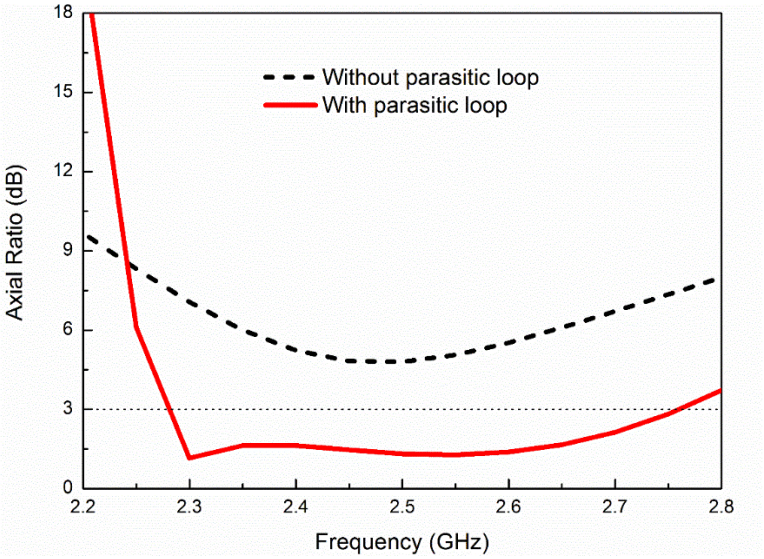

Figure 4.9 Axial ratio comparison with and without the parasitic loop under LHCP state.

Figure 4.10 and Figure 4.11 show the AR variation with different R_2 and β, respectively. It is found from these two figures that the radius of parasitic loop R_2 and the angle β play an important role in AR bandwidth enhancement for the proposed antenna. By changing these parameters, the coupling between the parasitic loop and primary loop can be tuned to achieve a maximum 3 dB AR bandwidth.

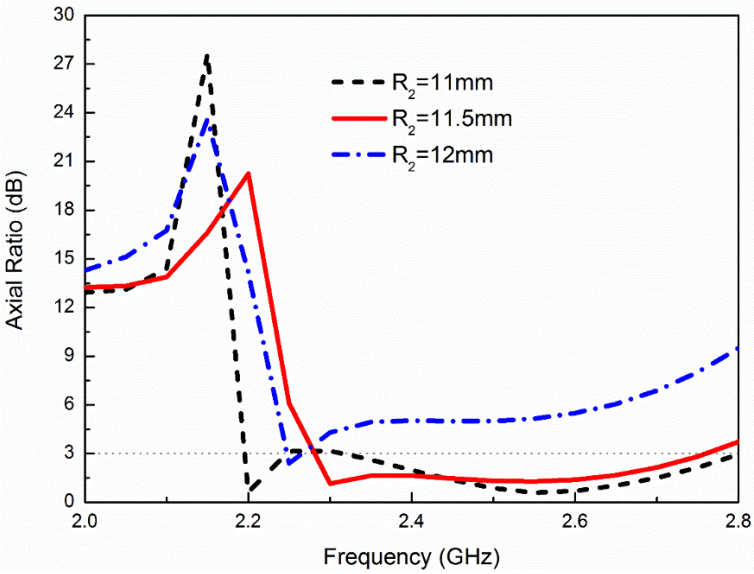

Figure 4.10 Axial ratio variation with different R_2 under LHCP state.

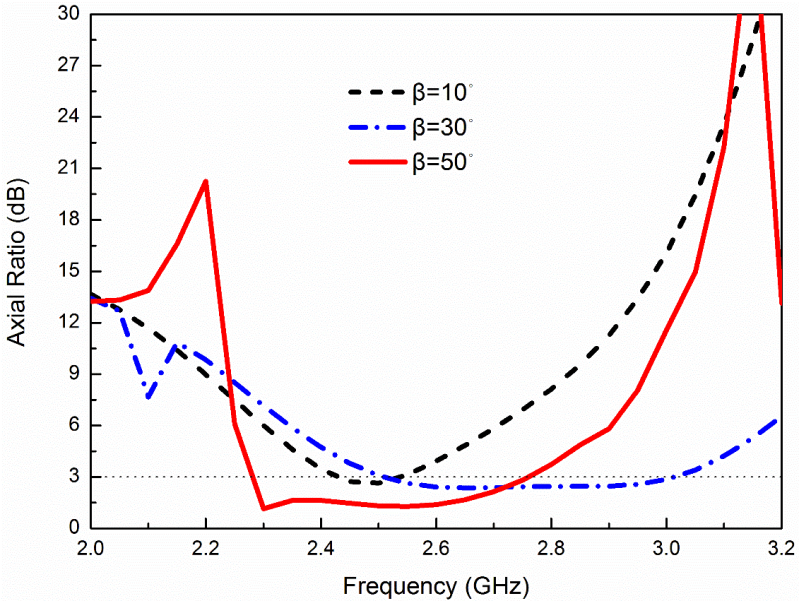

Figure 4.11 Axial ratio variation with different β under LHCP state.

4.3.3 Analysis of Impedance Matching

CPS lines were introduced to feed both the dual-loop and single-loop antennas and also act as an impedance transformer. The length of this single-section line is not one quarter wavelength and thus this impedance transformer is not equal to the quarter-wave transformer analyzed in [106].

Using a single-section transmission line with specific characteristic impedance and non-quarter wavelength length to match an antenna with complex input impedance has been widely used. To obtain an in-depth understanding of the impedance matching technique and also make this method easier to implement, a detailed analysis is given in this sub-section. Figure 4.12 shows the circuit employing a single-section transmission line with specific characteristic impedance and length. By determining the transmission line characteristic impedance Z_o and length L, it is feasible to transform the terminal impedance Z_L to desirable impedance Z_{in}, typically 50 Ω in the scenario of antenna impedance matching.

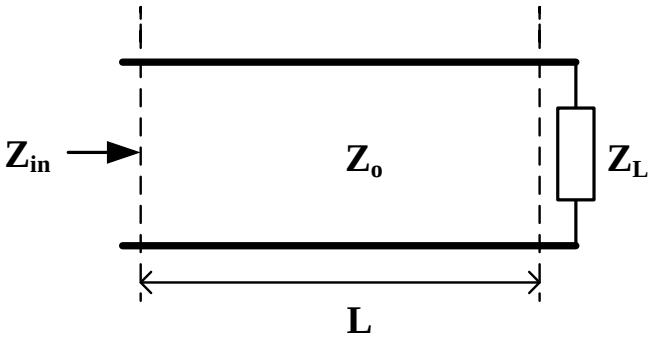

Figure 4.12 Circuit model of single-section transformer.

4.3.3.1 Theoretical Analysis

Refering to Figure 4.12, the input impedance can be expressed as

$$Z_{in} = Z_o \frac{Z_L + jZ_o \, tan\, \beta L}{Z_o + jZ_L \, tan\, \beta L} \tag{4.1}$$

Where $\beta = 2\pi/\lambda$ is the phase constant of the line.

Instead of normalizing all impedance by dividing transmission line characteristic impedance Z_o, here Z_o and Z_L are normalized by Z_{in}, that is:

$$\frac{Z_o}{Z_{in}} = r, \qquad \frac{Z_L}{Z_{in}} = x + jy \tag{4.2}$$

It is desired to make Z_{in} equal to 50 Ω, which is usual for antenna impedance matching. Therefore, Z_o/Z_{in} can be represented by a real number r. After this normalization, the proposed impedance matching method can be performed by solving (4.1).

After normalization, (4.1) can be rewritten by the following equation and the desirable Z_{in} can be obtained, through the proposed method,

$$1 = r\frac{(x + jy) + jr \tan \beta L}{r + j(x + jy) \tan \beta L} \tag{4.3}$$

When $L = \frac{\lambda}{4} + n\frac{\lambda}{2}$, $\tan \beta L = \infty$, and (4.3) becomes

$$\frac{r^2}{x + jy} = 1 \tag{4.4}$$

This means that the proposed method is equivalent to the traditional '$\lambda/4$ impedance transformer' for real terminal impedance (y=0).

When $L \neq \frac{\lambda}{4} + n\frac{\lambda}{2}$, we can rearrange (4.3) and equate the real and imaginary parts to yield:

$$\begin{cases} y\tan \beta L = r(1 - x) \\ (x - r^2)\tan \beta L = ry \end{cases} \tag{4.5}$$

Apart from $r^2 = x$ and $y = 0$, which is already included in the situation $L = \frac{\lambda}{4} + n\frac{\lambda}{2}$, (4.5) can be rewritten more clearly by

$$\begin{cases} \tan \beta L = r(1 - x)/y \\ \tan \beta L = ry/(x - r^2) \end{cases} \tag{4.6}$$

Through this identical equation set, r can be represented by

$$r^2 = x + \frac{y^2}{x - 1} \tag{4.7}$$

Considering arbitrary terminal impedance Z_L, the normalized terminal impedance is arbitrary as well, i.e. x and y are arbitrary. Therefore, the solving process for r can be divided into four cases.

A: $x > 1$

When $x > 1$, then r can be expressed by

$$r = \sqrt{x + \frac{\mathrm{y}^2}{x - 1}} \tag{4.8}$$

B: $0 < x < 1$

In this case, r can be expressed by equation (4.8) only if

$$\left(\mathrm{x} - \frac{1}{2}\right)^2 + \mathrm{y}^2 < \frac{1}{4} \tag{4.9}$$

C: $x = 1$

Through (4.5), when $\mathrm{y} = 0$, then $r = 1$ is the only solution. This means when $Z_L = Z_{in}$, Z_o should equal to Z_L in order to get a good impedance match.

D: $x = 0$

(4.7) is insoluble under this case. Actually this situation is non-existent in the application of antenna impedance matching, since all antennas have a real part of its input impedance; otherwise it cannot be treated as a radiation device.

When r is solvable under cases A and B, the length of transmission line L can be expressed as

$$L = \frac{\lambda}{2\pi} tan^{-1}\left(\frac{1 - x}{y}\sqrt{x + \frac{y^2}{x - 1}}\right) \tag{4.10}$$

It is noticed that the length of transmission line L should be a positive number and thus $\theta = \tan^{-1}\left(\frac{1-x}{y}\sqrt{x + \frac{\mathrm{y}^2}{x-1}}\right)$ can be solved only in the interval $[0, \pi]$.

Overall, the impedance of the proposed transmission line Z_o and its length L can be determined by the following equations,

$$\begin{cases} Z_O = Z_{in}\sqrt{x + \dfrac{y^2}{x - 1}} \\ L = \dfrac{\lambda}{2\pi} tan^{-1}\left(\dfrac{1 - x}{y}\sqrt{x + \dfrac{y^2}{x - 1}}\right) \end{cases} \tag{4.11}$$

where $\frac{Z_L}{Z_{in}} = x + jy$ and x, y should be subject to

$$x > 1 \ or \ \begin{cases} 0 < x < 1 \\ \left(x - \frac{1}{2}\right)^2 + y^2 < \frac{1}{4} \end{cases} \tag{4.12}$$

4.3.3.2 Verification of Theoretical Analysis

Considering two different antenna input impedances, $Z_{L1} = (200 - 400j)\ \Omega$ and $Z_{L2} = (10 + 15j)\ \Omega$, which are both subject to 4.12, it is feasible to use a single-section transmission line with length L (or electrical length θ) and impedance Z_o matching Z_{L1} and Z_{L2} to a 50 Ω system.

For $Z_{L1} = (200 - 400j)\ \Omega$, it can be calculated by (4.11) that the characteristic impedance of the single-section transmission line Z_{o1} should be 251 Ω and the electrical length θ_1 should be 62° to complete an ideal impedance matching.

Similarly, for $Z_{L2} = (10 + 15j)\ \Omega$, we can get Z_{o2} =14 Ω and θ_2=38°.

To verify these two sets of result obtained from (4.11), the commercial software ADS is utilized to simulate the circuit shown in Figure 4.12. The antenna input impedance and the input impedance after matching are shown in Figure 4.13.

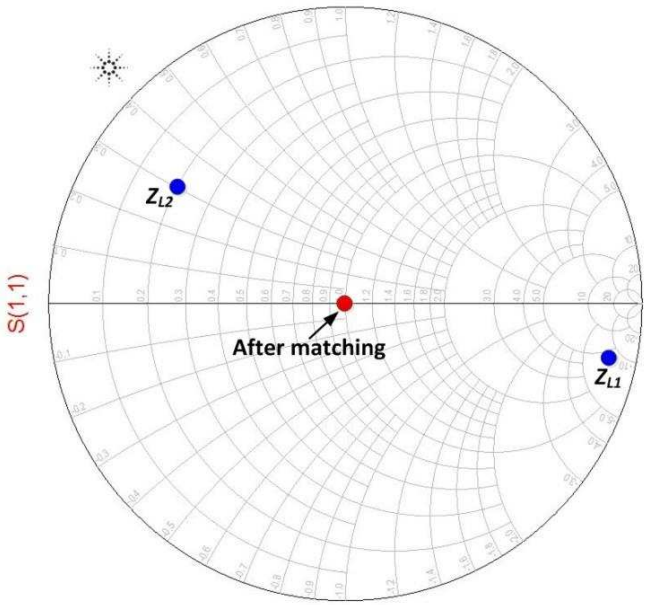

Figure 4.13 Verification of the proposed impedance matching method using ADS.

As can be seen from Figure 4.13, the antenna input impedance Z_{L1} and Z_{L2} can be matched to 50 Ω after using a single-section transmission line with the above calculated values.

To explain how this method is used to tune the impedance matching of the single-loop antenna, the impedance loci of the proposed single-loop antenna before and after matching are given in Figure 4.14.

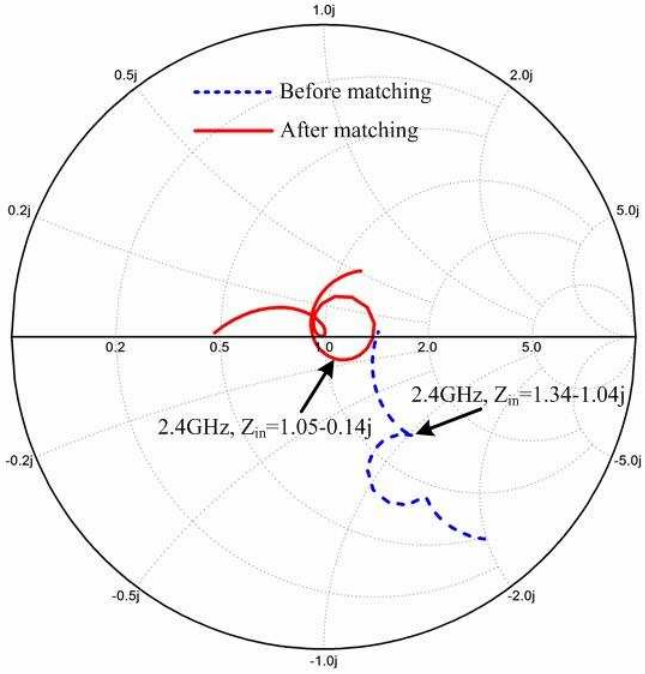

Figure 4.14 Impedance loci of the proposed antenna before and after matching.

As shown, the input impedance of the proposed antenna at 2.4 GHz is 50 × (1.3-j) Ω. As it is aimed to tune the antenna at this frequency point, the characteristic impedance and the electrical length of the CPS line are calculated to be 106 Ω and 35°, respectively. It is also shown that the antenna input impedance at 2.4 GHz has changed to 50 × (1-0.1j) Ω after using the CPS line with the calculated values. The impedance locus of the proposed antenna has also shifted to the matching point, which proves that the impedance matching method using single-section transmission line with specific characteristic impedance and electrical length works effectively.

4.3.4 Measurement and Simulation Results

4.3.4.1 Reflection Coefficient

The prototype of the proposed single-loop antenna is shown in Figure 4.15. As can be seen, four DC bias lines are soldered perpendicularly to the antenna board and then connected to a single-pole double-throw (SPDT) switch for controlling the two PIN diodes. Through shielding the DC lines and the switch by the ground plane, the influence of the lines and switches can be minimized.

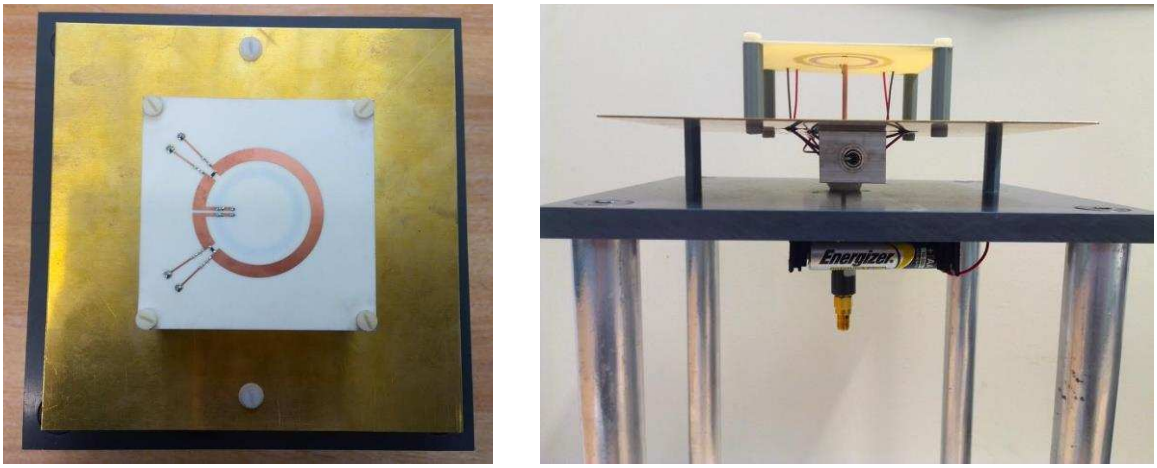

Figure 4.15 Prototype of the proposed antenna.

Two Skyworks SMP1345-079LF PIN diodes with small capacitance (smaller than 0.2 pf) and series resistance 2 Ω are used in the prototype. To drive the PIN diodes, two 1.5 V AA batteries with 1.5 V voltages are mounted in a battery bracket and then are connected to a SPDT switch. The polarization status of the antenna can be changed to LHCP or RHCP electronically by controlling the state of the switch.

As shown in Figure 4.16, the simulated and experimental reflection coefficients are in good agreement. From the measured results, a 32% impedance bandwidth is achieved for LHCP while a 39% bandwidth is obtained for RHCP. The difference between LHCP and RHCP results may be caused by the two diodes' different characteristics as well as the unbalanced coaxial cable feeding.

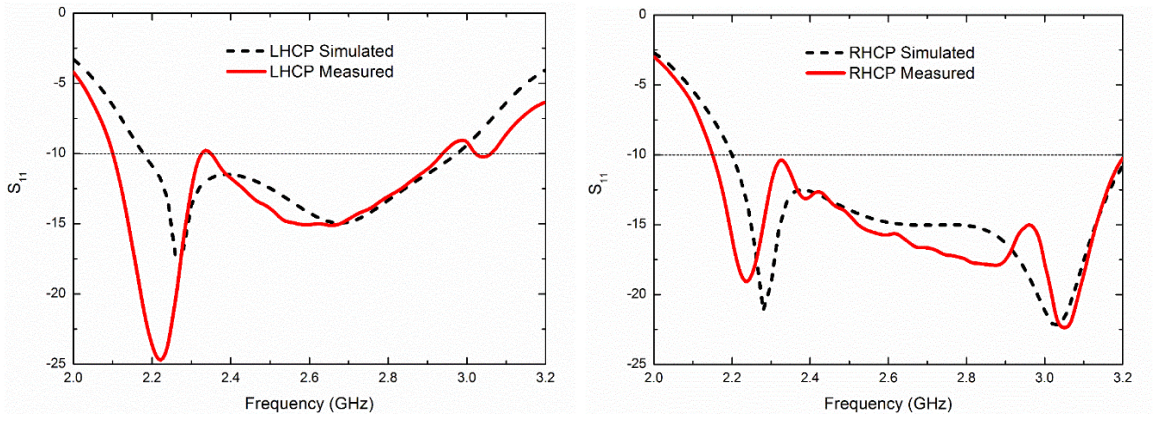

(a) (b)

Figure 4.16 Simulated and measured reflection coefficients under different polarization status: (a) LHCP, (b) RHCP.

4.3.4.2 Axial Ratio

Figure 4.17 (a) and (b) show the experimental and simulated AR under the LHCP and RHCP states, respectively. As observed, the measured AR bandwidth is slightly smaller

than the simulated results and this is believed to be caused by the fabrication errors and the differences between simulation models and practical values of the lumped elements utilized in the proposed antenna.

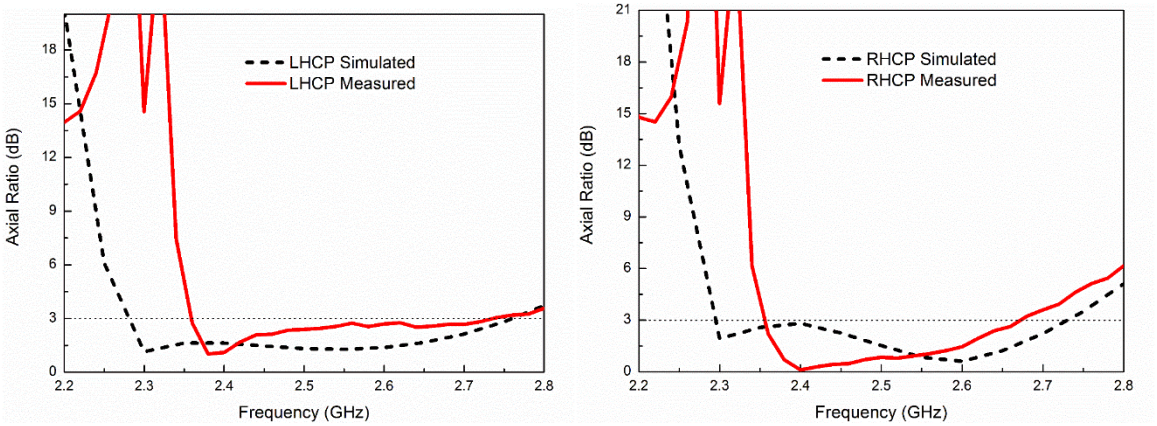

(a) (b)

Figure 4.17 Simulated and measured axial ratio under different polarization status: (a) LHCP, (b) RHCP.

For a polarization reconfigurable antenna with CP polarizations, the overlapped bandwidth between impedance bandwidth and AR bandwidth is usually used to evaluate the antenna bandwidth characteristic. Comparing Figures 4.16 and 4.17, it is found that the overlapped bandwidth is mainly determined by the AR bandwidth. The measured overlapped bandwidth under the RHCP and LHCP states is 12% and 14%, respectively.

4.3.4.3 Radiation Pattern

The radiation pattern of the proposed antenna is measured using a linearly polarized horn antenna and the method presented in [94] is employed to get the RHCP and LHCP radiation patterns. Figure 4.18 shows the radiation patterns under the LHCP and RHCP states at 2.4 GHz in the two main planes.

As shown, the measured radiation patterns are in good agreement with the simulation results. A unidirectional radiation pattern with low cross polarization can also be observed. It is noted that the measured back lobe level is much lower than the simulation results and this is caused by the antenna mounting as shown in Figure 4.19 which shows the measurement setup of the proposed antenna in the chamber. To avoid the reflection from the positioner, an absorber is mounted behind the ground plane of the proposed antenna. The back radiation is suppressed by this absorber and thus the measured back lobe is much lower than the simulation results. Considering that there is a ground plane under the proposed antenna and the main beam characteristic is of major concern in evaluating the

antenna performance, it is believed that the measurement method is reasonable and relatively accurate for this antenna.

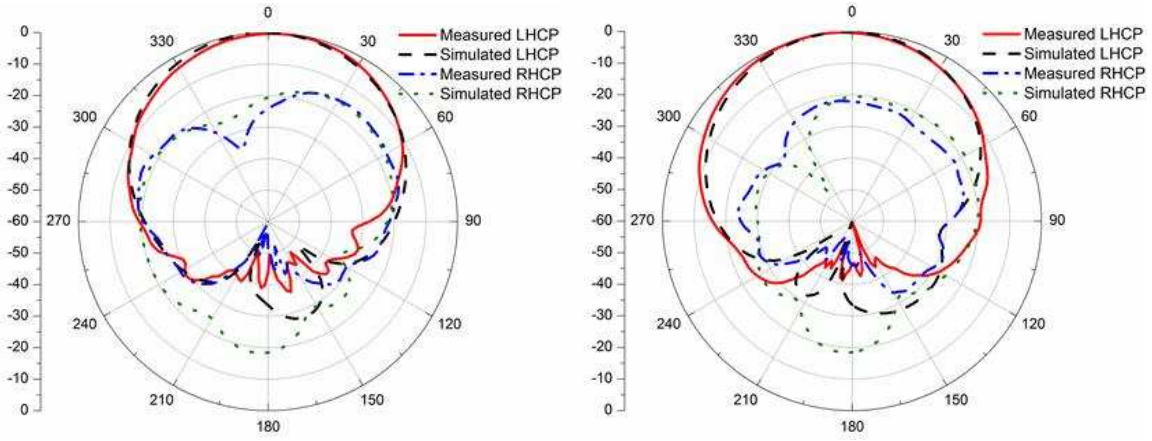

(a)

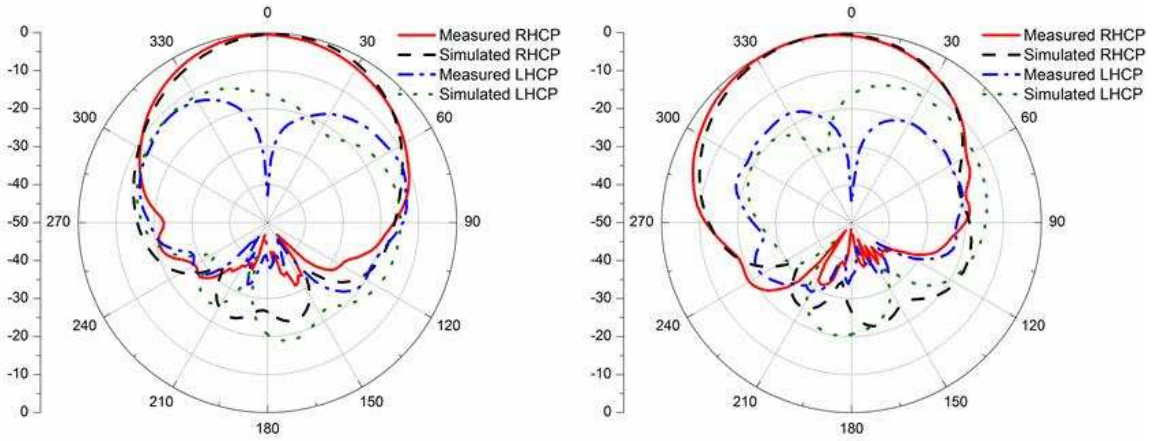

(b)

Figure 4.18 Simulated and measured radiation patterns at 2.4 GHz: (a) LHCP state, XoZ plane and YoZ plane, (b) RHCP state, XoZ plane and YoZ plane.

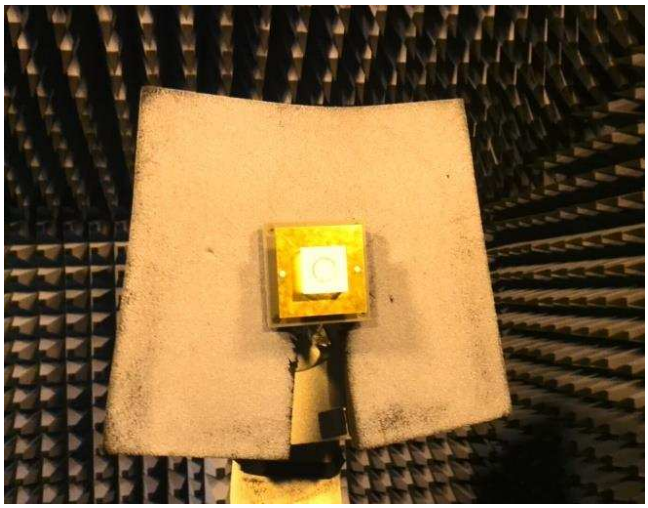

Figure 4.19 Measurement setup of the proposed antenna in the chamber.

4.4 Summary

This Chapter presents two polarization reconfigurable loop antennas for polarization diversity applications. A novel polarization reconfigurable dual-loop antenna which could alter its polarization states electronically to RHCP, LHCP or LP was designed at first. To reduce the size of the dual-loop structure, a wideband single-loop antenna with switchable circular polarization was presented. The proposed single-loop antenna can achieve more than 12% overlapped operating bandwidth under both the LHCP and RHCP states. Both the dual-loop and single-loop antenna have utilized a single-stage impedance transformer to realize good impedance matching. Detailed theoretical analysis of this impedance matching technique is provided and the derived analytical formulas can be applied to other various types of antennas for impedance matching.

Chapter 5. Inverted-S Antenna with Wideband Circular Polarization and Wide Axial Ratio Beamwidth

5.1 Introduction

Chapters 3 and 4 investigate two different types of CP antennas which have wide 3 dB AR bandwdith. Besides improving the AR bandwidth, widening the AR beamwidth of CP antennas has received increasing interest recently since wide CP beams are beneficial for receivers in global navigation satellite systems (GNSS) [7] and are necessary for wide-angle CP beam-scanning array [13]. Therefore, it is meaningful to design wideband CP antennas with wide AR beamwidth

Despite the importance of wideband CP antennas with wide AR beamwidth, only several researches were reported. Two pairs of parallel dipoles were orthogonally placed in a square contour and were excited in phase quadrature to acquire wide AR beamwidth when the space between the parallel dipoles was appropriately chosen [107]. The AR bandwidth of this antenna is from 1.52 GHz to 1.65 GHz (8%) and 126^o AR beamwidth is achieved at 1.6 GHz. However, the AR beamwidth decreases when frequency shifts away from 1.6 GHz. A stacked patch antenna with 10% CP bandwidth and 140^o AR beamwidth was presented in [108]. Likewise, the AR beamwidth is measured at only 2.4 GHz and the AR beamwidths at other frequency points within the working band are not provided. In [109], a wideband magneto-electric dipole which has 33% AR bandwidth and 85^o AR beamwidth within the AR passband in the two main planes was reported. Stable wide angular CP radiation could also be observed in [110], where a crossed dipole was loaded with a magneto-electric dipole to realize good CP performance. In [110], 27% AR bandwidth was achieved and over 165^o AR beamwidth could be realized from 1.45 GHz to 1.7 GHz (15%) in the two main planes. Although the antenna presented in [109, 110] can achieve wideband CP radiation with wide angular CP coverage in the two main planes, it is not clear whether wide AR beamwidths can be maintained in other elevation planes. Moreover, these antennas have complicated structures, which make them difficult to be implemented in wideband CP arrays.

In this Chapter, a novel inverted S-shaped CP antenna with a simple configuration is presented, which achieves wide CP bandwidth and wide AR beamwidth simultaneously. Stable wide angular CP radiation characteristics are maintained in a wide frequency range in the XOZ plane. In other elevation planes, the AR beamwidths are wider than the half power beamwidths (HPBWs). Compared with other reported antennas, the proposed

antenna achieves a wider CP bandwidth and a more stable AR beamwidth within the operational bandwidth. Moreover, it can be easily extended to a wideband CP array with wide AR beamwidth, which is also discussed in this Chapter.

This Chapter is organized as follows: Section 5.2 introduces the antenna configuration and operational principles of wide angular CP radiation; Section 5.3 presents the simulation results and measurement results of the proposed antenna as well as the comparison with other reported wideband wide AR beamwidth antennas; Section 5.4 presents a linear array consisting of the proposed antenna element and the results of this array; the summary of this Chapter is given in Section 5.5.

5.2 Antenna Configuration and Operating Principles

5.2.1 Antenna Configuration

Linearly polarized (LP) dipole antennas are widely deployed due to their simple configuration and expandability to various arrays. One attractive feature of LP dipoles is that they have omnidirectional radiation pattern in the H-plane. This characteristic inspires the proposed design, which is explained below.

Figure 5.1 shows the configuration of a LP dipole and the proposed CP S-shaped antenna. As shown, both the LP dipole and the CP "S" antenna have two arms and are fed by an AC source which provides 180^o phase differences to the two arms. By bending the LP dipole into a curved shape with variable wire width, it is found that travelling current is excited once the "S" shaped conductor is designed to have enough curve length ($1.4\lambda_g$-$1.8\lambda_g$). As indicated in Section 2.2.3, CP radiation can be achieved if travelling-wave current is excited along curved structure. Therefore, the proposed S-dipole can realize CP radiation.

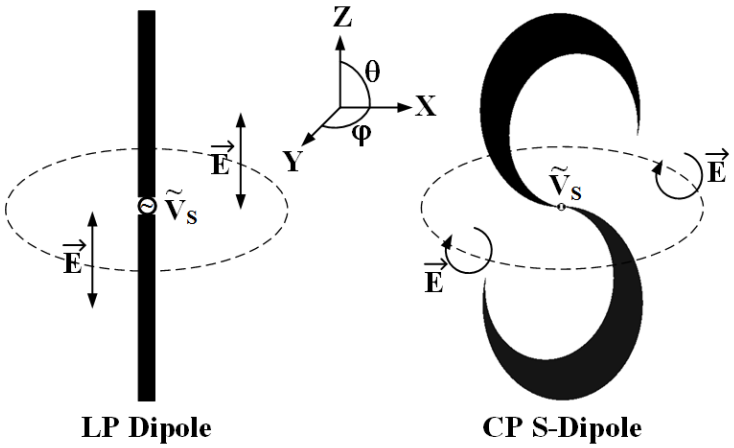

Figure 5.1 Linearly polarized dipole and circularly polarized S-shaped antenna [111, 112].

Moreover, similar to the omnidirectional radiation of LP dipoles in their H-plane, the presented CP S-dipole antenna can radiate CP waves at nearly all angles in the xoy plane except for the ±X direction, which results in a wide 3 dB AR beamwidth in the xoy plane. The AR degradation along ±X direction is caused by the alteration of wave propagating direction. Considering that clockwise traveling-wave current is excited along the "S" structure, the radiated CP E-field in the xoy plane rotates in the clockwise direction, the change of the propagating direction results in LHCP radiation in the +Y region and RHCP in the –Y region. At the interface of these two orthogonal CP waves, LP radiation occurs.

Anti-clockwise travelling-wave current can be excited to realize RHCP radiation if the "S" shaped dipole is converted into an inverted "S" shaped dipole, as shown in Figure 5.2. The antenna is printed on the bottom layer of a 0.508mm thick Rogers RO4003C substrate with a size of $W_1 \times L_1$. To feed the antenna, an integrated balun which transforms the unbalanced microstrip feed to balanced slot line feed is utilized. The balun is printed on a 0.813mm thick Rogers RO4003C substrate which has a size of $W_1 \times H_7$. An $L_2 \times L_2$ sized ground plane is placed below the antenna with a distance of H_1 for directional radiation.

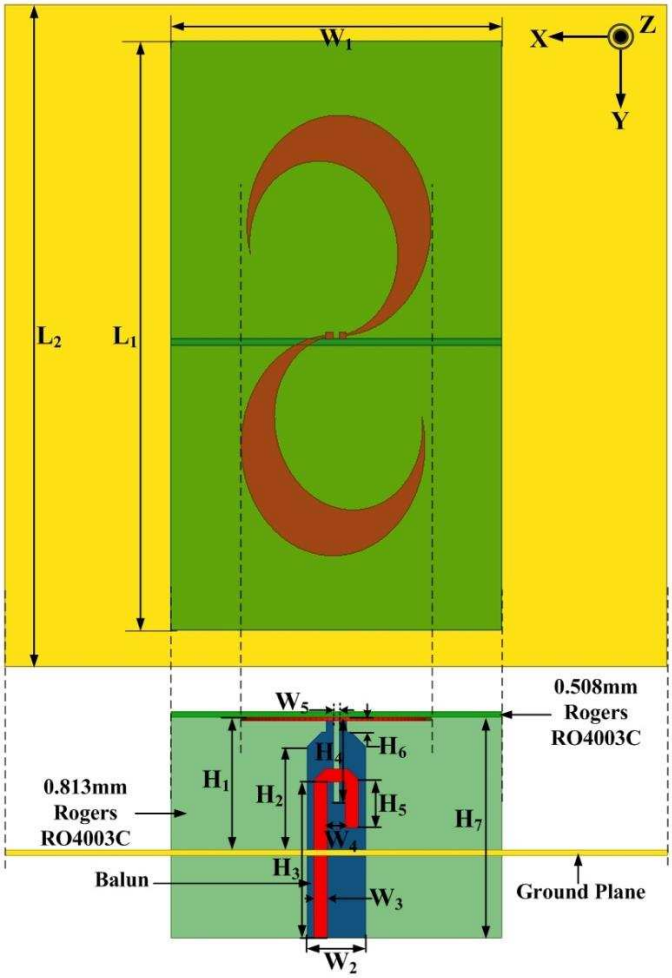

Figure 5.2 Geometry of the inverted-S antenna.

The curved arm can be obtained through cutting a bigger ellipse by a smaller rotated ellipse, as shown in Figure 5.3. This method is inspired by [113], where two concentric semi-circles are used to form a vortex slot. As can be seen from Figure 5.3, the bigger ellipse has a major axis radius R_1 and minor axis radius R_2 while the smaller ellipse major and minor axis radius are R_3 and R_4, respectively. The smaller ellipse is counterclockwise rotated along point O with an angle of α and then it is subtracted from the bigger ellipse.

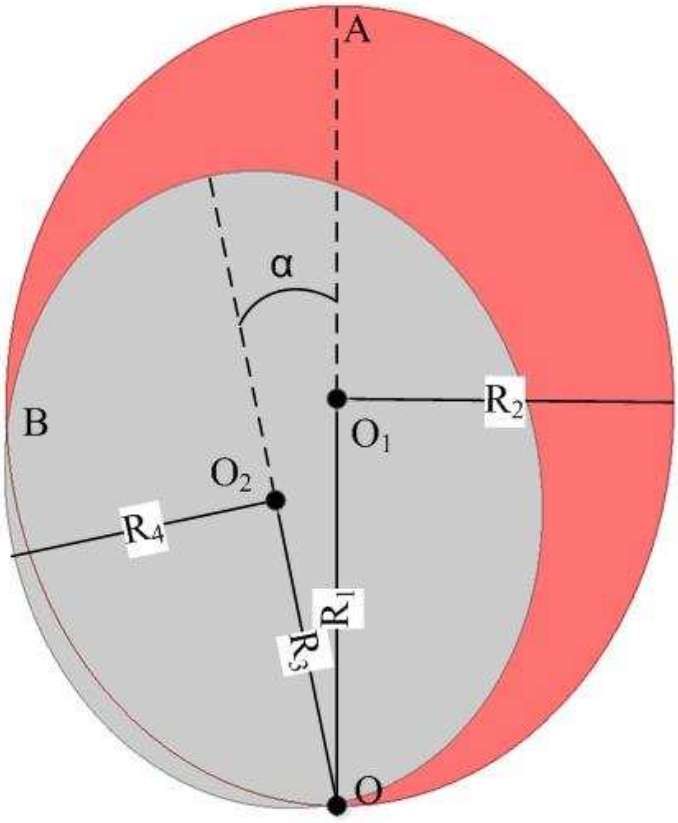

Figure 5.3 Detailed geometry of the curved arm.

Table 5.1 gives the antenna parameters and the rotation angle α is 10^o. The lengths of the outer curve and inner curve are around 65 mm and 52 mm equaling to about $1.8\lambda_g$ and $1.4\lambda_g$ at the center frequency 5 GHz, which provides enough paths for a travelling-wave current flowing along the curved arm. The distance between the antenna and the ground plane (H_1) is chosen to be 18 mm to achieve maximum AR bandwidth. Meanwhile, the antenna gain can also be maintained at a reasonable value at this height. The ground plane size ($L_2 \times L_2$) is determined by taking into consideration the performance of AR and radiation patterns. Generally, the AR bandwidth degrades but the back lobe is decreased with larger L_2. The size of the ground plane is chosen to be 90 mm×90 mm to achieve wide AR bandwidth and good radiation patterns.

Table 5.1 Inverted-S Antenna Parameters

L_1	L_2	W_1	W_2	W_3	W_4	W_5	H_1	H_2
80	90	45	8	1.77	2.46	0.8	18	14
H_3	H_4	H_5	H_6	H_7	R_1	R_2	R_3	R_4
21.5	11.5	6.23	2	30	15	12.5	12	10

5.2.2 Operating Principle of CP Radiation

To explain the operating principle of the CP radiation, the surface current distribution on the curved arms at different times is shown in Figure 5.4. The null of the surface current is propagating along the curved arms, which is similar to the phenomenon observed in [114]. According to Section 2.2.3, once a travelling-wave electric current is generated along a curved structure, CP radiation can be obtained. It is reported in [114] that a travelling-wave current is realized along the equiangular strip and aperture edge. Different from [114], in this design the travelling-wave current is excited along the curved arms even without any ground plane or cavity, which simplifies the fabrication and makes the presented antenna a better candidate for the array application. Furthermore, the proposed antenna exhibits wide AR beamwidth characteristics which do not exist in [114].

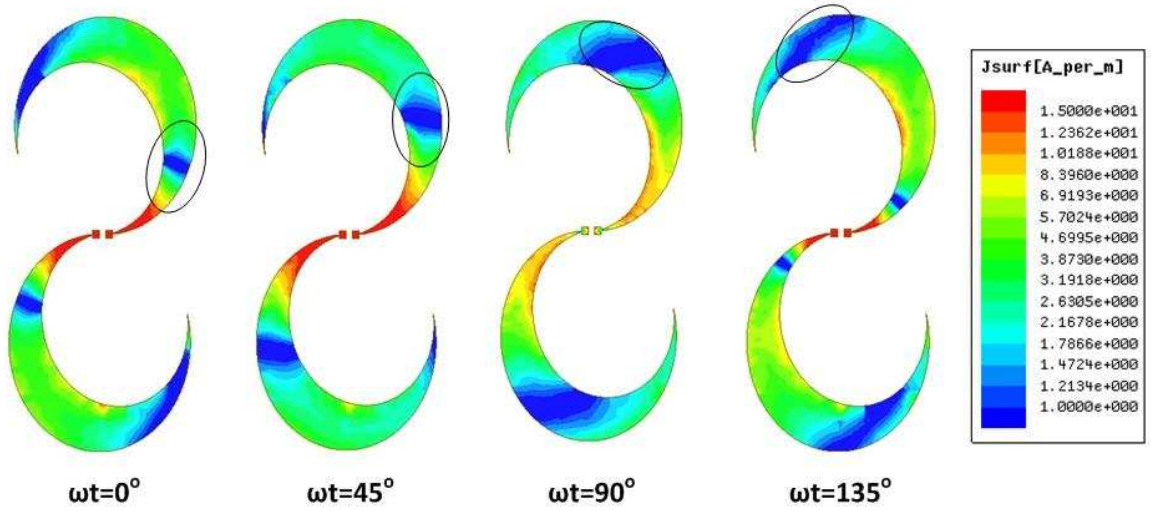

Figure 5.4 The surface current on curved arms at different phases.

5.2.3 Mechanism of Wide AR Beamwidth

Considering that the antenna consists of two curved arms fed out of phase, the far-field radiation of the proposed antenna can be synthesized using a 2-element array. To validate this assumption, a 2-element array with the same size as the proposed S-antenna was simulated and each curved arm is fed by a lumped port like a horizontal monopole as shown in Figure 5.6 (a), and with 180^o phase difference between the two ports.

For a fair comparison of the radiated electric field, the distance between the ground plane and the 2-element array is kept at 18 mm, the same as the height of the proposed antenna. The antenna is fed by a lumped port to eliminate the need for a balun. Figure 5.5 shows the comparison of radiation patterns in RHCP and LHCP components between the proposed antenna and the 2-element array at 4.7 GHz in the XOZ plane. As shown, the far-field radiation between the proposed antenna and the 2-element array is nearly the same. The agreement of the radiation patterns can also be observed at other frequencies and different elevation planes. Therefore, it is reasonable to deem the proposed antenna as a 2-element array as shown in Figure 5.6.

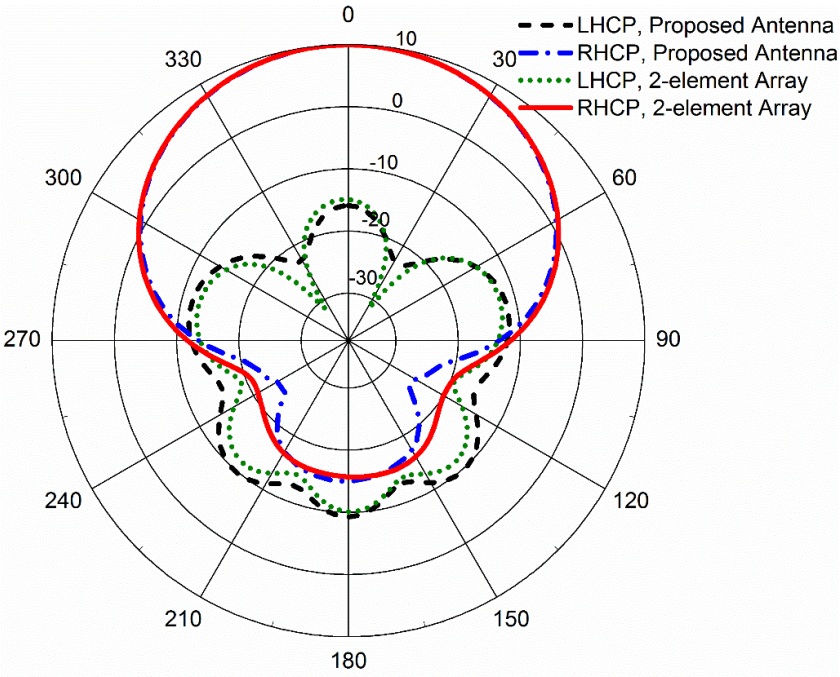

Figure 5.5 The radiation patterns of the proposed antenna and the 2-element array in XOZ plane

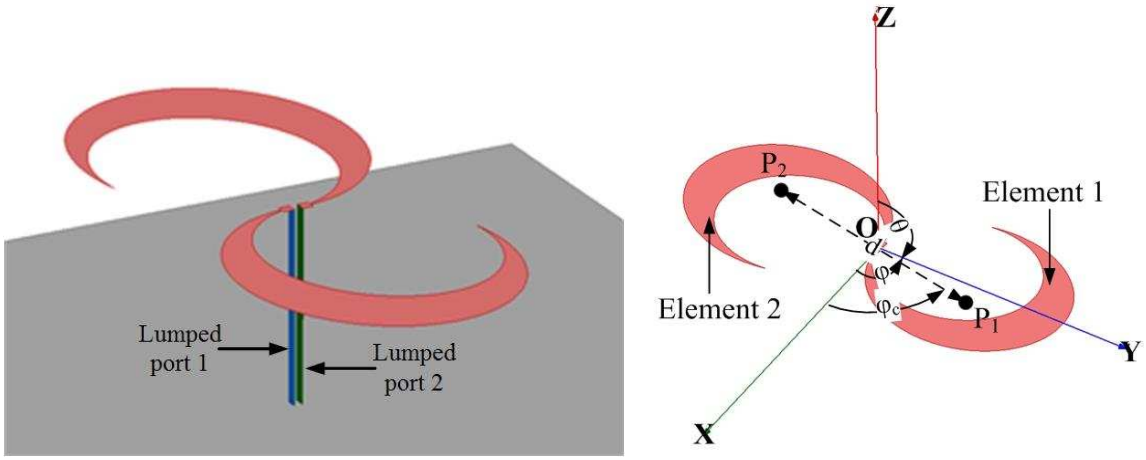

(a) (b)

Figure 5.6 Geometrical arrangement of 2-element array: (a) feeding structure, (b) geometry parameters.

The radiated fields of the proposed antenna can then be obtained by vector summing of the fields radiated by each element (curved arm). As shown in Figure 5.6, P1 and P_2 denote the phase center of each element respectively. Because element 2 is acquired through rotating element 1 by 180° at the origin point O, the points P_1, P_2 and O are in a line. Denoting the distance between P_1 and P_2 by d and the angle between the line P_1OP_2 and axis X by φ_c, the spatial phase delay of the two elements in XOZ plane can then be represented by:

$$\delta = k_0 d \cos\varphi_c \sin\theta \tag{5.1}$$

where k_0 is the wavenumber in free space. For an elliptically polarized antenna, the radiated electric field of element 1 can be written by [115]:

$$\overrightarrow{E_1}(\theta,\varphi) = a(\theta,\varphi)\overrightarrow{e_\theta} + b(\theta,\varphi)\overrightarrow{e_\varphi}e^{j\frac{\pi}{2}} \tag{5.2}$$

Here, $a(\theta,\varphi)$ and $b(\theta,\varphi)$ are the amplitude of the two orthogonal unit vectors $\overrightarrow{e_\theta}$ and $\overrightarrow{e_\varphi}$, which are functions of θ and φ. For a qualitative analysis, the total field in the XOZ plane is deduced while the fields in other planes can also be derived by using different spatial phase delay between the two elements.

As element 2 is axisymmetric to element 1, the radiated field of element 2 in XOZ plane can be written as follows:

$$\overrightarrow{E_2}(\theta,0) = -\overrightarrow{E_1}(\theta,\pi) = -\overrightarrow{E_1}(-\theta,0) \tag{5.3}$$

Here, the negative sign stems from the physical rotation angle π which results in a reverse direction of the electric field. The total electric field in XOZ plane is given by:

$$\overrightarrow{E_t}(\theta,0) = \overrightarrow{E_1}(\theta,0) + \overrightarrow{E_2}(\theta,0)e^{j\pi}e^{j\delta} \tag{5.4}$$

The $e^{j\pi}$ component in (5.4) comes from the feeding phase difference π. Substituting (5.2) and (5.3) into (5.4) and (5.4) can be rewritten as

$$\overrightarrow{E_t}(\theta,0) = \left[a(\theta,0) + a(-\theta,0)e^{j\delta}\right]\overrightarrow{e_\theta} + \left[b(\theta,0) + b(-\theta,0)e^{j\delta}\right]\overrightarrow{e_\varphi}e^{j\frac{\pi}{2}} \tag{5.5}$$

(5.5) indicates that the total field $\overrightarrow{E_t}$ in the XOZ plane equals to the summation of field $\overrightarrow{E_1}(\theta,0)$ and $\overrightarrow{E_1}(-\theta,0)e^{j\delta}$. The physical insight of (5.5) is that the total field $\overrightarrow{E_t}$ originates from two elliptically polarized fields while the phase difference between them is δ. Due to the asymmetric radiation pattern to Z axis of each element, $\overrightarrow{E_1}(-\theta,0)$ does not equal to $\overrightarrow{E_1}(\theta,0)$ for a given elevation angle θ (except for $\theta = 0$). Denoting the axial ratio

of $\overrightarrow{E_1}(\theta, 0)$ by $AR_1(\theta)$ and the axial ratio of $\overrightarrow{E_1}(-\theta, 0)$ by $AR_2(\theta)$, then

$$AR_2(\theta) = AR_1(-\theta) = a(-\theta, 0)/b(-\theta, 0) \tag{5.6}$$

Also, $AR_2(\theta) \neq AR_1(\theta)$ except for $\theta = 0$. According to (5.5), for a given θ, the AR of the total field $\overrightarrow{E_t}$ is determined by AR_1, AR_2 and δ. Since $AR_2(\theta) \neq AR_1(\theta)$, it gives the possibility to realize a total field with a better AR_t ($AR_t < AR_1$ *or* AR_2).

For a more visual explanation, the phase differences of the RHCP and LHCP electric field component between the two elements in the XOZ plane is given by Figure 5.7. For an easier comparison, element 2 is fed with an 180° phase difference to element 1. The far-field RHCP component phase difference is calculated by $Phase_{RHCP,elment\ 1} - Phase_{RHCP,elment\ 2}$ while the phase difference of LHCP component is calculated by $Phase_{LHCP,elment\ 1} - Phase_{LHCP,elment\ 2}$.

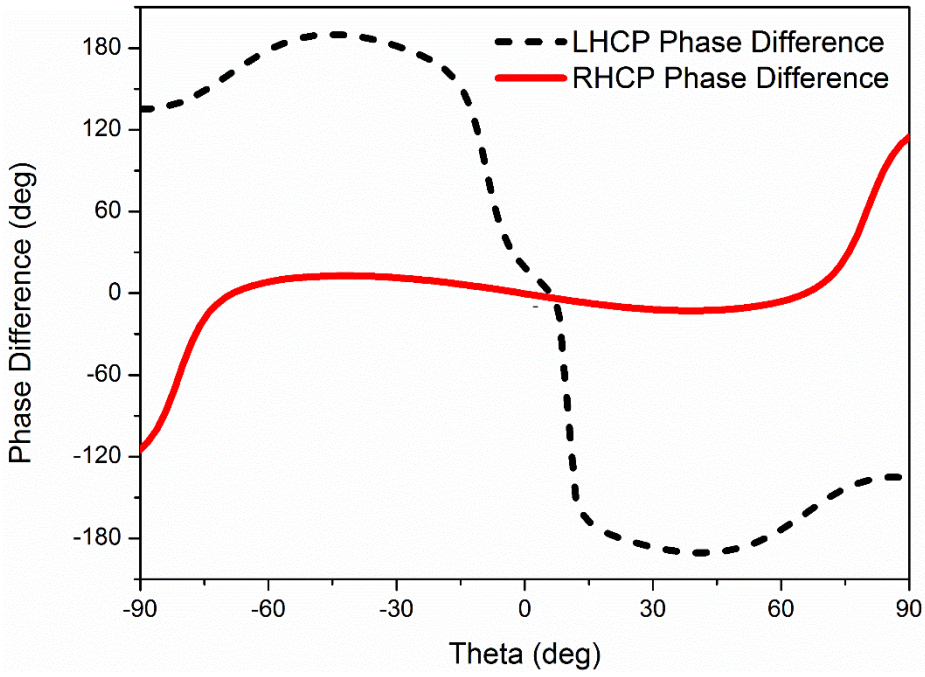

Figure 5.7 Phase differences of RHCP and LHCP component between the two elements at 4.7 GHz in the XOZ plane.

As shown in Figure 5.7 , the phase difference of the RHCP component (co-pol component) is around 0° from -70° to 70° angular range. This means that the RHCP components of the two elements are nearly in phase and can be superposed in a wide angular range. Meanwhile, the phase difference of the LHCP component (cross-pol component) is around -180° from 15° to 70° angular range and around 180° from -15° to -70° angular range. The LHCP components of the two elements are therefore canceled by each other in the angular range of 15° to 70° and -15° to -70°. As the RHCP component of the 2-element array gets enhanced and the LHCP component gets decreased in a wide

angular range, the AR improves in a wide angular range and wide angular CP radiation can be achieved.

From (5.5), the fields of two elements will be superposed in phase in the broadside direction ($\theta = 0$). However, the phase difference of the LHCP component is slightly larger than 0^o. This phase error may be caused by the mutual coupling between the two elements. It is worth pointing out that these equations can also be applied to the "S" shaped antenna which radiates LHCP wave.

Figure 5.8 shows the simulated AR and HPBW of the proposed antenna (without balun) in the upper hemisphere area at 4.7 GHz, which are obtained by using Ansys HFSS 15. The dark area denotes the region where the AR is smaller than 3 dB and the HPBW is bounded by the two red curves. Figure 5.8 clearly demonstrates that the AR beamwidths in each elevation planes are larger than the HPBWs. The decrease of the AR beamwidth is along with the decrease of HPBW, leading to a wide AR beamwidth covering HPBW in the whole upper hemisphere.

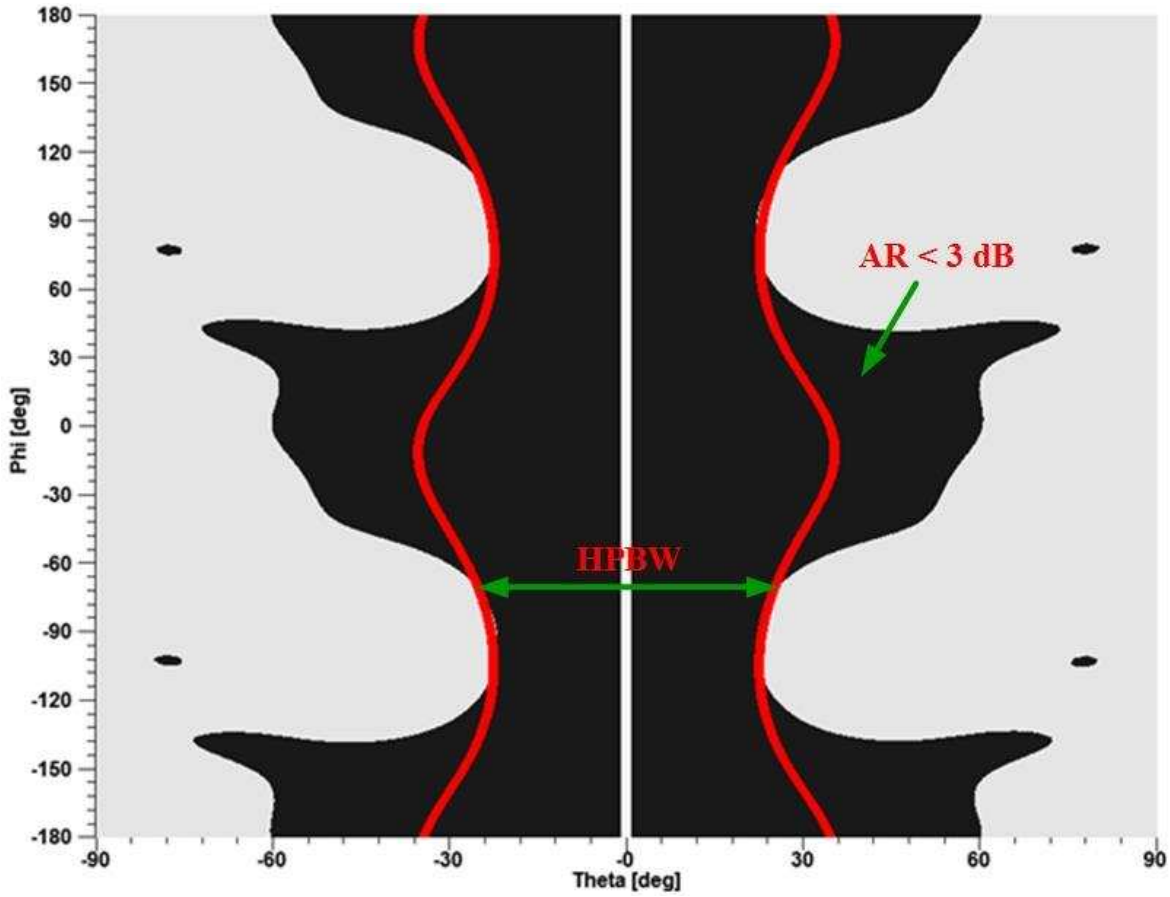

Figure 5.8 The Axial Ratio and HPBW of the proposed antenna at 4.7 GHz.

5.3 Results and Discussion

5.3.1 Antenna Prototype and VSWR

The prototype of the proposed antenna is shown in Figure 5.9. As shown, a coaxial connector is connected to the end of the balun to feed the antenna. Four plastic pillars are used to support an 18mm air gap between the antenna and the ground plane.

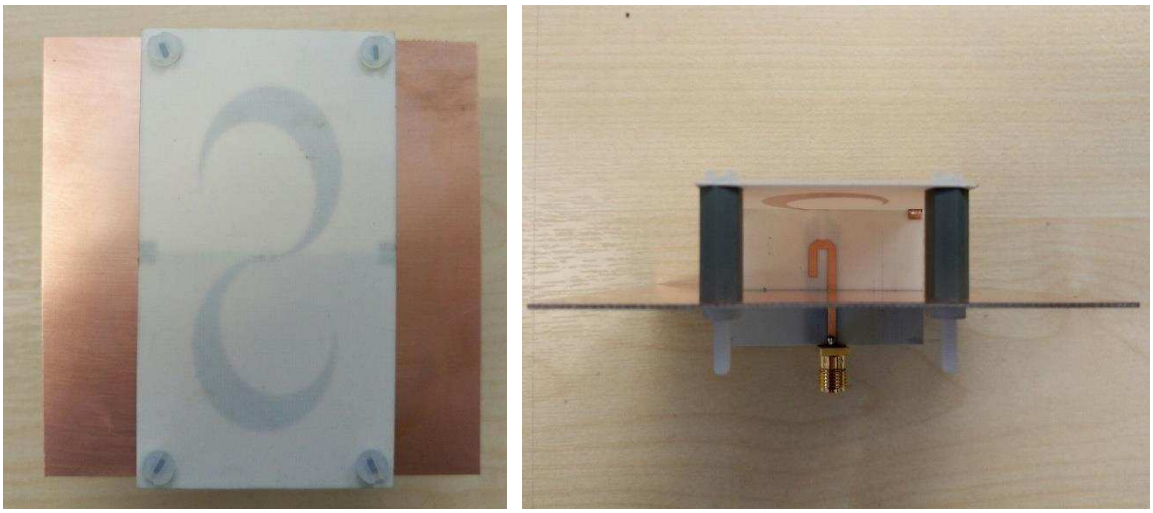

Figure 5.9 The prototype of the inverted-S antenna.

The simulated and measured VSWR of the proposed antenna is given by Figure 5.10. As can be seen, the measured impedance bandwidth (VSWR<2) is from 3.4 GHz to 6.5 GHz (63%). Compared with the simulated VSWR, the measured result is slightly shifted to lower frequency, which is caused by fabrication and measurement errors.

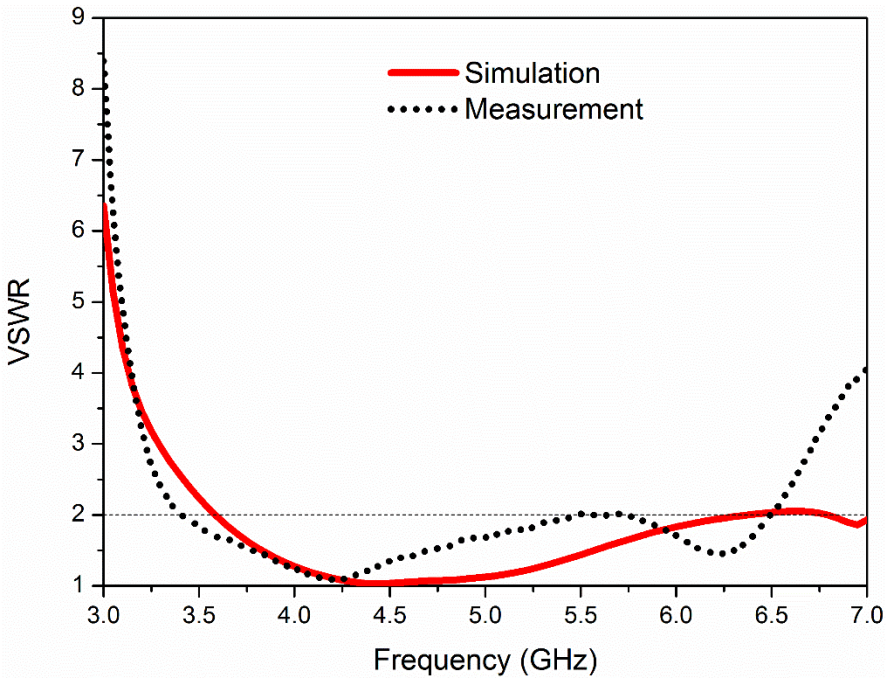

Figure 5.10 The simulated and measured VSWR of the proposed antenna.

5.3.2 Axial Ratio Bandwidth

The AR bandwidth of the proposed antenna is shown in Figure 5.11, which indicates the AR values in the broadside direction. The measured AR bandwidth (AR<3 dB) is from 4 GHz to 6.15 GHz, results in a fractional bandwidth of 42%. Different to the simulated AR, the frequency of measured minimum AR point is shifted to a higher frequency which is around 5 GHz.

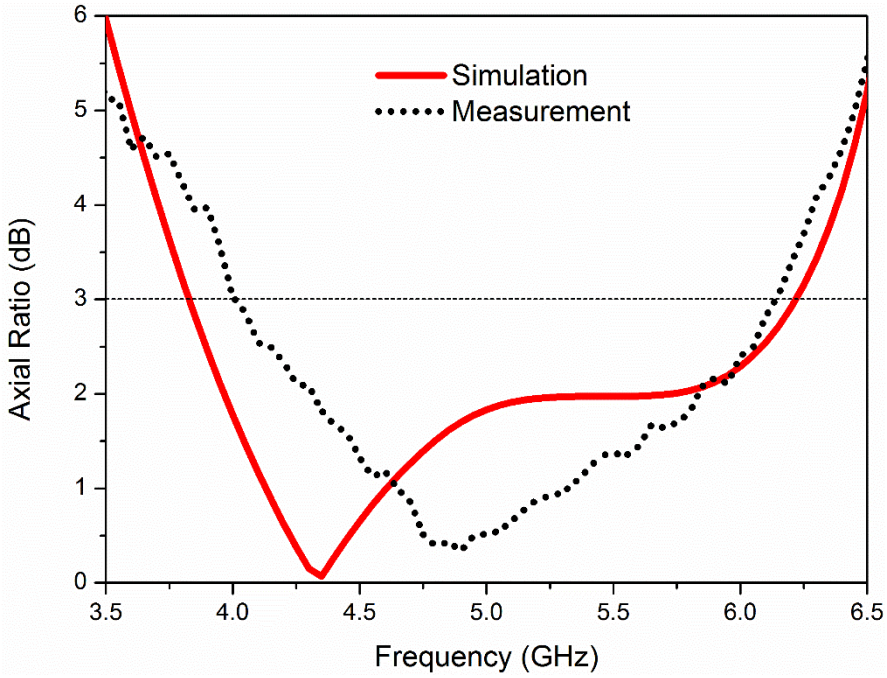

Figure 5.11 The simulated and measured AR bandwidth of the proposed antenna.

5.3.3 Axial Ratio Beamwidth

As aforementioned, the proposed antenna exhibits stable wide AR beamwidth apart from its wide AR bandwidth. The stable wide AR beamwidth of the proposed antenna not only rests on its wide AR beamwidth in the symmetric plane (XOZ plane) but also lies in its AR beamwidths in other cutting planes, which are wider than HPBWs.

Figure 5.12 shows the simulated and measured AR beamwidth in the XOZ plane at different frequency points. As shown, the measured AR beamwidths in the XOZ plane are 117°, 138° and 123° at 4.2 GHz, 4.8 GHz and 5.4 GHz, respectively. In line with the measured AR bandwidth shown in Figure 5.11, the measured AR in other elevation angles is smaller than the simulated AR at higher frequencies, which also verifies the shifting of minimum AR point to a higher frequency. The difference between the measurement and simulation results may come from the fabrication and measurement errors. It is also observed that the AR beamwidth is asymmetric to $\theta = 0^{o}$, which is different to the sym-

metric AR beamwidth observed in Figure 5.8. This asymmetry is caused by the integrated balun which has an asymmetric microstrip line to $\theta = 0^{\circ}$ direction. Although the radiation of this microstrip line is small, it still introduces different influences to the CP radiation in different elevation angle θ [116].

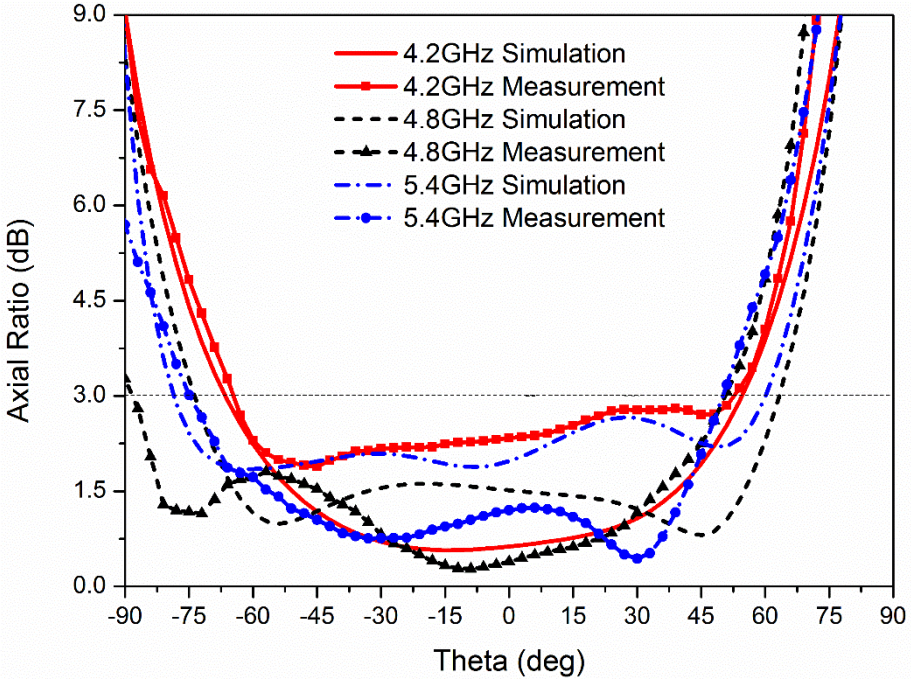

Figure 5.12 The simulated and measured AR beamwidth in the XOZ plane at different frequencies.

To give an understanding of the AR beamwidths in other cutting planes and the comparison between the AR beamwidths and HPBWs, the values of measured AR beamwidths and measured HPBWs in planes $\varphi = 0^{o}, 30^{o}, 60^{o}, 90^{o}$ are given by Figure 5.13. As can be seen, in elevation planes $\varphi = 0^{o}, 30^{o}, 60^{o}$, the AR beamwidths are larger than the HPBWs from 4 GHz to 6 GHz. However, in the $\varphi = 90^{o}$ plane, the AR beamwidth is slightly smaller than the HPBW at some frequency points. As the value of AR is determined by the RHCP and LHCP component, slightly increase of cross-pol (LHCP) component makes the AR larger than 3 dB and results in a narrower AR beamwidth. In spite of this, the measured results still indicate that the proposed antenna can achieve a wide angular CP radiation in the upper-hemisphere. It is also noticed that the HPBW increases as the frequency goes up in the $\varphi = 0^{o}$ plane but decreases as the frequency rises in $\varphi = 30^{o}, 60^{o}, 90^{o}$ planes. According to [22], the antenna directivity is in reverse proportional to the product of HPBWs in two perpendicular planes. Although the HPBW's variation of the proposed antenna is different in each plane, the product of the HPBWs in each two perpendicular planes always increases as the frequency goes up, indicating a decrease of antenna directivity as the frequency rises, which is verified by Figure 5.14.

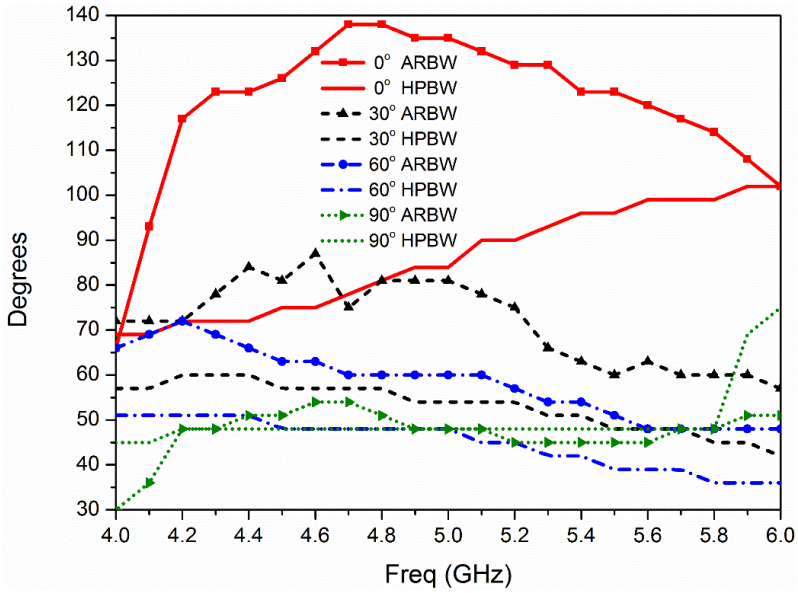

Figure 5.13 The measured AR beamwidths and HPBWs in different cutting planes.

5.3.4 Radiation Patterns and Antenna Gain

The simulated and measured antenna gain is shown in Figure 5.14.

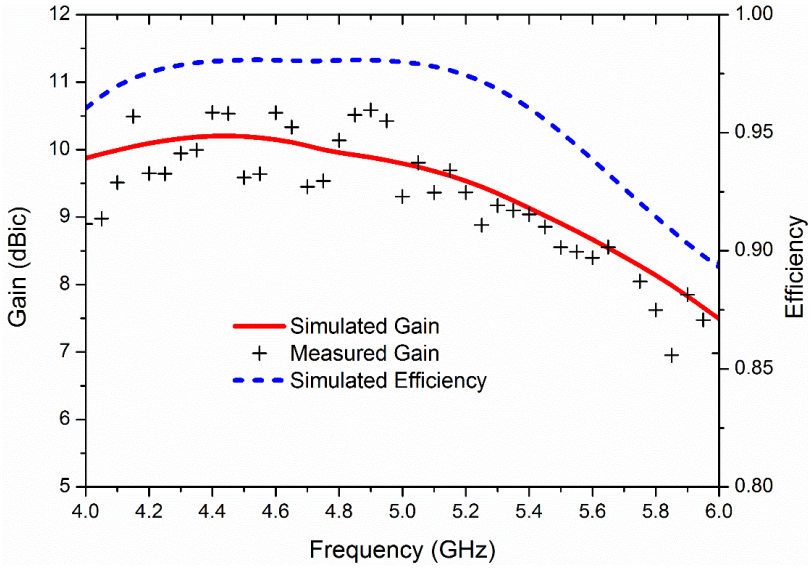

Figure 5.14 Antenna gain and simulated efficiency.

As shown, the measured antenna gain is around 9-10 dBic from 4 to 5.4 GHz. Figure 5.14 also shows the simulated efficiency which is larger than 90% across the whole operation bandwidth. It is indicated by the simulation that the insertion loss of the balun increases as the frequency increases, around 0.2 dB at 4 GHz and 0.8 dB at 6 GHz. It is worth pointing out that the insertion loss includes dielectric loss, conductor loss and radiation loss. From the simulation, it is found that the radiation loss of the balun accounts for the major proportion of the insertion loss, which makes the simulated efficiency a little higher than the actual antenna radiation efficiency.

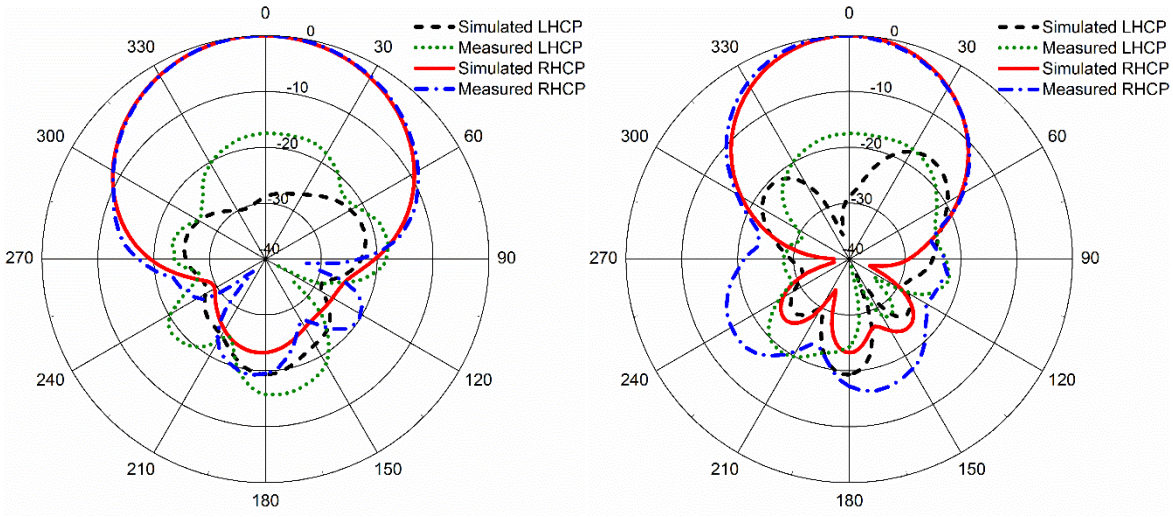

(a)

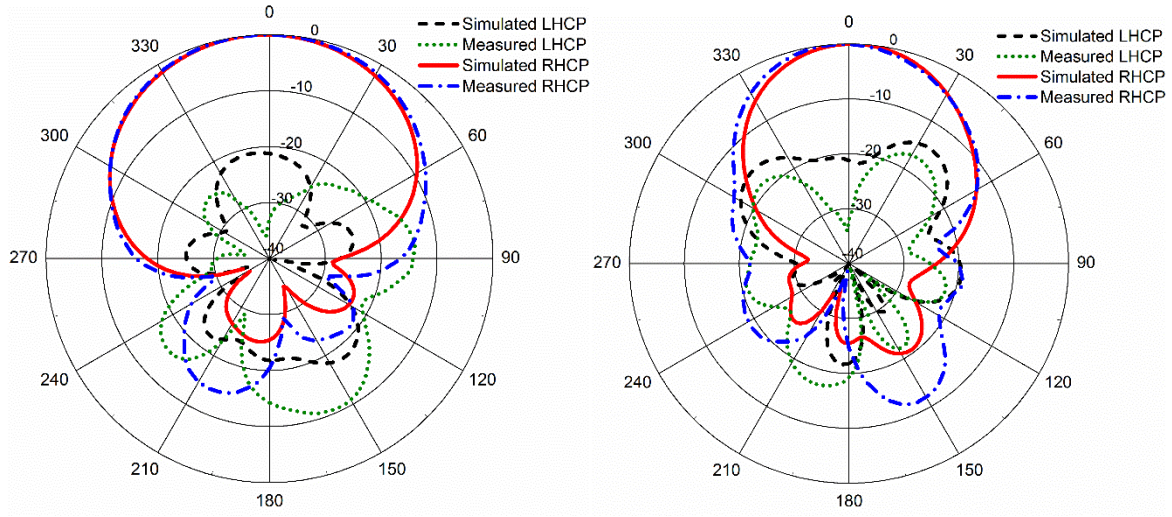

(b)

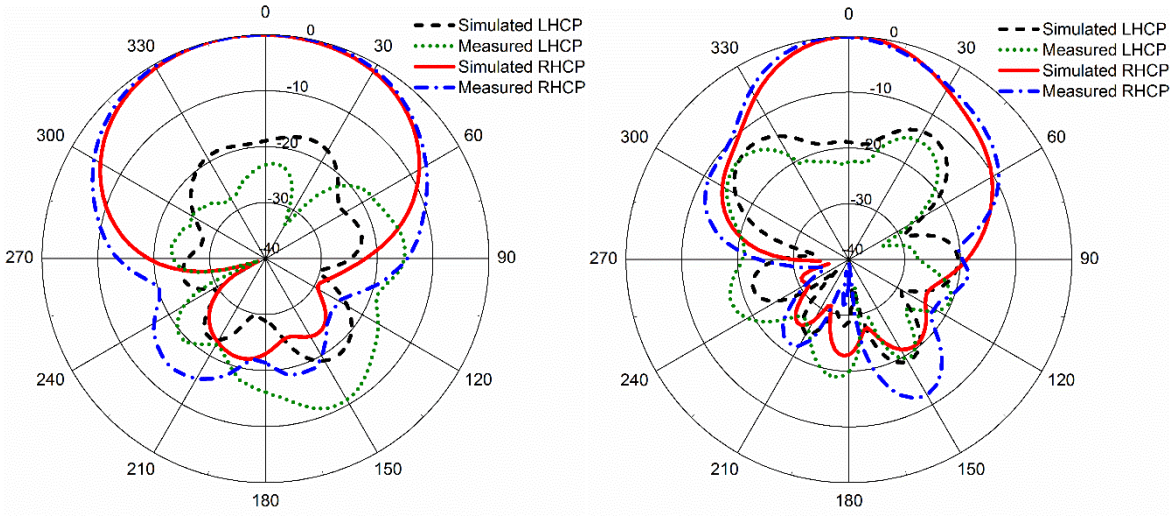

(c)

Figure 5.15 The measured and simulated radiation patterns of the proposed antenna in two main planes at: (a) 4.2 GHz, (b) 4.8 GHz, (c) 5.4 GHz.

The radiation patterns of the proposed antenna at different frequency points are shown in Figure 5.15. As can be seen from the figure, good agreements are observed between the simulation and measurement results of all co-pol components (RHCP) in the upper hemisphere region. The differences in the back lobe are caused by the scattering of the cable and antenna holder. To measure the back lobe of the proposed antenna, an antenna holder is fabricated and placed above the positioner, which brings an extension of test cable and antenna holder behind the proposed antenna.

5.3.5 Comparison with Other Antennas Reported

To demonstrate the advantages of the proposed antenna, Table 5.2 compares the proposed antenna with other reported wideband wide AR beamwidth antennas.

Table 5.2 Comparison with Other Wideband Wide AR Beamwidth Antennas

	Impedance Bandwidth (GHz)	AR Bandwidth (GHz)	Maximum AR beam-width and correspond-ing HPBW (°)	AR beam-width vs Frequency in Main Planes	AR beam-width in other Planes	Antenna Size (at center freq.)
[107]	1.35-1.85, 31%	1.52-1.65, 8%	AR beam-width:126° HPBW: –	—	—	0.5λ×0.53λ (no ground plane)
[108]	1.85-3.38, 58%	2.23-2.47, 10%	AR beam-width:175° HPBW:150°	—	—	0.4λ×0.4λ×0.1λ
[109]	1.6-2.42, 40%	1.63-2.27, 32%	AR beam-width:85° HPBW:-	AR beam-width=85° from 1.8 to 2.1 GHz (15%)	—	1λ×1λ×0.25λ
[110]	1.27-2.36, 59%	1.39-1.82, 26%	AR beam-width:175° HPBW: -	AR beam-width>165° from 1.45 to 1.7 GHz (15%)	—	0.7λ×0.7λ×0.18 λ
Simulated Spiral (no ground plane)	—	5.38-6.9, 25%	AR beam-width:100° HPBW:71°	AR beam-width>90° from 5.4 to 6 GHz (10%)	AR beam-width< HPBW	1.2λ×0.9λ
This Design (no ground plane)	—	5.32-6.48, 20%	AR beam-width:138° HPBW:69°	AR beam-width>94° from 5.5 to 6.3 GHz (13%)	AR beam-width> HPBW	1.2λ×0.5λ
Simulated Spiral	—	5.15-6.24, 19%	AR beam-width:64° HPBW:117°	—	AR beam-width< HPBW	1.7λ×1.7λ×0.3λ
This Design	3.4-6.5, 62%	4-6.15, 42%	AR beam-width:142° HPBW:82°	AR beam-width>100° from 4.2 to 6 GHz (35%)	AR beam-width> HPBW	1.4λ×1.4λ×0.3λ

A 3/4 turn Archimedean spiral is also simulated and compared with the proposed antenna. In order to provide a fair comparison, the spiral antenna was designed by using the same substrate that is used for the proposed antenna and the size of the spiral is adjusted to be similar physical size as the presented antenna. Table 5.2 gives the comparison between the proposed antenna and other antennas in terms of impedance bandwidth, AR bandwidth, and AR beamwidth. From Table 5.2, it is shown that the proposed antenna has wider CP bandwidth and more stable AR beamwidth within the operational bandwidth when a ground plane is used. Moreover, the AR beamwidths of the proposed antenna are larger than the HPBWs in other elevation planes, which were not investigated by other researchers. Besides, the proposed antenna has narrower AR bandwidth but wider AR beamwidth than the 3/4 turn Archimedean spiral without ground plane backed. The antenna can be easily extended to an antenna array which is shown in the following section.

5.4 Linear Array using Inverted-S Antenna

5.4.1 Array Configuration

Compared with other reported wideband wide AR beamwidth CP antennas, another advantage of the proposed antenna is that it can be easily extended to an antenna array.

To prove this concept, a four-element linear array is designed and prototyped. Figure 5.16 shows the presented antenna array, which consists of 4 inverted S-shaped elements.

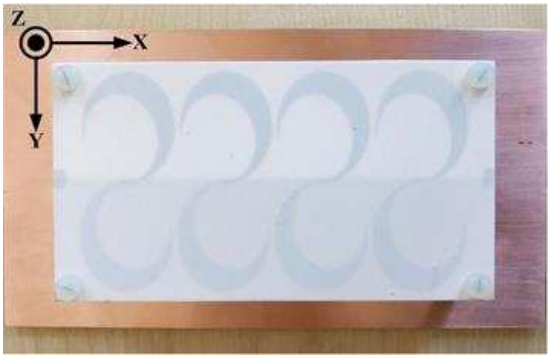

(a)

(b)

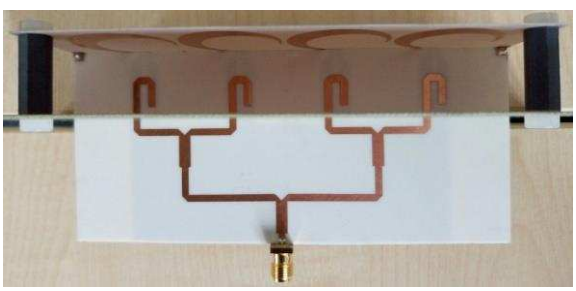

(c)

Figure 5.16 The prototype of the proposed array: (a) top view, (b) left side view, (c) right side view.

The element space is 26.5 mm which is about $0.35\lambda_0$, $0.44\ \lambda_0$ and $0.53\lambda_0$ for 4 GHz, 5 GHz and 6 GHz, respectively. The small element space chosen in this design helps enhance the bandwidth of the antenna array, which is also observed in sub-wavelength array [117] and can be explained by the cancelling of the imaginary part of mutual impedances [21]. The presented array is printed on a 0.508 mm thick Rogers RO4003C substrate with a size of 65 mm×120 mm while a 1:4 power divider is printed on a 0.813 mm thick Rogers RO4003C substrate with a size of 60 mm×120 mm. Below the antenna board, there is a ground plane with the size of 90 mm×165 mm. The distance between the antenna and the ground plane is kept 18mm, which is the same as the antenna element.

It is worth pointing out that the ground plane of each balun is also kept the same size as in the antenna element. By doing this, the influence of the balun to the performance of the array can be minimized. This is because reducing the size of the ground plane of the balun effectively decrease the surface current flowing area, which makes the radiation of the balun relatively far away from the radiation region of the antenna [116].

5.4.2 VSWR and Axial Ratio Bandwidth

The comparison between the simulated and measured VSWR of the proposed array is shown in Figure 5.17. As shown in the figure, the measurement result is in good agreement with the simulation result. The measured impedance bandwidth is from 3.6 GHz to 6.3 GHz (55%). The simulated and measured AR of the presented array is given by Figure 5.18. The measured CP bandwidth of the presented array is from 3.5 GHz to 6.5 GHz.

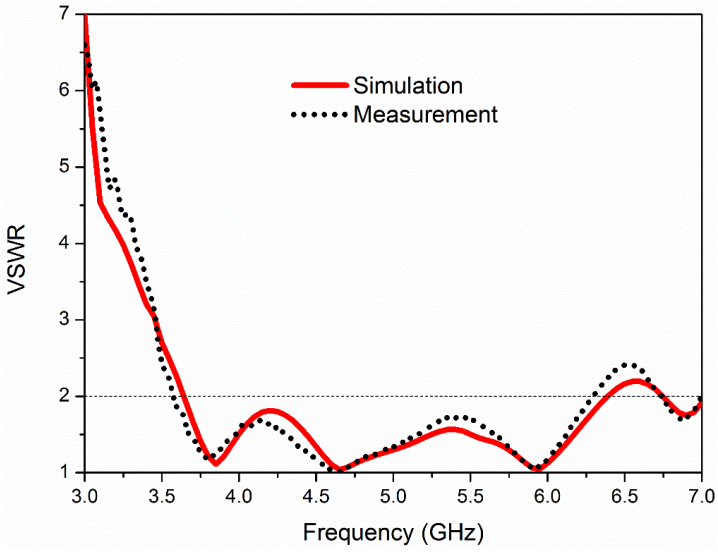

Figure 5.17 The simulated and measured VSWR of the proposed array.

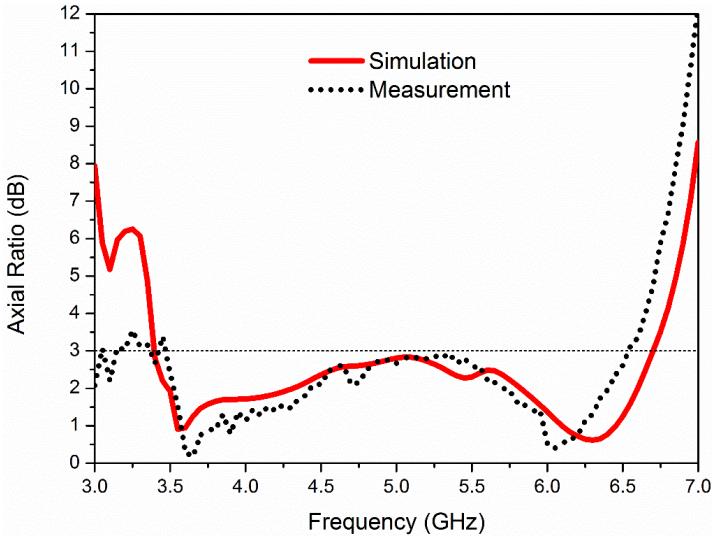

Figure 5.18 The simulated and measured AR of the proposed array.

5.4.3 Axial Ratio Beamwidth of the Array

To evaluate the AR beamwidth characteristics of the array, Figure 5.19 shows the measured AR beamwidths and HPBWs in planes $\varphi = 0^o, 30^o, 60^o, 90^o$. As shown, the AR beamwidths are larger than the HPBWs from 4 GHz to 6 GHz in elevation planes $\varphi = 0^o, 30^o, 60^o$. However, the AR beamwidth is smaller than the HPBW in plane $\varphi = 90^o$, which may due to the narrow AR beamwidth of the antenna element in this plane and the effect of mutual coupling between each element.

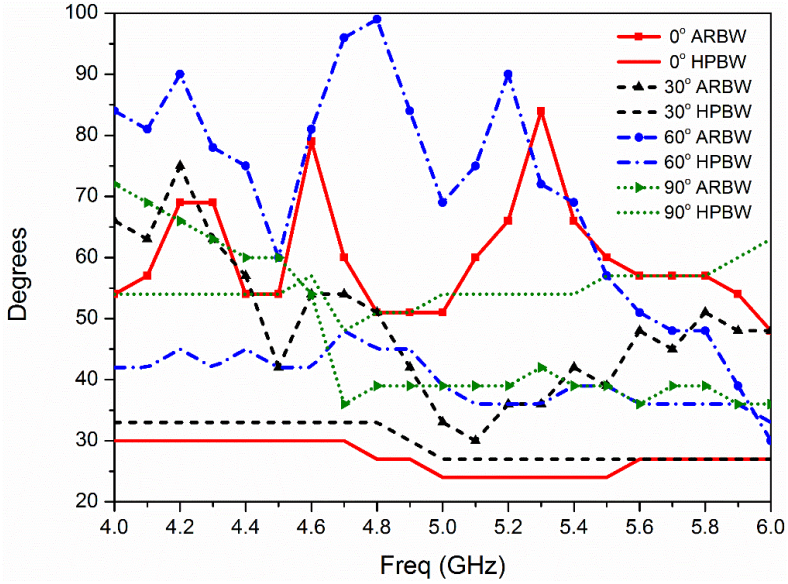

Figure 5.19 The measured AR beamwidth of the proposed array.

5.4.4 Radiation Pattern and Gain

To evaluate the radiation performance of the presented array, radiation patterns of the proposed array at 4 GHz and 6 GHz are given by Figure 5.20. As shown, the measurement

results agree well with the simulation results. Better agreements are obtained due to the fact that the array has a larger ground plane which provides better shielding to the cables and antenna holder which are placed behind the antenna during the measurement.

Figure 5.21 shows the measured and simulated gain of the presented antenna array. As shown, the measured gain is around 12-14 dBic from 4 GHz to 6 GHz. The simulated insertion loss of the array feeding network is around 0.5-1.2 dB from 4 GHz to 6 GHz. The difference of the gain between the array and the antenna element increases as frequency goes higher, which mainly attributes to the decreased mutual coupling at higher frequencies. Besides, the increase of the ground plane size has some effect on the antenna gain as well. The simulated efficiency of the antenna array, as shown in Figure 5.21, is larger than 85% from 4 GHz to 6 GHz.

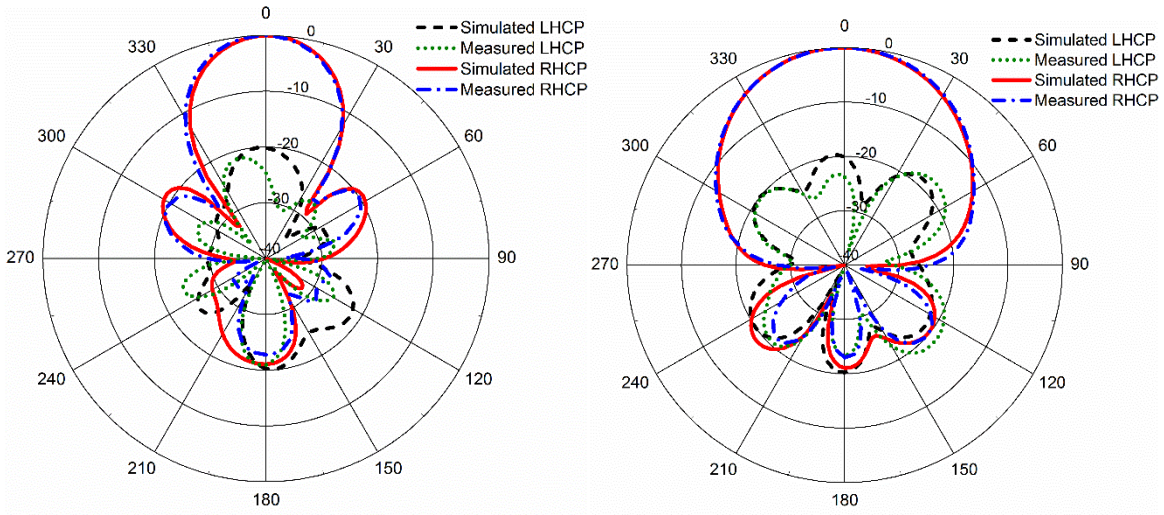

(a)

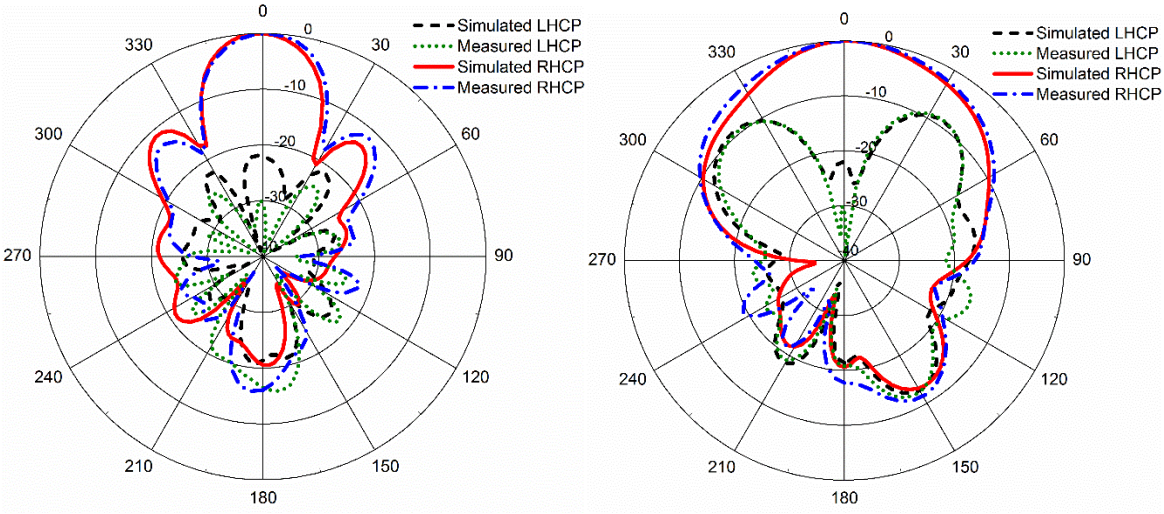

(b)

Figure 5.20 The measured and simulated radiation patterns of the proposed array in two main planes at: (a) 4 GHz, (b) 6 GHz.

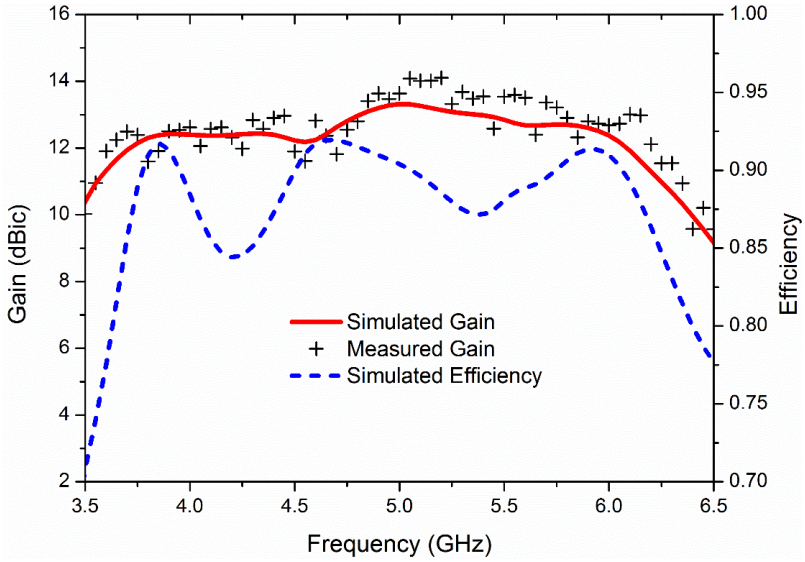

Figure 5.21 Gain and simulated efficiency of the antenna array.

5.5 Summary

A wideband CP antenna with wide AR beamwidth within its operational bandwidth is presented in this Chapter. The proposed inverted-S antenna achieves a CP bandwidth of 42% and over 140^{o} 3 dB AR beamwidth, leading to a wider CP bandwidth compared with other reported wide AR beamwidth CP antennas. Besides, the AR beamwidths of the presented antenna are larger than the HPBWs in other elevation planes. Due to its simple configuration, the presented antenna could be easily extended to an array antenna with 60% CP bandwidth. Owing to these advantages, the proposed antenna is promising for the applications in GNSS systems and wide-angle CP beam-scanning arrays.

Chapter 6. Wideband Dual Circularly Polarized Array

6.1 Introduction

Chapter 3 to Chapter 5 investigates three different wideband CP antenna elements. Although they exhibit excellent performances, for some applications such as the satellite communications where high antenna gain is needed, it is preferable to deploy array antennas. In this Chapter, a wideband CP patch array operating at Ka-band is developed for the EU FP7 GanSAT project. To fulfill the system requirements, the array needs to have dual-CP operating ability, i.e., capable of radiating RHCP and LHCP waves, from 27.5 GHz to 30 GHz. Moreover, the isolation between the two orthogonal polarized ports should be larger than 15dB across the whole working bandwidth.

To design such a wideband dual-CP array, it is necessary to design appropriate wideband dual-CP element at first. Currently, there are several ways to design a dual CP antenna. A quasi-ring shaped microstrip line fed patch antenna with dual CP radiation was presented in [118]. By feeding at different ports, the flowing direction of the current on the microstrip line can be changed. By this means, the antenna could radiate RHCP and LHCP waves. In [119], a branch line coupler fed patch antenna with H-shaped slots on the ground plane was proposed. Through using hybrid coupler and feeding at the two input ports, dual CP radiation was achieved. A coplanar waveguide transmission line which exploited the even and odd modes was used to feed a patch antenna and achieved dual CP radiation [120]. The presented antenna in [120] realized high isolation without any hybrid coupler, but the limited bandwidth made it not suitable for the project requirements. Generally, the antenna element presented in [119] achieves high port isolation and relatively wide bandwidth. But the achieved bandwidth is still smaller than the required bandwidth. Moreover, the aperture feeding technique imposes very high fabrication accuracy which is hard to realize at Ka-band.

On the other hand, wideband dual CP beam-scanning arrays with high isolation between the orthogonally polarized ports can be utilized to improve the spectrum efficiency and thus is vital to the project target. To enhance the isolation between the two orthogonally polarized ports, different approaches were adopted [121-123]. In [121], disparate elements were employed to suppress the coupling and higher than 20 dB isolation was achieved. By using linearly polarized equilateral triangular patches with orthogonally placed feeds, a sequentially rotated dual CP patch array was realized with more than 20 dB isolation [122]. However, the axial ratio (AR) bandwidth of this array is

relatively narrow. Dual CP array with larger bandwidth was achieved by using a three-stage hybrid coupler [123]. This array achieved wide bandwidth within which the isolation of the dual CP ports was higher than 20 dB. Nevertheless, the scanning performance was not investigated.

In this Chapter, a wideband multi-layer CP patch element for Ka-band satellite communications is presented at first. Then a wideband dual CP beam-scanning array with high isolation between the two orthogonally polarized ports is developed. Through the integration of two separated beam-forming networks (BFNs) to the LHCP and RHCP port, the proposed array can scan the LHCP beam and the RHCP beam independently. Moreover, the presented array maintains the wide bandwidth, good circular polarization and high ports isolation with beams of different scanning angles.

This Chapter is organized as follows: Section 6.2 introduces the Ka-band multi-layer CP element; Section 6.3 presents two passive dual CP array with different scanning angles. The simulation results and measurement results of the proposed dual CP array are also given in this section and the summary of this Chapter is given in Section 6.4.

6.2 Ka-band Multi-layer Element

6.2.1 Element Configuration

As the element size is bounded by 15 mm×8 mm for the purpose of beam scanning of the array, a single-CP multi-layer element is fabricated due to the insufficient spaces for mounting two connectors. The isolation between the two orthogonal polarized ports can be examined by simulation. Figure 6.1 shows the configuration and geometry dimensions of the proposed antenna element. As shown, the driven square patch is printed on the middle substrate (Rogers RO3006, $\varepsilon_r = 6.15$, $\tan\delta = 0.0025$) with a thickness of 0.254 mm while the parasitic patch is etched on the bottom layer of the top substrate (Rogers RO5880, $\varepsilon_r = 2.2$, $\tan\delta = 0.0009$) with a thickness of 0.254 mm. Between the top and middle substrate, a 1 mm thick Rohacell foam is used to form an air gap. To achieve CP radiation, a single-stage 90^o hybrid coupler is employed. Two signal vias are placed at the end of the hybrid coupler, which constitutes a microstrip-via-microstrip signal transmission structure. A surface mount SMPM connector is soldered on the 0.254 mm thick bottom substrate (Rogers RO5880) to connect one output port of the coupler and a 50 ohms RF resistor is connected to the other output port. It is worth mentioning that this element can be easily transformed to a dual CP element by connecting the two output ports of the coupler both

with SMPM connectors. Two rows of shielding vias are drilled along the long edges of the substrate to suppress the propagation of surface waves when used in array circumstances.

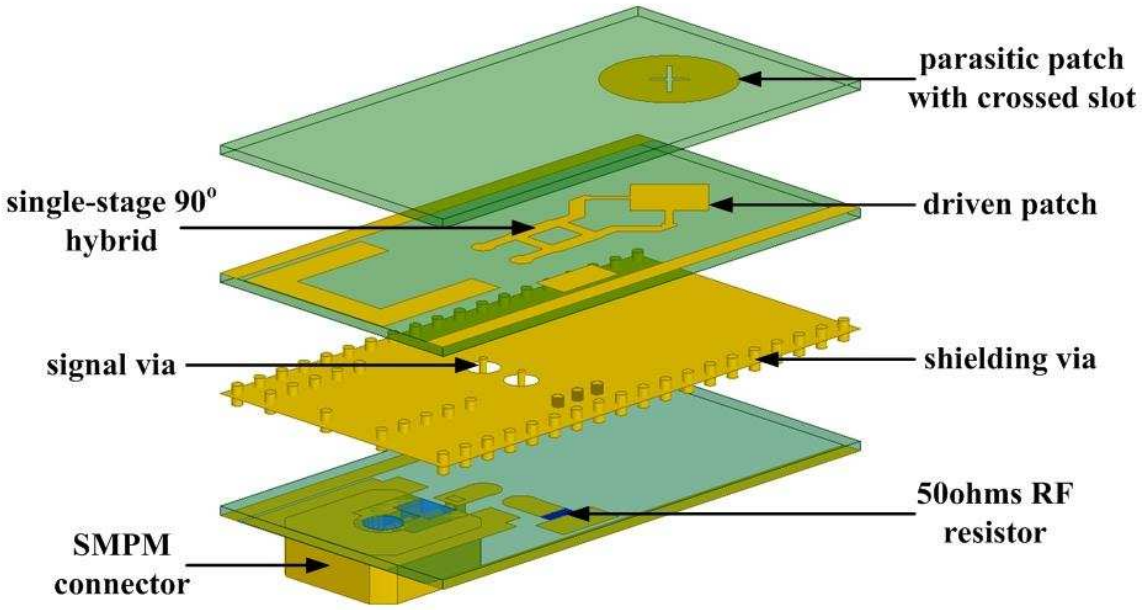

(a)

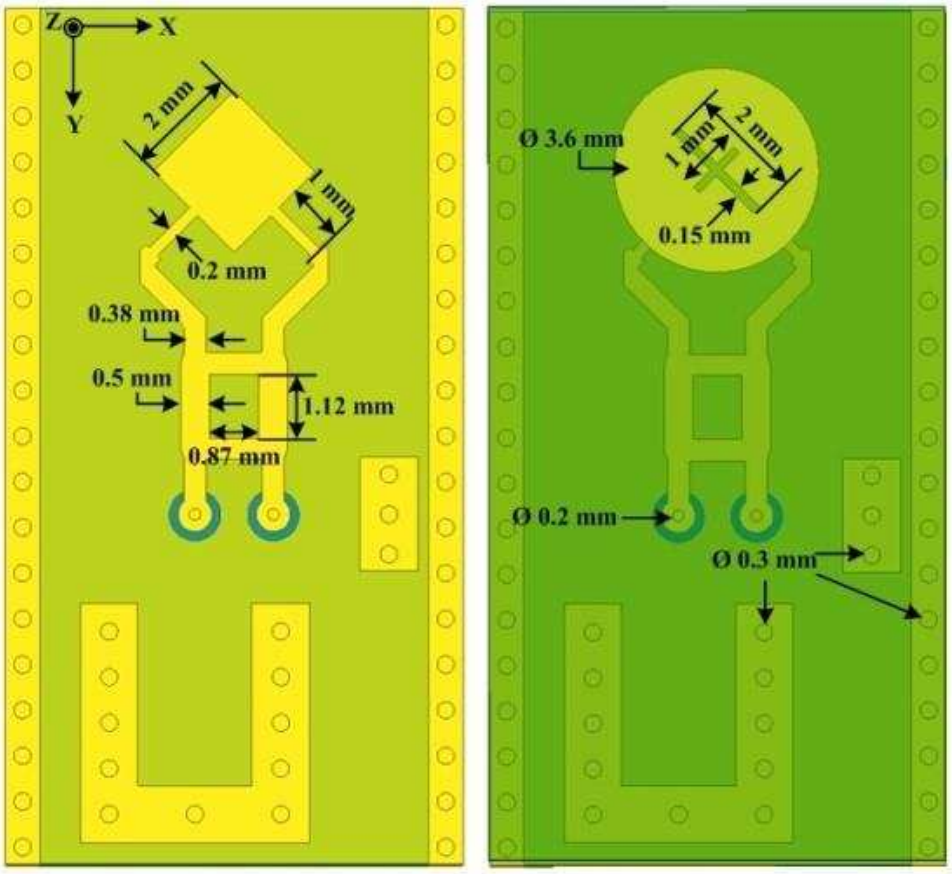

(b)

Figure 6.1 Antenna configuration and geometry dimensions: (a) Exploded view, (b)Top view: left without the parasitic patch, right with the parasitic patch.

6.2.2 Simulation and Measurement Results

To verify the performance of the proposed element, a prototype is fabricated, as shown in Figure 6.2. As can be seen from the figure, the width of the prototype is around the 9.5 mm and the actual antenna size (bounded by the shielding vias) is 8 mm×15 mm.

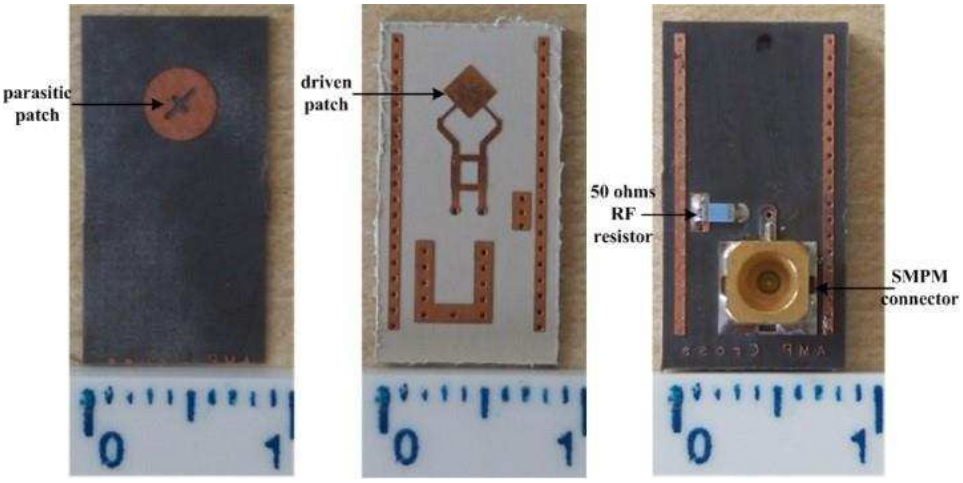

Figure 6.2 Prototype of the proposed element.

By etching a crossed slot on the parasitic patch, it is found that the AR performance can be enhanced. Figure 6.3 gives the simulated AR with and without the crossed slot. As shown, the AR is improved by 0.5-1 dB at 27-28.5 GHz and 30.5-31.5 GHz when the crossed slot exists. Figure 6.3 also indicates that the AR does not vary drastically when the width of the slot (w_{slot}) changes. This characteristic ensures the antenna can maintain good AR performance even with 0.1 mm fabrication errors.

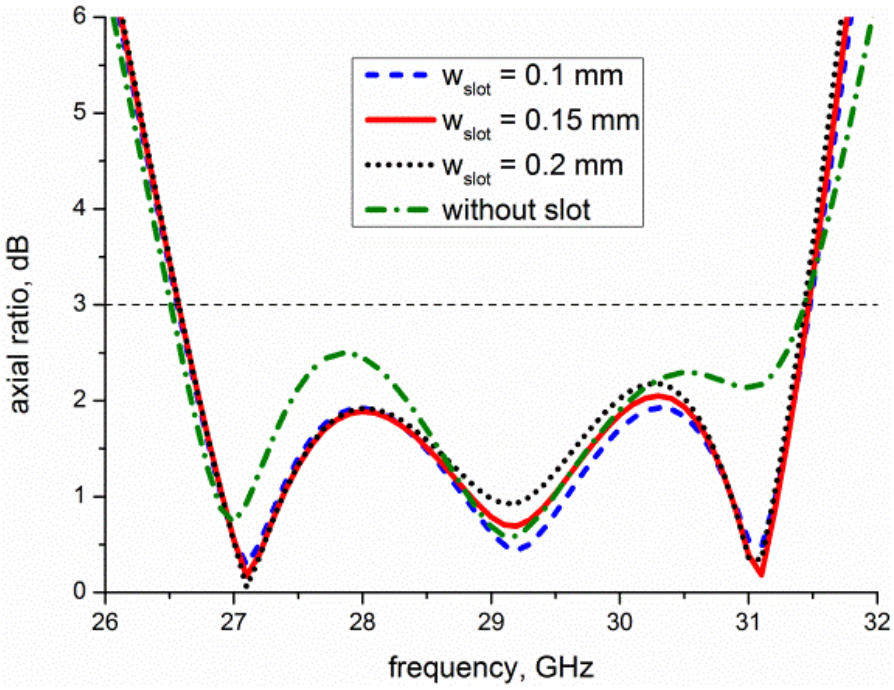

Figure 6.3 Simulated axial ratio with and without the crossed slot.

The simulated and measured reflection coefficients are shown in Figure 6.4. As shown, the measured impedance bandwidth of the proposed antenna is from 26.8 GHz to 32.5 GHz. To evaluate the CP performance of the proposed antenna, the axial ratio is measured and shown in Figure 6.5. As can be seen, the measured AR bandwidth is from 26 GHz to 30.3 GHz. Compared with the simulated AR, the measured result is shifted to lower frequency by around 3% at Ka-band, which may be caused by the misalignment between the driven patch and the parasitic patch during the assembling procedure. Both the measured impedance bandwidth and AR bandwidth indicate that the proposed antenna has wide bandwidth.

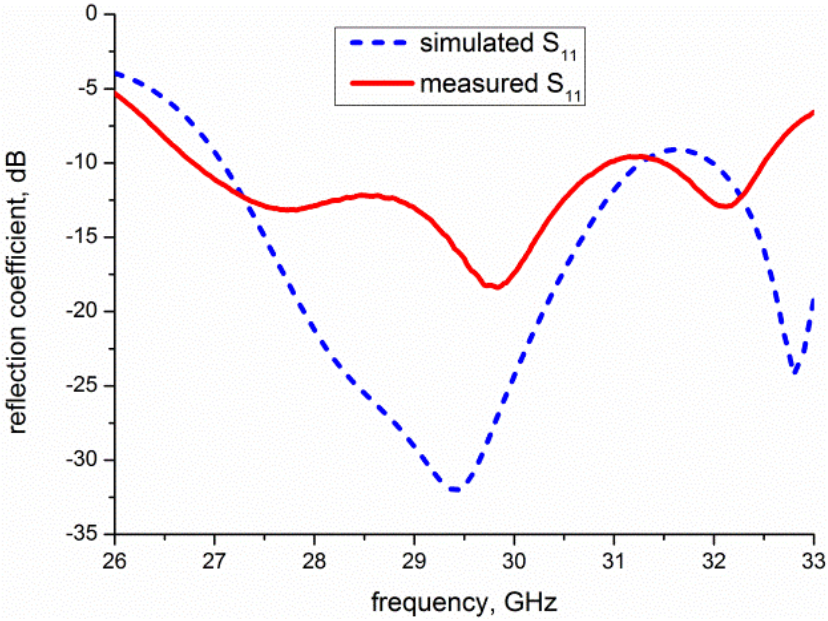

Figure 6.4 Simulated and measured reflection coefficient of the proposed element.

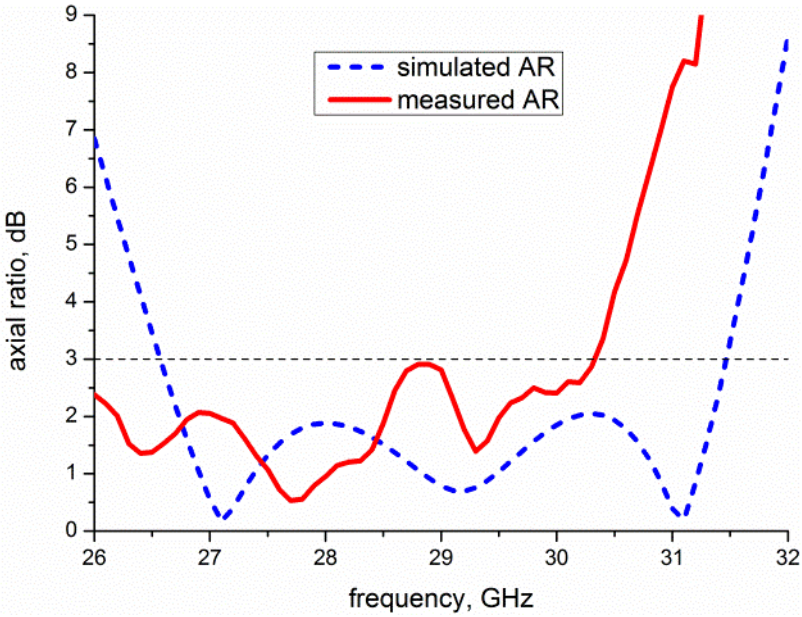

Figure 6.5 Simulated and measured AR of the proposed element.

Figure 6.6 shows the measured radiation patterns at 30 GHz. As shown, good CP radiation is achieved in the broadside direction.

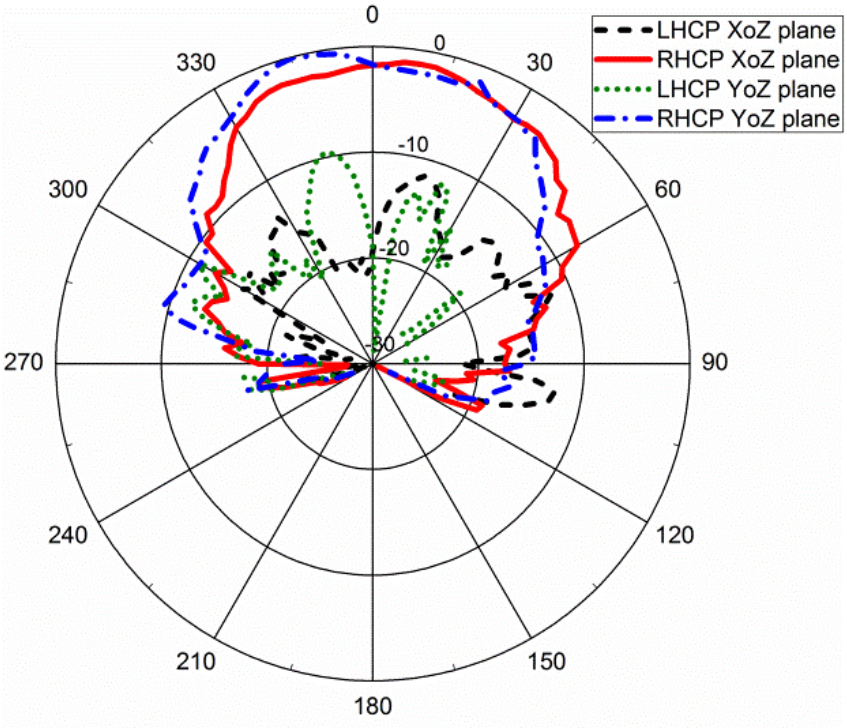

Figure 6.6 Measured radiation patterns at 30 GHz.

The simulated and measured gain is shown in Figure 6.7. As can be seen, good agreement between the simulated and measured results are observed and the antenna gain is around 7 dBic from 27 GHz to 31 GHz. The simulated radiation efficiency is also given by Figure 6.7, which indicates that the radiation efficiency is around 90% at the desired operational band.

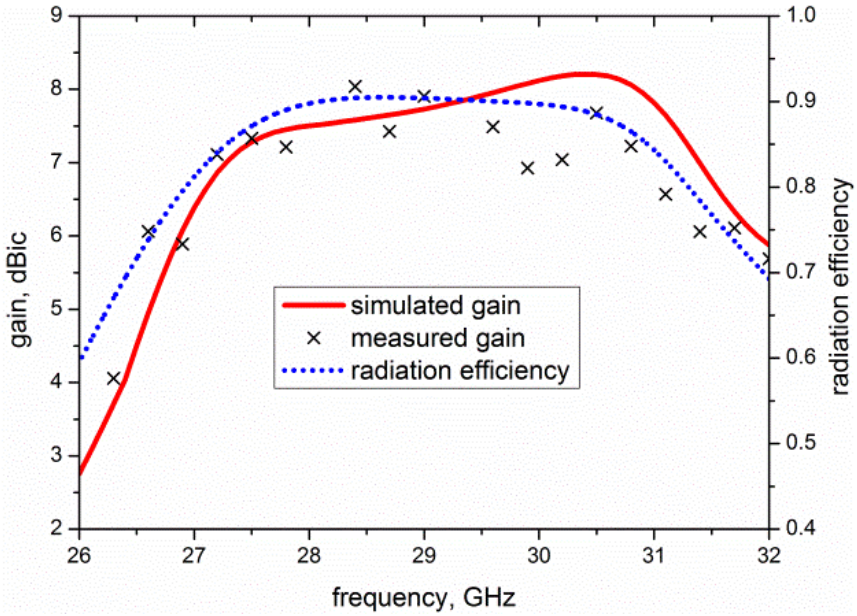

Figure 6.7 Gain and radiation efficiency of the proposed element.

6.3 Ka-band Dual CP Array

6.3.1 Dual CP Array Scanning to ±23º

Based on the element presented in Section 6.2, a linear dual CP array with independent beam-scanning ability is developed. The configuration of the proposed array scanning to +23º in LHCP and -23º in RHCP is shown in Figure 6.8.

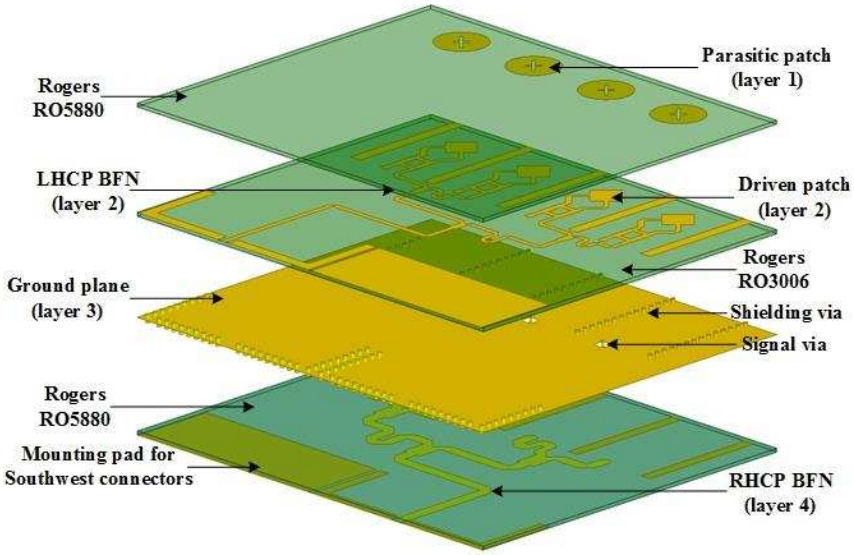

(a)

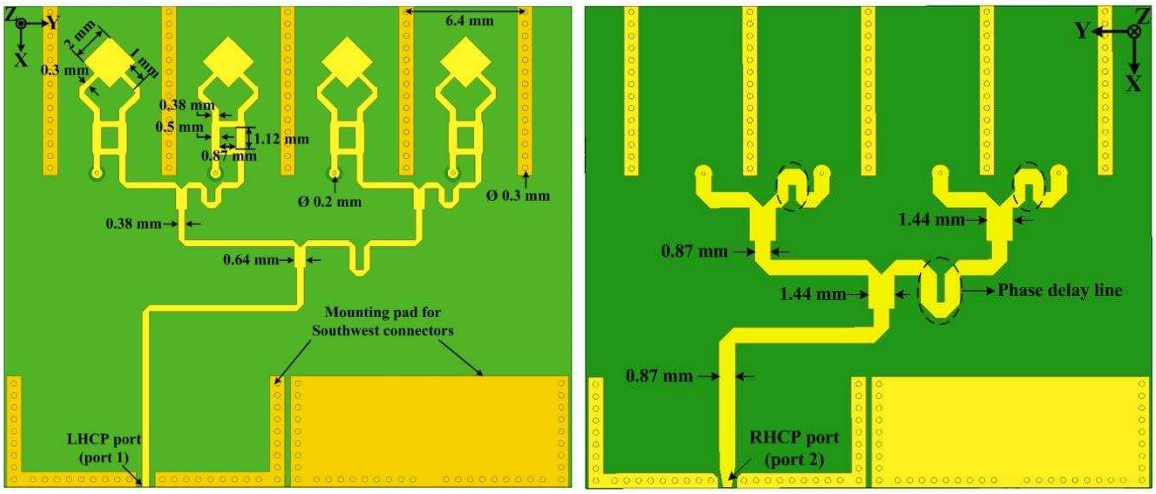

(b) (c)

Figure 6.8 Configuration of the proposed array scanning to ±23º: (a) exploded view, (b) layer 2 (driven patches and LHCP BFN), (c) layer 4 (RHCP BFN).

As shown in Figure 6.8 (a), the proposed array is printed on three substrates, each with 0.254 mm thickness. Circular parasitic patches with diameter of 3.6 mm are printed on the bottom layer of the top substrate (Rogers RO5880). The square driven patches and the LHCP BFN are printed on the top layer of the middle substrate (Rogers RO3006) while the ground plane is printed on the other side of this substrate. Rohacell HF51 foam with 1 mm

thickness is used to form an air gap between the top substrate and the middle one, which helps improve the bandwidth. To realize RHCP radiation, four signal vias are placed at RHCP output ports of the hybrid coupler, which transmits the RHCP signals to the RHCP BFN printed on the bottom substrate. The overall array configuration features a planar and compact structure.

The detailed geometry dimensions of the dual CP element are shown in Figure 6.8 (b). Through stacking circular parasitic patches above the driven patches and employing substrates with different dielectric constants, the bandwidth of the dual CP element is significantly enhanced. Besides, five columns of ground vias are placed between each element to improve the isolation between the elements.

As the array is designed to scan to +23^o with LHCP radiation and -23^o with RHCP radiation, different phase shifts should be given to each element when the array radiates in different polarization. The relationship between the phase increment $\Delta\varphi$ and scanning angle θ_s can be written as follows.

$$\Delta\varphi = \frac{360^o \cdot d \cdot \sin\theta_s}{\lambda} \tag{6.1}$$

where d represents the element space and λ represents the free-space wavelength. Using the above equation, the phase increment between each element at 30 GHz is 90^o and -90^o for LHCP and RHCP beam, respectively.

Figure 6.9 shows the prototype of the proposed array.

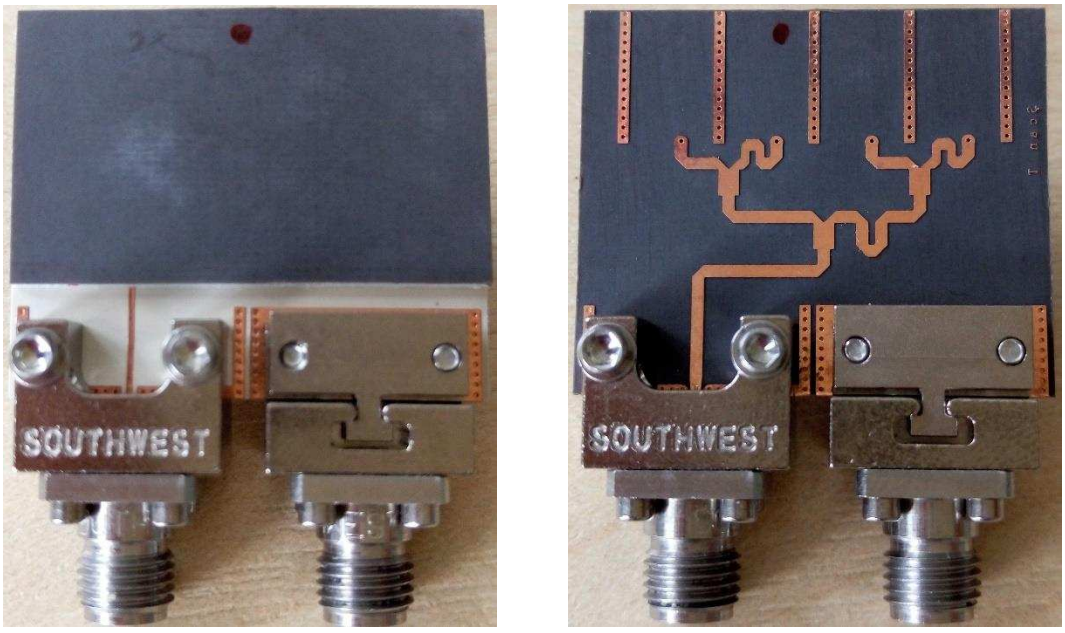

(a) (b)

Figure 6.9 Prototype of the proposed array scanning to ±23^o: (a) top view, (b) bottom view.

As shown, two end-launch Southwest connectors are used to feed the array. Since the parasitic patches are printed on the bottom layer of the top substrate, the parasitic patches, the driven patches and the LHCP BFN are not visible in Figure 6.9 (a).

The measured S-parameters of the proposed array are shown in Figure 6.10. As shown, the measured reflection coefficients are lower than -10 dB from 26 GHz to 33 GHz in both RHCP and LHCP status. The isolation between the RCHP and LHCP ports is higher than 10 dB from 26 GHz to 33 GHz and higher than 20 dB from 27 GHz to 31.2 GHz.

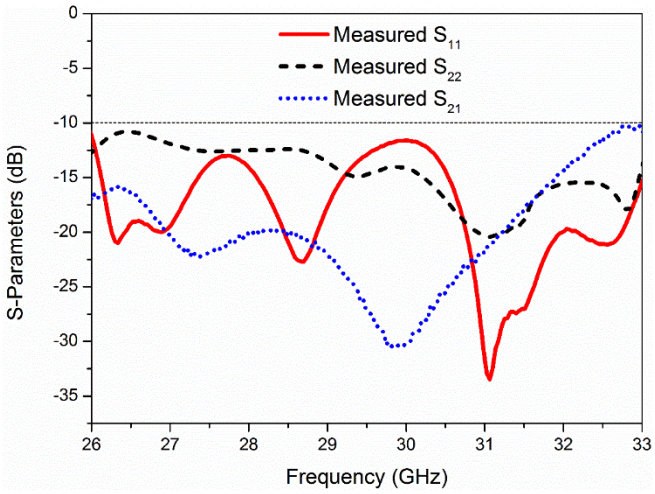

Figure 6.10 Measured S-parameters of the dual CP array scanning to ±23º.

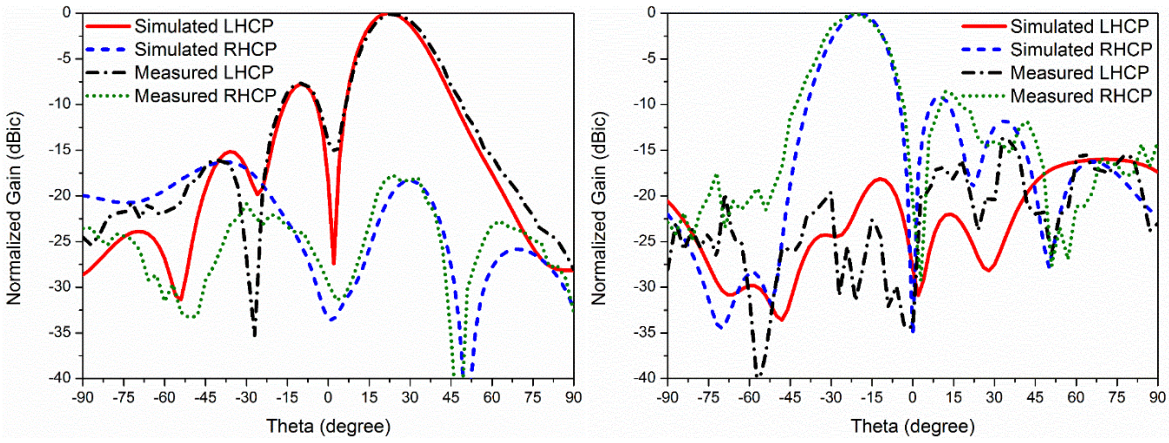

(a) (b)

Figure 6.11 Radiation patterns of the dual CP array in YOZ plane at 29 GHz: (a) LHCP excited, scanning to 23º, (b) RHCP excited, scanning to -23º.

Figure 6.11 shows the simulated and measured radiation patterns of the dual CP array scanning to ±23º at 29 GHz. As shown, the array can scan its beam to +23º and -23º independently with orthogonal polarization. When the LHCP port is excited, the beam is scanned to 23º with good LHCP radiation. Likewise, the beam is scanned to -23º with good RHCP radiation when the RHCP port is excited.

Figure 6.12 shows the simulated and measured AR of the proposed array. The AR bandwidth of the array is calculated at θ=23° for LHCP beam and θ=-23° for RHCP beam. As shown, the measured AR bandwidth of the proposed array is 26.4-30.4 GHz and 26.2-29.7 GHz for LHCP beam and RHCP beam, respectively. The differences between the simulated and measured results are caused by fabrication and measurement errors.

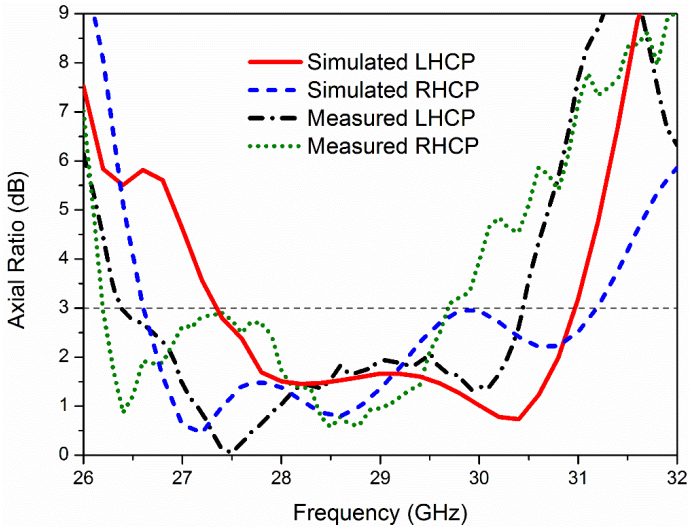

Figure 6.12.Simulated and measured AR of the dual CP array scanning to ±23°.

6.3.2 Dual CP Array Scanning to Broadside Direction

Another linear dual CP array with LHCP and RHCP beam both scanned to 0° is designed in this sub-section to evaluate the performance of the array scanning to broadside direction. The configuration and the fabricated prototype of the dual CP array scanning to broadside direction is shown in Figure 6.13. Different to the array shown in Figure 6.8, each element is fed in phase for both RHCP and LHCP radiation, which makes the array scan to broadside direction.

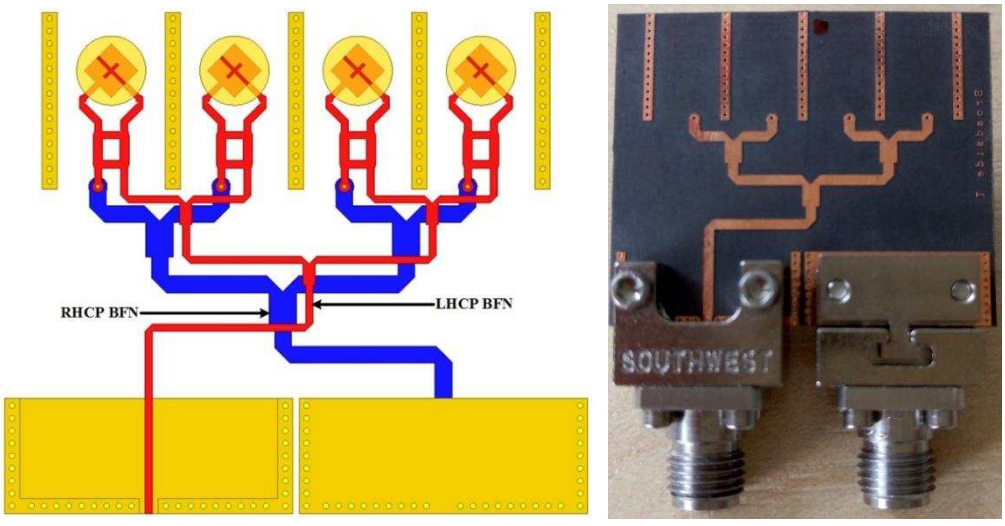

Figure 6.13. Configuration and prototype of the dual CP array scanning to broadside direction

Figure 6.14 shows the measured S-parameters of the dual CP array scanning to broadside direction. As shown, the measured impedance bandwidth is from 26.2 GHz to 33 GHz and from 27.2 GHz to 33 GHz under LHCP and RHCP status, respectively. The isolation between the RCHP and LHCP ports is higher than 10 dB from 26 GHz to 32.5 GHz and higher than 15 dB from 26.5 GHz to 31.3 GHz.

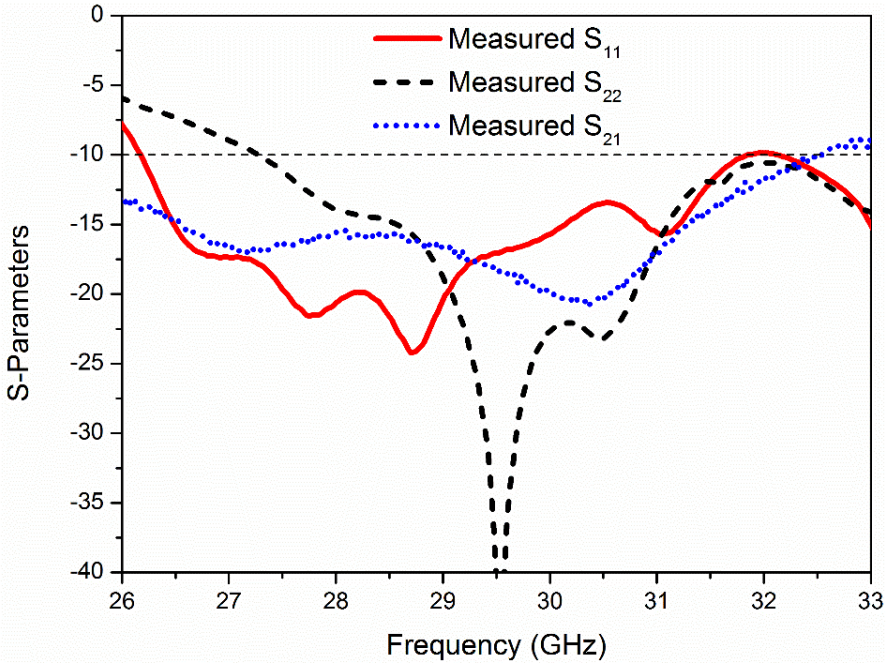

Figure 6.14 Measured S-parameters of the dual CP array scanning to broadside.

The simulated and measured radiation patterns of the dual CP array scanning to 0° are shown in Figure 6.15. As shown, good agreements between the simulated and measured results are obtained. The main beam of the array can scan to 0° with good CP radiation under both LHCP and RHCP excitation.

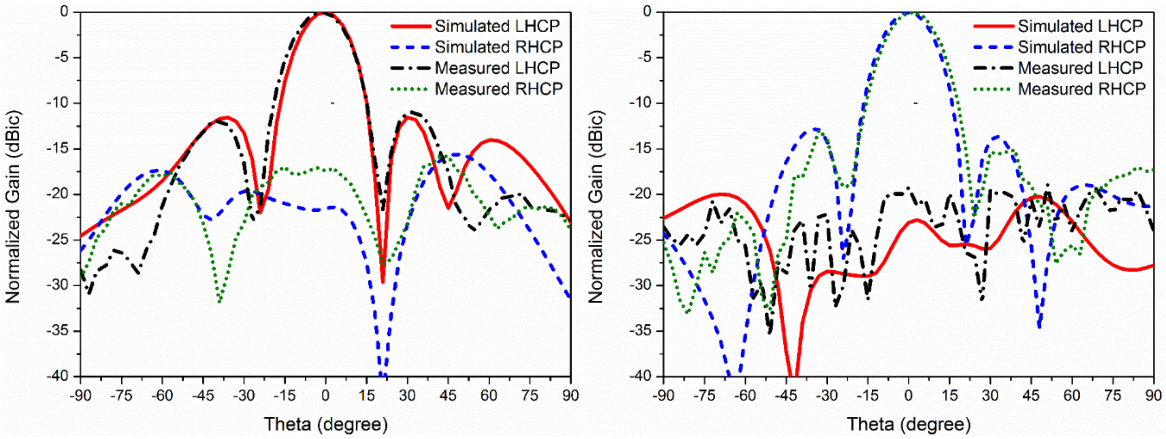

(a) (b)

Figure 6.15 Radiation patterns of the dual CP array in YOZ plane at 29 GHz: (a) LHCP excited, scanning to 0°, (b) RHCP excited, scanning to 0°.

Figure 6.16 shows the simulated and measured AR bandwidth when the array scan to broadside direction under both LHCP and RHCP radiation. As shown, when the array is fed by LHCP port, the measured AR bandwidth is from 26 GHz to 31.2 GHz while the measured AR bandwidth is from 26.5 GHz to 31 GHz when the RHCP port is excited.

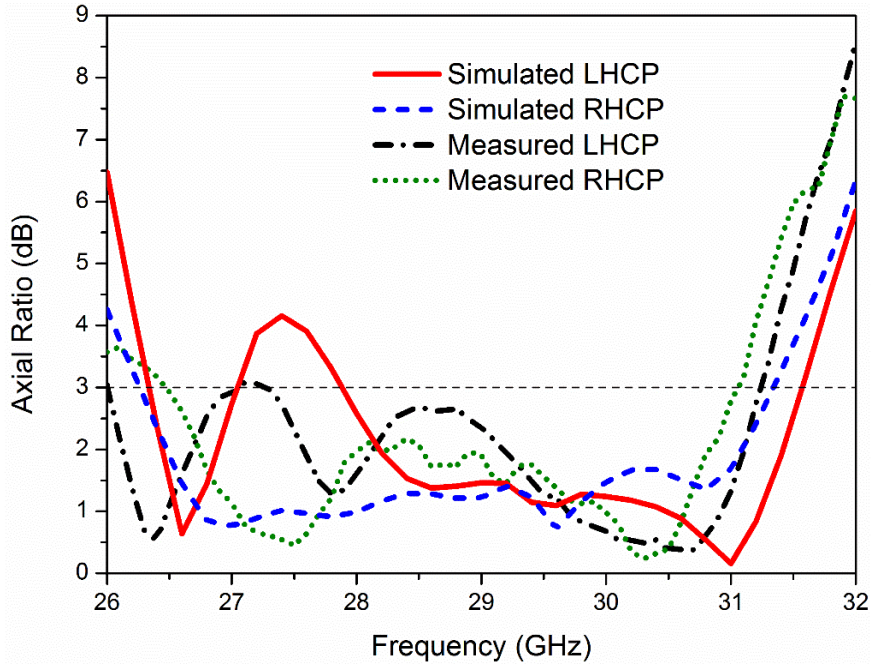

Figure 6.16.Simulated and measured AR of the dual CP array scanning to 0º.

6.4 Summary

A wideband multi-layer CP patch element operating at Ka-band is presented in this Chapter. Based on this wideband CP element, a wideband dual CP beam-scanning array with two independent orthogonally polarized beams is developed. The proposed array can scan the two independent beams to ±23º while maintaining high isolation between the two orthogonally polarized beams. The measured results verify that the array achieves simultaneously good impedance matching, good CP radiation and higher than 20 dB isolation from 27 GHz to 30 GHz. The presented design concept can be easily applied to the design of larger size linear array. It can also be extended to the design of planar arrays for the Gansat project by using the striplines to design the BFNs. Because of these advantages, the array is suitable for Ka-band satellite communications.

Chapter 7. Single-Layer Wideband High-Efficiency Circularly Polarized Reflectarray

7.1 Introduction

In chapter 6, a wideband dual-CP array is proposed for Ka-band satellite communications. As indicated by the dual-CP array structure, complicated feeding BFNs are needed to form planar phase front. For large-size arrays, such as a 30×30 elements array, the feeding network will be too complex to design and the insertion loss of such a complex feeding network shall be very high which decreases the total gain and aperture efficiency. To alleviate this issue, reflectarrays can be employed, which use the spatial feeding technique to feed an array aperture. Generally, reflectarrays consist of radiating elements with preadjusted phases and an illuminating feed antenna to form a planar phase front in the farfield [20]. Although they have many advantages, such as the significantly simplified feeding network, versatile beams, flat structure and low manufacturing cost, one major drawback of reflectarrays is their narrow bandwidth.

The narrow bandwidth of reflectarrays is mainly caused by two factors: the inherent narrow bandwidth of microstrip elements and the differential spatial phase delay caused by different path lengths from the feed to each element [124]. To improve the bandwidth of reflectarrays, several approaches were adopted, such as using stacked patches [125] subwavelength element [126], dual-frequency phase synthesis [127] and true time delay technique [128].

Designing circularly polarized (CP) reflectarray is necessary for some applications since the CP arrays possess the advantages of mitigation of multi-path fading, immunity of "Faraday rotation" and the reduction of polarization mismatching [6]. Two different ways have been introduced to design a CP reflectarray. The first one is using a linearly polarized (LP) feed to illuminate an aperture which is able to transform the incident LP wave to CP reflected wave and form a cophasal beam in the far-field [122, 129]. Another method to design a CP reflectarray is utilizing a CP feed as a primary source and the reflecting surface can reflect the incident CP wave directly and yields a planar phase front in the far-field. Various designs based on this approach were proposed, including using angular rotation elements [130, 131], variable sized elements [132] and elements with variable-length phase delay lines [133].

Considering that it is more difficult to design elements with wideband CP reflection performance and wideband CP feeds, the bandwidth enhancement of CP reflectarrays is

more challenging than LP reflectarrays. Different approaches were utilized to improve the bandwidth of CP reflectarrays [80-82, 84, 122]. By using rectangular-patch phasing element with subwavelength grid spacing, a 17% 1 dB gain bandwidth and 11% 3 dB axial ratio (AR) bandwidth was obtained [84]. The bandwidth of CP reflectarray was further improved by using a dual-layer T-shaped phasing element, with a 1 dB gain bandwidth of 20% and 3 dB AR bandwidth of 28% [80]. Since the elements used in [80, 84] are resonant type, the CP reflectarray using these resonant phasing elements demonstrates a typically smaller than 30% bandwidth. Multi-resonance phasing elements such as the Jerusalem cross and open loop combined subwavelength element [122] and the dual-ring element [81] based CP reflectarrays achieved more than 30% 3 dB AR bandwidth. Another way of realizing wide bandwidth of CP reflectarrays is using spatial time-delay units (TDUs) [82]. Although the CP reflectarray using TDUs achieved 40% 3 dB gain bandwidthand 3 dB AR bandwidth, the aperture efficiency was 40% only and the multi-layer structure increased the fabrication complexity.

In this Chapter, a novel S-shaped phasing element which achieves smaller than -15dB cross polarization (cross-pol) reflection in a 2:1 bandwidth is proposed. Based on this novel broadband element, a single-layer CP reflectarray using angular rotating elements is designed, fabricated and measured. The measured results indicate that the proposed single-layer reflectarray achieves a 68% 3 dB AR bandwidth and a 48% 3 dB gain bandwidth. The proposed reflectarray maintains undistorted pencil-shaped beams, at least -15dB side lobe and -15dB cross-pol component from 7 GHz to 14 GHz. Moreover, the aperture efficiency (AE) is larger than 50% in a 33% bandwidth and larger than 30% in a 64% bandwidth. To the best knowledge of the authors, it is the widest-bandwidth single-layer CP reflectarray developed up to now in terms of 3 dB AR, radiation pattern and larger than the 50% AE bandwidth.

This Chapter is organized as follows: Section 7.2 introduces the design of the novel S-shaped element; Section 7.3 presents the design and analysis of the proposed CP reflectarray; Section 7.4 presents the simulation and measurement results and comparisons with other reported wideband CP reflectarrays. The conclusion is given in Section 7.5

7.2 S-Shaped Reflectarray Element

Various antenna elements have been designed and deployed in CP reflectarrays, such as the patches, stacked patches, crossed dipoles and their derivatives, split rings and the combination of several types of these elements. All these reported elements demonstrate

bandwidths less than 50%. In this section, a novel S-shaped element is presented and analyzed, which can achieve a bandwidth over 66%.

7.2.1 Unit Cell Geometry

The geometry of the proposed S-shaped element is shown in Figure 7.1.

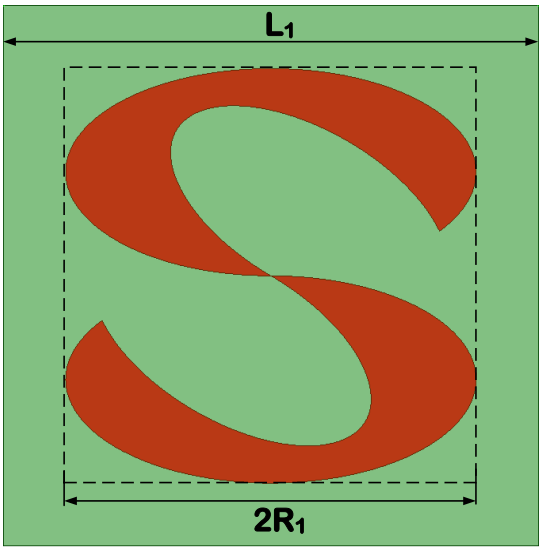

(a)

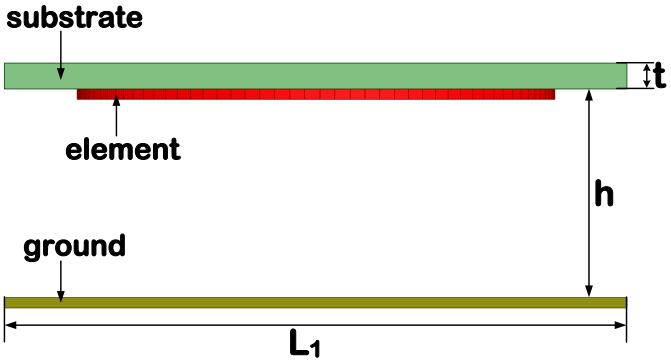

(b)

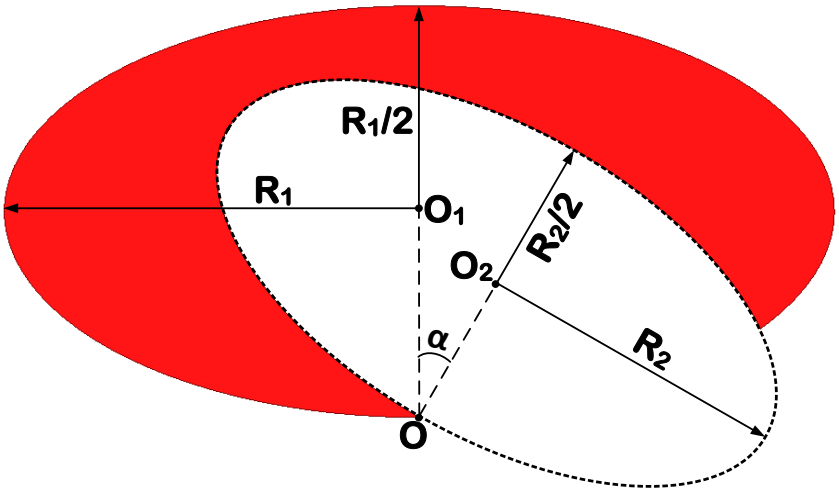

(c)

Figure 7.1 Geometry of the proposed element: (a) top view, (b) side view, (c) single arm [111, 112].

As shown in Figure 7.1 (a) and (b), the proposed element is printed on the bottom layer of a Rogers RO4003C substrate with relative dielectric constant of 3.55, loss tangent of 0.0027 and a thickness of t. A ground plane is placed below the substrate with a height of h. The size of the ground plane and the unit cell are $L_1 \times L_1$. The S-shaped element is composed of two single arms with the same size shown in Figure 7.1 (c). It can be seen from Figure 7.1 (c) that each arm is obtained by subtracting a smaller sized ellipse with a rotating angle α from a larger sized ellipse. To form a square-sized S-shaped element, the major radius of the bigger ellipse R_1 is two times as large as the minor radius.

The proposed element is a follow-on work of the antenna presented in Chapter 5, where an inverted S-shaped antenna with wideband CP radiation was presented. However, there are significant differences between the proposed element and the antenna in Chapter 5. The element proposed in this Chapter is used for reflectarray application and its reflection performance under periodical boundary environment is of major interest. The proposed phasing element has a more compact size ($0.32\lambda \times 0.32\lambda$) than the antenna presented in Chapter 5 ($0.99\lambda \times 0.42\lambda$). The size reduction is realized by choosing larger rotating angle α and larger R_1/R_2 ratio, which gives longer travelling-wave current path and the utilization of sub-wavelength technique. Although the size of the presented element is greatly reduced, the CP bandwidth is improved by 59% (from 42% in Chapter 5 to 67%). Furthermore, the proposed element can be placed in a square lattice while the antenna in Chapter 5 is only able to be placed in a rectangular lattice. The square-sized element is more advantageous to planar arrays because the rectangular-sized antenna has different electrical length along x-axis and y-axis direction, which results in uneven characteristics such as different beamwidth and AR beamwidth in the two orthogonal directions. On the contrary, the proposed element can provide relatively symmetry performance along x-axis and y-axis direction, which brings more equal mutual coupling between each elements in the two directions and thus facilitates the design and improves the performance of the reflectarray.

The detailed geometry dimensions of the proposed element are shown in Table 7.1.

Table 7.1 S-shaped Element Parameters

L_1	R_1	R_2	α	h	t
12mm	4.6mm	3.45mm	30^o	4mm	0.508mm

7.2.2 Reflection Performance

As the electrical length of the proposed element is mainly determined by geometry parameters R_1, R_2 and rotating angle α, the impact of these parameters to the element's performance needs to be investigated. For a brief investigation, the ratio R_2/R_1=0.75 and the rotating angle α is kept unchanged while only R_1 is varied.

The evaluation of the element performance is conducted by using a periodic boundary and a Floquet port excitation in HFSS. The incident field is set to be right-hand circularly polarized (RHCP). Figure 7.2 shows the magnitudes of reflected RHCP field (co-pol component) and left-hand circularly polarized (LHCP) field (cross-pol component) with different R_1. As shown, the available bandwidth ($|\Gamma_{cross-pol}| \leq$ -15 dB) of the element increases with larger R_1. As the ratio R_2/R_1 is kept unchanged, this phenomenon can be explained that increasing R_1 brings longer electrical length and pushes the lowest-frequency resonance to lower frequency while has little influence on higher-frequency resonance.

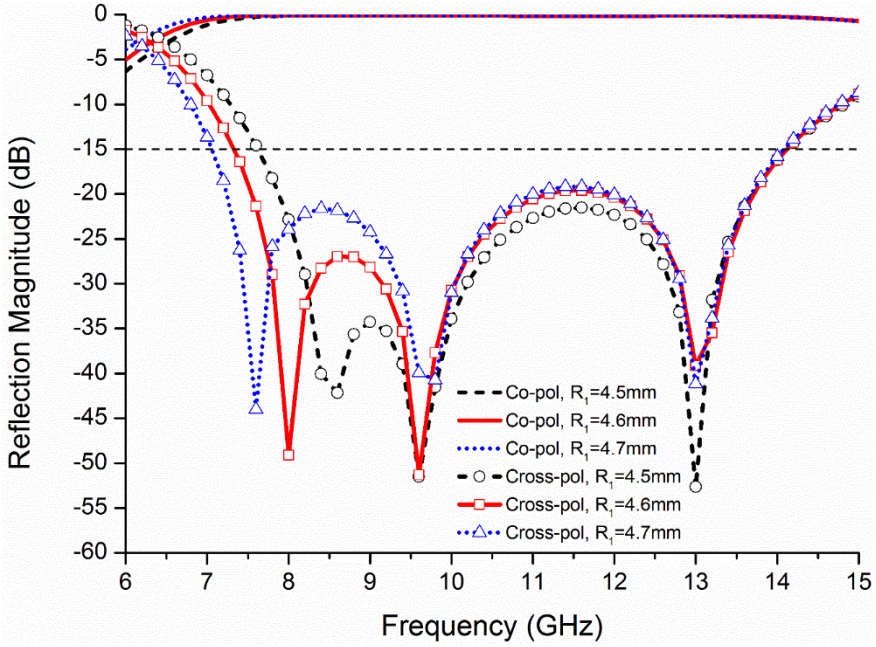

Figure 7.2 The magnitude of the reflected field with different R_1.

As shown in Figure 7.2, the element can provide a 2:1 bandwidth (7 GHz to 14 GHz) within which the reflected LHCP component is smaller than -15 dB ($|\Gamma_{cross-pol}| \leq$ -15 dB) when R_1 is 4.7mm. Notice that $|\Gamma_{cross-pol}|^2 + |\Gamma_{co-pol}|^2 \cong 1$ (the approximation rises from dielectric and conductor losses), thus $|\Gamma_{cross-pol}| \leq$ -15 dB makes $|\Gamma_{co-pol}| \geq$ -0.2 dB which indicates that the element has low-level cross-pol field reflection while keep the co-pol component nearly non-degraded. To acquire lower cross-pol component reflection and

adequate bandwidth simultaneously, R_1 is chosen to be 4.6 mm. In this case, the available bandwidth is from 7.3 GHz to 14.1 GHz and $|\Gamma_{cross-pol}| \leq$ -20 dB, $|\Gamma_{co-pol}| \geq$ -0.1 dB from 7.5 GHz to 13.7 GHz.

The element rotating method is used to provide the desired phases for each element. It is indicated that the angular rotation angle ψ of a CP element results in a 2ψ phase variation of the reflected co-pol field [130, 134]. Figure 7.3 shows the phase difference of the reflected co-pol field under different element rotation angle. As shown, the element achieves a rather linear phase response to the element rotation angle ψ in a 2:1 frequency range. The phase error (actual phase difference compared with 2ψ) is smaller than 10° within the bandwidth.

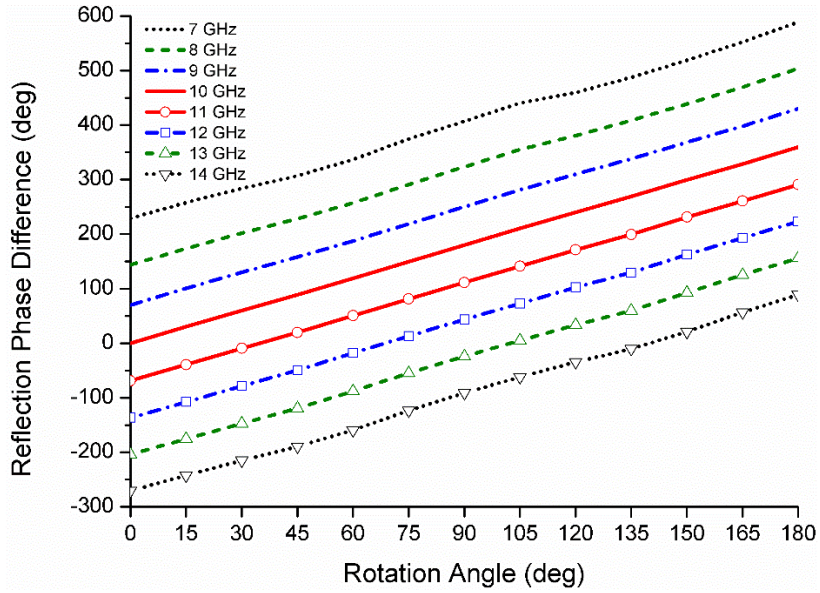

Figure 7.3 The phase difference of the reflected co-pol field with different element rotation angle.

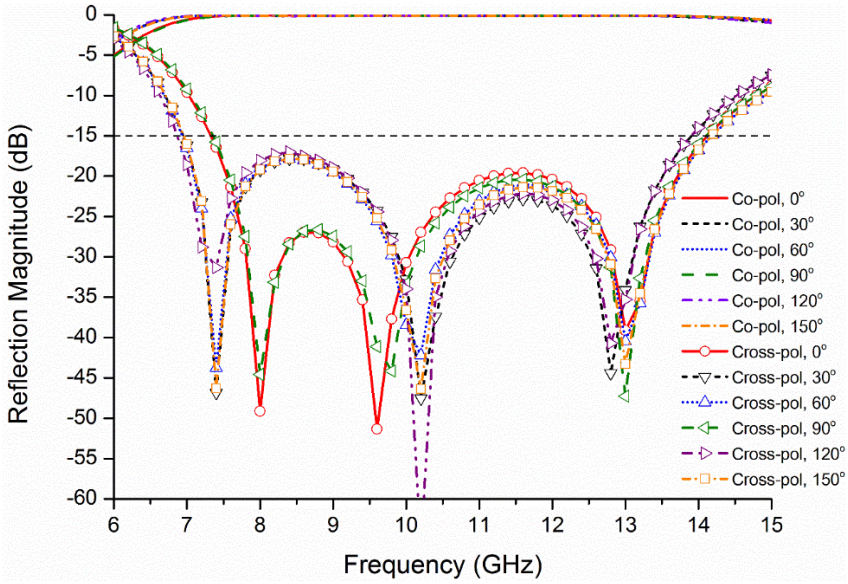

Figure 7.4 The magnitude of the reflected field with different element rotation angle.

The reflection magnitudes of the co-pol and cross-pol components with different rotation angle ψ are shown in Figure 7.4. As shown, the proposed element maintains low cross-pol and good co-pol reflection in a nearly 2:1 frequency range under all rotation angles. It is worthy pointing out that the proposed element exhibits the same reflection magnitude performance with the reflected LHCP field as co-pol component when the incident field changes to LHCP. In this case, the reflected phase variation of the co-pol field introduced by the element rotation angle ψ is -2ψ, which is different to the case that the incident wave is RHCP.

To give an understanding of the element reflection performance under oblique incidence, Figure 7.5 gives the reflection phase of the co-pol field under different oblique incidence angle theta. As shown, the phase discrepancy of about 7^o and 28^o are observed for theta=15^o and theta=30^o incidence at the design frequency 9GHz, respectively. It is also noticed that a ripple occurs at the frequency around 8GHz, which is assumed to be the main reason of the variation of simulated AR and gain at 8GHz shown in Figure 7.8 and Figure 7.9, respectively. Besides, it is observed from simulation that the phase error is smaller than 10^o at 9GHz under 30^o oblique incidence when the element is rotated, which yields not so much differences compared with the case under normal incidence. Considering that only the edge elements are illuminated at large incidence angle, thus the proposed reflectarray is designed based on the reflection phase under normal incident plane waves.

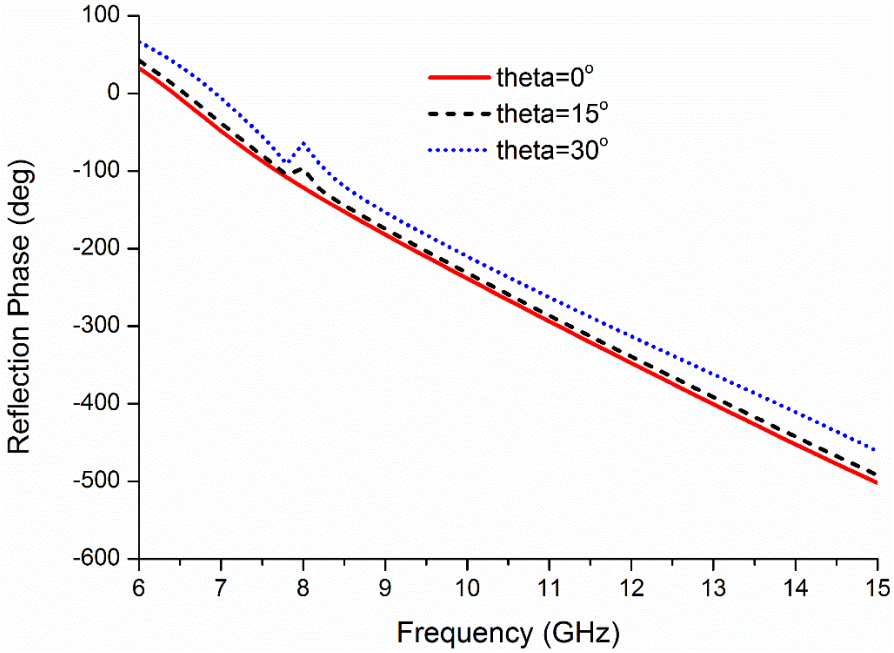

Figure 7.5 Reflection phase of the co-pol field with different oblique incidence angles.

7.3 Reflectarray Design and Analysis

In this section, the array configuration and the element phase distribution over the aperture are given at first. Then, the performance of the proposed reflectarray is analyzed theoretically and the conclusions are verified by using different feed horns. Finally, the effect of the differential spatial phase delay on the bandwidth of the proposed reflectarray is analyzed.

7.3.1 Array Geometry and Phase Distribution

The configuration of the proposed reflectarray is shown in Figure 7.6.

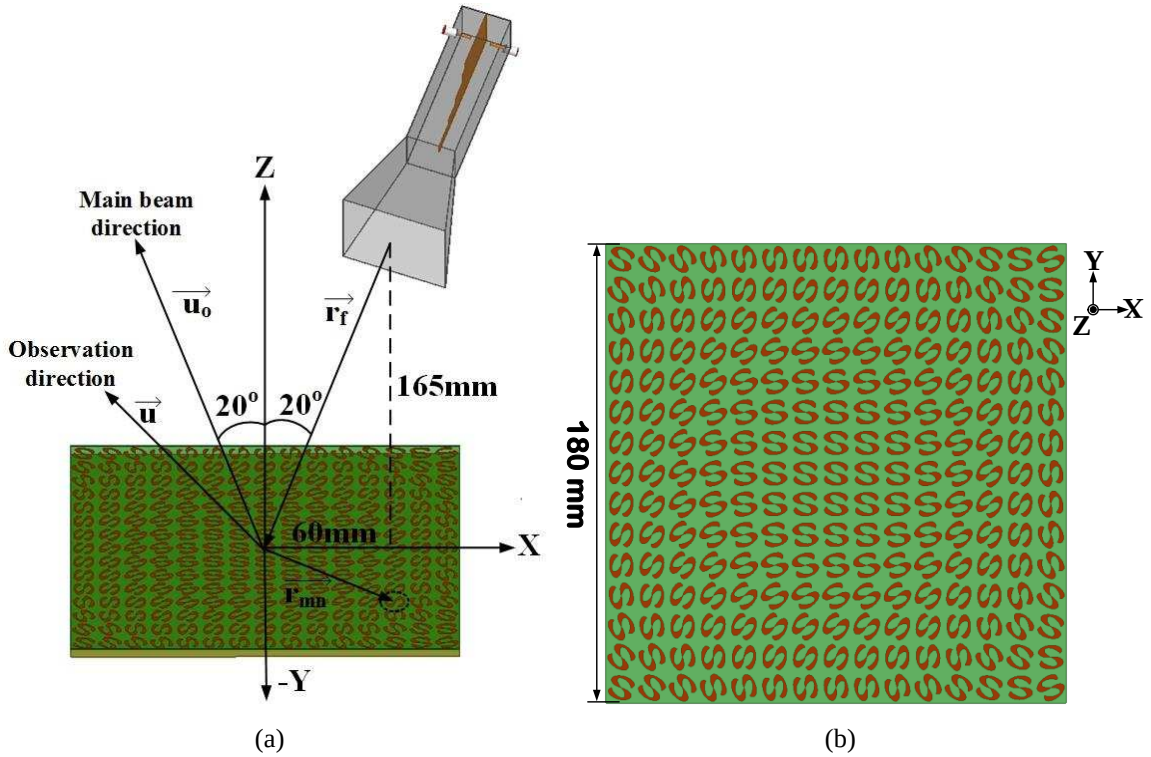

(a) (b)

Figure 7.6 Geometry of the proposed reflectarray: (a) side view, (b) top view of reflecting aperture.

As shown, the reflectarray consists of 225 (15×15) S-shaped elements, each with different rotation angle to provide required phase delay. The reflectarray is designed to be fed by a wideband dual-CP horn with an offset of 20° to the Z-axis. The offset configuration is mainly to minimize the blockage of the feed. It is indicated in [135] that an offset feed causes main beam scan with frequency due to a change in phase taper across the reflectarray with a change in frequency. This beam squint phenomenon can be minimized if the angle of the main beam is chosen to be close to the natural specular reflection angle. To eliminate the beam squint, the main beam direction is designed to $\theta = -20^o$.

The required phase distribution of each S-shaped element can be calculated by the following equation

$$\Phi(x_i, y_i) = -k_0 \sin\theta_b (x_i \cos\varphi_b + y_i \sin\varphi_b) + R_i k_0 \quad (7.1)$$

where $\Phi(x_i, y_i)$ is the required phase delay for the element (x_i, y_i), $(\theta_b, \varphi_b)$is the beam direction of the reflectarray and R_i is the distance from the phase center of the feed to the element. By using this formula, we can calculate the phase distribution over the reflecting surface for each element, which is shown in Figure 7.7. As the element rotation angle ψ results in a 2ψ phase variation of the reflected co-pol field, the phase distribution in Figure 7.7 can directly map into Figure 7.6 (b).

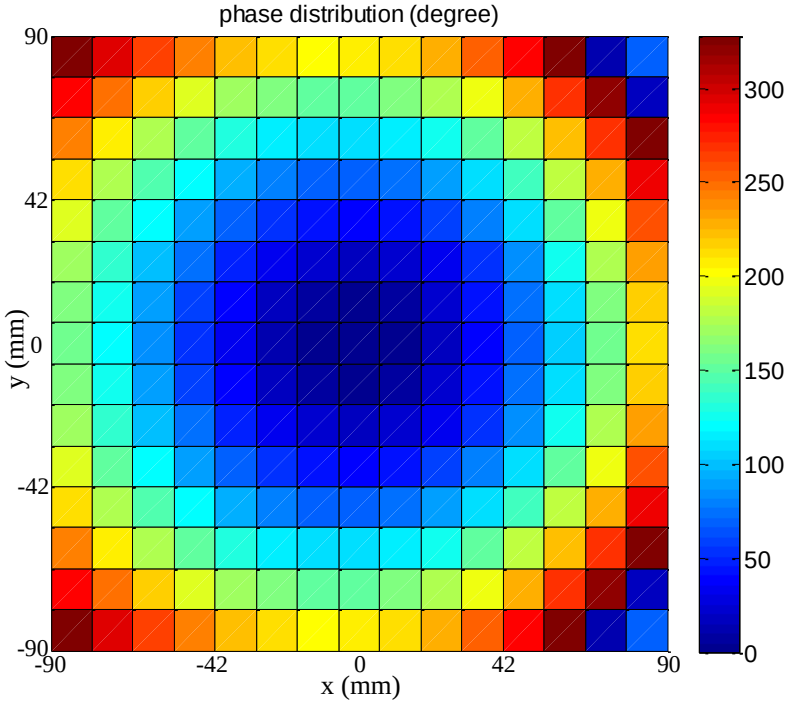

Figure 7.7 Required phase distribution for each element.

7.3.2 Analysis of Rotated Elements

It is implicit that the cross-pol of a reflectarray using element rotating method is degraded in the main beam region and thus the AR performance can be enhanced [130]. However, this phenomenon is not discussed in detail. Besides, the reflectarray proposed in [130] is a narrow-band array, it is important to investigate whether this phenomenon still exists in a wideband reflectarray.

When a two-dimensional planar array with 15×15 elements is non-uniformly illuminated by a horn at r_f, as shown in Figure 7.6 (a), the reradiated field from the array in an arbitrary direction $\vec{u}$ can be represented by

$$E(\vec{u}) = \sum_{m=1}^{15}\sum_{n=1}^{15} F(\overrightarrow{r_{mn}} \cdot \overrightarrow{r_f})\, A(\overrightarrow{r_{mn}} \cdot \overrightarrow{u_0}) A(\vec{u} \cdot \overrightarrow{u_0}) e^{-jk_0(|\overrightarrow{r_{mn}} - \overrightarrow{r_f}| + \overrightarrow{r_{mn}} \cdot \vec{u})} e^{j\phi_{mn}} \quad (7.2)$$

where F is the pattern function of the feed horn, A is the pattern function of the S-shaped element, $\overrightarrow{r_{mn}}$ is the position vector of the mnth element, $\overrightarrow{u_0}$ is the desired main beam direction and ϕ_{mn} is the required phase delay of the mnth element [130, 136]

Considering an incident wave radiated by the feed horn propagating in the $-Z$ direction, as shown in Figure 7.6 (a)

$$\vec{E}^{inc} = F_{RH}\left(\overrightarrow{E_x} - j\overrightarrow{E_y}\right)e^{jk_0z}e^{j\omega t} + F_{LH}\left(\overrightarrow{E_x} + j\overrightarrow{E_y}\right)e^{jk_0z}e^{j\omega t} \tag{7.3}$$

The former part represents the RHCP component of the radiated field from the horn with a magnitude of F_{RH}, the second part is the LHCP component with a magnitude of F_{LH}.

Denoting the physical counter-clockwise rotation angle of the mnth element by ψ_{mn}, the reflected RHCP field by the mnth S-shaped element can be written in the form

$$\begin{aligned}\vec{E}_{RHCP}^{refl} = &\left|\Gamma_{co-pol}\right| \cdot F_{RH}\left(\overrightarrow{E_x} + j\overrightarrow{E_y}\right)e^{-jk_0z}e^{j\omega t} \cdot e^{-2j\psi_{mn}} \\ &+\left|\Gamma_{cross-pol}\right| \cdot F_{LH}\left(\overrightarrow{E_x} + j\overrightarrow{E_y}\right)e^{-jk_0z}e^{j\omega t}\end{aligned} \tag{7.4}$$

The first part represents the reflected RHCP field from the incident RHCP component of the feed horn, and thus a counter-clockwise rotation angle ψ_{mn} of the element brings a $-2\psi_{mn}$ phase variation to the reflected co-pol field. The second part denotes the reflected RHCP field from the incident LHCP component of the feed horn, and no additional phase variation is introduced upon reflection [130].

Similarly, the reflected LHCP field by the mnth S-shaped element with rotation angle of ψ_{mn} can be represented by

$$\begin{aligned}\vec{E}_{LHCP}^{refl} = &\left|\Gamma_{co-pol}\right| \cdot F_{LH}\left(\overrightarrow{E_x} - j\overrightarrow{E_y}\right)e^{-jk_0z}e^{j\omega t} \cdot e^{2j\psi_{mn}} \\ &+\left|\Gamma_{cross-pol}\right| \cdot F_{RH}\left(\overrightarrow{E_x} - j\overrightarrow{E_y}\right)e^{-jk_0z}e^{j\omega t}\end{aligned} \tag{7.5}$$

It is worth pointing out that $\left|\Gamma_{cross-pol}\right|$ used in (7.4) and (7.5) is of the same value due to reciprocity and thus is denoted by the same expression. Considering that for a RHCP incident wave, the reflected co-pol component is the RHCP field while for a LHCP incident wave, the reflected co-pol component is LHCP field, the magnitudes of the reflection coefficient $\left|\Gamma_{co-pol}\right|$ are the same in these two cases for the proposed element. However, the phases of the reflection coefficient $\angle\Gamma_{co-pol}$ in these two cases differ in sign, i.e. $\angle\Gamma_{co-pol} = -2\psi_{mn}$ for a RHCP incident wave while $\angle\Gamma_{co-pol} = 2\psi_{mn}$ for a LHCP incident wave when the element is counter-clockwise rotated by an angle of ψ_{mn}.

From equation (7.2), the condition for the aperture distribution to be cophasal in the desired direction $\overrightarrow{u_0}$ is

$$\phi_{mn} - k_0\left(\left|\overrightarrow{r_{mn}} - \overrightarrow{r_f}\right| + \overrightarrow{r_{mn}} \cdot \overrightarrow{u_0}\right) = 2k\pi, k = 0,1,2\cdots \tag{7.6}$$

Here, the reflectarray is designed to radiate RHCP wave as its co-pol component. Thus, the co-pol component phase delay of the mnth element with a counter-clockwise rotation angle ψ_{mn} under RHCP incident wave satisfies

$$-2\psi_{mn} - k_0\left(\left|\overrightarrow{r_{mn}} - \overrightarrow{r_f}\right| + \overrightarrow{r_{mn}} \cdot \overrightarrow{u_0}\right) = 2k\pi, k = 0,1,2\cdots \tag{7.7}$$

Subsisting (7.4) and (7.7) into (7.2), the reradiated RHCP field in the desired direction $\overrightarrow{u_0}$ can be represented by

$$\begin{aligned} E_{RHCP}(\overrightarrow{u_0}) = \sum_{m=1}^{15}\sum_{n=1}^{15} A(\overrightarrow{r_{mn}} \cdot \overrightarrow{u_0})\{\left|\Gamma_{co-pol}\right| \cdot F_{RHCP}\left(\overrightarrow{r_{mn}} \cdot \overrightarrow{r_f}\right) \\ \cdot e^{j2k\pi} + \left|\Gamma_{cross-pol}\right| \cdot F_{LHCP}\left(\overrightarrow{r_{mn}} \cdot \overrightarrow{r_f}\right) \cdot e^{j2k\pi} e^{j2\psi_{mn}}\} \end{aligned} \tag{7.8}$$

where F_{RHCP} and F_{LHCP} denote the pattern function of the feed horn in RHCP and LHCP, respectively. As aforementioned, the co-pol component phase delay of the mnth element under LHCP incident wave is $2\psi_{mn}$. Therefore, the re-radiated LHCP field in the desired direction $\overrightarrow{u_0}$ can be written as

$$\begin{aligned} E_{RHCP}(\overrightarrow{u_0}) = \sum_{m=1}^{15}\sum_{n=1}^{15} A(\overrightarrow{r_{mn}} \cdot \overrightarrow{u_0})\{\left|\Gamma_{co-pol}\right| \cdot F_{LHCP}\left(\overrightarrow{r_{mn}} \cdot \overrightarrow{r_f}\right) \\ \cdot e^{j2k\pi} e^{j4\psi_{mn}} + \left|\Gamma_{cross-pol}\right| F_{RHCP}\left(\overrightarrow{r_{mn}} \cdot \overrightarrow{r_f}\right) e^{j2k\pi} e^{j2\psi_{mn}}\} \end{aligned} \tag{7.9}$$

For most of the elements, $\psi_{mn} \neq n\pi$, and it is evident that

$$\begin{aligned} \left|\sum_{m=1}^{15}\sum_{n=1}^{15} e^{j2\psi_{mn}}\, e^{j2k\pi}\right| < \left|\sum_{m=1}^{15}\sum_{n=1}^{15} e^{j2k\pi}\right| \\ \left|\sum_{m=1}^{15}\sum_{n=1}^{15} e^{j4\psi_{mn}}\, e^{j2k\pi}\right| < \left|\sum_{m=1}^{15}\sum_{n=1}^{15} e^{j2k\pi}\right| \end{aligned} \tag{7.10}$$

Since $\left|F_{RHCP}\left(\overrightarrow{r_{mn}} \cdot \overrightarrow{r_f}\right)\right| > \left|F_{LHCP}\left(\overrightarrow{r_{mn}} \cdot \overrightarrow{r_f}\right)\right|$ in the main beam region when the feed horn is RHCP and $\left|\Gamma_{co-pol}\right| > \left|\Gamma_{cross-pol}\right|$ across the element's bandwidth, it can be concluded from (7.8) - (7.10) that

1) To design an element rotated RHCP reflectarray with good performance in terms of antenna gain, the CP purity of the feed should be high. Otherwise, the incident LHCP field from the feed horn vanishes according to (7.8) and (7.9), which wastes the incident LHCP power and results in a low gain and poor AE. Moreover, the reflected cross-pol component of the element should be low enough to keep the reflection of the incident RHCP field superposed in-phase. If $\left|\Gamma_{cross-pol}\right|$ is large, one part of the reflected field $\left|\Gamma_{cross-pol}\right|F_{RHCP}\left(\overrightarrow{r_{mn}}\cdot\vec{r_f}\right)e^{j2k\pi}e^{j2\psi_{mn}}$ which does not superpose in-phase in the far-field, consumes the incident RHCP power substantially and also results in a decreased gain. It is necessary to keep a low cross-pol reflection for a phasing element across a wide bandwidth if a wideband reflectarray with good gain performance is desired.

2) It is possible to get an enhanced AR from the reflectarray even with a feed which has a large AR. Particularly considering a linearly polarized (LP) feed, the incident RHCP and LHCP power upon the aperture is the same. From (7.8), the reflected RHCP field can be greatly improved if $\left|\Gamma_{co-pol}\right|$ is close to 1. Under the same condition, the reflected LHCP field is not superposed in-phase and thus is much smaller than the reflected RHCP field according to (7.9). Subsequently, the AR of the reflectarray is improved compared with the feed. However, the gain and AE of the reflectarray is reduced in this case since the incident LHCP power contributes little to the total gain as analyzed in conclusion (1).

To verify the above analysis, the proposed reflectarray is illuminated by two different feed horns, one is a wideband dual-CP horn with RHCP port excited and the other one is an ideal RHCP horn which has infinite CP bandwidth (AR<3 dB). Besides, the aperture sizes of these two horns are all kept 50 mm × 50 mm to give a similar gain and beamwidth at each frequency. When conducting the comparison, the two different feeds are placed at the same position to make the f/D unchanged. With these conditions, the spillover under these two cases is considered to be close to each other.

Figure 7.8 shows the simulated AR of the proposed reflectarray with different feed horns. As shown, the AR bandwidth (AR<3 dB) of the dual-CP horn is from 6.7 GHz to 11.5 GHz and the AR bandwidth of the reflectarray using the dual-CP horn is from 7.2 GHz to 14.7 GHz. From 6.7 GHz to 7.2 GHz, the AR is degraded from the horn to the array since the element reflection performance is rather bad in this frequency range ($\left|\Gamma_{cross-pol}\right|$ approaches to -5 dB at 6.7 GHz as shown in Figure 7.2). However, from 11.5 GHz to 14.7 GHz, the AR of the array gets improved although the dual-CP horn demonstrates poor CP purity in this frequency range. This mainly attributes to the function of the

array as indicated in the above conclusion (2) and the relative good element reflection performance ($|\Gamma_{cross-pol}|$=-10.6 dB, $|\Gamma_{co-pol}|$=-0.5 dB at 14.7 GHz). It is also shown in Figure 7.8 that better AR performance can be realized with feed of better CP purity (referring to the AR of the reflectarray with ideal horn and dual-CP horn, respectively, from 11.5 GHz to 15 GHz)

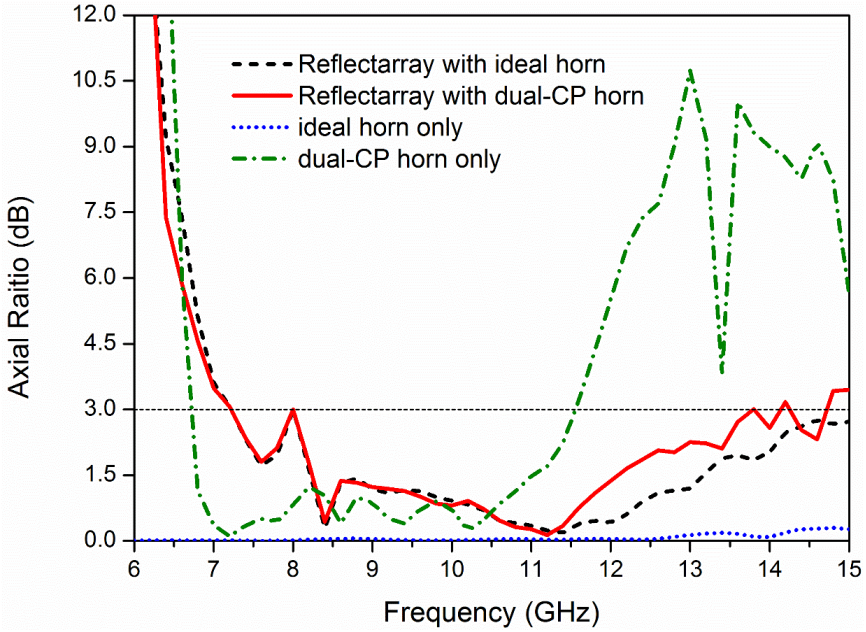

Figure 7.8 Simulated AR of the proposed reflectarray with different feed horns.

Figure 7.9 shows the simulated gain of the proposed reflectarray with different feed horns.

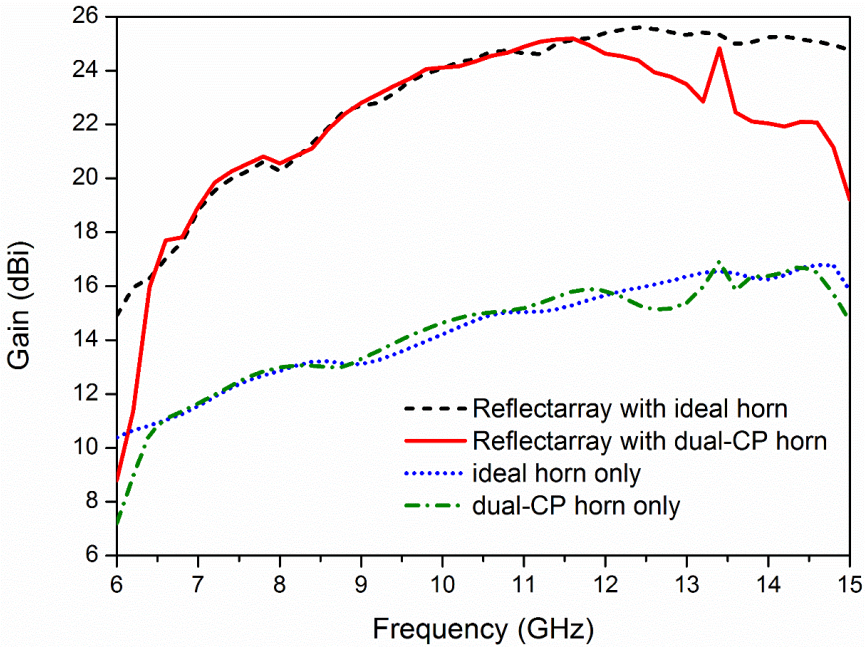

Figure 7.9 Simulated gain of the proposed reflectarray with different feed horns.

As shown, the gain of the reflectarray with dual-CP horn is smaller than the array with ideal horn from 11.5 GHz to 15 GHz. In this frequency range, the gain of the two horns is generally the same, especially from 13.5 GHz to 14.5 GHz. As analyzed in the aforementioned conclusion (1), the poor CP purity of the dual-CP horn in this frequency range results in the non-negligible LHCP incident field which contributes little to the gain of the array and yields a lower gain compared with the array using an ideal horn which has a much better CP purity in the same frequency range.

7.3.3 Effect of Differential Path Delay

As indicated in the last section, the proposed reflectarray achieves a 2:1 3 dB AR bandwidth. Due to this broad bandwidth, it is necessary to investigate the influence of the differential spatial phase delay to the gain bandwidth of the array, which increases as the working bandwidth increases. The bandwidth limitation of printed reflectarrays caused by the differential spatial phase delay is quantified for a broadside main beam and a prime focus feed in [137]. Here, equations are derived for more general cases, i.e. arbitrary feed position and arbitrary main beam direction to quantify the bandwidth limitation of reflectarrays due to the differential spatial phase delay.

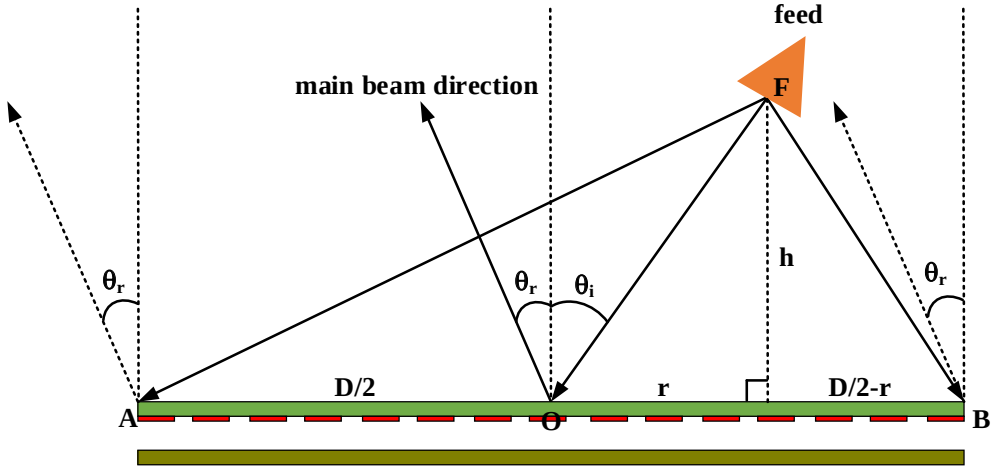

Figure 7.10 Geometry of the reflectarray with arbitrary feed position and arbitrary main beam direction.

Figure 7.10 shows the geometry of a reflectarray with arbitrary feed position and arbitrary main beam direction. As shown, the diameter of the reflectarray is denoted by D while the focal length $f = \sqrt{r^2 + h^2}$. The feed horn is placed at an arbitrary position with an incident angle θ_i to the aperture center O and the main beam direction is denoted by θ_r.

Denoting the spatial phase delay from the feed to the aperture center O by PD_{FO} and the spatial phase delay from the feed to the edge of the aperture by PD_{FA} and PD_{FB}. As the

main beam direction is θ_r, the additional spatial phase delay introduced by the offset beam between the aperture center and the edge of the aperture is $\frac{D}{2} \cdot \sin\theta_r$. Therefore, the phase delay required by the aperture edge element A and B with respect to the aperture center O can be represented by PD_{AO} and PD_{BO}, which satisfy

$$\begin{aligned} PD_{AO} &= PD_{FA} - PD_{FO} - D \cdot \sin\theta_r/2 \\ PD_{BO} &= PD_{FB} - PD_{FO} + D \cdot \sin\theta_r/2 \end{aligned} \tag{7.11}$$

Let k_0 and k_1 be the wavenumbers at the design frequency f_0 and operating frequency f_1, respectively. When the frequency shifts from the design frequency f_0 to the operating frequency f_1, phase errors will be introduced to each element. Denote the phase error at the edge element A and B, relative to the phase at the center element, by PE_{AO} and PE_{BO}, which are

$$\begin{aligned} PE_{AO} &= (k_1 - k_0)R_A \\ PE_{BO} &= (k_1 - k_0)R_B \end{aligned} \tag{7.12}$$

where $R_A = \left(\sqrt{(D/2+r)^2+h^2} - \sqrt{r^2+h^2} - D \cdot \sin\theta_r/2\right)$ and $R_B = \left(\sqrt{(D/2-r)^2+h^2} - \sqrt{r^2+h^2} + D \cdot \sin\theta_r/2\right)$, calculating from the geometry relationship shown in Figure 7.10. According to [137], a reasonable criterion for evaluating the effect of this phase error is to evaluate the frequency shift for which this error equals 180° at the edge of the aperture. The intervening elements will incur less phase error, but out-of-phase radiation from edge elements A and B will begin to detract from the overall gain of the aperture. Let PE_{AO} and PE_{BO} equal to 180° and solve the frequency shift, $\Delta f = f_1 - f_0$, we can get:

$$\begin{aligned} \frac{\Delta f}{f_0} &= \frac{\lambda_0}{2R_A}, for\ PE_{AO} = \pi \\ \frac{\Delta f}{f_0} &= \frac{\lambda_0}{2R_B}, for\ PE_{BO} = \pi \end{aligned} \tag{7.13}$$

Substituting geometry dimensions D, r, h and θ_r given in Figure 7.6 (a) to (7.13), the frequency bandwidth $2\,\Delta f/f_0$ is calculated to be 200% and 145.5% respectively for $PE_{AO} = \pi$ and $PE_{BO} = \pi$ (the design frequency f_0 is 9 GHz). This result indicates that the gain of the proposed reflectarray suffers very limited degradation due to the differential spatial phase delay within a 145.5% bandwidth. As this calculated bandwidth is much wider than the element bandwidth, the bandwidth of the proposed reflectarray is mainly determined by the element bandwidth.

Alternatively, if the bandwidth $2\Delta f/f_0$ is set to be 66%, then it can be calculated from 7.13 that the aperture diameter D equals to 344mm and 266mm respectively for $PE_{AO} = \pi$ and $PE_{BO} = \pi$. This indicates that the aperture diameter of the array can be enlarged to around 266mm within which the array gain will suffer limited degradation. If the array size exceeds this limit, the gain bandwidth of the proposed reflectarray will begin to decrease.

7.4 Results and Discussion

7.4.1 Prototype and Reflection Coefficient

The fabricated prototype of the proposed antenna and the measurement setup in the anechoic chamber are shown in Figure 7.11 . As shown, the reflectarray is fed by a wide-band dual-CP horn which uses a stepped-septum polarizer to simultaneously achieve TE_{10} and TE_{01} modes as well as a 90-degree phase shift between the two orthogonal electric field components [138].

The simulated and measured reflection coefficients of the proposed reflectarray are shown in Figure 7.12. As shown, the array achieves a smaller than -10dB reflection coefficient over a 2:1 frequency range. It is worthy pointing out that the S_{11} will degrade when a prime focus feed is utilized due to the blockage of the feed horn. To eliminate this phenomenon, an offset feed is chosen.

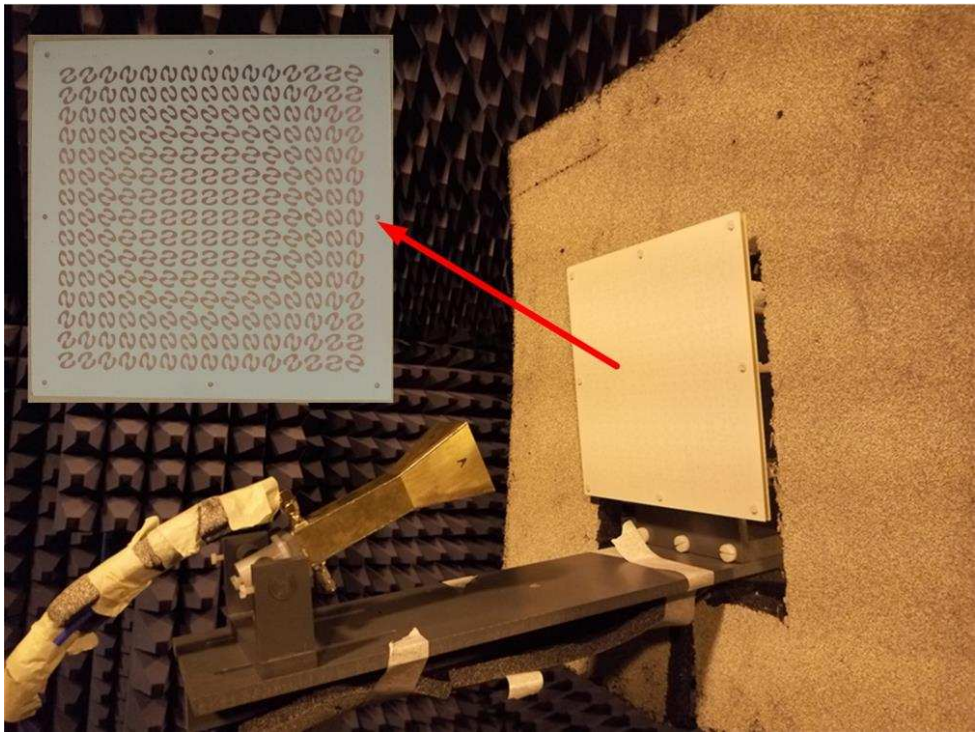

Figure 7.11 The fabricated prototype and measurement setup of the proposed reflectarray.

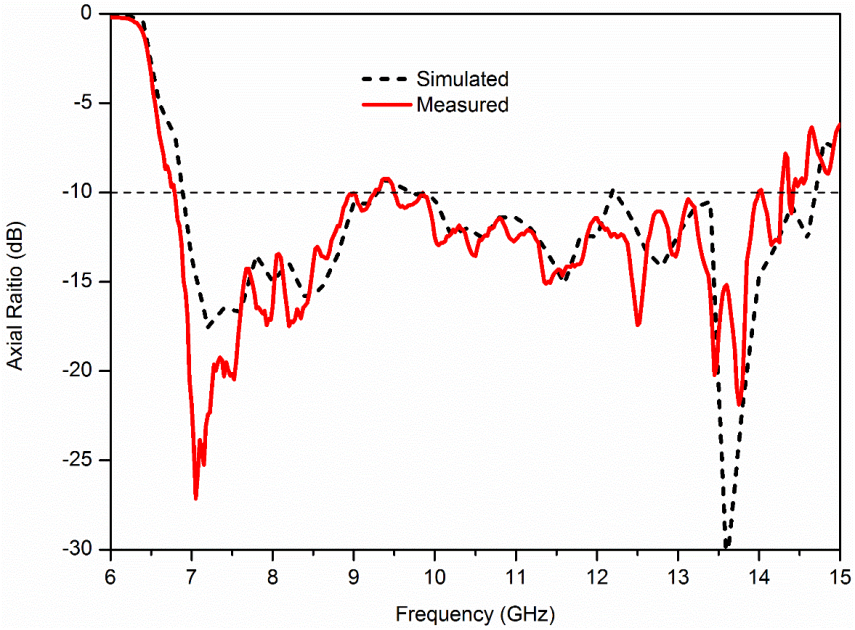

Figure 7.12 Simulated and measured reflection coefficients of the proposed reflectarray.

7.4.2 Axial Ratio Bandwidth

The simulated and measured AR of the proposed antenna is shown in Figure 7.13. As shown, the measured 3 dB AR bandwidth is from 7 GHz to 14.3 GHz, equaling to a fractional bandwidth of 68%.

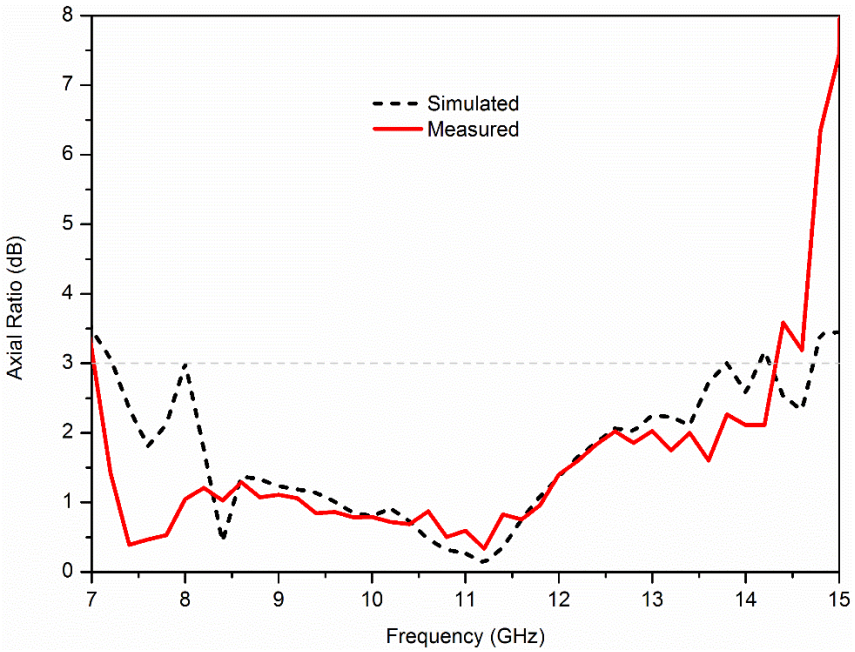

Figure 7.13 Simulated and measured AR of the proposed antenna.

7.4.3 Gain and Aperture Efficiency

Figure 7.14 gives the simulated realized gain and measured gain of the proposed reflectarray. It is shown that the realized gain decreases rapidly when the frequency is lower

than 7 GHz. This is mainly caused by the drastic deterioration of the horn's reflection coefficient when the frequency exceeds the working frequency range of the horn, as shown in Figure 7.12. As shown in Figure 7.14, the measured 3 dB gain variation bandwidth is from 8.6 GHz to 14 GHz (47%). The measured gain peaks at 11.4 GHz with a value of 25.25 dBic

The aperture efficiency is also given by Figure 7.14. The simulated AE is calculated based on the simulated realized gain while the measured AE is calculated by the measured gain. The difference between the results may stem from the fabrication errors of the horn and the array as well as the measurement errors. From the measured result, the reflectarray can achieve larger than 50% AE from 8.6 GHz to 12 GHz (33%) and larger than 30% AE from 7 GHz to 13.6 GHz (64%).

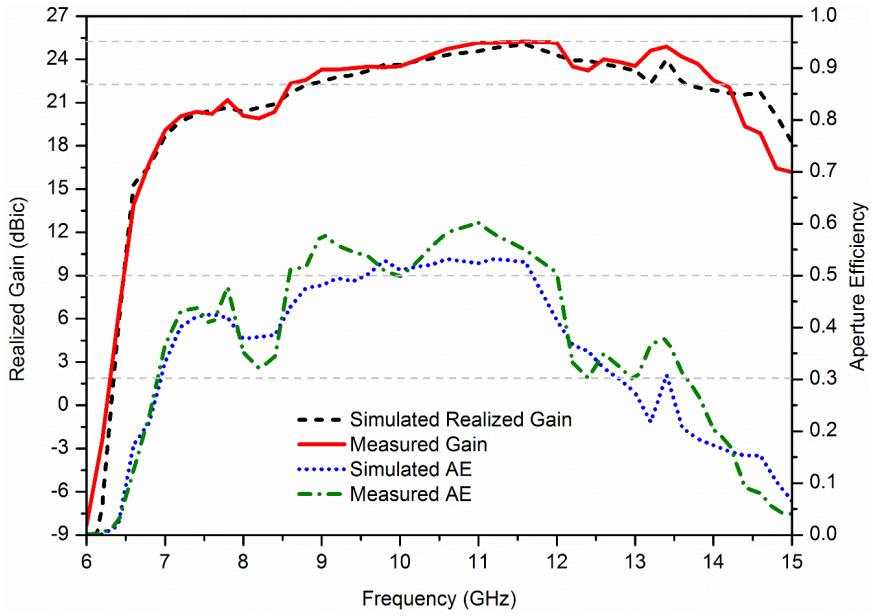

Figure 7.14 Simulated and measured gain and efficiency of the proposed antenna.

7.4.4 Radiation Patterns

As aforementioned, the proposed reflectarray achieves a nearly 2:1 bandwidth in terms of impedance bandwidth, 3 dB AR bandwidth and 30% AE bandwidth. Moreover, the proposed reflectarray can also maintain good radiation pattern performance such as undistorted radiation pattern shape, low sidelobe and low cross-pol component in a 2:1 bandwidth. To verify this, the radiation patterns at five different frequencies are shown in Figure 7.15 The main plane 1 in Figure 7.15 refers to the xoz plane as shown in Figure 7.6 while the main plane 2 the plane perpendicular to main plane 1 along the main beam direction.

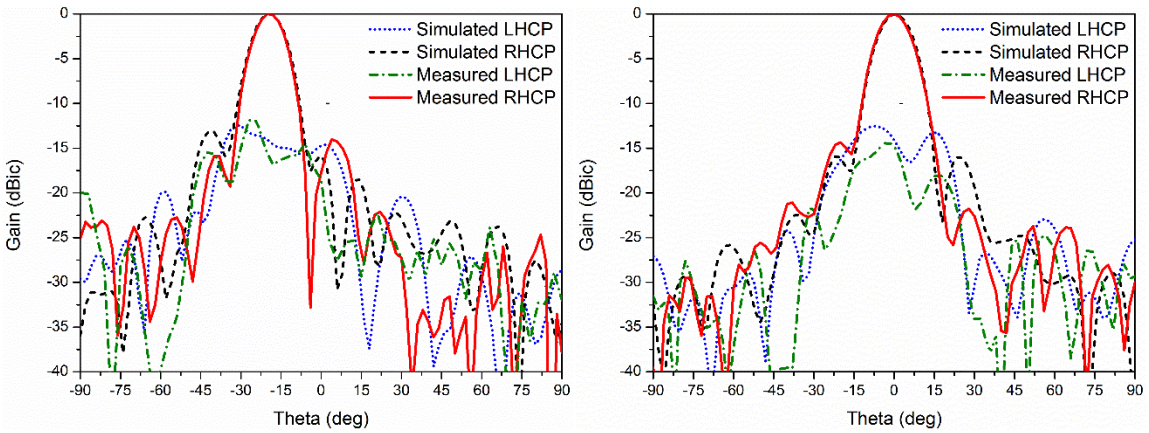
Simulated LHCP
Simulated RHCP
Measured LHCP
Measured RHCP
Gain (dBic)
Theta (deg)

(a)

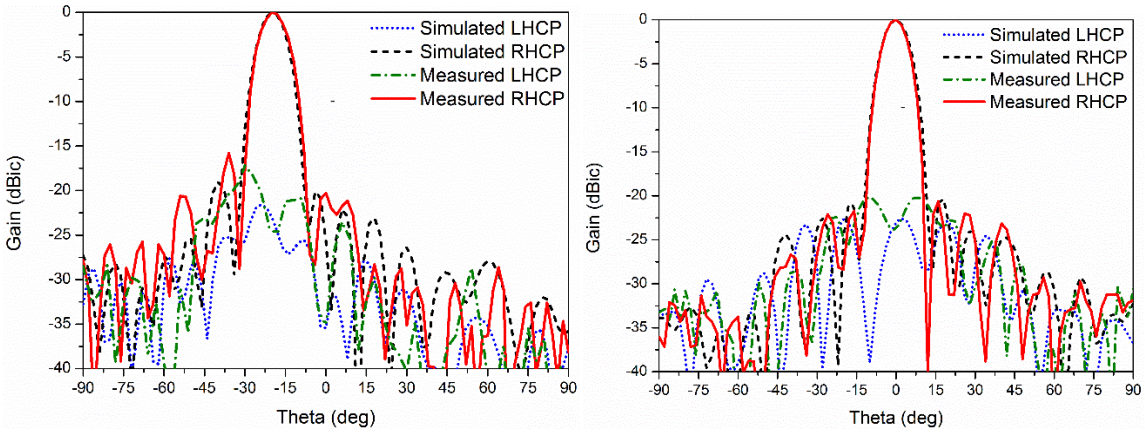
Simulated LHCP
Simulated RHCP
Measured LHCP
Measured RHCP
Gain (dBic)
Theta (deg)

(b)

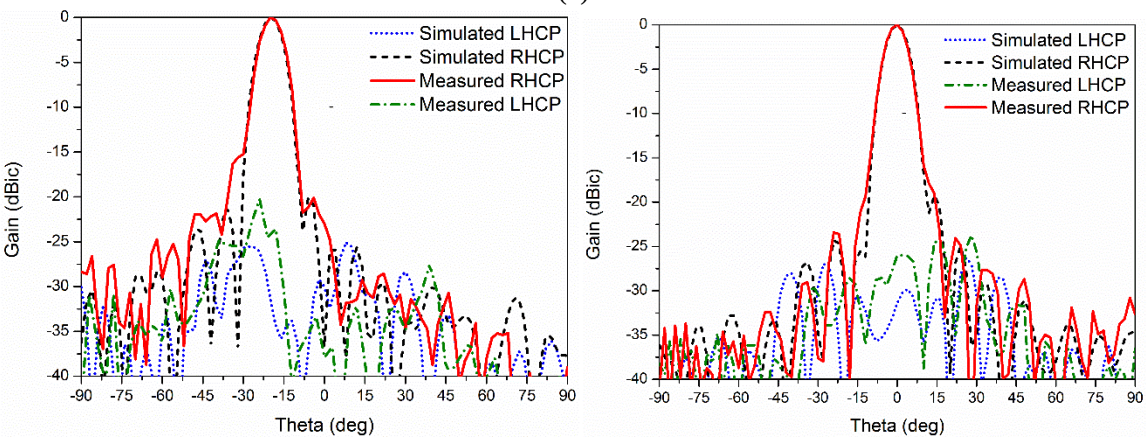
Simulated LHCP
Simulated RHCP
Measured RHCP
Measured LHCP
Gain (dBic)
Theta (deg)

(c)

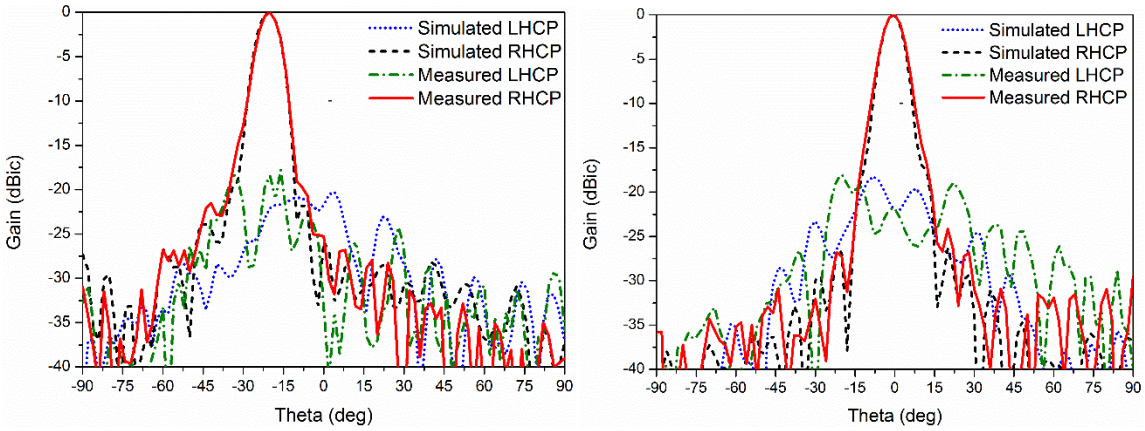
Simulated LHCP
Simulated RHCP
Measured LHCP
Measured RHCP
Gain (dBic)
Theta (deg)

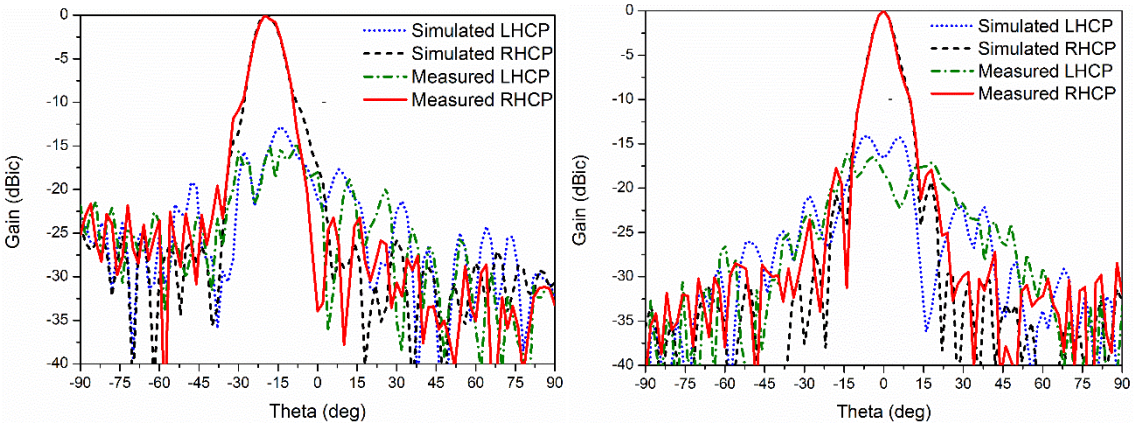

Main plane 1 (e) Main plane 2

Figure 7.15 Simulated and measured radiation patterns of the proposed antenna: (a) 7 GHz, (b) 9 GHz, (c) 10.6 GHz, (d) 12 GHz, (e) 14 GHz.

As shown in Figure 7.15, the measured radiation pattern agrees well with the simulated radiation pattern at each frequency. It is also observed from the results that the array maintains undistorted pencil-shaped beams, at least -15dB side lobe and -15dB cross-pol component from 7 GHz to 14 GHz.

7.4.5 Comparison with Other Wideband CP Reflectarrays

Due to the wideband characteristic of the novel S-shaped phasing element, the presented reflectarray achieves wide bandwidth in all aspects. To demonstrate its advantages more clearly, a comparison between the proposed design and other reported wideband CP reflectarrays is given by Table 7.2.

Table 7.2 Comparison with Other Wideband CP Reflectarrays

Ref. No.	Layers	3 dB AR BW	Gain BW	AE BW	Radiation Pattern BW
[79]	Dual	28%	1-dB gain 20%	-	-
[80]	Single	43%	1 dB gain 31% 3 dB gain ~40%	-	-
[81]	Multiple	40%	3 dB gain 40%	-	40%
[83]	Single	11%	1 dB gain 17%	-	-
[84]	Single	50%	1 dB gain 12%	-	-
This work	Single	68%	3 dB gain 48%	>50%: 33% >30%: 64%	67%

As shown in the table, the presented design provides wider bandwidth (BW) in terms of 3 dB AR BW, 3 dB gain BW and radiation pattern BW. More importantly, the proposed reflectarray can maintain higher than 50% aperture efficiency in a 33% bandwidth, which is not available in the current literature.

7.5 Summary

A single layer wideband circularly polarized reflectarray using a novel S-shaped phasing element is presented in this Chapter. The proposed S-shaped element achieves low cross-polar reflection and very linear phase shift to the element rotation angle in a 2:1 bandwidth. Theoretical analysis indicates that the AR bandwidth of the CP reflectarray can be improved using element rotation method even with incident fields poor in CP purity. Moreover, the influence of differential spatial phase delay on the bandwidth of the proposed array is proved to be very limited. The measurement results demonstrate that the proposed reflectarray has a 3 dB AR bandwidth of 68% and a 3 dB gain bandwidth of 48%. More importantly, the aperture efficiency of the proposed array is larger than 50% in a 33% bandwidth and larger than 30% in a 64% bandwidth. These excellent performances make the proposed reflectarray a good candidate for high-data-rate satellite communications.

Chapter 8. Ultra-Wideband Circularly Polarized Tightly Coupled Array

8.1 Introduction

Although a wideband CP reflectarray with 2:1 bandwidth is investigated in Chapter 7, it seems that the bandwidth of this array is hard to be improved further. One reason is that the bandwidth of CP feeding horn is limited due to the occurrence of higher modes in waveguides. Another factor is that the bandwidth of the reflectarray element is also limited and is difficult to exceed 2:1 frequency range at this stage. Therefore, to design ultra-wideband CP arrays, the direct radiating array is still the only option. Normally, to design wideband direct radiating arrays, wideband antenna elements, such as the Vivaldi antenna [139] and "bunny-ear" antenna [140] are used. However, the considerable height limits their applications to some extent.

Instead of using elements with inherent broad bandwidth to build a wideband array, Munk used capacitively coupled short dipoles to design a wideband array which achieved 4.5:1 impedance bandwidth [21]. The idea was to alleviate inductive loading introduced by the ground plane using capacitive coupling among neighboring elements. Due to the closely spaced dipole configuration, these elements are tightly coupled and the electric current along each dipole is almost constant, which is different from the electric current on a single dipole where a sinusoidal magnitude distribution with nulls at the termination exists [141]. This kind of dipole array emulated Wheeler's electric current sheet which can support radiation at much lower frequencies than the element's self-resonant frequency [142].

Two different types of arrays were proposed to realize Wheeler's current sheet and both obtained wide bandwidth. The first one was the "connected arrays" which interconnected array elements to achieve relatively constant electric current across the array aperture and large array bandwidth [143-147]. Another type was the "tightly coupled array" which utilized closely spaced dipoles, where the strong mutual coupling among the dipole elements facilitated the improvement of array bandwidth [148-151].

Although the aforementioned arrays achieved several octave bandwidths, they were all linearly polarized or dual linearly polarized and only the impedance bandwidth was considered. For applications such as the high-data-rate satellite communications, wideband circularly polarized (CP) antennas and arrays are preferred [6]. To improve the bandwidth especially the axial ratio (AR) bandwidth of CP arrays, various methods were adopted, such as sequential rotation [152] and using metamaterial-line based feeding network [153].

However, there are few reported CP array designs based on the concept of connected array or tightly-coupled array, which utilize narrow-bandwidth element to obtain wide array AR bandwidth. A dual-CP spiral array in which neighboring spirals of orthogonal polarizations were connected achieved 1.8 times AR bandwidth than the single spiral [154]. The AR bandwidth enhancement in this design was mainly due to the doubling of the electric travelling-wave current path. By connecting more spirals in a ring-array structure, the AR bandwidth was further improved [155]. However, the elements used in [154, 155] are spirals which have inherent ultra-wideband AR bandwidth and the relative large element space makes them different to those tightly coupled arrays.

Recently, a crossed dipole structure which incorporated 90^o phase shift line between the orthogonally placed dipoles were presented [47, 48]. Attributed to the incorporated 90^o phase shift line, the crossed dipole antenna was able to be fed by a coaxial connector directly without any baluns and still achieved good CP performance. Based on the CP crossed dipole, a CP tightly coupled array is investigated in this Chapter. By decreasing the element space and choosing appropriate overlapped structure between adjacent elements, it is shown that not only the impedance bandwidth but also the AR bandwidth of the array is greatly improved compared with the single isolated element. To verify the concept, a 4×4 array is prototyped and measured and the measurement results confirm that the proposed CP tightly coupled array achieves a 3.14:1 VSWR<3 bandwidth and a 2.38:1 3 dB AR bandwidth, which shows much wider bandwidth than the conventional crossed dipole array using the same element. To the best knowledge of the author, it is the first CP tightly coupled crossed dipole array which aims to improve the AR bandwidth of an antenna array by taking advantages of strong mutual coupling among the elements.

This Chapter is organized as follows: Section 8.2 gives a brief introduction of LP tightly coupled array and its operating principles; Section 8.3 introduces the tightly coupled crossed dipole unit cell and the AR bandwidth enhancement of the unit cell compared with an isolated crossed dipole antenna; Section 8.4 presents the configuration of the 4×4 CP-TCCDA and the 1:16 Wilkinson power divider network as well as the analysis of the bandwidth enhancement mechanism; Section 8.5 presents the fabricated 4×4 CP-TCCDA and measurement results. The conclusion is given in Section 8.6.

8.2 LP Tightly Coupled Array

Figure 8.1 shows the configuration of a LP tightly coupled array which is constituted by capactively coupled dipoles. As shown, each dipole is fed individually with a very

small element space and thus the adjacent dipoles are strongly coupled. Since each element interacts significantly with its neighboring elements, its effective electrical length will be increased. In this case, the individual elements no longer operate as isolated antennas, and the bandwidth is not limited by the dimension of the unit cell. Arrays with strong mutual coupling can support currents at wavelengths that are much larger than the dimensions of a single element. In this way, the low end performance of the tightly coupled array can be significantly improved while high-frequency performance is determined by the onset of grating lobes and keeps nearly unchanged. Therefore, the tightly coupled arrays can achieve much wider impedance bandwidth than those convention dipole arrays.

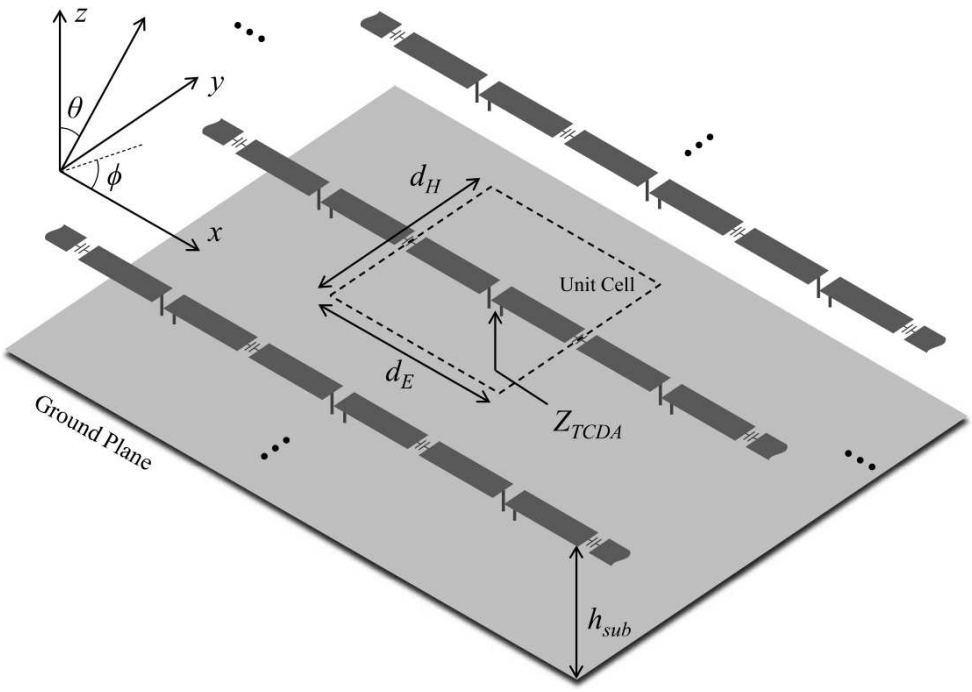

Figure 8.1 A linearly polarized tightly coupled array consisting of capacitively coupled dipole elements.

Normally, dipole arrays are required to be placed above a ground plane for directional radiation. As tightly coupled array can operate at much lower frequencies than an isolated dipole, the ground plane will short-circuit the array and prevent efficient radiation at low frequencies considering that the electric length of the distance from the ground plane to the array will be very small at low frequencies. For tightly coupled array, the ground plane can be modeled as a short circuited transmission line in parallel with the radiation resistance [21], as shown in Figure 8.2. To compensate the reactance from the ground plane, capacitance between neighboring elements are introduced. This capacitance along with the self-inductance of the dipoles constitute a series L-C circuit which serves an impedance matching network for the shunt reactance of the transmission line stub. In this manner, the impedance bandwidth of the tightly coupled array can be further tuned.

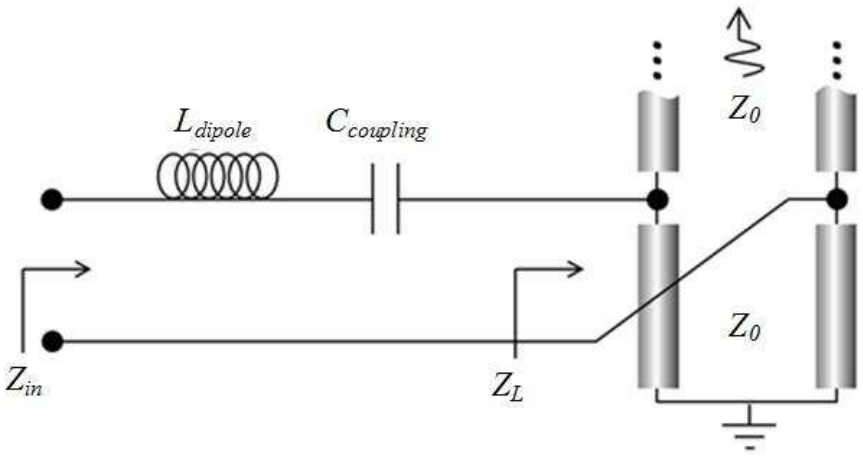

Figure 8.2 Equivalent circuit for a tightly coupled array [21].

8.3 CP Tightly Coupled Crossed Dipole Unit Cell

8.3.1 Unit Cell Configuration

To predict the performance of an infinite array, the unit cell under periodical boundary gives a good approximation. For building a UWB CP tightly coupled array, a CP tightly coupled dipole unit cell is investigated at first, whose configuration is shown in Figure 8.3.

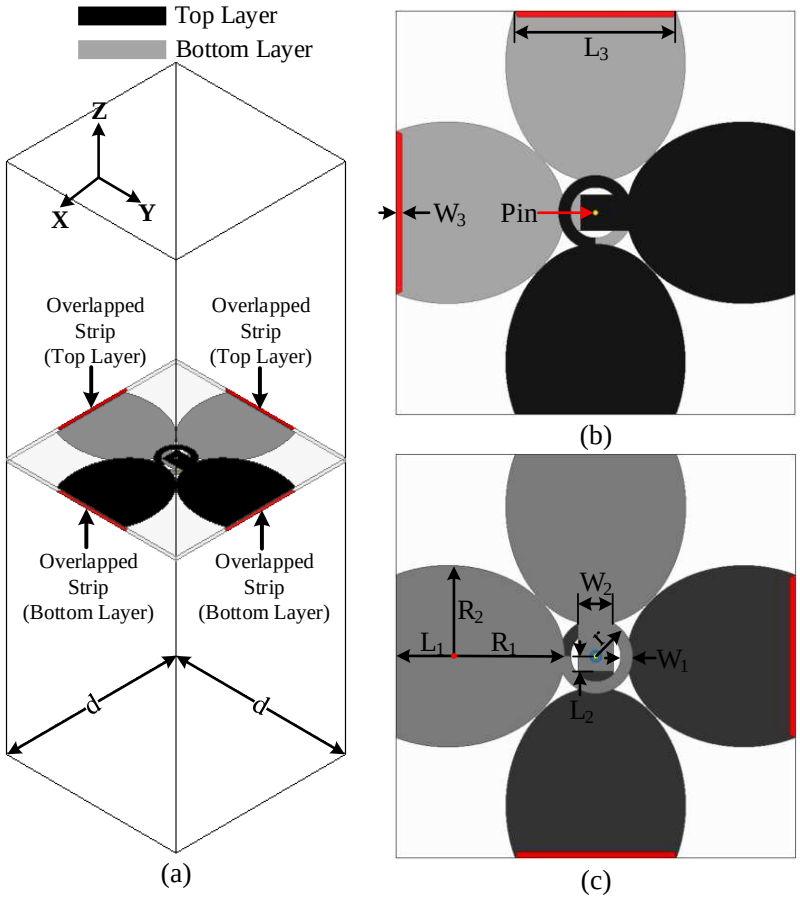

Figure 8.3 Configuration of the unit cell: (a) 3D view, (b) top view, (c) bottom view.

The proposed element is printed on both sides of a 0.813mm thick Rogers RO4003C substrate. As shown, two neighboring cut-off elliptical arms are connected by a ¾ ring shaped phase shift line with outer radius r and line width W_1. To imitate an infinite tightly coupled array, the proposed element is placed in periodical boundaries with unit cell size of d × d and four overlapped strips are utilized to provide strong capacitive coupling between adjacent elements along both x- and y- directions. Besides, the element is fed by a coaxial cable directly and no ground plane is used. The detailed geometry dimensions of the unit cell are given in Table 8.1.

Table 8.1 Unit Cell Dimensions

d	L_1	L_2	L_3	W_1	W_2	W_3	R_1	R_2	r
40	5.2	1.5	16.1	1.2	3.5	0.6	11.7	9	3.7

8.3.2 Comparison with Isolated Crossed Dipole

Figure 8.4 shows the configuration of an isolated crossed dipole. As shown, the overlapped strips shown in Figure 8.3 are attached to the end of each elliptical arm. In this manner, the size of the isolated element is exactly the same as the element existed in an infinite tightly coupled crossed dipole array.

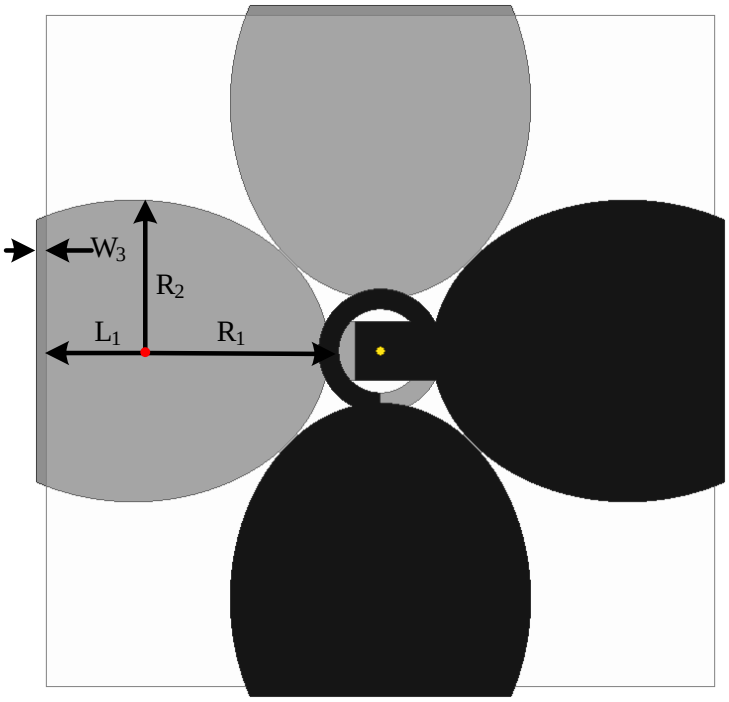

Figure 8.4 Configuration of the isolated crossed dipole.

The comparison between the isolated element and the tightly coupled unit cell under periodical boundary in terms of VSWR and AR is shown in Figure 8.5 and Figure 8.6, respectively.

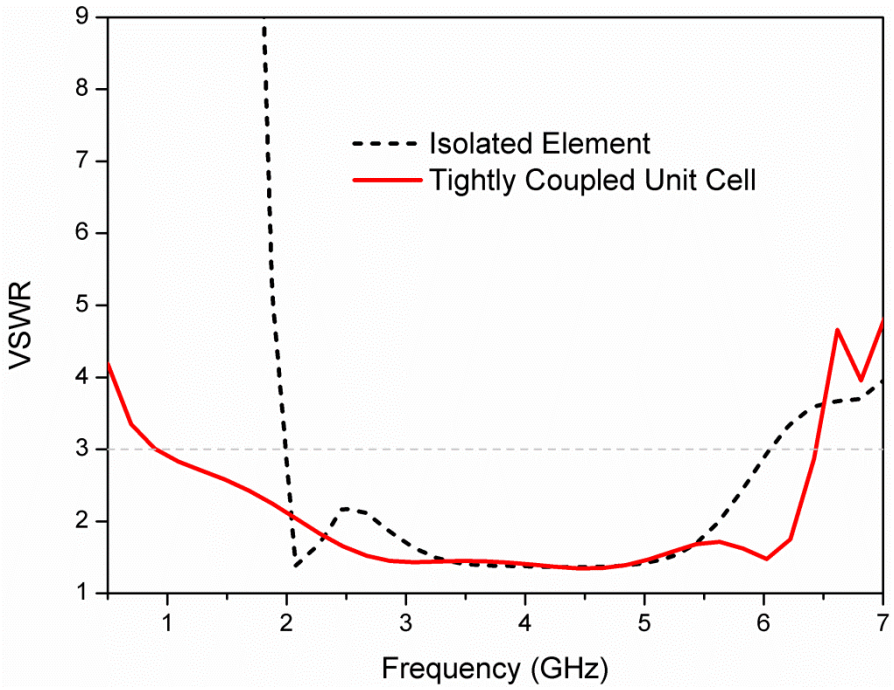

Figure 8.5 Comparison of the VSWR between the isolated element and the tightly coupled unit cell.

As shown in Figure 8.5, the simulated VSWR<3 bandwidth of the isolated element is 2-6 GHz (3:1) while the corresponding bandwidth of the tightly coupled unit cell is 0.9-6.4 GHz (7.1:1). Greatly improved impedance bandwidth at lower frequency is observed, similar to those linearly polarized tightly coupled unit cell [148-151]. Furthermore, it is shown in Figure 8.6 that the AR bandwidth improves from 4-5.3 GHz (1.3:1) to 2.4-5.3 GHz (2.2:1) by the tightly coupled unit cell.

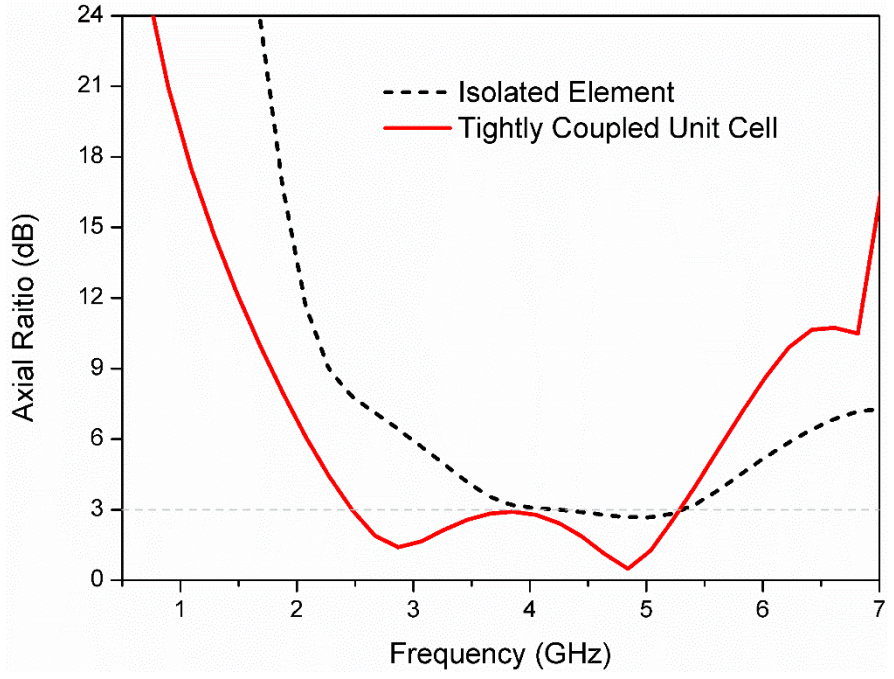

Figure 8.6 Comparison of the AR between the isolated element and the tightly coupled unit cell.

8.4 Analysis and Design of the 4×4 CP-TCCDA

As indicated in the previous section, not only the impedance bandwidth but also the AR bandwidth of the CP crossed dipole element is greatly improved when placed in a tightly coupled infinite array environment. In this section, the principle of bandwidth enhancement especially the AR bandwidth improvement is analyzed and the analysis is verified by the radiated E-fields of the array. The configuration of the 4×4 CP-TCCDA as well as the 1:16 Wilkinson power divider network and their performances are also presented.

8.4.1 Analysis of the Bandwidth Enhancement

As demonstrated in Section 8.3, the bandwidth of a CP crossed dipole can be improved by using a tightly coupled array. The impedance bandwidth enhancement can be explained by the lengthening of the electric current or equivalent increase of the antenna electrical length, which lowers down the array lower limit working frequency range while the upper limit of the working frequency range is mainly controlled by the element and thus varies slightly.

The phase difference between the two orthogonally placed dipoles is mainly introduced by the ¾ ring shaped phase shift line and its length is calculated by

$$l_{phase\ shift} = 2\pi \times (r - W_1/2) \times 3/4 \tag{8.1}$$

where r, W_1 and W_2 are parameters shown in Table 8.1. The calculated physical length of the ¾ ring shaped phase shift line is around 14.6mm which equals to a quarter of the guided wavelength at 3.08 GHz.

Considering an elliptically polarized wave propagating along +Z direction with the following form

$$\vec{E}(z,t) = \vec{x}E_x \cos(\omega t - kz) + \vec{y}E_y \cos(\omega t - kz + \delta) \tag{8.2}$$

where $\vec{x}$ and $\vec{y}$ represent the unit vector along x and y direction and k is the free space wavenumber. The AR of this elliptically polarized wave is calculated by [22]

$$AR = \frac{E_{major\ axis}}{E_{minor\ axis}} = \frac{OA}{OB},\ 1 \le AR \le \infty \tag{8.3}$$

where

$$OA = \left\{\frac{1}{2}\left[{E_x}^2 + {E_y}^2 + \left({E_x}^4 + {E_y}^4 + 2{E_x}^2{E_y}^2 \cos 2\delta\right)^{\frac{1}{2}}\right]\right\}^{\frac{1}{2}} \tag{8.4}$$

$$OOB = \left\{\frac{1}{2}\left[{E_x}^2 + {E_y}^2 - \left({E_x}^4 + {E_y}^4 + 2{E_x}^2{E_y}^2\cos 2\delta\right)^{\frac{1}{2}}\right]\right\}^{\frac{1}{2}} \tag{8.5}$$

Since the infinite CP-TCCDA can radiate at 2.4 GHz effectively, it is reasonable to deem the magnitude of the radiated E-fields along x- and y- direction is close to each other at 2.4 GHz, i.e.,

$$E_x \approx E_y \tag{8.6}$$

As the phase difference introduced by the ¾ ring shaped phase shift line is around 90° at 3.08 GHz, the phase difference between E_x and E_y at 2.4 GHz is

$$\delta = \frac{\pi}{2} \times \frac{2.4}{3.08} = 0.39\,\pi \tag{8.7}$$

Substituting (8.6) and (8.7) into (8.3) – (8.5) and calculate the AR at 2.4 GHz yields a result of 1.425 (3.07 dB), which is very close to the simulation result shown in Figure 8.6. From the above analysis and calculation result, we could obtain the following conclusions

1) The AR bandwidth enhancement of the CP-TCCDA is mainly attributed to the strong mutual coupling which enables the array to radiate effectively at much lower frequencies. Although the VSWR of the single isolated element at 2.4 GHz is around 2, the smaller electrical length makes it radiate less efficient than the CP-TCCDA and results in deterioration of the magnitude balance and possible phase difference variations between x- and y- direction. This can be verified by Figure 8.6 which demonstrates that the CP-TCCDA always shows better AR than the single isolated element below 4 GHz.

2) Although the impedance bandwidth of CP-TCCDA can reach a lower limit of 0.9 GHz, the AR bandwidth cannot approach this limit. Considering that the phase difference between $\overrightarrow{E_x}$ and $\overrightarrow{E_y}$ is determined by the electrical length of the ¾ ring shaped phase shift line, the phase difference between the two orthogonal E-fields at 0.9 GHz is around 26.3°. Once again, assuming $E_x = E_y$ and we could calculate the AR at 0.9 GHz is 12.6 dB. Notice that at the lowest working frequency 0.9 GHz, actually the magnitudes of the E-fields along x- and y- direction may have certain differences and thus the AR should be worse than 12.6 dB.

8.4.2 4×4 CP-TCCDA and 4×4 Conventional Crossed Dipole Array

To verify the above analysis and the presented concept, a 4×4 CP-TCCDA is designed. The configuration of the 4×4 CP-TCCDA is shown in Figure 8.7 while the magnified picture demonstrates the overlapped area in detail.

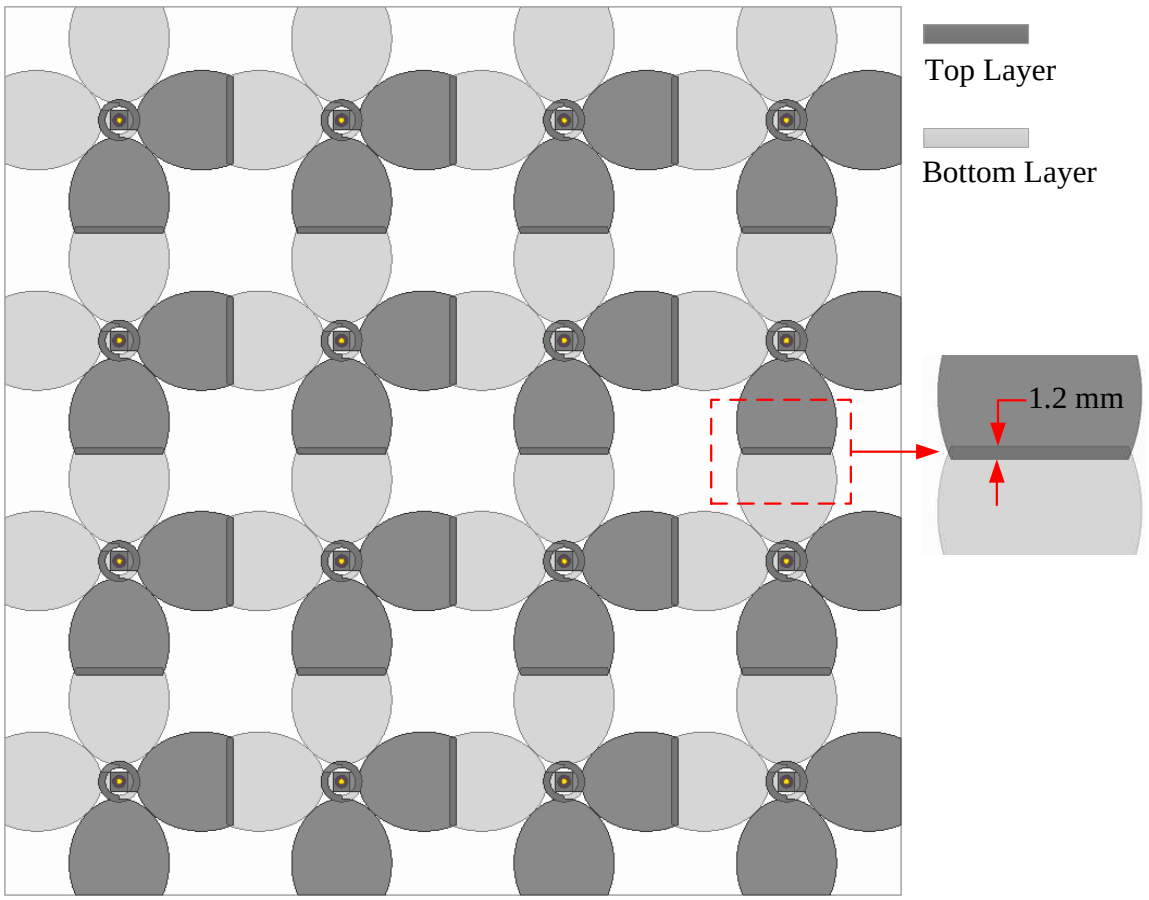

Figure 8.7 Configuration of the 4×4 CP-TCCDA.

As shown, the width of the overlapped part is 1.2 mm which is twice the width of the overlapped strip in the unit cell. The element space is 40 mm which is the same as the unit cell size given in Figure 8.3. Furthermore, to make a direct comparison with a conventional array, a 4×4 conventional coupled array (conventional array) using the isolated crossed dipole element shown in Figure 8.4 is also designed, which is shown in Figure 8.8. The element space of the 4×4 conventional coupled array is chosen to be half free-space wavelength at 2.4 GHz (62.5 mm). With this element space, the array is deemed to have much smaller coupling than the CP-TCCDA.

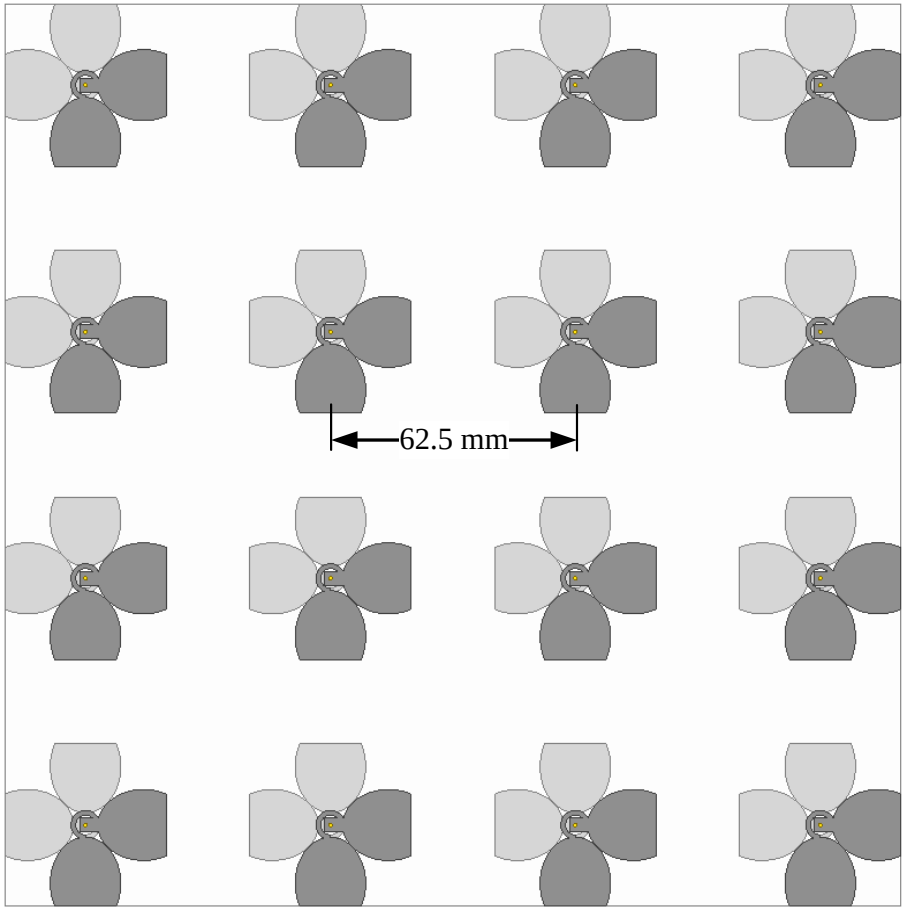

Figure 8.8 Configuration of the 4×4 conventional coupled array.

Figure 8.9 shows simulated E-fields of the two arrays at 2.4 GHz in a plane parallel to the array aperture at the height of 55 mm. The magnitudes of the two fields are normalized to the same color bar for more clear comparison. As the E-fields along broadside direction relate to the array AR bandwidth, the E-fields at the center area of each graph are of major interest. As shown, both the 4×4 CP-TCCDA and the 4×4 conventional coupled array have a rotated E-fields distribution with different time slot. However, the magnitudes of the E-fields of the 4×4 conventional coupled array at $\omega t = 0^o$ and $\omega t = 90^o$ are quite different, which indicates large differences between the magnitudes of radiated E-fields along x- and y- direction (E_x and E_y). On the contrary, the radiated E-fields of the 4×4 CP-TCCDA along x- and y- direction are nearly the same in the center area, which verifies the assumption of (8.5). As the phase difference between $\overrightarrow{E_x}$ and $\overrightarrow{E_y}$ of the two arrays are both determined by the ¾ ring shaped phase shift line, the phase differences between $\overrightarrow{E_x}$ and $\overrightarrow{E_y}$ of the two arrays are the same at 2.4 GHz. However, the unequal (unbalanced) magnitudes of $\overrightarrow{E_x}$ and $\overrightarrow{E_y}$ of the 4×4 conventional coupled array result in a larger AR compared with the 4×4 CP-TCCDA, according to (8.3) – (8.5).

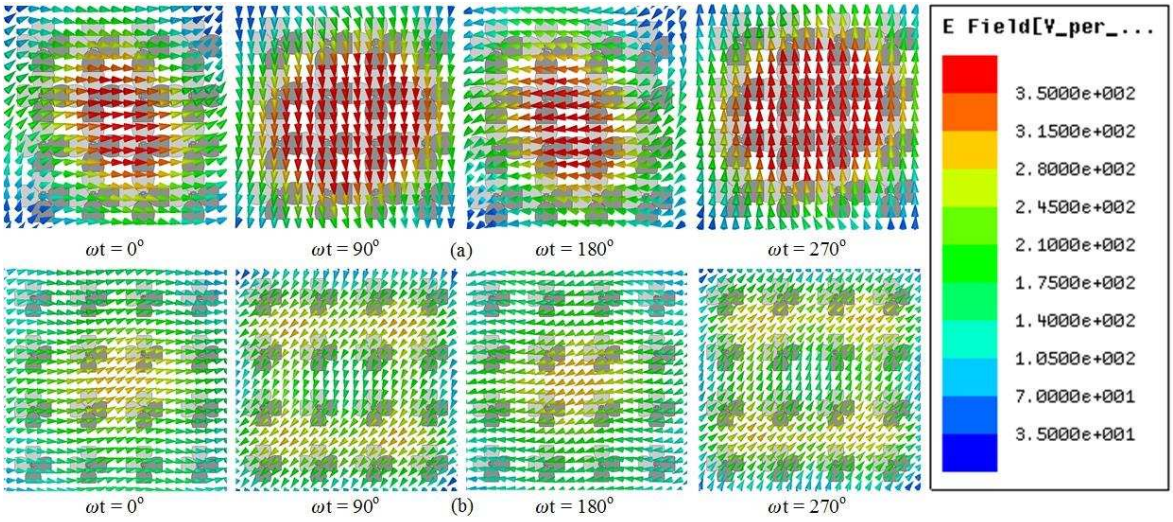

Figure 8.9 Comparison of the E-fields at 2.4 GHz: (a) 4×4 CP-TCCDA, (b) 4×4 Conventional array.

The comparison of the AR between the 4×4 CP-TCCDA and 4×4 conventional crossed dipole array is shown in Figure 8.10.

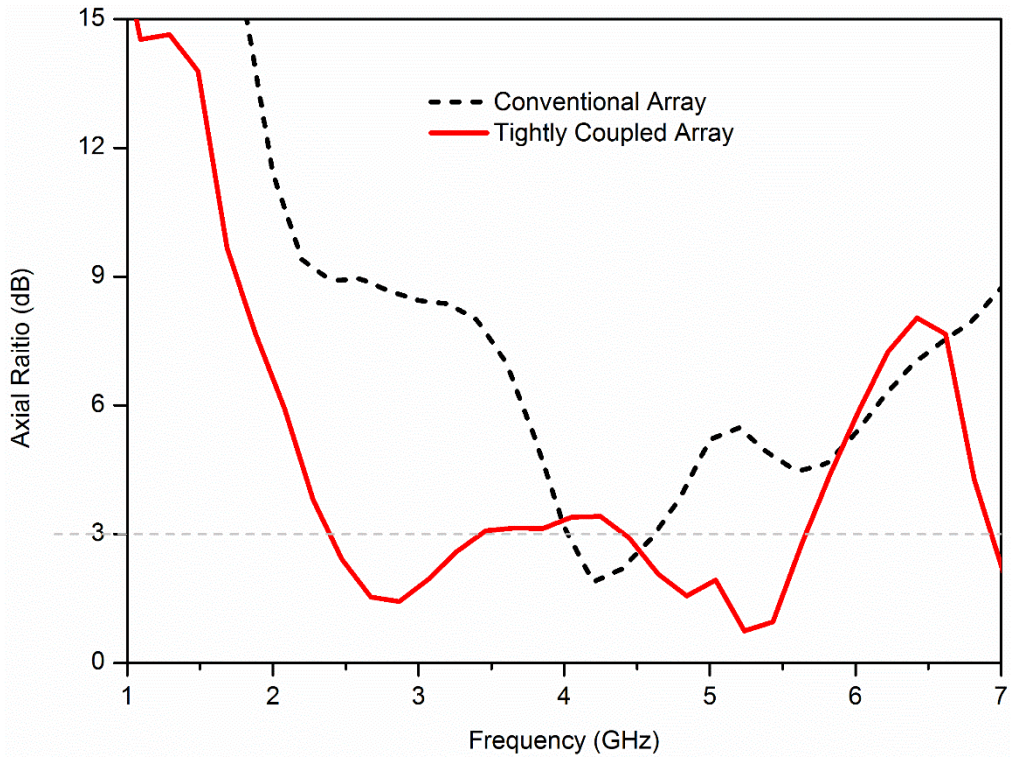

Figure 8.10 Comparison of the AR between the 4×4 CP-TCCDA and 4×4 conventional crossed dipole array.

As shown, the 3 dB AR bandwidth of the 4×4 CP-TCCDA is much wider than the conventional crossed dipole array. Moreover, the simulated AR performance of the 4×4 CP-TCCDA is very close to the simulated AR of the infinite array due to the fact that the 4×4 CP-TCCDA is able to maintain balanced magnitudes of $\overrightarrow{E_x}$ and $\overrightarrow{E_y}$ from 2.4 GHz. Further increase of the array size will improve the impedance bandwidth but has limited

effect to the AR bandwidth. From Figure 8.10, it is also observed that the AR bandwidth of the 4×4 conventional array is narrower than the AR bandwidth of a single isolated crossed dipole.

8.4.3 Power Divider Network Design

To feed the 4×4 CP-TCCDA, a 1:16 Wilkinson power divider network is designed and shown in Figure 8.11. Since the CP-TCCDA achieves a 3 dB AR bandwidth from 2.4 to 5.3 GHz (2.2:1), the bandwidth of the power divider network is designed to cover this frequency range. Moreover, to reduce the fabrication complexity and cost, a two-stage Wilkinson power divider is used at the input port and a single-stage Wilkinson power divider with fan-shaped stub is used at the output port. With this arrangement, the presented power divider network can meet the bandwidth requirement while keeping a relatively simple configuration.

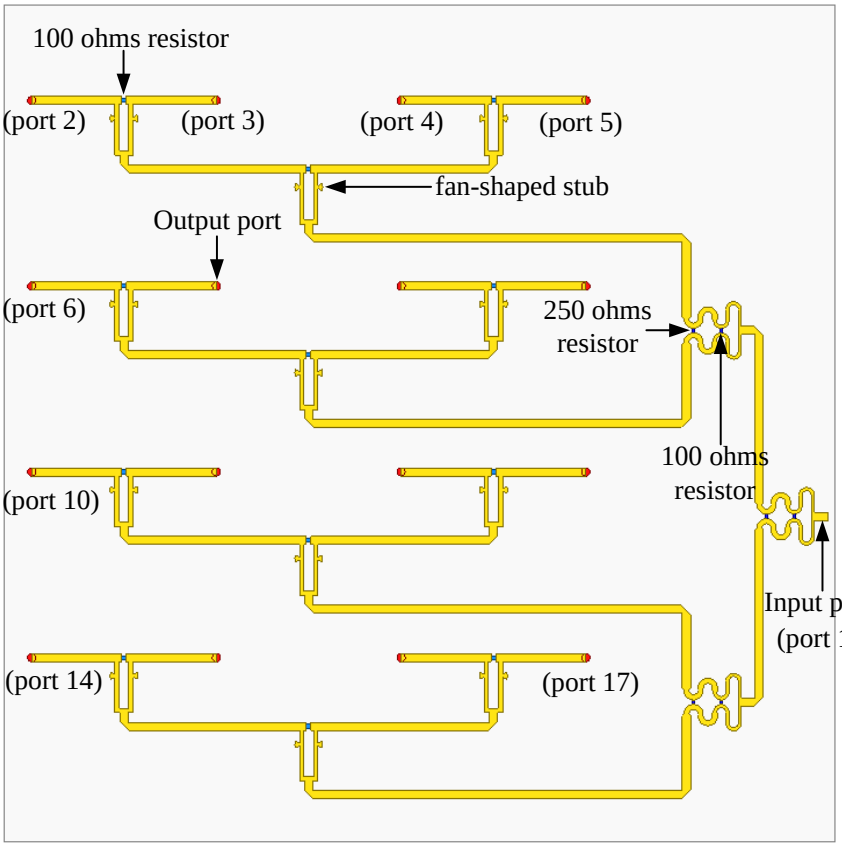

Figure 8.11 1:16 Wilkinson power divider network.

The simulated reflection coefficients of all ports are shown in Figure 8.12. As shown, the input port (port 1) achieves -10 dB reflection coefficient from 2.1 to 6.3 GHz while all other ports' reflection coefficients are smaller than -10dB from 1 to 6.3 GHz.

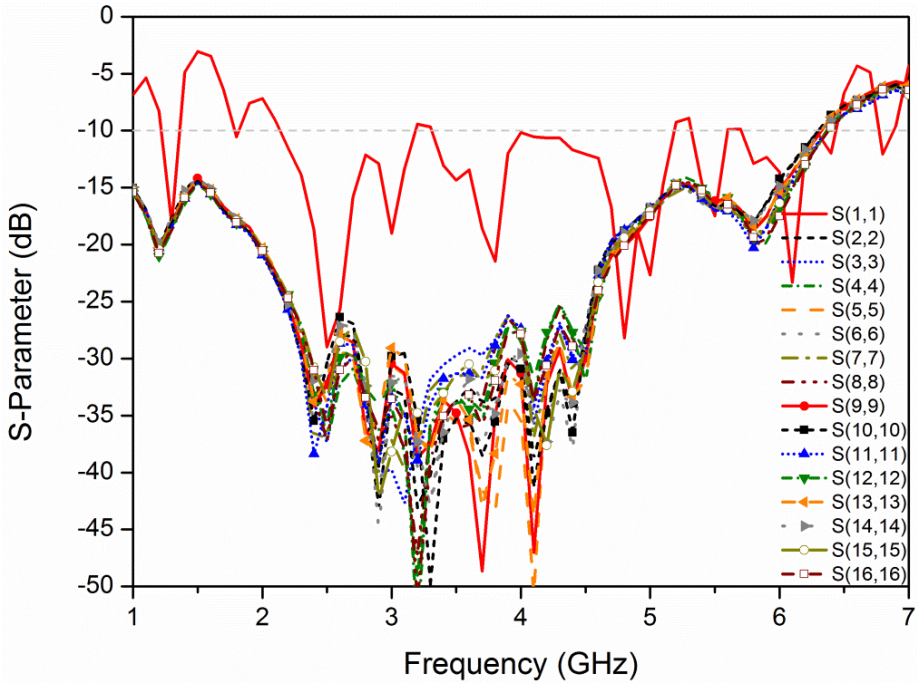

Figure 8.12 Simulated reflection coefficients of the power divider network.

The insertion losses from the input port to all 16 output ports are shown in Figure 8.13. From the simulated results, it is shown that the input power is divided equally to the 16 output ports and the insertion loss is around 1-2 dB from 2 to 6.3 GHz, which meets the bandwidth coverage requirement.

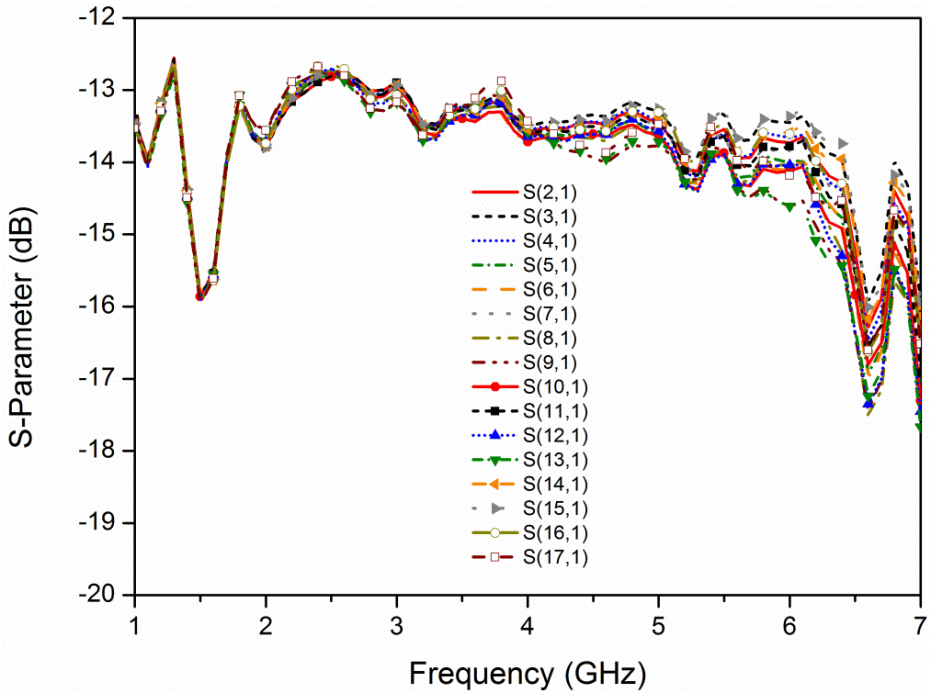

Figure 8.13 Simulated insertion loss of the power divider network.

The isolation between all 16 output ports is shown in Figure 8.14. As shown, all output port isolations are larger than 10 dB from 1.5 GHz to 7 GHz.

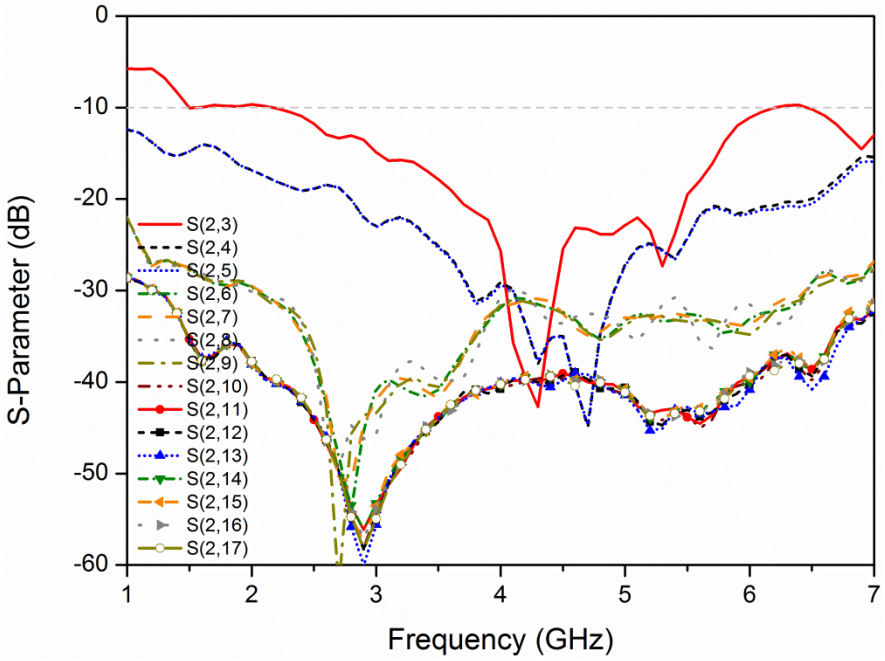

Figure 8.14 Simulated port isolation of the power divider network.

8.5 Results and Disussion

To verify the aforementioned design concept and analysis, a 4×4 CP-TCCDA with feeding network was prototyped and measured.

8.5.1 Prototype and VSWR

The fabricated 4×4 CP-TCCDA is shown in Figure 8.15.

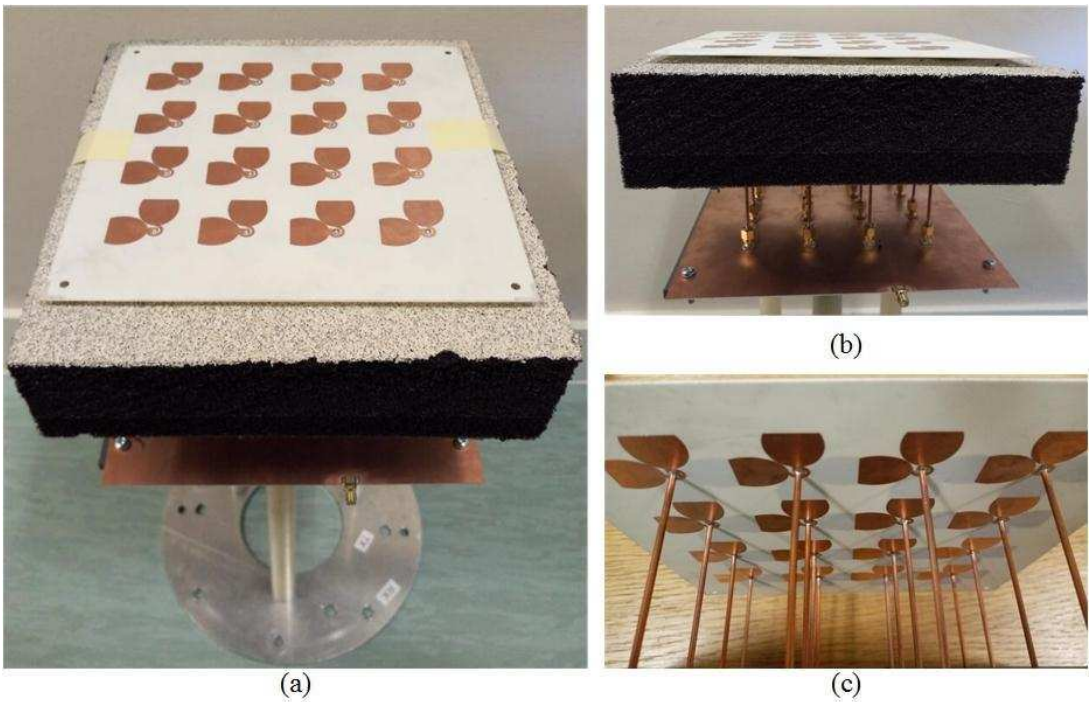

Figure 8.15 4×4 CP-TCCDA prototype: (a) front view, (b) side view, (c) feeding structure.

As shown, the array is placed above an absorber which helps achieve directional radiation and maintain good bandwidth performance. There are 16 coaxial cables with outer conductor soldered to the bottom-layer arms and inner pin soldered to the top-layer arms of the proposed array. These cables are then connected to the 1:16 power divider network which is shown in Figure 8.16.

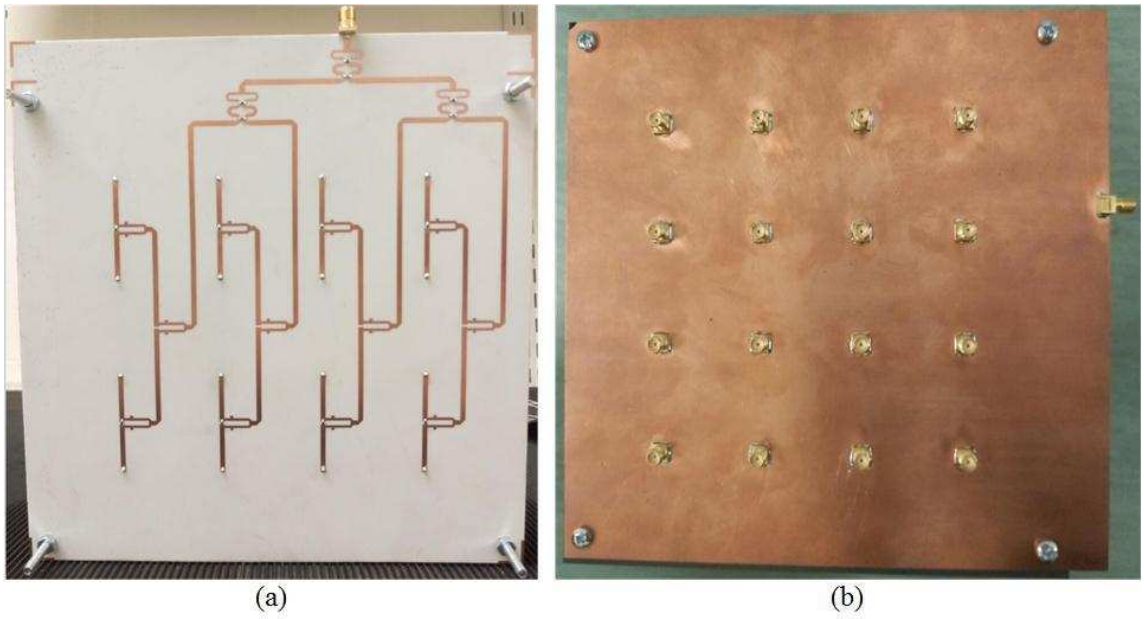

Figure 8.16 1:16 Wilkinson power divider network prototype: (a) top view, (b) bottom view (ground plane with 16 coaxial connectors).

The simulated and measured VSWR of the proposed 4×4 CP-TCCDA is shown in Figure 8.17.

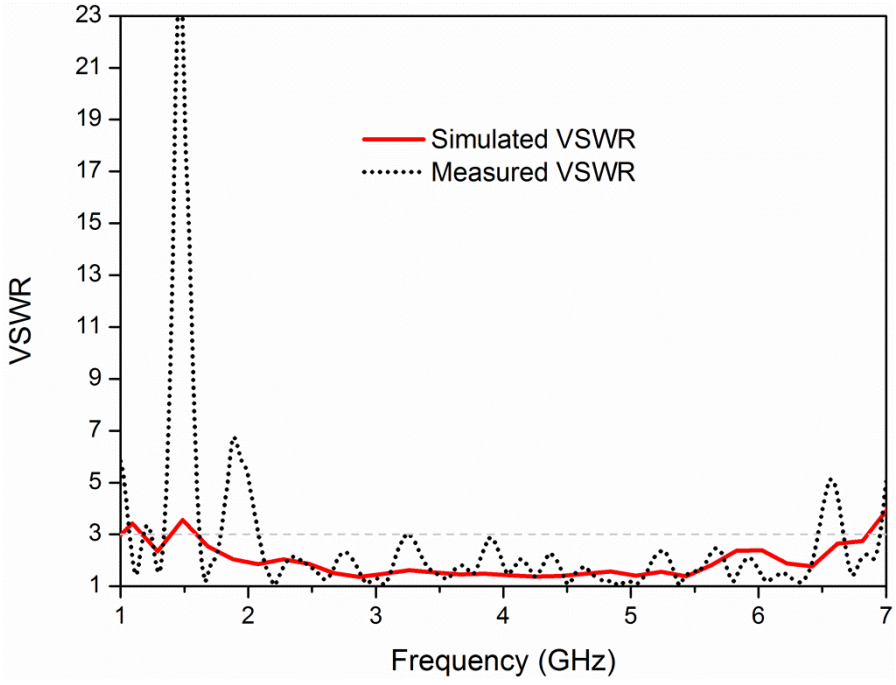

Figure 8.17 Simulated and measured VSWR.

As shown, the measured VSWR<3 bandwidth is from 2.06 GHz to 6.46 GHz (3.1:1). The measured VSWR is smaller than 2.5 within most of the bandwidth. Compared with the simulated VSWR, ripples are constantly occurring, which is attributed to the oscillation of the power divider network S_{11}, as shown in Figure 8.12. Besides, it is evident that the simulated VSWR of the 4×4 CP-TCCDA is worse than the simulated VSWR of tightly coupled unit cell shown in Figure 8.5. The main reason for this phenomenon is the cut-off of the infinite array to a finite array. Generally, larger-size CP-TCCDA will bring better performance at the expense of more complicated structure and higher fabrication cost.

8.5.2 Axial Ratio Bandwidth

Figure 8.18 shows the simulated and measured AR bandwidth. The measured result indicates that the proposed 4×4 CP-TCCDA achieves 3 dB AR bandwidth from 2.35 GHz to 5.6 GHz (2.4:1), which is close to the unit cell result shown in Figure 8.6. Although the size of the array is small, the 4×4 CP-TCCDA still radiates efficiently within a 3.1:1 bandwidth according to Figure 8.17. Within this 3.1:1 bandwidth, the amplitudes of the two E-fields ($\overrightarrow{E_x}$ and $\overrightarrow{E_y}$) keep balanced and the AR is mainly determined by the phase shift line based on the analysis in section 8.4. Therefore, it is reasonable that the AR bandwidth of the 4×4 CP-TCCDA is close to the unit cell's AR bandwidth.

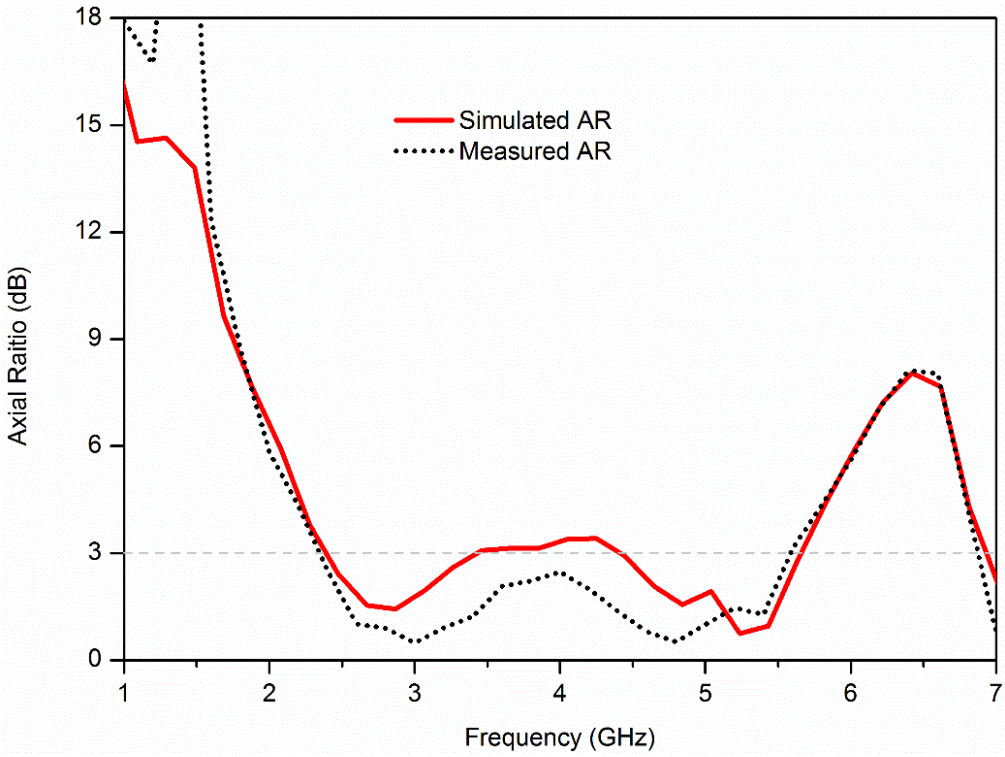

Figure 8.18 Simulated and measured AR.

8.5.3 Radiation Patterns

The simulated and measured radiation patterns are shown in Figure 8.19. The left column shows the radiation patterns in xoz plane while the right column shows the patterns in the yoz plane. Good agreement between the simulation and measurement results is observed. It is also shown that the proposed array achieves undistorted beams and -15dB cross-pol over a 2.1:1 frequency range.

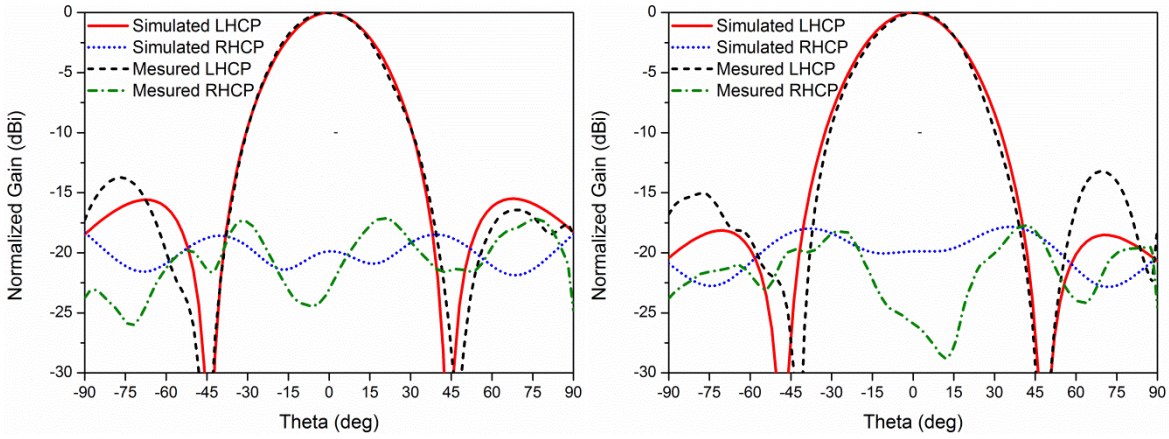

(a)

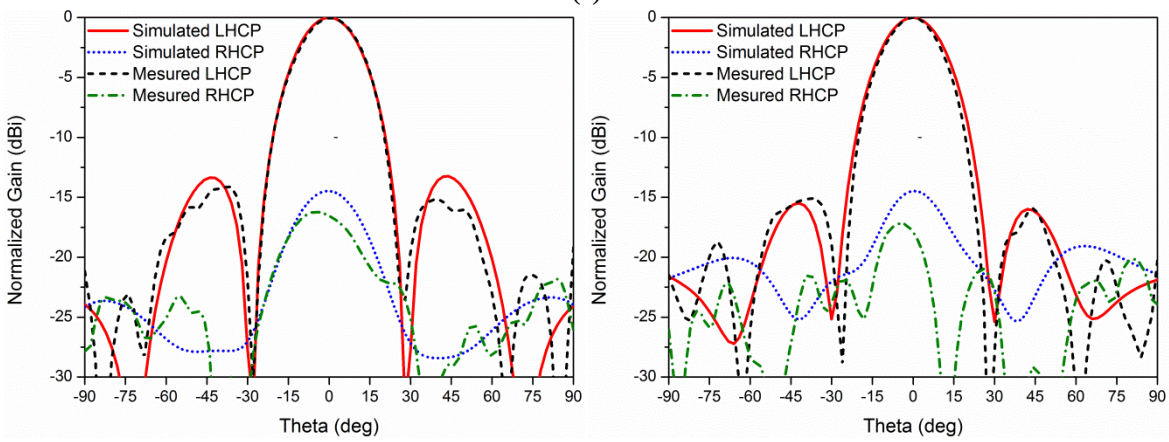

(b)

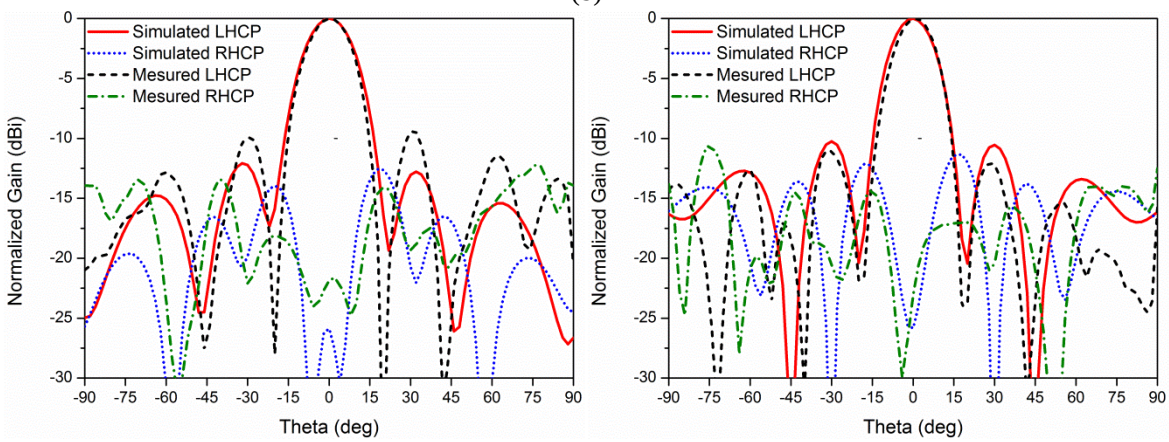

(c)

Figure 8.19 Simulated and measured radiation patterns at: (a) 2.6 GHz, (b) 4 GHz, (c) 5.4 GHz

8.5.4 Gain

The simulated and measured gain is shown in Figure 8.20. It is worth pointing out that the insertion loss of the feeding network is compensated when calculating the measured gain. As shown, the antenna gain increases as frequency increases within the working bandwidth, which is similar to reported linearly polarized tightly coupled arrays.

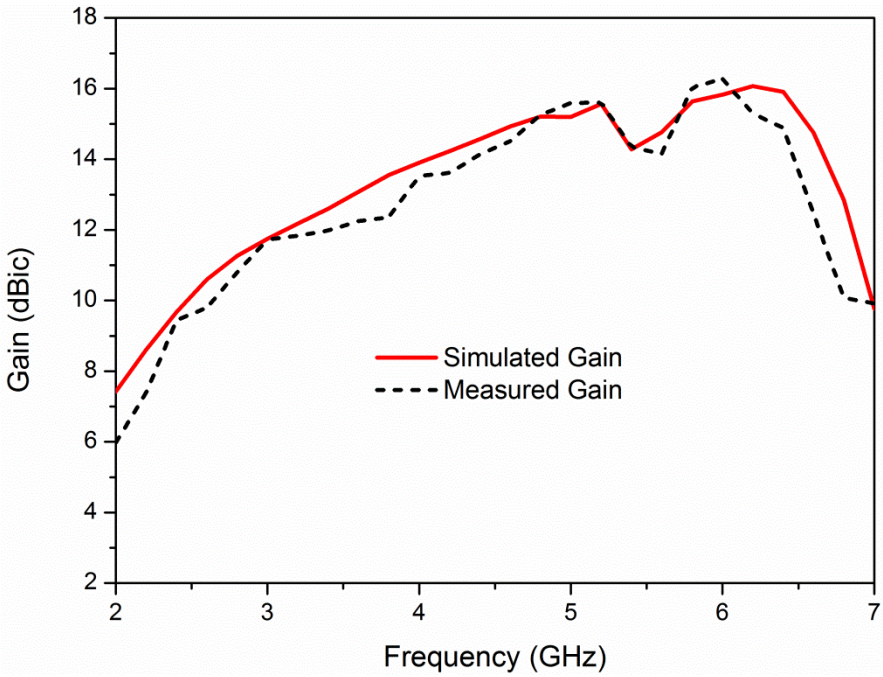

Figure 8.20 Simulated and measured gain.

A similar CP tightly coupled array using conventional dipoles is also investigated. From simulation results, it is found that the AR performance is degraded compared with the proposed array.

8.6 Summary

An ultra-wideband circularly polarized tightly coupled crossed dipole array which uses strong coupling between adjacent elements to improve the AR bandwidth of the array is proposed in this Chapter. Theoretical analysis is given to interpret the AR bandwidth improvement mechanism and it is found that the balanced electric fields along x- and y-directions over a wide frequency range facilitate the enhancement of AR performance. A 4×4 CP-TCCDA with feeding network is fabricated and measured and the measured results provide good support of the design concept. Owing to the concurrent wide impedance bandwidth and wide AR bandwidth, the proposed CP-TCCDA is promising for applications in various wireless systems which need large bandwidth.

Chapter 9. Conclusion and Future Work

9.1 Conclusion

Circularly polarized antenna elements and arrays are extensively deployed in various wireless systems due to their distinctive advantages over linearly polarized antennas. Like LP antennas, CP antennas are also demanded to achieve wider and wider bandwidth to meet the growing requirements of high data rate, good quality of service (QoS) and larger system capacity. Furthermore, these wideband CP antennas need to be tailored for specific applications, for example, the wideband CP antennas are always required to have high FBR as a GNSS receiving antenna, they need to have polarization re-configurability to implement polarization diversity and are necessary to have wide AR beamwidth for wide-angle beam-scanning systems. As it is impossible to design such a CP antenna with all these attractive features, different wideband CP antenna elements and arrays are developed in this thesis.

Three different ways to design a CP antenna were introduced and analyzed theoretically. These approaches included using orthogonal modes (TM_{01} and TM_{10}) of patch antennas, utilizing orthogonal E-fields of crossed-dipoles and generating travelling-wave current along curved structures. According to the classification of CP antennas by their different operating principles, various types of wideband CP antenna elements were reviewed and a detailed comparison of these wideband CP antenna elements gave a clear overview of the state-of-the-art. In the same Chapter, wideband CP arrays are also reviewed with a particular focus on the sequentially rotated array and CP reflectarray.

Chapter 3 to Chapter 5 discussed the design and characterization of one wideband CP antenna elements while three different wideband CP arrays were developed and discussed from Chapter 6 to Chapter 8. All these proposed CP antenna elements and arrays demonstrate superior bandwidth performance compared with other CP elements and arrays of the same type.

Chapter 3 presented an ultra-wideband CP antenna with 100% 3 dB AR bandwidth. To achieve impedance matching over this UWB frequency range, a simple but effective impedance matching method without using external matching circuit was implemented and yields good impedance matching over a 3:1 bandwidth. Besides, a novel cavity was designed to improve the FBR of the proposed antenna, which helped achieve an average 30dB FRB over the GNSS bands. With these good features, the CP antenna is very promising for high-performance GNSS applications.

In Chapter 4, two polarization reconfigurable loop antennas were presented for realizing polarization diversity in wireless systems. One of them is with a dual-loop structure while the other one has a single-loop structure, but both of them have the ability to change their polarization to RHCP or LHCP. The latter one has smaller size than the prior one but with wider bandwidth. The bandwidth improvement of the single-loop antenna is realized by introducing another dual-gap loaded parasitic loop. The impedance matching for these two antennas are both implemented by a non-quarter-wavelength single-section transmission line, which is analyzed theoretically and the derived formulas can also be used to achieve good impedance matching for other antennas.

An inverted S-shaped antenna which radiates RHCP wave in a 42% bandwidth was presented and analyzed in Chapter 5. Different to the CP antenna elements discussed in chapters 3 and 4, this inverted S-shaped antenna has wide AR beamwdith in nearly all elevation planes compared with corresponding HPBWs. This unique advanatge makes it very suitable for wide-angle CP beam-scanning applications. In addition, it can be easily extended to arrays and a 4-element linear array with 60% 3 dB AR bandwidth was also designed and investigated in this Chapter.

A wideband multi-layer CP patch element and a dual-CP beam-scanning array with independent beam-scanning ability of its orthogonal polarizations were designed, prototyped and characterized in Chapter 6. As indicated by the measurement results, the presented dual-CP array can scan its beam from broadside to $\pm 23^{o}$ with good impedance matching, high port isolation and good CP radiation from 27 GHz to 30 GHz. It can also be extended to larger-size arrays by using the striplines to design the BFNs. Due to these advantages, the array is suitable for Ka-band satellite communications.

In Chapter 7, a single-layer CP reflectarray which has the widest bandwidth compared with other reported CP reflectarrays was presented. The broad bandwidth feature of the proposed reflectarray mainly attributes to the phasing element which can achieve good CP reflection performance over a 2:1 frequency range. Other factors, such as the angular rotated element method to form a planar phase front in far field were theoretically proved to be beneficial to the bandwidth improvement. Besides, the influence of the differetial spatial phase delay was also discussed quantitatively. With a 68% 3 dB AR bandwidth, a 48% 3 dB gain bandwidth, a 33% larger than 50% aperture efficiency bandwidth and a 2:1 radiation pattern bandwidth, the proposed CP reflectarray shows a breakthrough of bandwidth limitations to CP reflectarrays and shrinks the gap between reflectarrays and other conventional arrays in terms of bandwidth performances.

In the final Chapter, a wideband CP tightly coupled array was presented for the first time. Through the comparison of the bandwidth of a 4×4 CP-TCCDA and a 4×4 conventional CP array using the same element, it is found that both the impedance bandwidth and AR bandwidth can be greatly improved if tightly coupled elements are deployed. Theoretical analysis indicates that the AR bandwidth of the array is bounded by the integrated phase shift line within each element and thus cannot reach the lowest limit of impedance bandwidth. To verify the design concept, a 4×4 CP-TCCDA with complete feeding network were fabricated and measured. The measured results confirm that the proposed array achieves VSWR<3 bandwidth from 2.06 GHz to 6.46 GHz (3.1:1) and 3 dB AR bandwidth from 2.35 GHz to 5.6 GHz (2.4:1), which are much wider than the bandwidth of an isolated element and a conventional array using the same element. As current tightly coupled arrays are all linearly polarized or dual linearly polarized, the presented work offers pioneering method to design wideband CP arrays through the exploiting of strong mutual coupling among array elements.

9.2 Future Work

Although various wideband CP antenna elements and arrays are investigated and designed in this thesis, there are some other works need to be carried out in the future to advance the previous researches. These works include:

- Investigation of wideband millimeter-wave (mm-wave) CP antennas. Millimeter-wave technology is one of the key technologies for next-generation wireless systems, such as the 5G mobile communications and 60 GHz inter-satellite communications. Due to the drastically decreased wavelength and increased dielectric losses at mm-wave bands, it becomes more difficult to design and fabricate wideband CP antennas.
- Investigation of mm-wave wide-angle CP beam-scanning array for satellite communications on the move. For advanced satellite communications, it is preferable that the CP beams can be steered to wide angles for large coverage. Normally, the propagation of surface waves at mm-wave bands shall be greater than the cases at lower frequencies. This makes the wide-angle beam scanning more hard to be implemented at mm-wave bands. Substrate integrated waveguide (SIW) based CP arrays can mitigate the propagation of surface waves effectively and thus are good candidates for wide-angle CP beam-scanning array at mm-wave bands.

- Integration of mm-wave circuits with mm-wave CP antennas. Because of the increased losses at mm-wave bands, there is an increasing trend to integrate mm-wave circuits with antennas, which can reduce the insertion losses of the mm-wave circuits. However, integrating mm-wave circuits with CP antennas will degrade the performance of CP antennas due to the interferences of the circuits. Therefore, it is meaningful to investigate how to mitigate these influences and achieve wide bandwidth for the integrated antennas.
- Large-scale CP arrays with massive CP elements for massive MIMO applications. Massive MIMO technology is promising to achieve very large system capacities and is one of the key technologies for next-generation wireless systems. It is really challenging to deploy numerous CP elements in a CP array while maintaining that the performance of each element is not degraded. Moreover, the mutual coupling among the elements become more severe compared with that in small-size arrays. It is thus meritorious to investigate the large-scale CP arrays.
- Investigation of Terahertz (THz) CP antennas. Recently, there is increased interest in THz antennas due to their growing applications in medical imaging, security screening, and communication. It is valuable to investigate wideband high-gain THz CP antennas, especially for THz imaging systems to increase the detection efficiency. However, the high loss at THz bands is one of the main obstacles for designing THz CP antennas. To reduce the overall size and the loss, integrated on-chip antennas are one promising solution.

References

[1] R. S. Elliot, Antenna theory and design: John Wiley & Sons, 2006.

[2] B. W. Parkinson, Global positioning system: Theory and applications vol. 1: AIAA, 1996.

[3] C. C. Counselman, "Multipath-rejecting GPS antennas," Proceedings of the IEEE, vol. 87, pp. 86-91, 1999.

[4] E. Brookner, W. M. Hall, and R. H. Westlake, "Faraday loss for L-band radar and communications systems," IEEE transactions on aerospace and electronic systems, pp. 459-469, 1985.

[5] W. A. Imbriale, S. Gao, and L. Boccia, Space antenna handbook: John Wiley & Sons, 2012.

[6] S. Gao, Q. Luo, and F. Zhu, Circularly polarized antennas: John Wiley & Sons, 2013.

[7] J. J. Wang, "Antennas for global navigation satellite system (GNSS)," Proceedings of the IEEE, vol. 100, pp. 2349-2355, 2012.

[8] L. I. Basilio, R. L. Chen, J. T. Williams, and D. R. Jackson, "A new planar dual-band GPS antenna designed for reduced susceptibility to low-angle multipath," IEEE Transactions on Antennas and Propagation, vol. 55, pp. 2358-2366, 2007.

[9] J. M. Tranquilla, J. Carr, and H. M. Al-Rizzo, "Analysis of a choke ring groundplane for multipath control in global positioning system (GPS) applications," IEEE Transactions on Antennas and Propagation, vol. 42, pp. 905-911, 1994.

[10] F. Yang and Y. Rahmat-Samii, "A reconfigurable patch antenna using switchable slots for circular polarization diversity," IEEE Microwave and Wireless Components Letters, vol. 12, pp. 96-98, 2002.

[11] S. Gao, A. Sambell, and S. Zhong, "Polarization-agile antennas," IEEE Antennas and Propagation Magazine, vol. 48, pp. 28-37, 2006.

[12] P.-Y. Qin, Y. J. Guo, and C.-H. Liang, "Effect of antenna polarization diversity on MIMO system capacity," IEEE Antennas and Wireless Propagation Letters, vol. 9, pp. 1092-1095, 2010.

[13] X. Bai, S.-W. Qu, S. Yang, J. Hu, and Z.-P. Nie, "Millimeter-wave circularly polarized tapered-elliptical cavity antenna with wide axial-ratio beamwidth," IEEE Transactions on Antennas and Propagation, vol. 64, pp. 811-814, 2016.

[14] X. Qing and Z. N. Chen, "A compact circularly polarized slotted patch antenna for GNSS applications," IEEE Transactions on Antennas and Propagation, vol. 62, pp. 6506-6509, 2014.

[15] Y. Anjani and A. Alphones, "A wide-beam circularly polarized asymmetric-microstrip antenna," IEEE Transactions on Antennas and Propagation, vol. 63, pp. 3764-3768, 2015.

[16] K.-B. Ng, C. H. Chan, and K.-M. Luk, "Low-cost vertical patch antenna with wide axial-ratio beamwidth for handheld satellite communications terminals," IEEE Transactions on Antennas and Propagation, vol. 63, pp. 1417-1424, 2015.

[17] G. C. Tavik, C. L. Hilterbrick, J. B. Evins, J. J. Alter, J. G. Crnkovich, J. W. de Graaf, W. Habicht, G. P. Hrin, S. A. Lessin, and D. C. Wu, "The advanced multifunction RF concept," IEEE Transactions on Microwave Theory and Techniques, vol. 53, pp. 1009-1020, 2005.

[18] P. S. Hall, P. Gardner, and A. Faraone, "Antenna requirements for software defined and cognitive radios," Proceedings of the IEEE, vol. 100, pp. 2262-2270, 2012.

[19] J. P. Doane, K. Sertel, and J. L. Volakis, "A wideband, wide scanning tightly coupled dipole array with integrated balun (TCDA-IB)," IEEE Transactions on Antennas and Propagation, vol. 61, pp. 4538-4548, 2013.
[20] J. Huang and J. A. Encinar, Reflectarray Antennas: John Wiley & Sons, 2007.
[21] B. A. Munk, Finite antenna arrays and FSS: John Wiley & Sons, 2003.
[22] C. A. Balanis, Antenna theory: analysis and design: John Wiley & Sons, 2016.
[23] K. Carver and J. Mink, "Microstrip antenna technology," IEEE Transactions on Antennas and Propagation, vol. 29, pp. 2-24, 1981.
[24] W. Richards, Y. Lo, and D. Harrison, "An improved theory for microstrip antennas and applications," IEEE Transactions on Antennas and Propagation, vol. 29, pp. 38-46, 1981.
[25] H. Iwasaki, "A circularly polarized small-size microstrip antenna with a cross slot," IEEE Transactions on Antennas and Propagation, vol. 44, pp. 1399-1401, 1996.
[26] P. Sharma and K. Gupta, "Analysis and optimized design of single feed circularly polarized microstrip antennas," IEEE Transactions on Antennas and Propagation, vol. 31, pp. 949-955, 1983.
[27] W. Richards and Y. Lo, "Design and theory of circularly polarized microstrip antennas," in IEEE Antennas and Propagation Society International Symposium, 1979, 1979, pp. 117-120.
[28] L. Shen, "The elliptical microstrip antenna with circular polarization," IEEE Transactions on Antennas and Propagation, vol. 29, pp. 90-94, 1981.
[29] J. R. James and P. S. Hall, Handbook of microstrip antennas: IET, 1989.
[30] G. Yang, M. Ali, and R. Dougal, "A wideband circularly polarized microstrip patch antenna for 5 – 6 - GHz wireless LAN applications," Microwave and optical technology letters, vol. 45, pp. 279-285, 2005.
[31] C. W. Su, F. S. Chang, and K. L. Wong, "Broadband circularly polarized inverted - L patch antenna," Microwave and optical technology letters, vol. 38, pp. 134-136, 2003.
[32] S. S. Yang, K.-F. Lee, A. A. Kishk, and K. M. LUK, "Design and study of wideband single feed circularly polarized microstrip antennas," Progress In Electromagnetics Research, 2008.
[33] W. Lo, J. L. Hu, C. Chan, and K. Luk, "L - Shaped probe - feed circularly polarized microstrip patch antenna with a cross slot," Microwave and optical technology letters, vol. 25, pp. 251-253, 2000.
[34] K. L. Chung, "A wideband circularly polarized H-shaped patch antenna," IEEE Transactions on Antennas and Propagation, vol. 58, pp. 3379-3383, 2010.
[35] X. Tang, Y. Long, H. Wong, and K. Lau, "Broadband circularly-polarised patch antenna with 3D meandering strip feed," Electronics letters, vol. 47, pp. 1060-1062, 2011.
[36] F.-S. Chang, K.-L. Wong, and T.-W. Chiou, "Low-cost broadband circularly polarized patch antenna," IEEE Transactions on Antennas and Propagation, vol. 51, pp. 3006-3009, 2003.
[37] N. Herscovici, Z. Sipus, and D. Bonefacic, "Circularly polarized single-fed wide-band microstrip patch," IEEE Transactions on Antennas and Propagation, vol. 51, pp. 1277-1280, 2003.
[38] N. C. Karmakar and M. E. Bialkowski, "Circularly polarized aperture-coupled circular microstrip patch antennas for L-band applications," IEEE Transactions on Antennas and Propagation, vol. 47, pp. 933-940, 1999.

[39] S. D. Targonski and D. M. Pozar, "Design of wideband circularly polarized aperture-coupled microstrip antennas," IEEE Transactions on Antennas and Propagation, vol. 41, pp. 214-220, 1993.
[40] K. P. Esselle and A. Verma, "Wideband circularly polarized stacked microstrip antennas," IEEE Antennas and Wireless Propagation Letters, vol. 6, pp. 21-24, 2007.
[41] R. B. Waterhouse, "Stacked patches using high and low dielectric constant material combinations," IEEE Transactions on Antennas and Propagation, vol. 47, pp. 1767-1771, 1999.
[42] S. Kim and W. Yang, "Single feed wideband circular polarised patch antenna," Electronics letters, vol. 43, pp. 703-704, 2007.
[43] H. Oraizi and R. Pazoki, "Wideband circularly polarized aperture-fed rotated stacked patch antenna," IEEE Transactions on Antennas and Propagation, vol. 61, pp. 1048-1054, 2013.
[44] K.-L. Wong and T.-W. Chiou, "Broad-band single-patch circularly polarized microstrip antenna with dual capacitively coupled feeds," IEEE Transactions on Antennas and Propagation, vol. 49, pp. 41-44, 2001.
[45] Y.-X. Guo, K.-W. Khoo, and L. C. Ong, "Wideband circularly polarized patch antenna using broadband baluns," IEEE Transactions on Antennas and Propagation, vol. 56, pp. 319-326, 2008.
[46] J.-W. Baik, K.-J. Lee, W.-S. Yoon, T.-H. Lee, and Y.-S. Kim, "Circularly polarised printed crossed dipole antennas with broadband axial ratio," Electronics letters, vol. 44, pp. 785-786, 2008.
[47] J.-W. Baik, T.-H. Lee, S. Pyo, S.-M. Han, J. Jeong, and Y.-S. Kim, "Broadband circularly polarized crossed dipole with parasitic loop resonators and its arrays," IEEE Transactions on Antennas and Propagation, vol. 59, pp. 80-88, 2011.
[48] Y. He, W. He, and H. Wong, "A wideband circularly polarized cross-dipole antenna," IEEE Antennas and Wireless Propagation Letters, vol. 13, pp. 67-70, 2014.
[49] S. X. Ta and I. Park, "Crossed dipole loaded with magneto-electric dipole for wideband and wide-beam circularly polarized radiation," IEEE Antennas and Wireless Propagation Letters, vol. 14, pp. 358-361, 2015.
[50] X. Qing and Y. Chia, "Broadband circularly polarised slot loop antenna fed by three-stub hybrid coupler," Electronics letters, vol. 35, pp. 1210-1211, 1999.
[51] L. Y. Tseng and T. Y. Han, "Microstrip ‐ fed circular slot antenna for circular polarization," Microwave and optical technology letters, vol. 50, pp. 1056-1058, 2008.
[52] Y. Chen, X. Liu, Y. Jiao, and F. Zhang, "CPW-fed broadband circularly polarised square slot antenna," Electronics letters, vol. 42, p. 1, 2006.
[53] J.-Y. Sze, K.-L. Wong, and C.-C. Huang, "Coplanar waveguide-fed square slot antenna for broadband circularly polarized radiation," IEEE Transactions on Antennas and Propagation, vol. 51, pp. 2141-2144, 2003.
[54] J.-Y. Sze, C.-I. Hsu, Z.-W. Chen, and C.-C. Chang, "Broadband CPW-fed circularly polarized square slot antenna with lightening-shaped feedline and inverted-L grounded strips," IEEE Transactions on Antennas and Propagation, vol. 58, pp. 973-977, 2010.
[55] J.-S. Row and S.-W. Wu, "Circularly-polarized wide slot antenna loaded with a parasitic patch," IEEE Transactions on Antennas and Propagation, vol. 56, pp. 2826-2832, 2008.
[56] H. Nakano, Helical and spiral antennas: Wiley Online Library, 1987.

[57] D. K. John and J. M. Ronald, "Antennas: for all applications," Mc Graw Hill, 2002.
[58] J. D. Kraus, "The helical antenna," Proceedings of the IRE, vol. 37, pp. 263-272, 1949.
[59] J. Dyson, "The equiangular spiral antenna," IRE Transactions on Antennas and Propagation, vol. 7, pp. 181-187, 1959.
[60] H. Nakano, K. Nogami, S. Arai, H. Mimaki, and J. Yamauchi, "A spiral antenna backed by a conducting plane reflector," IEEE Transactions on Antennas and Propagation, vol. 34, pp. 791-796, 1986.
[61] J. Kaiser, "The Archimedean two-wire spiral antenna," IRE Transactions on Antennas and Propagation, vol. 8, pp. 312-323, 1960.
[62] H. Nakano, S. Okuzawa, K. Ohishi, H. Mimaki, and J. Yamauchi, "A curl antenna," IEEE Transactions on Antennas and Propagation, vol. 41, pp. 1570-1575, 1993.
[63] R.-L. Li, V. F. Fusco, and H. Nakano, "Circularly polarized open-loop antenna," IEEE Transactions on Antennas and Propagation, vol. 51, pp. 2475-2477, 2003.
[64] R. Li, G. DeJean, J. Laskar, and M. M. Tentzeris, "Investigation of circularly polarized loop antennas with a parasitic element for bandwidth enhancement," IEEE Transactions on Antennas and Propagation, vol. 53, pp. 3930-3939, 2005.
[65] H. Nakano, H. Takeda, T. Honma, H. Mimaki, and J. Yamauchi, "Extremely low-profile helix radiating a circularly polarized wave," IEEE Transactions on Antennas and Propagation, vol. 39, pp. 754-757, 1991.
[66] H. Nakano, N. Mizobe, K. Kuriyama, and J. Yamauchi, "Low-profile helical antenna with a cavity," in Wireless Information Technology and Systems (ICWITS), 2012 IEEE International Conference on, 2012, pp. 1-4.
[67] R. Barts and W. Stutzman, "A reduced size helical antenna," in IEEE Antennas and Propagation Society International Symposium, 1997., 1997, pp. 1588-1591.
[68] S.-G. Mao, J.-C. Yeh, and S.-L. Chen, "Ultrawideband circularly polarized spiral antenna using integrated balun with application to time-domain target detection," IEEE Transactions on Antennas and Propagation, vol. 57, pp. 1914-1920, 2009.
[69] W.-H. Tu and K. Chang, "Wide-band microstrip-to-coplanar stripline/slotline transitions," IEEE Transactions on Microwave Theory and Techniques, vol. 54, pp. 1084-1089, 2006.
[70] R. Li, J. Laskar, and M. Tentzeris, "Wideband probe-fed circularly polarised circular loop antenna," Electronics letters, vol. 41, pp. 997-999, 2005.
[71] R. Li, A. Traille, J. Laskar, and M. M. Tentzeris, "Bandwidth and gain improvement of a circularly polarized dual-rhombic loop antenna," IEEE Antennas and Wireless Propagation Letters, vol. 5, pp. 84-87, 2006.
[72] H. Zhou and W. Hong, "Compact Circularly Polarized Patch Array Antenna," IEEE Antennas and Wireless Propagation Letters, vol. 15, pp. 778-781, 2016.
[73] Z.-y. Zhang, N.-w. Liu, S. Zuo, Y. Li, and G. Fu, "Wideband circularly polarised array antenna with flat-top beam pattern," IET Microwaves, Antennas & Propagation, vol. 9, pp. 755-761, 2015.
[74] R. R. Ramirez and N. G. Alexopoulos, "Single feed proximity coupled circularly polarized microstrip monofilar Archimedean spiral antenna array," IEEE Transactions on Antennas and Propagation, vol. 47, pp. 406-407, 1999.
[75] J. Huang, "A technique for an array to generate circular polarization with linearly polarized elements," IEEE Transactions on Antennas and Propagation, vol. 34, pp. 1113-1124, 1986.

[76] P. Hall, J. Dahele, and J. James, "Design principles of sequentially fed, wide bandwidth, circularly polarised microstrip antennas," in IEE Proceedings H (Microwaves, Antennas and Propagation), 1989, pp. 381-389.
[77] A. Chen, Y. Zhang, Z. Chen, and C. Yang, "Development of a Ka-band wideband circularly polarized 64-element microstrip antenna array with double application of the sequential rotation feeding technique," IEEE Antennas and Wireless Propagation Letters, vol. 10, pp. 1270-1273, 2011.
[78] A. R. Weily and Y. J. Guo, "Circularly polarized ellipse-loaded circular slot array for millimeter-wave WPAN applications," IEEE Transactions on Antennas and Propagation, vol. 57, pp. 2862-2870, 2009.
[79] J. Huang, Reflectarray antenna: Wiley Online Library, 2007.
[80] L.-S. Ren, Y.-C. Jiao, F. Li, J.-J. Zhao, and G. Zhao, "A dual-layer T-shaped element for broadband circularly polarized reflectarray with linearly polarized feed," IEEE Antennas and Wireless Propagation Letters, vol. 10, pp. 407-410, 2011.
[81] M.-Y. Zhao, G.-Q. Zhang, X. Lei, J.-M. Wu, and J.-Y. Shang, "Design of new single-layer multiple-resonance broadband circularly polarized reflectarrays," IEEE Antennas and Wireless Propagation Letters, vol. 12, pp. 356-359, 2013.
[82] S. M. A. M. H. Abadi and N. Behdad, "Broadband True-Time-Delay Circularly Polarized Reflectarray With Linearly Polarized Feed," IEEE Transactions on Antennas and Propagation, vol. 64, pp. 4891-4896, 2016.
[83] D. Pozar, "Wideband reflectarrays using artificial impedance surfaces," Electronics letters, vol. 43, pp. 148-149, 2007.
[84] G. Zhao, Y.-C. Jiao, F. Zhang, and F.-S. Zhang, "A subwavelength element for broadband circularly polarized reflectarrays," IEEE Antennas and Wireless Propagation Letters, vol. 9, pp. 330-333, 2010.
[85] G.-B. Wu, S.-W. Qu, S. Yang, and C. H. Chan, "Broadband, Single-Layer Dual Circularly Polarized Reflectarrays With Linearly Polarized Feed," IEEE Transactions on Antennas and Propagation, vol. 64, pp. 4235-4241, 2016.
[86] M. Nurnberger and J. Volakis, "A new planar feed for slot spiral antennas," IEEE Transactions on Antennas and Propagation, vol. 44, pp. 130-131, 1996.
[87] F. Scire-Scappuzzo and S. N. Makarov, "A low-multipath wideband GPS antenna with cutoff or non-cutoff corrugated ground plane," IEEE Transactions on Antennas and Propagation, vol. 57, pp. 33-46, 2009.
[88] J. Tranquilla, J. Carr, and H. M. Al-Rizzo, "Analysis of a choke ring groundplane for multipath control in global positioning system (GPS) applications," IEEE Transactions on Antennas and Propagation, vol. 42, pp. 905-911, 1994.
[89] M. Maqsood, S. Gao, T. Brown, M. Unwin, R. de vos Van Steenwijk, and J. Xu, "A Compact Multipath Mitigating Ground Plane for Multiband GNSS Antennas," IEEE Transactions on Antennas and Propagation, vol. 61, pp. 2775-2782, 2013.
[90] Y.-F. Lin, Y.-K. Wang, H.-M. Chen, and Z.-Z. Yang, "Circularly polarized crossed dipole antenna with phase delay lines for RFID handheld reader," IEEE Transactions on Antennas and Propagation, vol. 60, pp. 1221-1227, 2012.
[91] S. Ta, H. Choo, I. Park, and R. Ziolkowski, "Multi-band, wide-beam, circularly polarized, crossed, asymmetrically barbed dipole antennas for GPS applications," IEEE Transactions on Antennas and Propagation, vol. 61, pp. 5771-5775, 2013.
[92] K. Saurav, D. Sarkar, and K. Srivastava, "Dual Band Circularly Polarized Cavity Backed Crossed Dipole Antennas," IEEE Antennas and Wireless Propagation Letters, vol. 14, pp. 52-55.

[93] H. Nishiyama and M. Nakamura, "Form and capacitance of parallel-plate capacitors," IEEE Transactions on Components, Packaging, and Manufacturing Technology, Part A, vol. 17, pp. 477-484, 1994.
[94] B. Y. Toh, R. Cahill, and V. F. Fusco, "Understanding and measuring circular polarization," IEEE Transactions on Education, vol. 46, pp. 313-318, 2003.
[95] M. Boti, L. Dussopt, and J. Laheurte, "Circularly polarised antenna with switchable polarisation sense," Electronics letters, vol. 36, pp. 1518-1519, 2000.
[96] X. X. Yang and S. S. Zhong, "Analysis of two dual‐polarization square‐patch antennas," Microwave and optical technology letters, vol. 26, pp. 153-156, 2000.
[97] P.-Y. Qin, Y. Guo, and C.-H. Liang, "Effect of antenna polarization diversity on MIMO system capacity," IEEE Antennas and Wireless Propagation Letters, vol. 9, pp. 1092-1095, 2010.
[98] B. A. Cetiner, E. Akay, E. Sengul, and E. Ayanoglu, "A MIMO system with multifunctional reconfigurable antennas," IEEE Antennas and Wireless Propagation Letters, vol. 5, pp. 463-466, 2006.
[99] P.-Y. Qin, A. R. Weily, Y. Guo, and C.-H. Liang, "Polarization reconfigurable U-slot patch antenna," IEEE Transactions on Antennas and Propagation, vol. 58, pp. 3383-3388, 2010.
[100] S.-H. Hsu and K. Chang, "A novel reconfigurable microstrip antenna with switchable circular polarization," IEEE Antennas and Wireless Propagation Letters, vol. 6, pp. 160-162, 2007.
[101] R.-H. Chen and J.-S. Row, "Single-fed microstrip patch antenna with switchable polarization," IEEE Transactions on Antennas and Propagation, vol. 56, pp. 922-926, 2008.
[102] F. Ferrero, C. Luxey, R. Staraj, G. Jacquemod, M. Yedlin, and V. Fusco, "A novel quad-polarization agile patch antenna," IEEE Transactions on Antennas and Propagation, vol. 57, pp. 1563-1567, 2009.
[103] A. Garcia-Aguilar, J. Inclan-Alonso, L. Vigil-Herrero, J. Fernandez-Gonzalez, and M. Sierra-Pérez, "Low-profile dual circularly polarized antenna array for satellite communications in the X band," IEEE Transactions on Antennas and Propagation, vol. 60, pp. 2276-2284, 2012.
[104] R. Li, N. A. Bushyager, J. Laskar, and M. M. Tentzeris, "Determination of reactance loading for circularly polarized circular loop antennas with a uniform traveling-wave current distribution," IEEE Transactions on Antennas and Propagation, vol. 53, pp. 3920-3929, 2005.
[105] R. Li, J. Laskar, and M. M. Tentzeris, "Broadband circularly polarized rectangular loop antenna with impedance matching," IEEE Microwave and Wireless Components Letters, vol. 16, p. 52, 2006.
[106] D. M. Pozar, Microwave engineering: John Wiley & Sons, 2009.
[107] Y. Luo, Q.-X. Chu, and L. Zhu, "A low-profile wide-beamwidth circularly-polarized antenna via two pairs of parallel dipoles in a square contour," IEEE Transactions on Antennas and Propagation, vol. 63, pp. 931-936, 2015.
[108] H. Jiang, Z. Xue, W. Li, and W. Ren, "Broad beamwidth stacked patch antenna with wide circularly polarised bandwidth," Electronics letters, vol. 51, pp. 10-12, 2014.
[109] K. M. Mak and K. M. Luk, "A circularly polarized antenna with wide axial ratio beamwidth," IEEE Transactions on Antennas and Propagation, vol. 57, pp. 3309-3312, 2009.

[110] S. X. Ta and I. Park, "Crossed dipole loaded with magneto-electric dipole for wideband and wide-beam circularly polarized radiation," IEEE Antennas Wireless Propagation Letters, vol. 14, pp. 358-361, 2015.

[111] H. Elkamchouchi and M. A. Nasr, "The S-shaped dipole antenna," in Microwave and Millimeter Wave Technology, 2004. ICMMT 4th International Conference on, Proceedings, 2004, pp. 19-22.

[112] L. Zhang, S. Gao, Q. Luo, and W. Li, "Wideband circularly polarized wide-beamwidth antenna using S-shaped dipole," in Antenna Technology: Small Antennas, Innovative Structures, and Applications (iWAT), 2017 International Workshop on, 2017, pp. 118-121.

[113] D. Yu, S.-X. Gong, Y.-T. Wan, Y.-L. Yao, Y.-X. Xu, and F.-W. Wang, "Wideband omnidirectional circularly polarized patch antenna based on vortex slots and shorting vias," IEEE Transactions on Antennas and Propagation, vol. 62, pp. 3970-3977, 2014.

[114] K.-F. Hung and Y.-C. Lin, "Novel broadband circularly polarized cavity-backed aperture antenna with traveling wave excitation," IEEE Transactions on Antennas and Propagation, vol. 58, pp. 35-42, 2010.

[115] P. Hall, J. Dahele, and J. James, "Design principles of sequentially fed, wide bandwidth, circularly polarised microstrip antennas," in IEE Proceedings H Microw. Antennas and Propag. , 1989, pp. 381-389.

[116] R. Bawer and J. Wolfe, "A printed circuit balun for use with spiral antennas," IRE Transactions on on Microwave Theory and Techniques, vol. 8, pp. 319-325, 1960.

[117] D. Pozar, "Wideband reflectarrays using artificial impedance surfaces," Electronics Letters, vol. 43, p. 1, 2007.

[118] C. Zhang, X. Liang, X. Bai, J. Geng, and R. Jin, "A broadband dual circularly polarized patch antenna with wide beamwidth," IEEE Antennas Wireless Propagation Letters, vol. 13, pp. 1457-1460, 2014.

[119] X.-Z. Lai, Z.-M. Xie, Q.-Q. Xie, and X.-L. Cen, "A dual circularly polarized RFID reader antenna with wideband isolation," IEEE Antennas Wireless Propagation Letters, vol. 12, pp. 1630-1633, 2013.

[120] A. Narbudowicz, X. Bao, and M. J. Ammann, "Dual circularly-polarized patch antenna using even and odd feed-line modes," IEEE Transactions on Antennas and Propagation, vol. 61, pp. 4828-4831, 2013.

[121] S. Ye, J. Geng, X. Liang, Y. J. Guo, and R. Jin, "A compact dual-band orthogonal circularly polarized antenna array with disparate elements," IEEE Transactions on Antennas and Propagation, vol. 63, pp. 1359-1364, 2015.

[122] Q. Luo, S. Gao, M. Sobhy, J. T. S. Sumantyo, J. Li, G. Wei, J. Xu, and C. Wu, "Dual Circularly Polarized Equilateral Triangular Patch Array," IEEE Transactions on Antennas and Propagation, vol. 64, pp. 2255-2262, 2016.

[123] A. García-Aguilar, J.-M. Inclán-Alonso, L. Vigil-Herrero, J.-M. Fernández-González, and M. Sierra-Pérez, "Low-profile dual circularly polarized antenna array for satellite communications in the X band," IEEE Transactions on Antennas and Propagation, vol. 60, pp. 2276-2284, 2012.

[124] J. A. Encinar and J. A. Zornoza, "Broadband design of three-layer printed reflectarrays," IEEE Transactions on Antennas and Propagation, vol. 51, pp. 1662-1664, 2003.

[125] J. A. Encinar, "Design of two-layer printed reflectarrays using patches of variable size," IEEE Transactions on Antennas and Propagation, vol. 49, pp. 1403-1410, 2001.

[126] P.-Y. Qin, Y. J. Guo, and A. R. Weily, "Broadband Reflectarray Antenna Using Subwavelength Elements Based on Double Square Meander-Line Rings," IEEE Transactions on Antennas and Propagation, vol. 64, pp. 378-383, 2016.

[127] Y. Mao, S. Xu, F. Yang, and A. Z. Elsherbeni, "A novel phase synthesis approach for wideband reflectarray design," IEEE Transactions on Antennas and Propagation, vol. 63, pp. 4189-4193, 2015.

[128] E. Carrasco, J. A. Encinar, and M. Barba, "Bandwidth improvement in large reflectarrays by using true-time delay," IEEE Transactions on Antennas and Propagation, vol. 56, pp. 2496-2503, 2008.

[129] Y. Li, M. E. Bialkowski, and A. M. Abbosh, "Single layer reflectarray with circular rings and open-circuited stubs for wideband operation," IEEE Transactions on Antennas and Propagation, vol. 60, pp. 4183-4189, 2012.

[130] J. Huang and R. J. Pogorzelski, "A Ka-band microstrip reflectarray with elements having variable rotation angles," IEEE Transactions on Antennas and Propagation, vol. 46, pp. 650-656, 1998.

[131] A. Yu, F. Yang, A. Elsherbeni, J. Huang, and Y. Kim, "An offset-fed X-band reflectarray antenna using a modified element rotation technique," IEEE Transactions on Antennas and Propagation, vol. 60, pp. 1619-1624, 2012.

[132] R. Deng, Y. Mao, S. Xu, and F. Yang, "A Single-Layer Dual-Band Circularly Polarized Reflectarray With High Aperture Efficiency," IEEE Transactions on Antennas and Propagation, vol. 63, pp. 3317-3320, 2015.

[133] R. S. Malfajani and Z. Atlasbaf, "Design and implementation of a dual-band single layer reflectarray in X and K bands," IEEE Transactions on Antennas and Propagation, vol. 62, pp. 4425-4431, 2014.

[134] A. Mahmoud, A. A. Kishk, Z. Hao, and W. Hong, "Ka-band circularly polarized reflectarray: Using a double-layers cross slot," IEEE Antennas and Propagation Magazine, vol. 58, pp. 60-68, 2016.

[135] D. M. Pozar, S. D. Targonski, and H. Syrigos, "Design of millimeter wave microstrip reflectarrays," IEEE Transactions on Antennas and Propagation, vol. 45, pp. 287-296, 1997.

[136] P. Nayeri, A. Z. Elsherbeni, and F. Yang, "Radiation Analysis Approaches for Reflectarray Antennas," IEEE Antennas and Propagation Magazine, vol. 55, pp. 127-134, 2013.

[137] D. M. Pozar, "Bandwidth of reflectarrays," Electronics letters, vol. 39, pp. 1490-1491, 2003.

[138] J. Bornemann and V. A. Labay, "Ridge waveguide polarizer with finite and stepped-thickness septum," IEEE Transactions on on Microwave Theory and Techniques, vol. 43, pp. 1782-1787, 1995.

[139] J. Shin and D. H. Schaubert, "A parameter study of stripline-fed Vivaldi notch-antenna arrays," IEEE Transactions on Antennas and Propagation, vol. 47, pp. 879-886, 1999.

[140] J. Lee, S. Livingston, and R. Koenig, "A low-profile wide-band (5: 1) dual-pol array," IEEE Antennas and Wireless Propagation Letters, vol. 2, pp. 46-49, 2003.

[141] E. Yetisir, N. Ghalichechian, and J. L. Volakis, "Ultrawideband Array With 70° Scanning Using FSS Superstrate," IEEE Transactions on Antennas and Propagation, vol. 64, pp. 4256-4265, 2016.

[142] H. Wheeler, "Simple relations derived fom a phased-array antenna made of an infinite current sheet," IEEE Transactions on Antennas and Propagation, vol. 13, pp. 506-514, 1965.

[143] R. Hansen, "Linear connected arrays [coupled dipole arrays]," IEEE Antennas and Wireless Propagation Letters, vol. 3, pp. 154-156, 2004.
[144] A. Neto and J. Lee, "Ultrawide-band properties of long slot arrays," IEEE Transactions on Antennas and Propagation, vol. 54, pp. 534-543, 2006.
[145] D. Cavallo, A. Neto, G. Gerini, A. Micco, and V. Galdi, "A 3-to 5-GHz wideband array of connected dipoles with low cross polarization and wide-scan capability," IEEE Transactions on Antennas and Propagation, vol. 61, pp. 1148-1154, 2013.
[146] D. Cavallo and A. Neto, "A connected array of slots supporting broadband leaky waves," IEEE Transactions on Antennas and Propagation, vol. 61, pp. 1986-1994, 2013.
[147] R. J. Bolt, D. Cavallo, G. Gerini, D. Deurloo, R. Grooters, A. Neto, and G. Toso, "Characterization of a Dual-Polarized Connected-Dipole Array for Ku-Band Mobile Terminals," IEEE Transactions on Antennas and Propagation, vol. 64, pp. 591-598, 2016.
[148] W. F. Moulder, K. Sertel, and J. L. Volakis, "Superstrate-enhanced ultrawideband tightly coupled array with resistive FSS," IEEE Transactions on Antennas and Propagation, vol. 60, pp. 4166-4172, 2012.
[149] I. Tzanidis, K. Sertel, and J. L. Volakis, "UWB low-profile tightly coupled dipole array with integrated balun and edge terminations," IEEE Transactions on Antennas and Propagation, vol. 61, pp. 3017-3025, 2013.
[150] J. A. Kasemodel, C.-C. Chen, and J. L. Volakis, "Wideband planar array with integrated feed and matching network for wide-angle scanning," IEEE Transactions on Antennas and Propagation, vol. 61, pp. 4528-4537, 2013.
[151] M. H. Novak and J. L. Volakis, "Ultrawideband antennas for multiband satellite communications at UHF–Ku frequencies," IEEE Transactions on Antennas and Propagation, vol. 63, pp. 1334-1341, 2015.
[152] L. Di Palma, A. Clemente, L. Dussopt, R. Sauleau, P. Potier, and P. Pouliguen, "Circularly Polarized Transmitarray With Sequential Rotation in Ka-Band," IEEE Transactions on Antennas and Propagation, vol. 63, pp. 5118-5124, 2015.
[153] K. L. Chung, "High-performance circularly polarized antenna array using metamaterial-line based feed network," IEEE Transactions on Antennas and Propagation, vol. 61, pp. 6233-6237, 2013.
[154] R. Guinvarc'h and R. L. Haupt, "Connecting spirals for wideband dual polarization phased array," IEEE Transactions on Antennas and Propagation, vol. 59, pp. 4534-4541, 2011.
[155] I. D. H. Sáenz, R. Guinvarc'h, R. L. Haupt, and K. Louertani, "A 6: 1 Bandwidth, Low-Profile, Dual-Polarized Ring Array of Spiral Antennas With Connecting Arms," IEEE Transactions on Antennas and Propagation, vol. 64, pp. 752-756, 2016.